

MATERIALS PHYSICS AND MECHANICS

Vol. 52, No. 1, 2024

125[®]

MATERIALS PHYSICS AND MECHANICS

Principal Editors:

Alexander Belyaev

Andrei Rudskoi

Institute for Problems in Mechanical Engineering of the Russian Academy of Science (RAS), Russia

Peter the Great St . Petersburg Polytechnic University, Russia

Founder and Honorary Editor: Ilya Ovid'ko (1961-2017)

Institute for Problems in Mechanical Engineering of the Russian Academy of Sciences (RAS), Russia

Associate Editor:

Anna Kolesnikova

Artem Semenov

Institute for Problems in Mechanical Engineering of the Russian Academy of Sciences (RAS), Russia

Peter the Great St. Petersburg Polytechnic University, Russia

Editorial Board:

E.C. Aifantis

Aristotle University of Thessaloniki, Greece

K.E. Aifantis

University of Florida, USA

U. Balachandran

Argonne National Laboratory, USA

A. Bellosi

Research Institute for Ceramics Technology, Italy

S.V. Bobylev

Institute for Problems in Mechanical Engineering (RAS), Russia

A.I. Borovkov

Peter the Great St.Petersburg Polytechnic University, Russia

G.-M. Chow

National University of Singapore, Singapore

Yu. Estrin

Monash University, Australia

A.B. Freidin

Institute for Problems in Mechanical Engineering (RAS), Russia

Y. Gogotsi

Drexel University, USA

I.G. Goryacheva

Institute of Problems of Mechanics (RAS), Russia

D. Hui

University of New Orleans, USA

G. Kiriakidis

IESL/FORTH, Greece

D.M. Klimov

Institute of Problems of Mechanics (RAS), Russia

G.E. Kodzhaspirov

Peter the Great St. Petersburg Polytechnic University, Russia

S.A. Kukushkin

Institute for Problems in Mechanical Engineering (RAS), Russia

T.G. Langdon

University of Southampton, U.K.

V.P. Matveenko

Institute of Continuous Media Mechanics (RAS), Russia

A.I. Melker

Peter the Great St. Petersburg Polytechnic University, Russia

Yu.l. Meshcheryakov

Institute for Problems in Mechanical Engineering (RAS), Russia

N.F. Morozov

St. Petersburg State University, Russia

R.R. Mulyukov

Institute for Metals Superplasticity Problems (RAS), Russia

Yu.V. Petrov

St. Petersburg State University, Russia

N.M. Pugno

Politecnico di Torino, Italy

B.B. Rath

Naval Research Laboratory, USA

A.E. Romanov

Ioffe Institute (RAS), Russia

A.M. Sastry

University of Michigan, Ann Arbor, USA

B.A. Schrefler

University of Padua, Italy

N.V. Skiba

Institute for Problems in Mechanical Engineering (RAS), Russia

A.G. Sheinerman

Institute for Problems in Mechanical Engineering (RAS), Russia

R.Z. Valiev

Ufa State Aviation Technical University, Russia

K. Zhou

Nanyang Technological University, Singapore

"Materials Physics and Mechanics" Editorial Office:

Phone: +7(812)552 77 78, ext. 224 E-mail: mpmjournal@spbstu.ru Web-site: http://www.mpm.spbstu.ru

International scientific journal "Materials Physics and Mechanics" is published by Peter the Great St. Petersburg Polytechnic University in collaboration with Institute for Problems for Mechanical Engineering in the Russian Academy of Sciences in both hard copy and electronic versions. The journal provides an international medium for the publication of reviews and original research papers written in English and focused on the following topics:

- Mechanics of composite and nanostructured materials.
- Physics of strength and plasticity of composite and nanostructured materials.
- Mechanics of deformation and fracture processes in conventional materials (solids).
- Physics of strength and plasticity of conventional materials (solids).
- Physics and mechanics of defects in composite, nanostructured, and conventional materials.
- Mechanics and physics of materials in coupled fields.

Owner organizations: Peter the Great St. Petersburg Polytechnic University; Institute of Problems of Mechanical Engineering RAS.

Materials Physics and Mechanics is indexed in Chemical Abstracts, Cambridge Scientific Abstracts,
Web of Science Emerging Sources Citation Index (ESCI) and Elsevier Bibliographic Databases (in particular, SCOPUS).

© 2024, Peter the Great St. Petersburg Polytechnic University © 2024, Institute for Problems in Mechanical Engineering RAS



МЕХАНИКА И ФИЗИКА МАТЕРИАЛОВ

Materials Physics and Mechanics

Том 52, номер 1, 2024 год

Учредители:

Редакционная коллегия журнала Главные редакторы:

д.ф.-м.н., чл.-корр. РАН А.К. Беляев Институт проблем машиноведения Российской академии наук (РАН)

д.т.н., академик РАН А.И. Рудской Санкт-Петербургский политехнический университет Петра Великого

Основатель и почетный редактор: д.ф.-м.н. И.А. Овидько (1961-2017)

Институт проблем машиноведения Российской академии наук (РАН)

Ответственные редакторы

д.ф.-м.н. А.Л. Колесникова

Институт проблем машиноведения

Российской академии наук (РАН)

д.ф.-м.н. А.С. Семенов Санкт-Петербургский политехнический университет Петра Великого

Международная редакционная коллегия:

д.ф.-м.н. С.В. Бобылев

Институт проблем машиноведения РАН, Россия

к.т.н., проф. А.И. Боровков

Санкт-Петербургский политехнический ун-т Петра Великого, Россия

д.ф.-м.н., проф. Р.З. Валиев

Уфимский государственный технический университет, Россия

д.ф.-м.н., академик РАН И.Г. Горячева

Институт проблем механики РАН, Россия д.ф.-м.н., академик РАН Д.М. Климов

Институт проблем механики РАН, Россия

д.т.н., проф. Г.Е. Коджаспиров

Санкт-Петербургский политехнический ун-т Петра Великого, Россия

д.ф.-м.н., проф. С.А. Кукушкин

Институт проблем машиноведения РАН, Россия

д.ф.-м.н., академик РАН В.П. Матвеенко

Институт механики сплошных сред РАН, Россия

д.ф.-м.н., проф. А.И. Мелькер

Санкт-Петербургский политехнический ун-т Петра Великого, Россия

д.ф.-м.н., проф. Ю.И. Мещеряков

Институт проблем машиноведения РАН, Россия

д.ф.-м.н., академик РАН Н.Ф. Морозов

Санкт-Петербургский государственный университет, Россия

д.ф.-м.н., чл.-корр. РАН **Р.Р. Мулюков**

Институт проблем сверхпластичности металлов РАН, Россия д.ф.-м.н., чл.-корр. РАН Ю.В. Петров

Санкт-Петербургский государственный университет, Россия

д.ф.-м.н., проф. А.Е. Романов

Физико-технический институт им. А.Ф. Иоффе РАН, Россия

д.ф.-м.н. **Н.В. Скиба** Институт проблем машиноведения РАН, Россия

д.ф.-м.н., проф. А.Б. Фрейдин

Институт проблем машиноведения РАН, Россия

д.ф.-м.н. А.Г. Шейнерман

Институт проблем машиноведения РАН, Россия

Prof., Dr. E.C. Aifantis

Aristotle University of Thessaloniki, Greece

Dr. K.E. Aifantis

University of Florida, USA

Dr. U. Balachandran

Argonne National Laboratory, USA

Dr. A. Bellosi

Research Institute for Ceramics Technology, Italy

Prof., Dr. G.-M. Chow

National University of Singapore, Singapore

Prof., Dr. Yu. Estrin

Monash University, Australia

Prof., Dr. Y. Gogotsi

Drexel University, USA

Prof., Dr. **D. Hui**

University of New Orleans, USA

Prof., Dr. G. Kiriakidis

IESL/FORTH, Greece

Prof., Dr. T.G. Langdon

University of Southampton, UK Prof., Dr. N.M. Pugno

Politecnico di Torino, Italy

Dr. B.B. Rath

Naval Research Laboratory, USA

Prof., Dr. A.M. Sastry

University of Michigan, Ann Arbor, USA

Prof., Dr. B.A. Schrefler

University of Padua, Italy

Prof. Dr. K. Zhou Nanyang Technological University, Singapore

Тел.: +7(812)552 77 78, доб. 224 E-mail: mpmjournal@spbstu.ru Web-site: http://www.mpm.spbstu.ru

Тематика журнала

Международный научный журнал "Materials Physics and Mechanics" издается Санкт-Петербургским политехническим университетом Петра Великого в сотрудничестве с Институтом проблем машиноведения Российской академии наук в печатном виде и электронной форме. Журнал публикует обзорные и оригинальные научные статьи на английском языке по следующим тематикам:

- Механика композиционных и наноструктурированных материалов.
- Физика прочности и пластичности композиционных и наноструктурированных материалов.
- Механика процессов деформации и разрушения в традиционных материалах (твердых телах).
- Физика прочности и пластичности традиционных материалов (твердых тел).
- Физика и механика дефектов в композиционных, наноструктурированных и традиционных материалах.
- Механика и физика материалов в связанных полях.

Редколлегия принимает статьи, которые нигде ранее не опубликованы и не направлены для опубликования в другие научные издания. Все представляемые в редакцию журнала "Механика и физика материалов" статьи рецензируются. Статьи могут отправляться авторам на доработку. Не принятые к опубликованию статьи авторам не возвращаются.

Журнал "Механика и физика материалов" ("Materials Physics and Mechanics") включен в систему цитирования Web of Science Emerging Sources Citation Index (ESCI), SCOPUS и РИНЦ.

> © 2024, Санкт-Петербургский политехнический университет Петра Великого © 2024, Институт проблем машиноведения Российской академии наук

Contents

Impact of non-local, two temperature and impedance parameters on propagation of waves in generalized thermoelastic medium under modified Green-Lindsay model S. Kaushal, R. Kumar, I. Bala, G. Sharma	1-17
Subcritical growth of repolarization nuclei in polycrystalline ferroelectric films A.Yu. Belov	18-25
Moment-membrane theory of elastic cylindrical shells as a continual model of deformation of a single-layer carbon nanotube <i>S.H. Sargsyan</i>	26-38
Emission of lattice dislocations from triple junctions of grain boundaries in high-temperature ceramics with amorphous intercrystalline layers <i>M.Yu. Gutkin, N.V. Skiba</i>	39-48
Analytical description of the Bauschinger effect using experimental data and the generalized Masing principle S.I. Feoktistov, I.K. Andrianov	49-59
E-Green's function molecular dynamics method for contact mechanics with a viscoelastic layer V.G. Petrenko, I.U. Solovyov, E.V. Antonov, L.M. Dorogin, Y. Murugesan	60-68
Numerical estimation of fatigue life of aluminum alloy specimen with surface defects based on stress-life approach L.A. Almazova, O.S. Sedova	69-80
Microstructure, mechanical properties and heat resistance of AL30 piston alloy produced via electromagnetic casting M.Yu. Murashkin, L.I. Zainullina, M.M. Motkov, A.E. Medvedev, V.N. Timofeev, N.A. Enike	81-94 eev
Influence of various friction stir processing (FSP) schemes on the microstructure and properties of AD31 aluminium alloy busbar A.E. Medvedev, V.V. Atroshchenko, A.S. Selivanov, A.R. Bogdanov, M.V. Gorbatkov, Y.V. Logachev, V.S. Lobachev	95-107
Role of heat treatment on mechanical and wear characteristics of Al-TiC composites T.P. Gowrishankar, B. Sangmesh	08-117
Influence of aging on fatigue strength of carbon fiber reinforced plastics A.R. Arutyunyan	18-125

Influence of glass fibers on the physico-mechanical and performance properties of rubber based on general and special purpose caoutchoucs E.N. Egorov, N.I. Kol'tsov	126-131
Experimental investigation on flexural fatigue strength of graphene oxide modified E-glass epoxy composite beam A.R. Ropalekar, R.R. Ghadge, N.A. Anekar	132-141
Formation features of microstructure, elemental and phase compositions of the C-Cr-Mn-V-Fe coatings under conditions of electron beam (EB) surfacing in vacuum N.K. Galchenko, B.V. Dampilon, K.A. Kolesnikova	142-149 n
Evaluation of the efficiency of anti-corrosive protective coating based on epoxy polymers for protecting pipelines and metal structures T.A. Grigoryeva, E.A. Khabarov, Z.V. Khabarova	150-155

Submitted: August 8, 2023 Revised: September 11, 2023 Accepted: December 6, 2023

Impact of non-local, two temperature and impedance parameters on propagation of waves in generalized thermoelastic medium under modified Green-Lindsay model

S. Kaushal ^{1⊠}, ^{1□} R. Kumar ², ^{1□} I. Bala ¹, ^{1□} G. Sharma ^{1,3}, ^{1□}

ABSTRACT

This study is primarily focused on the behavior of propagation of waves through a homogeneous and isotropic thermoelastic half-space using the modified Green-Lindsay theory of thermoelasticity, along with the effects of non-local and two temperature (TT) parameters. A new set of governing equations is formulated and solved using the reflection technique after reducing the equations to two dimensions and a dimensionless form. The impact of different parameters namely non-local parameter, TT parameter, and impedance parameters along with different theories of thermoelasticity are shown graphically on amplitude ratios obtained from reflected waves i.e., longitudinal wave (LD-wave), thermal wave (T-wave), and transverse wave (SV-wave). The modified Green-Lindsay theory is widely used in fields such as heat transfer, and geophysics with potential practical applications in areas such as earthquake engineering and materials engineering. The study also includes the deduction of particular cases based on the obtained results.

KEYWORDS

modified Green-Lindsay theory • non-local • two temperature • impedance parameters

Citation: Kaushal S, Kumar R, Bala I, Sharma G. Impact of non-local, two temperature and impedance parameters on propagation of waves in generalized thermoelastic medium under modified Green-Lindsay model. *Materials Physics and Mechanics*. 2024;52(1): 1–17.

http://dx.doi.org/10.18149/MPM.5212024_1

Introduction

The mathematical framework known as the two temperature (TT) theory of thermoelasticity describes how materials respond to thermal loads and is an extension of the classical theory of elasticity. This theory finds use in several engineering disciplines that depend on the system's performance under thermal loads. For instance, in the semiconductor industry, the two temperature theory can be used to model electronic device behavior at elevated temperatures. Many authors have discussed different types of problems in the context of theory of thermoelasticity notable of them are [1–5].

Youssef [6] proposed a novel model of generalized thermoelasticity by incorporating two distinct temperatures, namely thermodynamic temperature and conductive temperature. Later on, [7–10] explored different types of problems in the context of TT theory of elasticity. Lofty et al. [11] established a memory-depended derivative (MDD) during the excitation processes by pulsed laser for a time-dependent material under the magneto thermoelasticity with TT. Al-Lehaibi [12] discussed the

¹Lovely Professional University, Phagwara, India

² Kurukshetra University, Haryana, India

³ Doaba College, Jalandhar, India

sachin kuk@yahoo.co.in

variational principle theorem without energy dissipation for an isotropic and homogeneous material in the context of the TT theory of thermoelasticity.

Green and Lindsay's (G-L) theory assumes linear behavior of the material, meaning that the response is assumed to be proportional to the applied loads and thermal gradients. This assumption may not hold for materials subjected to large deformations or high temperatures. The theory is typically formulated under the assumption of small temperature gradients. In situations where temperature changes are large, nonlinear effects may become significant, and the theory may not be accurate.

The modified Green-Lindsay (MG-L) theory is a revised version of the Green-Lindsay (G-L) theory that expands the classical linear thermoelasticity theory. This extended theory applies to extreme conditions, such as high temperatures, rapid heating or cooling, or other scenarios where the assumptions of the original theory may break down. This revised theory considers the impact of nonlinear thermal expansion to provide a more comprehensive description of the thermomechanical behavior of materials. By doing so, the MG-L theory offers improved predictions of the stress and strain in materials that are exposed to significant temperature changes and thermal gradients, which can result in significant mechanical stresses and deformations.

Yu et al. [13] used the extended thermodynamics principle to propose a model of generalized thermoelasticity that incorporates strain rate terms into the Green-Lindsay model. Quintanilla [14] reported some qualitative results for the MG-L thermoelasticity model. Ghodrat et al. [15] developed a numerical method to solve the governing equations for a large deformation domain in an elastic medium exposed to thermal shock under the MG-L theory of thermoelasticity. In the context of MG-L, Sarkar and De [16] examined the propagation of thermoelastic waves and determined that both MG-L and G-L have a significant impact on the amplitude ratios of reflected waves. A study that elaborates the response of a heat source along with thermomechanical loading in a MG-L generalized thermoelastic half-space with non-local and two temperature parameters is presented by Kumar et al. [17].

The non-local theory of thermoelasticity models the non-local effects by introducing a non-local constitutive equation that considers the temperature field over a larger region. This theory is useful in understanding the thermomechanical behavior of materials at small scales, where non-local effects can play a significant role in the material response. A non-local elasticity theory was developed by Eringen and Edelen [18], using global balance laws and the second law of thermodynamics. Initially, the non-local theory of elasticity was used to study screw dislocations and surface waves in solids (Lazar and Agiasofitou [19]).

A new model was discussed by Pramanik and Siddhartha [20] by using Eringen's non-local thermoelasticity theory, which explored the transmission of Rayleigh surface waves in a uniform, isotropic medium. Luo et al. [21] studied the temporary thermoelastic reactions of a slab with thermal properties that rely on the temperature, using a non-local thermoelastic model. In the case of non-local bio-thermoelastic media with diffusion, Kumar et al. [22] developed a dynamic model incorporating the impact of non-local and dual-phase lags.

Malischewsky [23] investigated the propagation of Rayleigh waves using impedance boundary conditions. In the context of thermoelastic medium, Singh [24] examined the

reflection of plane waves utilizing impedance boundary conditions. In a study conducted by Kaushal et al. [25], they investigated how diffusion and impedance parameters affect the propagation of plane waves in a thermoelastic medium using both the Green and Lindsay theory (G-L) and the Coupled theory (C-T) of thermoelasticity. Yadav [26] examined the influence of impedance parameters on the reflection of plane waves in a thermoelastic medium subjected to rotating and magnetic effects.

The purpose of the manuscript is to explore propagation of waves in thermoelastic media, which has been a focal point in seismology. Notably, these investigations play a crucial role in mineral ore exploration, hydrocarbon detection, and the planning and construction of infrastructure such as dams, bridges, roads, and highways.

The other authors explored various problems in the field of MG-L but the governing equations for a homogeneous and isotropic thermoelastic medium to determine the amplitude ratios of reflected LD-wave, T-wave, and SV-wave having impacts of non-local and TT under impedance boundary conditions is not explored. In the context of plane wave reflection, the consideration of impedance boundary conditions becomes paramount. These conditions are characterized by linear combinations of unspecified functions and their derivatives along the boundary. Such scenarios are frequently encountered in acoustics, electromagnetism, and seismology. This new model has the potential for application in fields such as geophysics, seismology, and earthquake engineering.

Basic equations

In the present investigation, we consider the MG-L model proposed by Yu et al. [13] along with non-local theory given by Eringen and Edelen [18] and two temperature theory of thermoelasticity given by Youssef [6]. So, in the absence of body forces and heat sources, the field equations and constitutive relations with non-local, TT under MG-L model of thermoelasticity in general cartesian coordinate system $Ox_1x_2x_3$ are given as:

$$\left(1 + \eta_1 \tau_1 \frac{\partial}{\partial t}\right) \left[(\lambda + \mu) \nabla (\nabla \cdot \vec{u}) + \mu \nabla^2 \vec{u} \right] - \beta_1 \left(1 + \eta_2 \tau_1 \frac{\partial}{\partial t}\right) \nabla T = \rho (1 - \xi_1^2 \nabla^2) \frac{\partial^2 \vec{u}}{\partial t^2}, \tag{1}$$

$$K^* \nabla^2 \varphi = \left(1 + \eta_3 \tau_0 \frac{\partial}{\partial t}\right) \left(\beta_1 T_0 \dot{u}_{k,k}\right) + \left(1 + \eta_4 \tau_0 \frac{\partial}{\partial t}\right) \rho C_e \dot{T},\tag{2}$$

$$t_{ij} = \left(1 + \eta_1 \tau_1 \frac{\partial}{\partial t}\right) \left[\lambda u_{k,k} \delta_{ij} + \mu \left(u_{i,j} + u_{j,i}\right)\right] - \beta_1 \left(1 + \eta_2 \tau_1 \frac{\partial}{\partial t}\right) T \delta_{ij} , \tag{3}$$

$$T = (1 - a\nabla^2)\varphi,\tag{4}$$

where λ , μ -Lame's constants, ξ_1 - non-local parameter, t - time, $\beta_1=(3\lambda+2\mu)\alpha_t$, α_t - coefficient of linear thermal expansion, ρ , C_e - density and specific heat, K^* - thermal conductivity, φ - conductive temperature, T - temperature, t_{ij} - components of stress tensor, τ_0 , τ_1 - the relaxation times, δ_{ij} - Kronecker delta, \vec{u} - displacement vector, T_0 -reference temperature, η_1 , η_2 , η_3 , η_4 - constants, a-TT parameter, ∇^2 - Laplacian operator.

The Eqs. (1)-(4) reduce to the following:

$$\eta_1 = \eta_2 = \eta_3 = \eta_4 = 1,$$
 Modified Green-Lindsay, (MG-L), (2018). $\eta_1 = \eta_3 = 0, \eta_2 = \eta_4 = 1,$ Green-Lindsay, (G-L), (1972). $\eta_1 = \eta_2 = 0, \eta_3 = \eta_4 = 1,$ Lord-Shulman, (L-S), (1967). $\eta_1 = \eta_2 = \eta_3 = \eta_4 = 0,$ Coupled thermoelasticity, (C-T), (1980).

Problem statement

A homogeneous, isotropic thermoelastic solid half space with TT and non-local is considered. The rectangular Cartesian coordinate system $Ox_1x_2x_3$ is taken such that the origin is located on the surface $x_3 = 0$ and x_3 -axis is pointing normally to the medium as shown in Fig. 1.

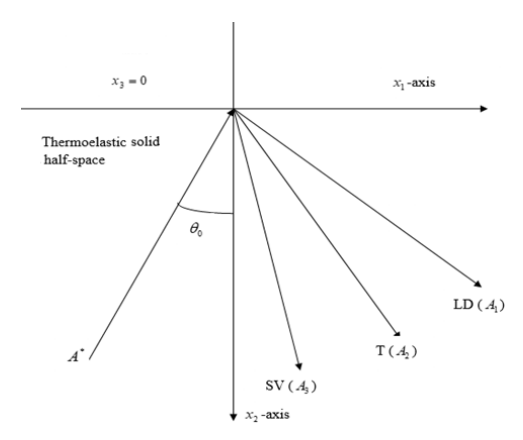


Fig. 1. Geometry of the problem

The components of displacement are taken as follows for a two-dimensional problem:

$$\vec{u} = (u_1, 0, u_3). \tag{5}$$

Dimensionless quantities are referred as:

$$\begin{split} &(x_i',u_i') = \frac{\omega_1}{c_1} \big(x_i,u_i \big), \qquad t_{3i}' = \frac{t_{3i}}{\beta_1 T_0}, \qquad (\varphi',T') = \frac{1}{T_0} \big(\varphi,T \big), \quad (t',\tau_0',\tau_1') = \omega_1(t,\tau_0,\tau_1), \\ &a' = \frac{\omega_1^2}{c_1^2} a, \qquad \xi_1' = \frac{w_1}{c_1} \xi_1, \quad (z_1',z_2') = \frac{c_1}{\beta_1 T_0} \big(z_1,z_2 \big), \qquad z_3' = \frac{c_1}{K^*} z_3, \qquad \iota = 1,3. \end{split} \tag{6}$$
 where $c_1^2 = \frac{\lambda + 2\mu}{\rho}$ and $\omega_1 = \frac{\rho C_e C_1^2}{K^*}$.

After removing the primes and introducing the values defined by Eq. (6) in addition to Eq. (5), in Eqs. (1)-(4) we get,

$$\left(1 + \eta_1 \tau_1 \frac{\partial}{\partial t}\right) \left[a_1 \frac{\partial e}{\partial x_1} + a_2 \nabla^2 u_1 \right] - a_3 \left(1 + \eta_2 \tau_1 \frac{\partial}{\partial t}\right) \frac{\partial T}{\partial x_1} = \left(1 - \xi_1^2 \nabla^2\right) \frac{\partial^2 u_1}{\partial t^2}, \tag{7}$$

$$\left(1 + \eta_1 \tau_1 \frac{\partial}{\partial t}\right) \left[a_1 \frac{\partial e}{\partial x_3} + a_2 \nabla^2 u_3 \right] - a_3 \left(1 + \eta_2 \tau_1 \frac{\partial}{\partial t}\right) \frac{\partial T}{\partial x_3} = \left(1 - \xi_1^2 \nabla^2\right) \frac{\partial^2 u_3}{\partial t^2}, \tag{8}$$

$$\nabla^2 \varphi = a_4 \left(1 + \eta_3 \tau_0 \frac{\partial}{\partial t} \right) \frac{\partial}{\partial t} (u_{1,1} + u_{3,3}) + \left(1 + \eta_4 \tau_0 \frac{\partial}{\partial t} \right) \frac{\partial T}{\partial t}, \tag{9}$$

$$T = (1 - a\nabla^2)\varphi,\tag{10}$$

$$t_{33} = \left(1 + \eta_1 \tau_1 \frac{\partial}{\partial t}\right) \left[a_5 \frac{\partial u_3}{\partial x_2} + a_6 \frac{\partial u_1}{\partial x_4} \right] - \left(1 + \eta_2 \tau_1 \frac{\partial}{\partial t}\right) T, \tag{11}$$

$$t_{33} = \left(1 + \eta_1 \tau_1 \frac{\partial}{\partial t}\right) \left[a_5 \frac{\partial u_3}{\partial x_3} + a_6 \frac{\partial u_1}{\partial x_1} \right] - \left(1 + \eta_2 \tau_1 \frac{\partial}{\partial t}\right) T, \tag{11}$$

$$t_{31} = \left(1 + \eta_1 \tau_1 \frac{\partial}{\partial t}\right) \left[a_7 \left(\frac{\partial u_3}{\partial x_1} + \frac{\partial u_1}{\partial x_3}\right) \right], \tag{12}$$

$$a_1 = \frac{\lambda + \mu}{\rho C_1^2}, a_2 = \frac{\mu}{\rho C_1^2}, a_3 = \frac{\beta_1 \tau_0}{\rho C_1^2}, a_4 = \frac{\beta_1 C_1^2}{K^* \omega_1}, a_5 = \frac{\lambda + 2\mu}{\beta_1 T_0}, a_6 = \frac{\lambda}{\beta_1 T_0}, a_7 = \frac{\mu}{\beta_1 T_0}, e = \frac{\partial u_1}{\partial x_1} + \frac{\partial u_3}{\partial x_3}.$$

To decouple the above system of equations, we take u_1 and u_3 in the dimensionless form as:

$$u_1 = q_{,1} - \psi_{,3}, \qquad u_3 = q_{,3} + \psi_{,1}.$$
 (13)

Using Eqs. (7)-(10) and (13), we get the following set of equations:

$$\left(1 + \eta_1 \tau_1 \frac{\partial}{\partial t}\right) (\nabla^2 q) - a_3 \left(1 + \eta_2 \tau_1 \frac{\partial}{\partial t}\right) T = \left(1 - \xi_1^2 \nabla^2\right) \frac{\partial^2 q}{\partial t^2},\tag{14}$$

$$a_2(1+\eta_1\tau_1\frac{\partial}{\partial t})(\nabla^2\psi)-(1-\xi_1^2\nabla^2)\frac{\partial^2\psi}{\partial t^2}=0, \tag{15}$$

$$\nabla^2 \varphi = a_4 \left(1 + \eta_3 \tau_0 \frac{\partial}{\partial t} \right) \frac{\partial}{\partial t} \nabla^2 \mathbf{q} + \left(1 + \eta_4 \tau_0 \frac{\partial}{\partial t} \right) \frac{\partial T}{\partial t}. \tag{16}$$

Dispersion equation and its solutions

Assuming the motion to be harmonic and for solving the Eqs. (14)-(16), we assume solutions in the form:

$$(q, \varphi, \psi) = (q^0, \varphi^0, \psi^0) e^{\iota k(x_{1} \sin \theta_0 - x_3 \cos \theta_0) + \iota \omega t}, \tag{17}$$

where k denotes as wave number, ι is known as iota, θ_0 is angle of inclination and quantities such as q^0, φ^0, ψ^0 are arbitrary constants. Using the values of q, φ, ψ we obtained following equations:

$$(A\nu^4 + B\nu^2 + C)(q, \varphi) = 0, (18)$$

$$(v^2 - A_1)\psi = 0, (19)$$

where A=
$$E_2 i\omega$$
, B= $(E_2 a\omega^3 i + \omega^2) + i\omega E_2(\xi_1^2 \omega^2 - E_1) - (a_3 a_4 E_3 E_4 i\omega)$, C= $(\xi_1^2 \omega^2 - E_1)(E_2 a\omega^3 i + \omega^2) - iaa_3 a_4 E_3 E_4 \omega^3$, $A_1 = (1 + \eta_1 \tau_1 i\omega)a_2 - \xi_1^2 \omega^2$, $E_1 = (1 + \eta_1 \tau_1 i\omega)$, $E_2 = (1 + \eta_4 \tau_0 i\omega)$, $E_3 = (1 + \eta_3 \tau_0 i\omega)$, $E_4 = (1 + \eta_2 \tau_1 i\omega)$.

Restriction on boundary

Impedance boundary conditions consist of unknown functions and their derivatives prescribed on the boundary. These conditions find widespread use in multiple disciplines such as thermoelasticity, acoustics, and electromagnetism within the realm of Physics. When dealing with seismic wave interactions involving discontinuities, the typical assumption is an ideally welded contact, ensuring continuity of relevant displacement and stress components. Consequently, it is suitable to treat these contact planes as extremely thin layers, giving rise to boundary conditions similar to impedance conditions. Hence, following Malischewsky [23] and Schoenberg [27], the impedance boundary conditions at $x_3 = 0$ are:

(i)
$$t_{33} + \omega z_1 u_3 = 0$$
, (ii) $t_{31} + \omega z_2 u_1 = 0$, (iii) $K^* \frac{\partial T}{\partial x_3} + \omega z_3 T = 0$, (20)

where z_1, z_2 and z_3 are impedance parameters, the boundary conditions at free surface can be obtained by setting $z_1 = z_2 = z_3 = 0$.

To obtain amplitude ratios, we consider q, φ, ψ as follows:

$$q = \sum (A_{0\iota}e^{\iota k_0(x_1Sin\theta_0 - x_3Cos\theta_0) + \iota\omega t} + A_{\iota}e^{\iota k_{\iota}(x_1Sin\theta_{\iota} + x_3Cos\theta_{\iota}) + \iota\omega t}), \tag{21}$$

$$\varphi = \Sigma (d_{\iota}A_{0\iota}e^{\iota k_{0}(x_{1}Sin\theta_{0} - x_{3}Cos\theta_{0}) + \iota\omega t} + d_{\iota}A_{\iota}e^{\iota k_{\iota}(x_{1}Sin\theta_{\iota} + x_{3}Cos\theta_{\iota}) + \iota\omega t}), \tag{22}$$

$$\psi = (A_{03}e^{ik_0(x_1Sin\theta_0 - x_3Cos\theta_0) + i\omega t} + A_3e^{ik_3(x_1Sin\theta_3 + x_3Cos\theta_3) + i\omega t}), \tag{23}$$

where $d_l = \frac{\iota \omega a_4 E_3 k_l^2}{k_l^2 + \iota \omega E_2 (1 + a k_l^2)}$, (l=1,2), A_{0l} are the amplitude of incident Longitudinal wave (LD-wave), thermal waves (T-wave) and shear waves (SV-wave). A_l are the amplitude of the reflected Longitudinal wave (LD-wave) and reflected Thermal waves (T-wave) and A_3 is the amplitude of the reflected Shear wave (SV-wave).

Snell's Law is given as

$$\frac{\sin\theta_0}{v_0} = \frac{\sin\theta_1}{v_1} = \frac{\sin\theta_2}{v_2} = \frac{\sin\theta_3}{v_3},\tag{24}$$

where

$$k_1v_1 = k_2v_2 = k_3v_3 = \omega, \text{ at } x_3 = 0,$$

$$v_0 = \begin{cases} v_1, \text{ for incident LD } - \text{ wave} \\ v_2, \text{ for incident T} - \text{ wave} \\ v_3, \text{ for incident SV} - \text{ wave} \end{cases}$$
(25)

Using potential defined by Eq. (13) along with Eqs. (21)-(25) in the boundary conditions given by Eq. (20), we obtained a system of equations defined as:

Unique cases

Modified Green-Lindsay model with two temperature. Let $\xi_1 \to 0$ in Eq. (26), we obtain the resulting expression for MG-L theory of thermoelasticity along with TT effect. The results tally with those obtained by Sarkar and Mondal [28].

Non-local modified Green-Lindsay model. As TT parameter vanishes i.e. *a*=0 in Eq. (26), we obtain the results for MG-L model involving non-local impact.

Non-local G-L generalized thermoelastic model with two temperature. Taking $\eta_1 = \eta_3 = 0$, $\eta_2 = \eta_4 = 1$, reduces the system of equation defined by Eq. (26) for G-L model having non-local and TT effect.

Non-local L-S generalized thermoelastic model with two temperature. Putting $\eta_1 = \eta_2 = 0$, $\eta_3 = \eta_4 = 1$, in Eq. (26) will yield the expression for L-S model involving non-local and TT. If we vanish the TT effect then the model reduces to L-S generalized thermoelastic model with non-local effects and the results tally with those obtained by Singh and Bijarnia [29].

Coupled thermoelastic model with non-local and two temperature. Let $\eta_1 = \eta_2 = \eta_3 = \eta_4 = 0$, i.e. in absence of relaxation time, Eq. (26) gives the corresponding expression for CT model along with non-local and TT.

Computational interpretation

To study the effect of various parameters, the numerical calculations are carried out for three different cases, the effect of (i) non-local and impedance parameters (ii) TT and impedance parameters (iii) different theories of thermoelasticity i.e. MG-L, G-L and L-S theories.

Following Dhaliwal and Singh [30], we take the case of magnesium crystal, the physical constants used are: $\lambda = 2.17 \times 10^{10} \ \mathrm{Nm^{-2}}$, $\mu = 3.278 \times 10^{10} \ \mathrm{Nm^{-2}}$, $K^* = 1.7 \times 10^2 \ \mathrm{Wm^{-1}deg^{-1}}$, $\omega_1 = 3.58 \times 10^{11} \ \mathrm{s^{-1}}$, $\beta_1 = 2.68 \times 10^6 \ \mathrm{Nm^{-2} deg^{-1}}$, $\rho = 1.74 \times 10^3 \ \mathrm{Kgm^{-3}}$, $C_e = 1.04 \times 10^3 \ \mathrm{JKg^{-1}deg^{-1}}$, $T_0 = 298 \ \mathrm{k}$, $T_0 = 0.1 \ \mathrm{s}$, $T_0 = 0.2 \ \mathrm{s}$. The values of impedance parameters for all the cases are $T_0 = 2.5 \ \mathrm{s}$, $T_0 = 2.5 \ \mathrm{s}$, and $T_0 = 2.5 \ \mathrm{s}$.

Non-local effects and impedance parameters. In this case, we consider fixed value of TT parameter as a=0.104 with $0^{\rm o} \leq \theta_0 \leq 90^{\rm o}$. Non-local parameter ($\xi_1=0.5$) along with TT and impedance parameters (NTI) is represented by a solid Black line. The case of non-local parameter($\xi_1=0.5$) along with TT and without impedance parameters (NTWI) is represented by a solid red. The case of absence of non-local parameter, i.e. ($\xi_1=0.0$) along with TT and impedance parameter (TI) is represented by a solid Blue line with center symbol ' Δ '. The case of absence of non-local parameter i.e.($\xi_1=0.0$) along with TT and without impedance (TWI) is shown by a violet line with center symbol ' \diamond '.

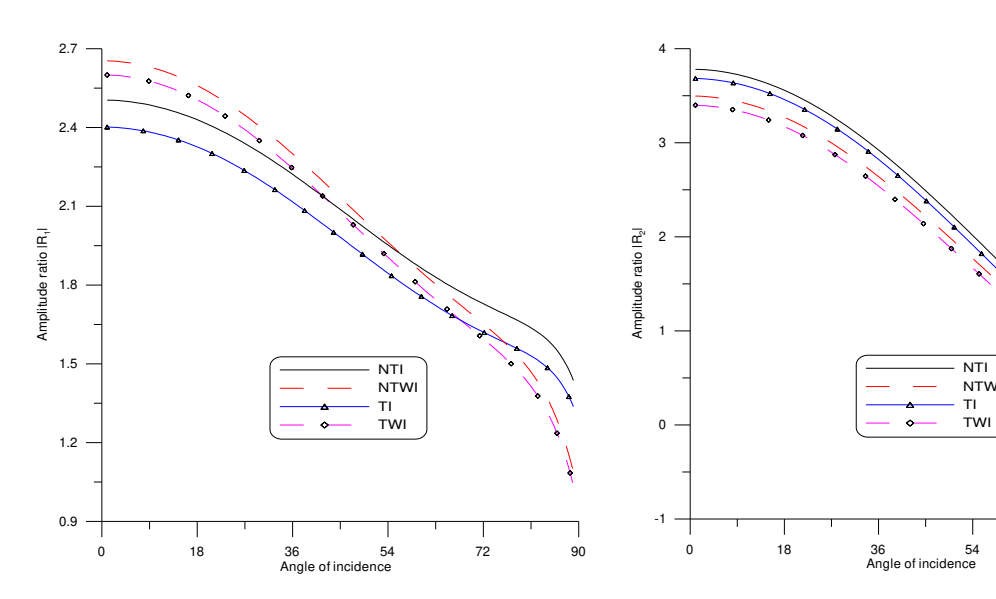


Fig. 2. Variation of Amplitude ratio |R₁| for LD-wave (Impact of non-Local and impedance parameters)

Fig. 3. Variation of Amplitude ratio $|R_2|$ for LD-wave (Impact of non-Local and impedance parameters)

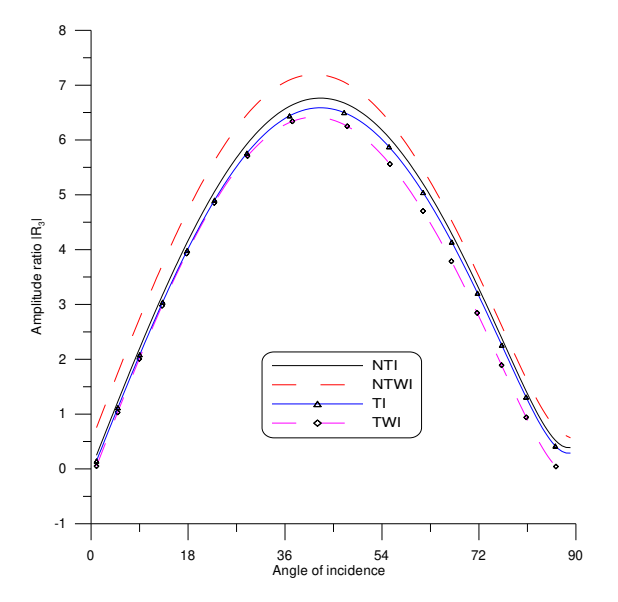


Fig. 4. Variation of Amplitude ratio |R₃| for LD-wave (Impact of non-Local and impedance parameters)

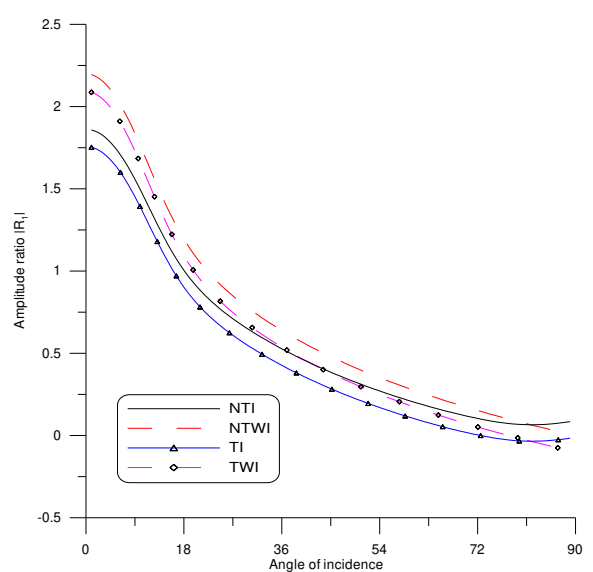


Fig. 5.Variation of Amplitude ratio |R₁| for T-wave (Impact of non-Local and impedance parameters)

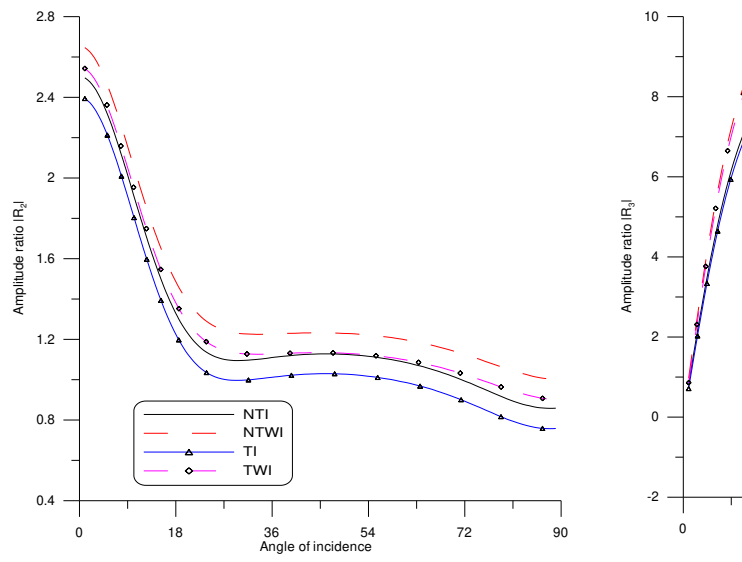
LD-wave. In Fig. 2, the changes in $|R_1|$ are depicted as a function of the angle of incidence. It is observed that $|R_1|$ decreases for all the cases considered throughout the entire range. Additionally, it is apparent that $|R_1|$ is more pronounced for the case NTI as compared to TI. Also, the value of $|R_1|$ for the case of NTWI is higher than that of TI, indicating the influence of non-local on $|R_1|$.

Figure 3 illustrates those variations of $|R_2|$ with θ_0 , it is noticed that $|R_2|$ decreases for all cases considered, namely NTI, NTWI, TI, and TWI, as θ_0 increases. Specifically, the value of $|R_2|$ for NTI and TI are higher than that of NTWI and TWI respectively, reveals the impact of non-local and impedance on the $|R_2|$.

The trend of variations of $|R_3|$ with θ_0 is shown in Fig. 4. It is observed that the value of $|R_3|$ increases in the first half of the interval and decreases in the remaining range for all considered cases. However, the magnitude of $|R_3|$ is higher for NTWI compared to other cases in the entire range.

T-wave. Figure 5 displays a plot of $|R_1|$ with θ_0 , it is evident that $|R_1|$ exhibits a significant downward trend for all the considered cases in the range of $0 \le \theta \le 18^\circ$ followed by a steady decline in the remaining interval. Moreover, the magnitude of variations appears to be relatively higher for the NTWI case compared to the other cases throughout the entire range.

Figure 6 illustrates the variations of $|R_2|$ with θ_0 , indicating that $|R_2|$ exhibits a downward trend within a range $0 \le \theta \le 27^\circ$ for all examined cases. As the values of θ_0 increases further, $|R_2|$ shows a small decrement for all considered cases.



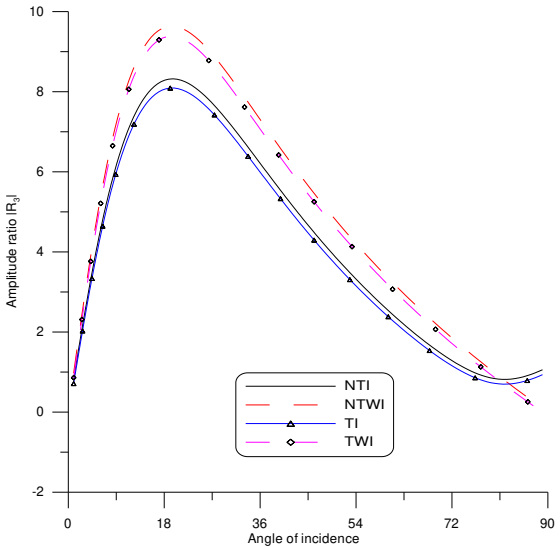
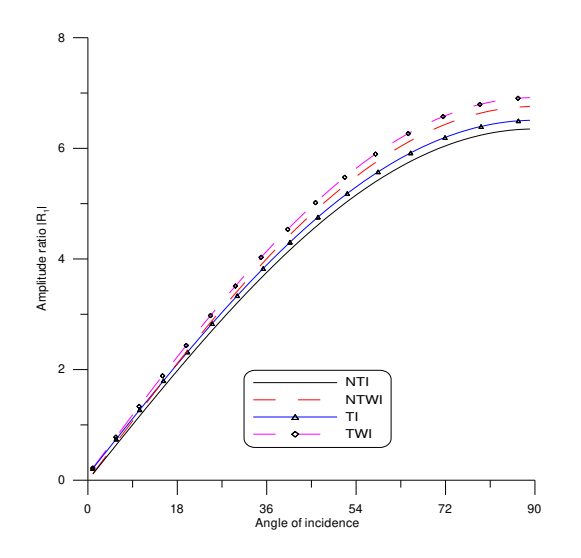


Fig. 6. Variation of Amplitude ratio |R₂| for T-wave (Impact of non-Local and impedance parameters)

Fig. 7. Variation of Amplitude ratio |R₃| for T-wave (Impact of non-Local and impedance parameters)

From Fig. 7 it is seen that value of $|R_3|$ increases in the interval $0 \le \theta \le 18^\circ$ for all considered cases, whereasit exhibits an opposite trend in the remaining range, implying that the amplitude ratio is adversely affected by the impedance parameter. Furthermore, the magnitudes of $|R_3|$ are relatively higher for NTWI, TWI than NTI and TI, which can be attributed to the absence of impedance parameter.

SV-wave. Figure 8 displays a plot of $|R_1|$ with θ_0 , indicating that the values of $|R_1|$ exhibit an upward trend for all the cases considered with increase in θ_0 . It is also seen that magnitude of values for TWI and NTWI are greater as compared to TI and NTI, which reveals the impact of impedance parameter.



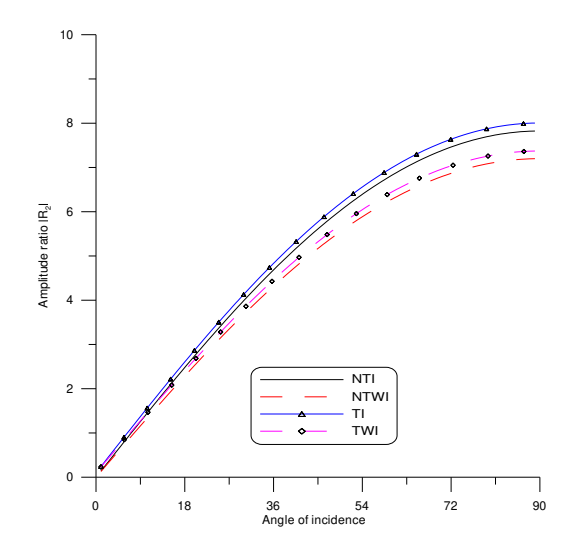


Fig. 8. Variation of Amplitude ratio $|R_1|$ for SV-wave (Impact of non-Local and impedance parameters)

Fig. 9. Variation of Amplitude ratio |R₂| for SV-wave (Impact of non-Local and impedance parameters)

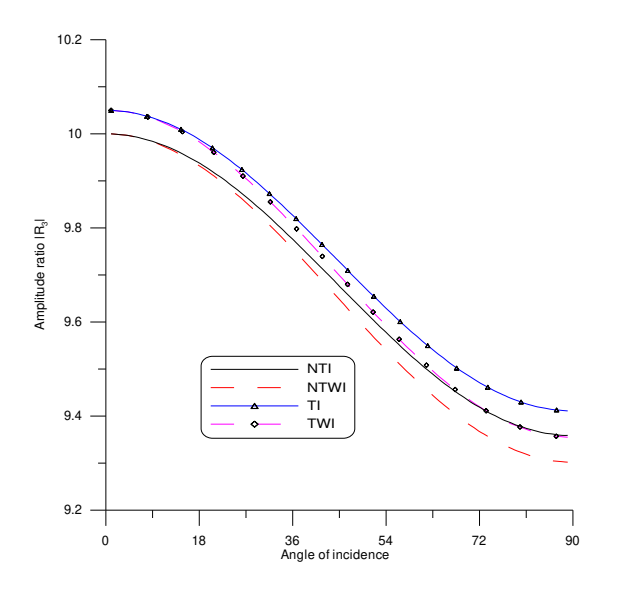
Figure 9 indicates a growing trend of variation of $|R_2|$ in the case of NTI, NTWI, TI and TWI for the entire range. Figure 10 demonstrates that the variations of amplitude ratio $|R_3|$ against θ_0 follows the decreasing trend for all the considered cases in the entire range, magnitude of decrement for NTWI is greater as compared to other cases.

Two temperature effects and impedance parameters. In this case, we consider the fixed value of non-local parameter ($\xi_1=0.5$) parameter and $0^{\circ} \leq \theta_0 \leq 90^{\circ}$. TT parameter (a=0.0104) along with non-local and impedance parameters (TNI) is represented by a solid Black line. The TT parameter (a=0.0104) along with non-local and without impedance parameters (TNWI) is represented by a solid red. The case of absence of TT i.e.(a=0.0) along with non-local with impedance parameter (NI) is represented by a solid Blue line with center symbol ' Δ '. The case of absence of TT i.e. (a=0.0) along with non-local and without impedance (NWI) is represented by a violet with center symbol ' \diamond '.

LD-wave. From Fig. 11 which is a plot of $|R_1|$ vs θ_0 . It is clear that the value of $|R_1|$ follows the descending trend for all the considered cases as θ_0 increases, magnitude of $|R_1|$ for TNI and TNWI are greater than NI and NWI respectively, which reveals the impact of TT parameter.

From Fig. 12, which presents the plot of $|R_2|$ vs θ_0 . The graph clearly shows a decline in $|R_2|$ for TNI, TNWI, NI, and NWI. Among these, TNI exhibits the largest variation, while NWI has the smallest. As θ_0 increases, the amplitude ratios eventually converge towards zero value. In Fig. 13, depicts the amplitude ratio $|R_3|$ vs θ_0 , demonstrating a positive trend during the first half of the interval, followed by a reversal in the second half for all the cases. Notably, TNWI experiences the largest magnitude of variation, while NWI exhibits the smallest.

T-wave. Figure 14 displays the trend of variations for $|R_1|$ with θ_0 . It is observed that the value of $|R_1|$ decreases monotonically throughout the entire range for all considered cases, with varying magnitudes of variation. Moreover, TNI and TNWI are smaller as compared to NI and NWI, which reveals the impact of TT parameter. Figure 15 illustrates the plot of $|R_2|$ against θ_0 . It is evident that TNI, NI, TNWI, and NWI exhibit a downward trend for the entire range except for $27 \le \theta_0 \le 60$, where $|R_2|$ shows a steady state.



2.8

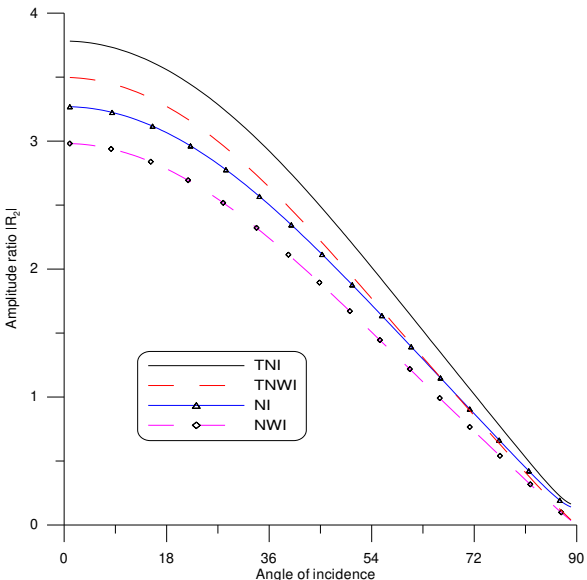
2.4

O 18

O

Fig. 10. Variation of Amplitude ratio |R₃| for SV-wave (Impact of non-Local and impedance parameters)

Fig. 11. Variation of Amplitude ratio $|R_1|$ for LD-wave (Impact of TT and impedance parameters)



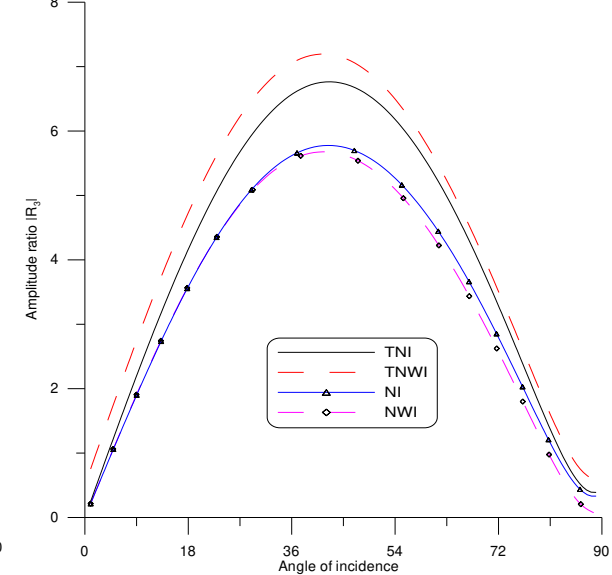
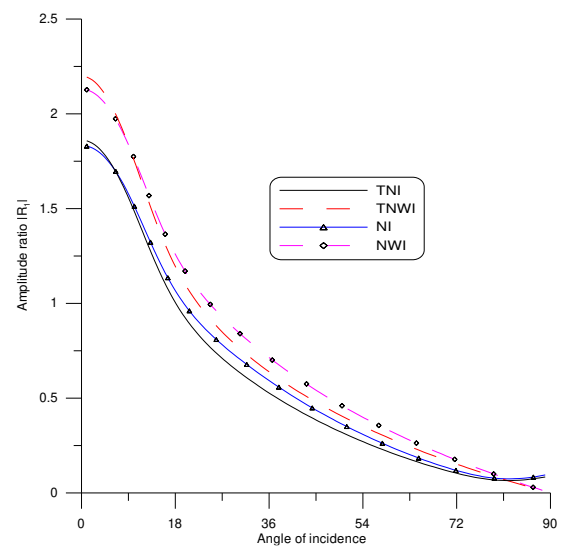


Fig. 12. Variation of Amplitude ratio $|R_2|$ for LD-wave (Impact of TT and impedance parameters)

Fig. 13. Variation of Amplitude ratio |R₃| for LD-wave (Impact of TT and impedance parameters)



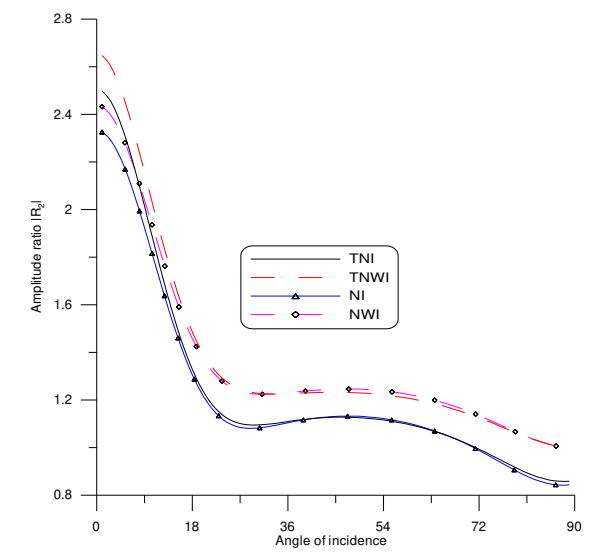


Fig. 14. Variation of Amplitude ratio |R₁| for T-wave (Impact of TT and impedance parameters)

Fig. 15. Variation of Amplitude ratio $|R_2|$ for T-wave (Impact of TT and impedance parameters)

From Fig. 16, which is a plot of $|R_3|$ vs θ_0 , it is noticed that $|R_3|$ exhibits an increasing trend in the interval $0 \le \theta \le 18$, and thereafter follows a descending behavior for the remaining range with significant difference in their magnitude.

SV-wave. From Fig. 17, which is a plot of $|R_1|$ vs θ_0 . It is clear that the value $|R_1|$ shows an increasing trend in the entire range for all the cases. It is also noticeable that magnitude of variations of $|R_1|$ is larger in case of TNI as compare to TNWI, which reveals impact of impedance. Figure 18 illustrates the plot of $|R_2|$ against θ_0 . It indicates the growing trend of variation of $|R_2|$ for all the considered cases with significant difference in magnitude. It is also noticed that the larger variation is seen for TNI as compared to remaining cases. Figure 19 demonstrates a plot of $|R_3|$ vs θ_0 , it is seen that impedance has decreasing effect on amplitude ratio $|R_3|$ and magnitude of variation is observed larger for the case of NI.

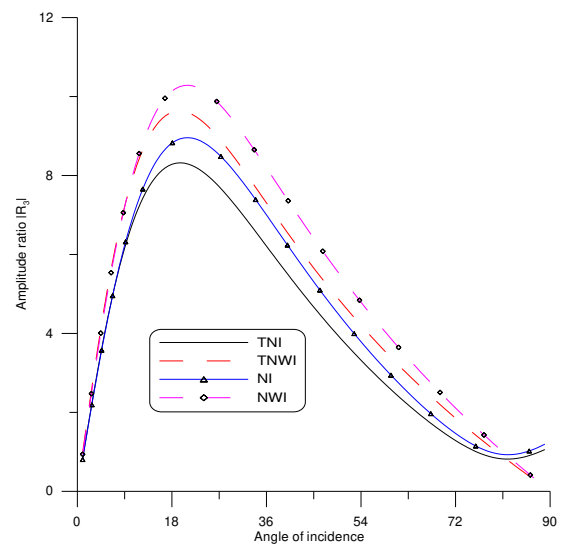


Fig. 16. Variation of Amplitude ratio $|R_3|$ for T-wave (Impact of TT and impedance parameters)

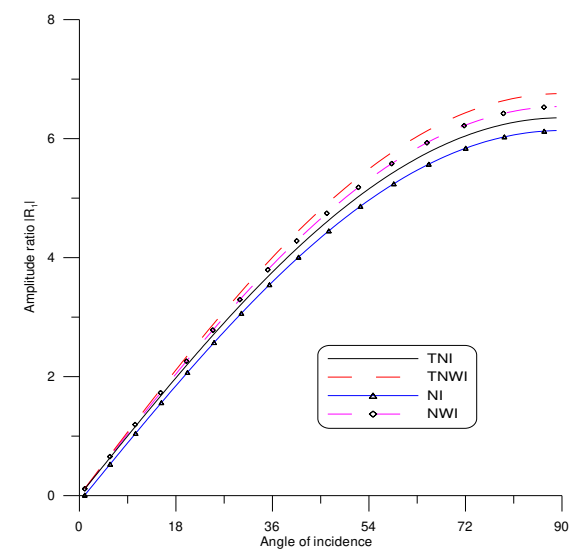


Fig. 17. Variation of Amplitude ratio $|R_1|$ for SV-wave (Impact of TT and impedance parameters)

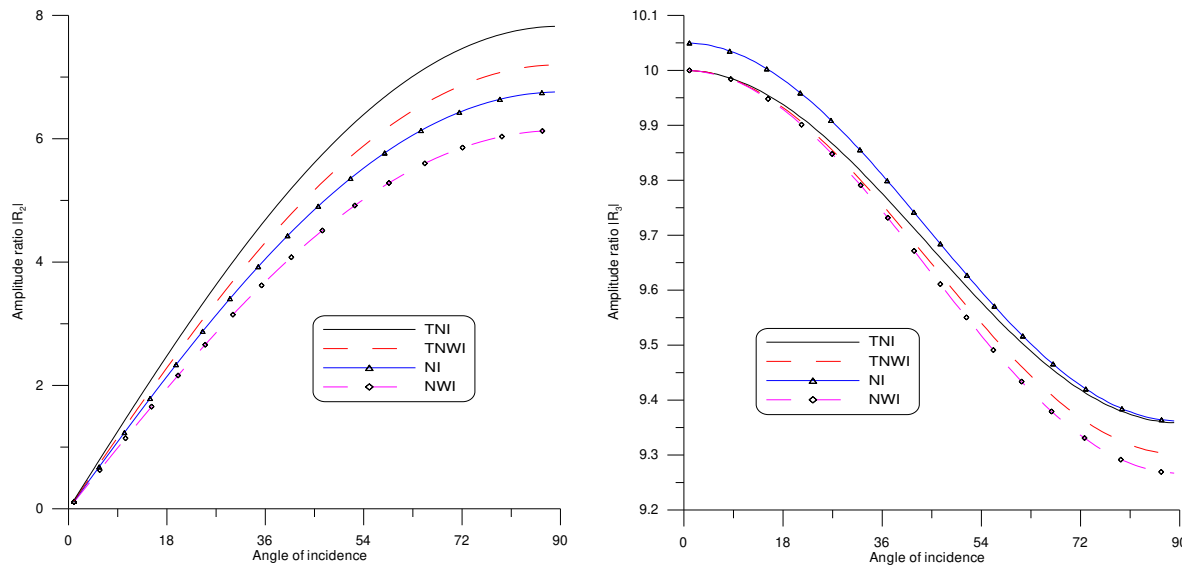


Fig. 18. Variation of Amplitude ratio $|R_2|$ for SV-wave (Impact of TT and impedance parameters)

Fig. 19. Variation of Amplitude ratio $|R_3|$ for SV-wave(Impact of TT and impedance parameters)

Different theories of thermoelasticity. LD-wave. Figure 20 depicts the variations of $|R_1|$ vs θ_0 . It is noticed that the value of $|R_1|$ shows decreasing trend. Moreover, the value of $|R_1|$ for G-L model is higher as compared with MG-L and L-S model. Figure 21 shows the variation of $|R_2|$ with θ_0 . It is seen that $|R_2|$ follows the similar trend as observed for $|R_1|$. Figure 22 illustrates that amplitude ratio $|R_3|$ vs θ_0 . It is noticed that the values of $|R_3|$ increases in first half of the interval and in remaining half the values shows a viceversa trend for all the considered cases.

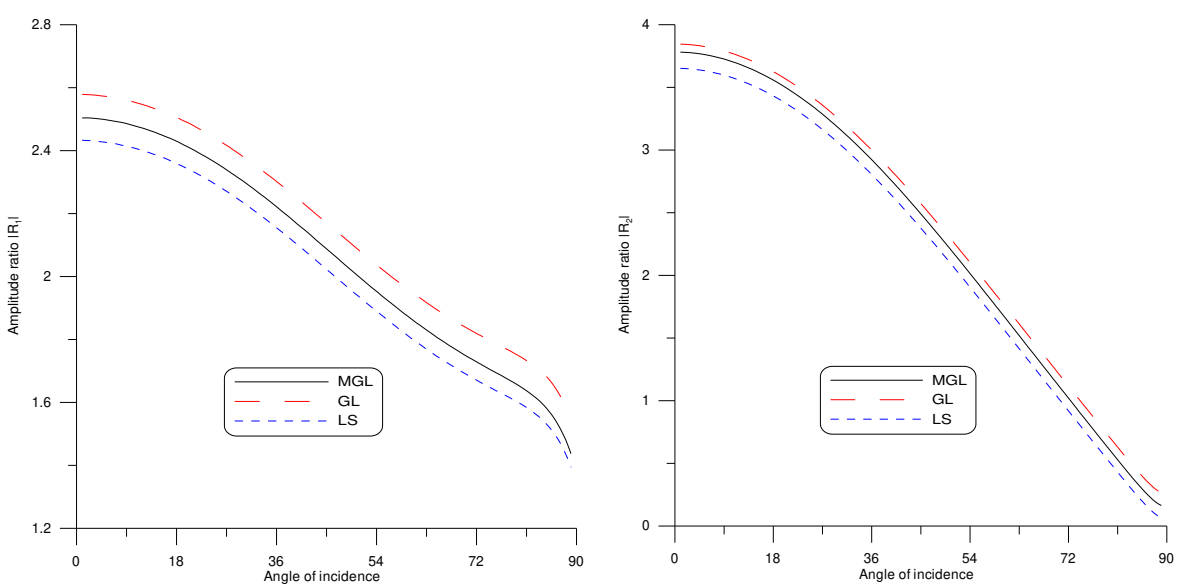
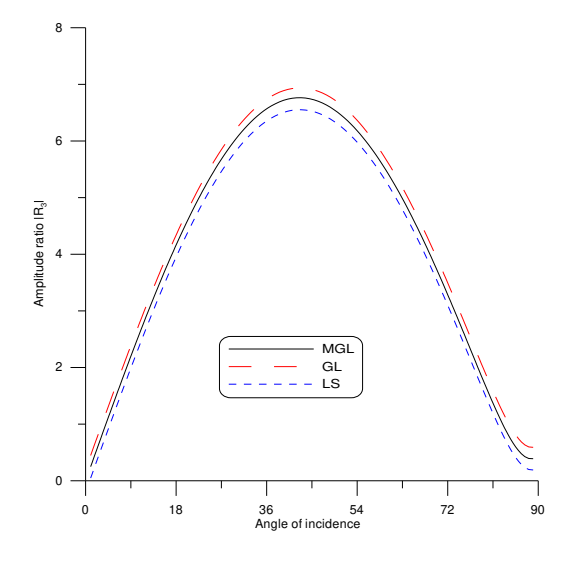


Fig. 20. Variation of Amplitude ratio $|R_1|$ for LD-wave(Impact of Different Theories)

Fig. 21. Variation of Amplitude ratio $|R_2|$ for LD-wave (Impact of Different Theories)



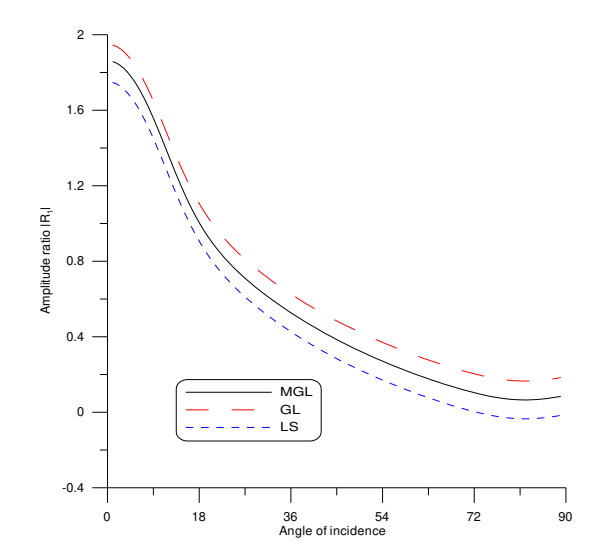


Fig. 22. Variation of Amplitude ratio $|R_3|$ for LD-wave (Impact of Different Theories)

Fig. 23. Variation of Amplitude ratio $|R_1|$ for T-wave (Impact of Different Theories)

T-wave. From Fig. 23, it is observed that the value of $|R_1|$ for MGL, G-L and L-S model follows decreasing trends while magnitude of $|R_1|$ is more for the G-L as compared to MG-L and L-S. From Fig. 24, which is plot of $|R_2|$ vs θ_0 . It is noticed that magnitude of $|R_2|$ for G-L is higher as compared to other two models i.e. MG-L model and L-S model. The variations of $|R_3|$ vs θ_0 are presented in Fig. 25. It is observed that the value of $|R_3|$ is in upward trend for all considered cases in the range $0 \le \theta \le 18^\circ$, $\theta \ge 80^\circ$ and is in downward trend in rest of the interval.

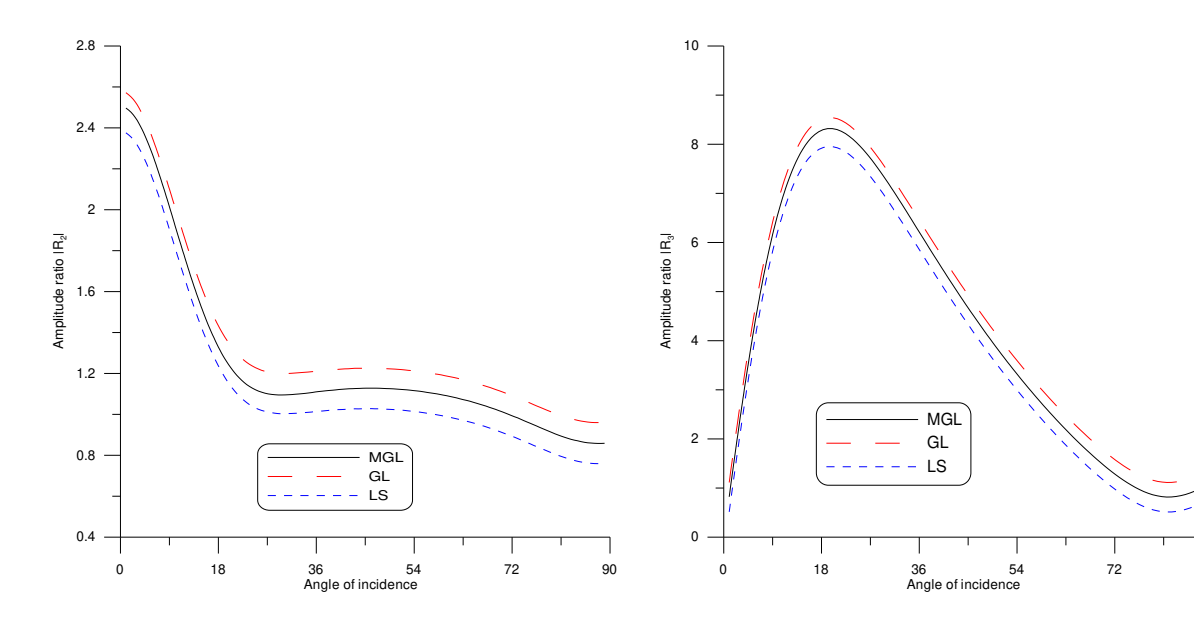


Fig. 24. Variation of Amplitude ratio $|R_2|$ for T-wave(Impact of Different Theories)

Fig. 25. Variation of Amplitude ratio $|R_3|$ for T-wave (Impact of Different Theories)

SV-Wave. Figure 26 depicts the variations of $|R_1|$ with θ_0 . It is observed that the value of $|R_1|$ are in uptrend for all the cases. It is also noticed that the values of $|R_1|$ for G-L model are more as compared to MG-L and L-S model. From Fig. 27, it is observed that the value of $|R_2|$ for G-L, MG-L and L-S follows rising trend for entire range but magnitude

of $|R_2|$ for G-L is higher than MG-L, L-S. Figure 28 depicts the variations of $|R_3|$ with θ_0 . It is observed that the value of $|R_3|$ follows decreasing trend for all the considered models. Also, the value of $|R_3|$ for G-L model is more as compared to MG-L and L-S model.

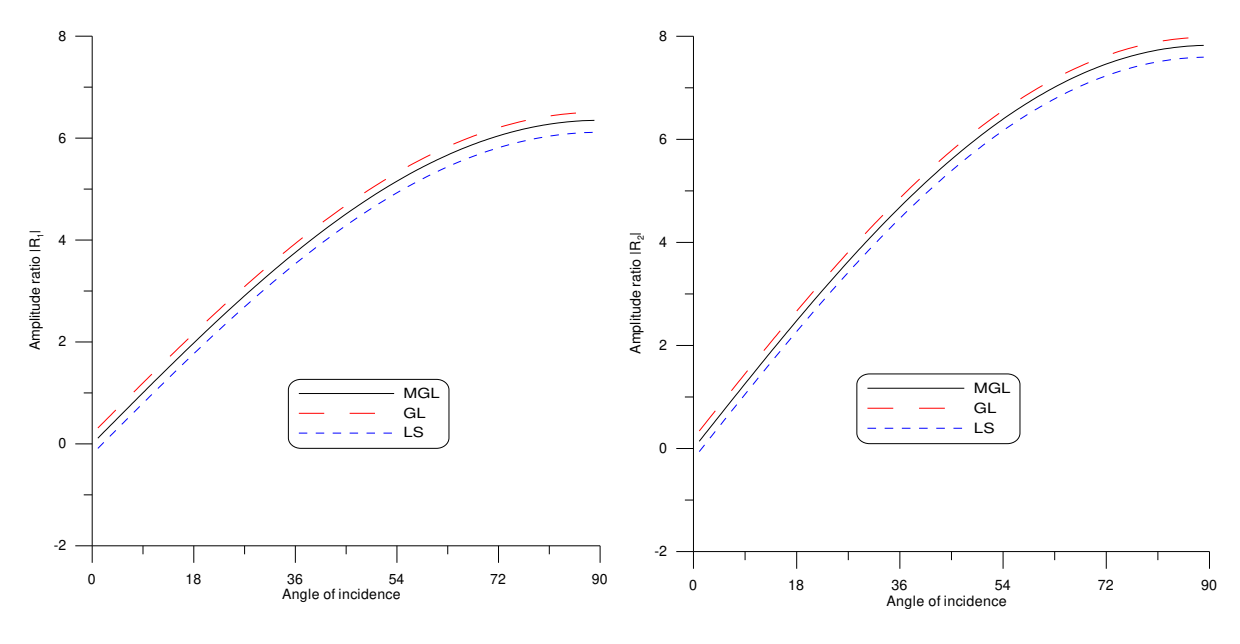


Fig. 26. Variation of Amplitude ratio $|R_1|$ for SV-wave (Impact of Different Theories)

Fig. 27. Variation of Amplitude ratio $|R_2|$ for SV-wave(Impact of Different Theories)

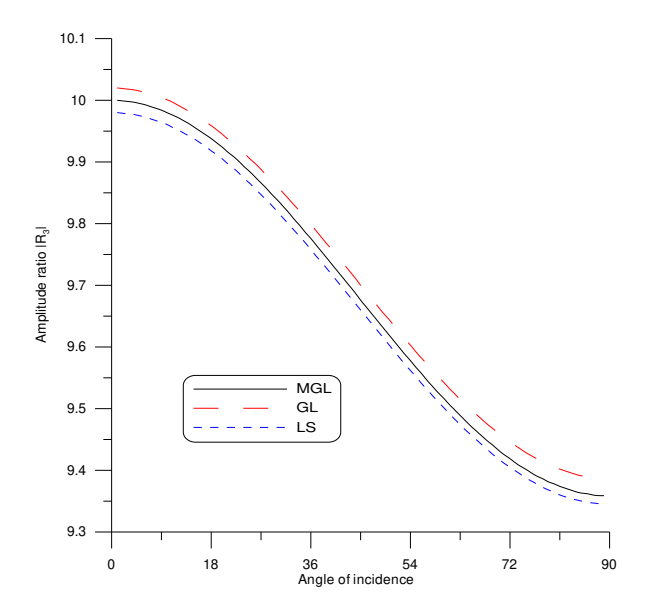


Fig. 28 Variation of Amplitude ratio |R₃| for SV-wave(Impact of Different Theories)

Conclusion

In this investigation, propagation of wave is studied, which is the central focus in seismology, generating precise results applicable to a wide range of economic activities. The amplitude ratios of various reflected waves are obtained by considering a homogenous, isotropic thermoelastic medium under MG-L model of thermoelasticity with the impact of non-local parameter, TT parameter and impedance parameters along with different theories of thermoelasticity. The following results have been obtained:

- 1. It is observed that for incident LD-wave under the influence of non-local, TT and impedance parameter $|R_1|$ and $|R_2|$ shows a descending behaviour in the entire interval, whereas $|R_3|$ shows uptrend in first half of the interval and thereafter it decreases for all the considered cases.
- 2. For incident T-wave, the value of $|R_1|$ and $|R_2|$ diminish with increase in θ_0 . While $|R_3|$ shows increasing behaviour in the initial range and with increase in θ_0 , $|R_3|$ shows downward trend.
- 3. It is observed that for incident SV-waves, the value of $|R_1|$ and $|R_2|$ continuously increases with increase in θ_0 , whereas for $|R_3|$ the values decrease with constant magnitude.
- 4. It is also seen that for incident LD-wave and T-wave, it is seen that for different theories of thermoelasticity, the values of $|R_1|$ and $|R_2|$ decays with increase in θ_0 , whereas for $|R_3|$ the values show uptrend initially and after attaining its maximum point the values of $|R_3|$ decreases. However, in case of incident SV-wave, an opposite behaviour is observed for $|R_1|$ and $|R_2|$ as compared with incident LD-wave and T-wave respectively. 5. The magnitude of $|R_1|$, $|R_2|$, and $|R_3|$ for LD-wave, T-wave, SV-wave in case of G-L model are more as compared with other two models of thermoelasticity.

Based on these findings, it is also concluded that the non-local parameter, TT parameters, and impedance parameters have significant effect on the amplitude ratios as non-local parameter enhances the amplitude ratios for LD-wave and T-wave. It is also observed that amplitude ratios are influenced by different theories of thermoelasticity as the values of amplitude ratios for MG-L are higher than L-S theory and lower than G-L theory of thermoelasticity for all the incident waves. The present new model is useful in developing more accurate representations of thermoelastic solids, making it particularly relevant for geophysical studies, especially in the investigation of seismic events and other phenomena in seismology and engineering.

References

- 1. Sherief HH, Ezzat MA. A problem in generalized magneto-thermoelasticity for an infinitely long annular cylinder. *Journal of Engineering Mathematics*. 1998;34: 387–402.
- 2. Ezzat MA, El- Karamany AS, El-Bary AA. Generalized thermo-viscoelasticity with memory-dependent derivatives. *International Journal of Mechanical Sciences*. 2014;89: 470–475.
- 3. Ezzat MA, El-Bary AA. Effect of variable thermal conductivity and fractional order of heat transfer on a perfect conducting infinitely long hollow cylinder. *International Journal of Thermal Sciences*. 2016;108: 62–69. 4. Shakeriaski F, Ghodrat M, Diaz JE, Behnia M. Recent advances in generalized thermoelasticity theory and the modified models. *Journal of Computational design and Engineering*. 2021;8(1): 15–35.
- 5. Ezzat MA, Ezzat SM, Alkharraz MY. State-space approach to non-local thermo-viscoelastic piezoelectric materials with fractional dual-phase lag heat transfer. *International Journal of Numerical Methods for heat & Fluid.* 2022;32(12): 3726–3750. 6. Youssef HM. Theory of two-temperature-generalized thermoelasticity. *IMA Journal of Applied Mathematics*. 2013;71(3): 383–390.
- 7. Ezzat MA, Bary AA. State space approach of two-temperature magneto-thermoelasticity with thermal relaxation in a medium of perfect conductivity. *International Journal of Engineering Science*. 2009;47(4): 618–630. 8. Kaushal S, Kumar R, Miglani A. Wave propagation in temperatures rate dependent thermoelasticity with TT. *Mathematical Sciences*. 2011;5: 125–146.
- 9. Ezzat MA, El-Bary AA. Magneto-thermoelectric viscoelastic materials with memory-dependent derivative involving two-temperature. *International Journal of Applied Electromagnetic and Mechanics*. 2016;50(4): 549–567. 10. Ezzat MA, El-Karamany AS, El-Bary AA. Two-temperature theory in Green-Naghdi thermoelasticity with fractional phase-lag heat transfer. *Microsystem Technologies*. 2018;24: 951–961.
- 11. Lofty Kh, El-Bary AA, Sarkar N. Investigation of Rotation on Plane Waves Under Two-Temperature Theory in Generalized Thermoelasticity. *Journal of Applied Mechanics and Technical Physics*. 2022;63(3): 448–457.

- 12. Al-Lehaibi EAN. The variationally principle of two temperature thermoelasticity in the absence of the energy dissipation theorem. *Journal of Umm Al-Qura University for Engineering and Architecture*. 2022;13: 81–85.
- 13. Yu YJ, Xue Z, Tian X. A modified Green-Lindsay thermoelasticity with strain rate to eliminate the discontinuity. *Meccanica*. 2018;53: 2543–2554.
- 14. Quintanilla R. Some qualitative results for a modification of the Green-Lindsay thermoelasticity. *Meccanica*. 2018;53(14): 3607 3613.
- 15. Ghodrat M, Shakeriaski F, Diaz JE, Mehnia B. Modified Green-Lindsay thermoelasticity wave propagation in elastic materials under thermal shocks. *Engineering J. Comput. Des. Eng.* 2021:8(1): 36-54.
- 16. Sarkar N, Soumen De. Waves in magneto-thermoelastic solids under modified Green-Lindsay model. *Journal of Thermal Stresses.* 2019;43(5): 594–611.
- 17. Kumar R, Kaushal S, Sharma G. Mathematical model for the deformation in a Modified Green-Lindsay thermoelastic medium with non-local and two-temperature effects. *Journal of Applied Mechanics and Technical Physics*. 2022;63: 448–457.
- 18. Eringen AC, Edelen DGB. On nonlocal elasticity. *International Journal of Eng. Science*. 1972;10(3): 233–248.
- 19. Lazar M, Agiasofitou E. Screw dislocation in non-local anisotropic elasticity. *International Journal of Eng. Science*. 2011;49(12): 1404–1414.
- 20. Pramanik AS, Siddhartha BS. Surface waves in non-local thermoelastic medium with state space approach. *Journal of Thermal Stresses*. 2020;43(6): 667–686.
- 21. Luo P, Li X, Tian X. Non-local thermoelasticity and its application in thermoelastic problem with temperature-dependent thermal conductivity. *European Journal of Mechanics A/Solids*. 2021;87: 104204.
- 22. Kumar R, Ghangas S, Vashishth AK. Fundamental and plane wave solutions in non-local biothermoelasticity diffusion theory. *Coupled Systems Mechanics*. 2021;10(1): 21–38.
- 23. Malischewsky PG. Surface Waves and Discontinuities. Amsterdam: Elsevier; 1987.
- 24. Singh B. Reflection of elastic waves from plane surface of a half-space with impedance boundary conditions. *Geosciences Research*. 2017;2(4): 242–253.
- 25. Kaushal S, Kumar R, Parmar K. Influence of diffusion and impedance parameters on wave propagation in thermoelastic medium. *International Journal of Applied Mechanics and Engineering*. 2021;26(4): 99–112.
- 26. Yadav AK. Effect of Impedance Boundary on the Reflection of Plane Waves in Fraction-Order Thermoelasticity in an Initially Stressed Rotating Half-Space with a Magnetic Field. *International Journal of Thermophysics*. 2021;42: 3.
- 27. Schoenberg M. Transmission and reflection of plane waves at an elastic viscoelastic interface. *Geophysical Journal International*. 1971;25(1-3): 35–47.
- 28. Sarkar N, Mondal S. Thermoelastic plane waves under the modified Green-Lindsay model with two temperature formulation. *ZAMM*. 2020;100(11): e201900267.
- 29. Singh B, Bijarnia R. Non-local effects on propagation of waves in a generalized thermoelastic solid half space. *Structural Engineering and Mechanics*. 2021;77(4): 473–479.
- 30. Dhaliwal RS, Singh A. *Dynamic Coupled Thermoelasticity*. New Delhi, India: Hindustan Publication Corporation; 1980.

About Authors



Kaushal Sachin D Sc

Sachin Kaushal born on 27th April 1984, did M. Sc (2006) from Guru Nanak Dev University (G.N.D.U.), Amritsar (Punjab). Completed Ph. D. (2012) on the topic of "Some Dynamic problems in micropolar thermoelastic media", from C.D.L. University (Sirsa). 2 students are awarded Ph.D. degrees, and 5 students are doing Ph.D. under his supervision. He has 40 papers published, communicated 5 research papers and 5 are ready to publish in the Journals of International repute. He is a reviewer of many International journals.





Rajneesh Kumar born on 08th June 1958, received his M.Sc. (1980) from Guru Nanak Dev University (G.N.D.U.), Amritsar (Punjab), M. Phil (1982) from Kurukshetra University Kurukshetra (K.U.K.) and Ph. D. (1986) in Applied Mathematics from Guru Nanak Dev University (G.N.D.U.), Amritsar. Guided 56 M.Phil. students, 21 students were awarded Ph.D. degrees and 9 students are doing Ph.D. under his supervision. He has 621 papers published in the Journal of International repute. His area of research work is Continuum Mechanics (Micropolar elasticity, thermoelasticity, poroelasticity, magnetoelasticity, micropolar porous couple stress theory, viscoelasticity, mechanics of fluid). He is a reviewer of many reputed journals.



Bala Indu 🗓 Sc

Indu Bala born on 4th April 2001, did M. Sc (2023) from Lovely Professional University, presently pursuing Ph.D. from Lovely Professional University (Phagwara). She has communicated 3 research papers and 1 is ready to publish in the Journal of International repute.



Sharma Gulshan 🗓 Sc

Gulshan Sharma did MSc Mathematics in 2002, qualified CSIR NET In June 2003. He has a teaching experience of 20 years, presently is an HoD of PG Department of Mathematics Doaba College.

Submitted: November 27, 2023

Revised: December 18, 2023

Accepted: January 9, 2024

Subcritical growth of repolarization nuclei in polycrystalline ferroelectric films

A.Yu. Belov ^{1,2}, 0

- ¹ Kurchatov Institute National Research Centre, Moscow, Russia
- ² Federal Scientific Research Center "Crystallography and photonics" of Russian Academy of Sciences,

Moscow, Russia

[™] belov@crys.ras.ru

ABSTRACT

The problem of subcritical growth of repolarization nuclei in ferroelectric crystals is considered. Following the approach of Barenblatt to the theory of equilibrium brittle cracks, a concept of cohesive forces, acting on adjacent domain walls in a region near the domain tip, is introduced. These cohesive forces are intimately related to the gradient term in the Ginzburg-Landau energy and become substantial as the separation between the domain walls compares with their thickness δ . The condition of equilibrium for a ferroelectric domain is formulated by taking into account the internal field associated with the cohesive forces. Criteria for stable subcritical growth of nuclei in non-uniform electric fields are presented in terms of a gradient modulus, which is an extension of the cohesion modulus concept of Barenblatt.

KEYWORDS

subcritical growth • ferroelectrics • ferroelectric domains • polycrystalline thin films

Acknowledgements. This work was performed within the State assignment of Federal Scientific Research Center "Crystallography and Photonics" of Russian Academy of Sciences.

The article was prepared based on the report presented at the Symposium "Micromechanics of Functional Materials" at the XIII All-Russian Congress on Theoretical and Applied Mechanics.

Citation: Belov AYu. Subcritical growth of repolarization nuclei in polycrystalline ferroelectric films. *Materials Physics and Mechanics*. 2024;52(2): 18–25.

http://dx.doi.org/10.18149/MPM.5212024_2

Introduction

One of the main factors that determines the efficacy of application of functional materials in various devices is the high sensitivity of their physical properties to the features of the real structure. In the case of ferroics (ferroelectrics, ferroelastics, ferromagnets), it is the behavior of the real (domain) structure that is the cause of physical nonlinearities observed in the form of hysteresis phenomena, the mechanism of which is often the subject of debate. Elucidation of the mechanism of the subcritical growth of ferroelectric domains in polycrystalline films is one of the current controversial issues in the physics of ferroelectrics.

The lead zirconate titanate $Pb(Zr_{1-x}Ti_x)O_3$ (PZT) solid solution near the morphotropic phase boundary x = 0.47, separating two ferroelectric phases — rhombohedral and tetragonal, is one of the most widely used smart materials due to unique combination of its piezoelectric and dielectric properties. In such applications as nonvolatile random access memories also the nonlinear properties of PZT become important, especially its resistance to dynamic fatigue resulting from the polarization switching and reducing life time of the memory cells. The experimental studies of the influence of dynamic fatigue on ferroelectric

19 A.Yu. Belov

hysteresis revealed a considerable difference in physical mechanisms, underlying the polarization reversal in polycrystalline PZT films of different microstructure. In particular, for (Pb_{1-y}La_y)(Zr_{1-x}Ti_x)O₃ (PLZT) polycrystalline films, including tetragonal Pb(Zr₅₀Ti₅₀)O₃, deposited on Pt/Ti-coated Si substrates [1] the grain size D of ~0.3 μ m was comparable with the film thickness $H = 0.55 \,\mu\text{m}$. These films show a frequency dependence of a coercive field $E_c(v)$ in the Merz form, $\ln(v/v_0) = -\alpha/E_c$, for a wide range of frequencies $v = 10^1 - 10^5$ Hz. An important observation made in [1] is that the dynamic fatigue does not affect the characteristic frequency v_0 , which lies around 10⁹ Hz for different PLZT compositions and can be considered as a signature of the physical mechanism of polarization switching. Unlike v_0 , the activation field α increases with the number of cycles used in fatigue tests and is the only parameter in the Merz equation that characterizes the degree of fatigue [1]. Surprisingly, it was found that in polycrystalline Pb(Zr_{0.53}Ti_{0.47})O₃ films deposited on Pt/Ti/SiO₂/Si substrates the frequency dependence of the coercive field $E_c(v)$ differs significantly from the Merz equation and follows the unusual law: $\ln(v/v_0) = -(\beta/E_c)^2$ [2], which was never observed before and can be referred to as $1/E^2$ -law. This result not only means the change in the physical mechanism governing the polarization switching rate in these films, but also implies the existence of a low limiting frequency v_0 , approaching which the coercive field diverges. The value of v_0 obtained by the extrapolation of the experimental dependence of $\ln \nu$ on $1/E_c^2$ to the point $1/E_c^2 = 0$ was about 10⁵ Hz [2]. This value is much less both the Debye frequency in ferroelectric crystals with perovskite structure (~10¹³ Hz for PZT [1]) and also the aforementioned limiting frequency for PZT films, in which the polarization switching rate is given by the Mertz equation. Fatigue tests [2] showed that the limiting frequency v_0 for the new mechanism is also independent of the number of cycles, whereas the activation field β increases with cycling, as shown in Fig. 1. Despite their importance, the results obtained in [2] remained unnoticed until they were reproduced in [3,4] for tetragonal Pb(Zr_{0.40}Ti_{0.60})O₃ films grown on Ir/SiO₂/Si substrates using the sol-gel process. Here, it is worth to mention that the $1/E^2$ -law was also reported for some other ferroelectric materials [5,6].

The existence of two principally different mechanisms of polarization switching in polycrystalline PZT films raises the question of what structural features of the films are responsible for realization of a particular mechanism. However, there is no information on the film thickness in [2]. The films grown in [3,4] had the thickness of 240 nm, but the grain size values were reported neither in [2] nor in [3,4]. Some insight into the microstructure can be gained from [7], where tetragonal Pb(Zr_{0.20}Ti_{0.80})O₃ films with thickness of 260 nm were composed of elongated single-domain grains with the mean size of ~ 50 nm. The switching of polarization by an electric field is a multistage process. It includes the stage of formation of repolarization nuclei; the stage of their forward growth into the crystal, which results in the formation of planar domain walls; and subsequent sideways motion of the domain walls. According to [8], it is the nucleation stage of the repolarization nuclei that is responsible for $1/E^2$ -law. Furthermore, as was shown in [8], thin repolarization nuclei arise as the result of thermal fluctuations. Taking into account the experimental value of $v_0 = 10^6$ Hz from [3], the activation energy was estimated as $\Delta G(E_c) \sim 10 \ kT$, where the coercive field E_c = 62.5 kV/cm corresponds to the hysteresis loop at a frequency v = 9.3 Hz [3] and kT - to room temperature. Thus the nucleation due to thermal fluctuations is not so prohibitive as is sometimes accepted. Among additional factors, which could contribute to the dependence of E_c on v, one should mention the thermally activated

sideways motion of domain walls in the field of short-range obstacles. For instance, such interactions become important in bulk PZT-based ceramics and lead to a logarithmic dependence of the coercive field on frequency [9-12].

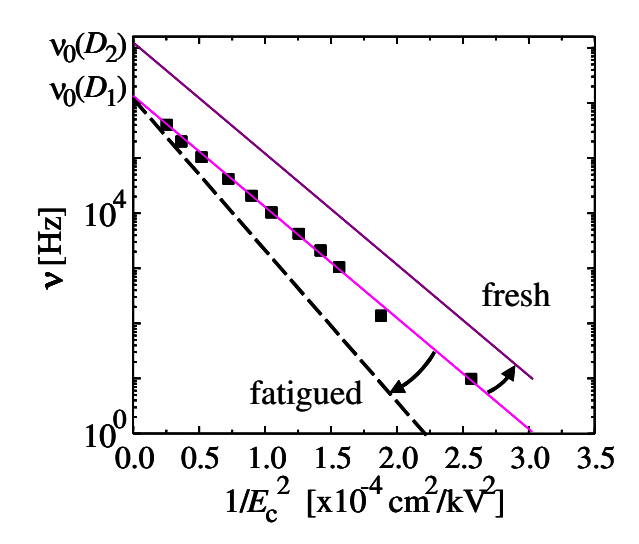


Fig. 1. Semi-log plots lnv vs $1/E_c^2$ illustrating schematically shift of the limiting frequency $v_0(D)$ with a change in the electrode diameter D ($D_2 < D_1$) in fresh PZT films (squares correspond to RT data and $D_1 = 320 \ \mu m$ [3]). An expected transformation of the plot in fatigued films is sketched

The original model [8] of the polarization reversal was not flexible enough to explain some features of the $1/E^2$ -law, namely some size (or geometric) effects. According to [3,4], the observable limiting frequency v_0 is not a fundamental characteristic of the film material or structure. It depends on the size of the upper electrode R as well: $v_0 = v_0(R)$. A qualitative phenomenological model [13], explaining the origin of such effects, assumes the existence of an additional mechanism for the growth of nuclei, which must be much faster than the usual nucleation due to thermal fluctuations. Further development [14] led to the conclusion that such mechanism is subcritical growth of repolarization nuclei in a nonuniform electric field at the edges of the electrode. In this work, following the approach of Barenblatt [15] to equilibrium brittle cracks, a concept of cohesive forces, acting on adjacent domain walls in a region near the domain tip, is introduced. These cohesive forces stem from the gradient term in the Ginzburg-Landau energy. The condition of equilibrium for a ferroelectric domain is formulated by explicit incorporation of the internal field associated with the cohesive forces. Criteria for stable subcritical growth of nuclei in nonuniform electric fields are presented in terms of a gradient modulus, which is an extension of the cohesion modulus of Barenblatt.

Thin domain approximation

In the theory of brittle cracks proposed by Barenblatt the concept of atomic cohesive forces is introduced to describe interaction of the crack surfaces in the cohesion zones near its tips. The cohesive forces are assumed to be local. Like surface forces in the continuum elasticity theory they are applied directly to the crack surfaces. Therefore, they differ from the real interatomic forces acting on atoms situated in a surface layer, which

21 A.Yu. Belov

$$h(x) = \begin{cases} c \int_{x}^{a_2} n(u) du, & (a_1 \le x \le a_2) \\ 0, & (x < a_1 \text{ or } x > a_2) \end{cases}$$
 (1)

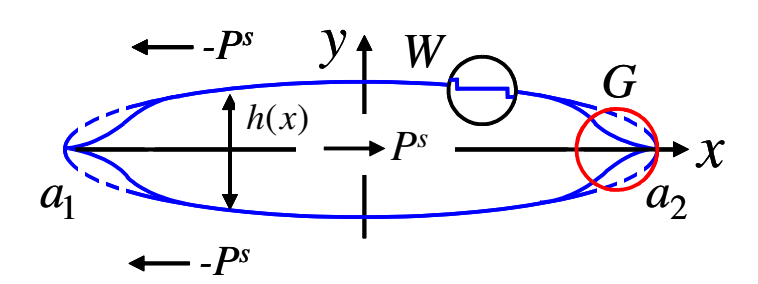


Fig. 2. A 180° domain of length $2a = a_2 - a_1$. Atomic steps on the domain wall W are schematically shown. The thickness of the domain cross section in the xy-plane is described by the function h(x). The gradient zone G is shown for the tip a_2

Further analysis throughout the paper is based on the thin domain approximation [8]. It means that all steps are situated in one plane y = 0 and we deal with a plane step distribution. Within the framework of this approximation the spontaneous polarization, which in our case has only one component, is localized in the plane y = 0 and can be expressed as:

$$P_x^0(x,y) = -P^s + \Delta P^s h(x)\delta(y), \tag{2}$$

where P^s denotes the value of spontaneous polarization and $\Delta P^s c = 2P^s c$ is the bound charge (per unit length along the z-axis) associated with a step on the domain wall. The shape of an equilibrium domain is to be found from the condition of vanishing the configuration force $f_x(x)$ acting on each step. Provided that the potentials of remote electrodes are fixed, it is to be derived from the electric free energy [8]. In general, the condition of step equilibrium contains three terms of different nature:

$$f_{x}(x) = f_{x}^{E}(x) + f_{x}^{GL}(x) + f_{x}^{lat}(x) = 0.$$
(3)

However, the main contribution to the configuration force in Eq. (3) is due to the cohesive (or gradient) force:

$$f_x^{GL}(x) = -(\Delta P^s c) E_x^*(x), \tag{4}$$

where $E_x^*(x) = E_x^*[h(x)]$ is the internal field associated with the Ginzburg-Landau energy, and the electric force:

$$f_x^E(x) = \Delta P^s c(E^U(x) + E_x^d(x, y = 0)).$$
 (5)

Here, $E^U(x) = E_x^U(x, y = 0)$ is the electric field of remote electrodes with an account of the depolarization field of the homogeneously poled ferroelectric crystal and

$$E_x^d(x, y = 0) = \frac{\Delta P^s c}{2\pi\varepsilon} \int_{a_1}^{a_2} \frac{n(u)}{x - u} du$$
 (6)

is the depolarization field due to bound charges of the steps. Correspondingly, $\varepsilon = (\varepsilon_{11}\varepsilon_{22})^{1/2}$ stands for the effective dielectric constant. As concerns the force $f_x^{lat}(x)$ in Eq. (3), it has the lattice periodicity and plays the same role as Peierls force on a crystal dislocation. Its mean value over the lattice period vanishes and we neglect it in the step equilibrium condition given in Eq. (3). Finally, taking into account Eq. (6), we obtain the equation of domain equilibrium:

$$\frac{1}{2\pi\varepsilon} \int_{a_1}^{a_2} \frac{n(u)}{x-u} du = E_x^U(x) - E_x^*(x), (a_1 < x < a_2), \tag{7}$$

which is a singular integral equation for the step density function n(x). The self-force on a step, resulting from Eq. (6) for the depolarization field, has a singularity at x = u, but it can be excluded, using the principal value of the integral in Eq. (7). Unlike the previous analysis [8,14], here we include explicitly the internal field $E_x^*(x)$ acting only on few steps in the neighbourhood of the domain tips. It is the field, which work gives rise to an increase in the domain wall surface energy as the domain grows. It cannot be derived within the framework of the semi-continuum approach used here. More details on properties of $E_x^*(x)$ following from the Ginzburg-Landau theory will be published elsewhere. Moreover, one can consider the internal field phenomenologically, like it was done for elastic twins [16-18] and brittle cracks [15]. In fact, the internal field is not a usual function of the step position x, namely, it is a functional of the domain thickness h(x) at this point and thereby is a functional of the step density n(x). Therefore, strictly speaking, Eq. (7) is nonlinear. However, this difficulty can be overcome in the same way as in Barenblatt's theory [15].

The concept of gradient modulus

Eq. (7) can be solved analytically, see [14] for details. Let's consider the solution for the depolarization field defined in Eq. (6). Ahead the right domain tip $x = a_2$ it has the form:

$$E_x^d(x > a_2, y = 0) = \frac{1}{\pi \sqrt{(x - a_1)(x - a_2)}} \int_{a_1}^{a_2} \frac{\sqrt{(a_2 - u)(u - a_1)}}{x - u} \left[E_x^U(u) - E_x^*(x) \right] du, \tag{8}$$

and near the tip shows a universal behaviour with a singularity:

$$E_{\chi}^{d}(x \to a_{2}, y = 0) = \frac{1}{\sqrt{2\pi (x - a_{2})}} \left\{ K(a_{2}) - \frac{1}{\sqrt{\pi a}} \int_{a_{1}}^{a_{2}} \sqrt{\frac{u - a_{1}}{a_{2} - u}} E_{\chi}^{*}(u) du \right\}, \tag{9}$$

where the quantity

$$K(a_2) = \frac{1}{\sqrt{\pi a}} \int_{a_1}^{a_2} \sqrt{\frac{u - a_1}{a_2 - u}} E_x^U(u) \ du \tag{10}$$

23 A.Yu. Belov

is a weighted average (or intensity factor) of the external field. Since for the equilibrium domain the depolarization field has to be non-singular, the singularity in Eq. (9) is to be eliminated. This requirement leads to the condition:

$$K(a_2) = \frac{1}{\sqrt{\pi a}} \int_{a_1}^{a_2} \sqrt{\frac{u - a_1}{a_2 - u}} E_{\chi}^*(u) \ du. \tag{11}$$

Since the internal field rapidly vanishes outside the gradient zone, Eq. (11) takes the form:

$$K(a_2) = K^*, (12)$$

where the quantity K^* characterizes the behaviour of the cohesive forces in the gradient zone and can be referred to as *gradient modulus*. It is a material constant and can be represented as:

$$K^* = \sqrt{\frac{2}{\pi}} \int_0^d \frac{E^*(u)}{\sqrt{u}} du = \sqrt{\frac{2}{\pi}} \int_0^\infty \frac{E^*(u)}{\sqrt{u}} du, \tag{13}$$

where d is the gradient zone size and $E^*(u) = |E_x^*(x)|$. In practice, one can use $d = \infty$, since beyond the gradient zone the internal field is vanishing. Eq. (12) is the first equation for the unknown positions a_1 and a_2 of the equilibrium domain tips. The second equation for a_1 and a_2 can be obtained similarly, eliminating the singularity at the left tip a_1 .

Subcritical growth of a repolarization nucleus

If the external field is uniform, the intensity factors for both domain tips coincide,

$$K(-a) = K(a) = E^{U}\sqrt{\pi a},\tag{14}$$

where the domain tip positions are chosen at $a_1 = -a$ and $a_2 = a$. The size of the equilibrium domain in terms of the gradient modulus is given as:

$$l_c = \frac{2}{\pi} \left(\frac{K^*}{E^U} \right)^2. \tag{15}$$

Such domain is unstable [14]. If the size of a repolarization nucleus exceeds the critical value given in Eq. (15), the nucleus can grow, thus reducing the thermodynamic potential, otherwise it shrinks. Comparing Eq. (15) with the results of [14], one can obtain the important relation between the gradient modulus and the domain wall surface energy γ_w ,

$$K^* = 2\sqrt{\gamma_w/\varepsilon}. (16)$$

In the case of non-uniform electric fields, the thermodynamics of the growth process can be analyzed by means of the known in fracture mechanics Irwin formula for a crack in an elastic solid. Its extension to the case of a ferroelectric domain was made in [14] and represents the variation in the electric free energy when the domain size changes by the value of δl ,

$$\frac{\delta \tilde{F}}{D} = -\frac{1}{2} \int_{a_2}^{a_2 + \delta l} [E_x^U(x) + E_x^d(x, y = 0)] \left(\int_{-\infty}^{\infty} \delta P_x^0(x - \delta l, y) dy \right) dx. \tag{17}$$

According to [14], calculation of the integral in Eq. (17) gives rise to a simple result,

$$\frac{\delta \tilde{F}}{D} = -\frac{\varepsilon K^2(a_2)}{2} \, \delta l, \tag{18}$$

for the electric free energy release, and the domain growth in a non-uniform electric field becomes thermodynamically favourable if

$$\frac{\delta G}{D} = \frac{\delta \tilde{F}}{D} + 2\gamma_w \delta l = \left(-\frac{\varepsilon K^2(a_2)}{2} + \frac{\varepsilon K^{*2}}{2} \right) \delta l \le 0.$$
 (19)

For the tip $x = a_1$ a similar condition takes place.

The mechanism of subcritical growth can be demonstrated within the framework of a simple model presented in Fig. 3, where it is assumed that a repolarization nucleus of size l=2a arose at the edge of the electrode x=-b as a result of thermal fluctuation. This model is directly relevant to the forward growth of nuclei near the electrode edges in PZT films. Analysis of the results of numerical calculations of the coefficients K(-a) and K(a) depending on the value of the geometric parameter b/a, where b is the distance from the edge of the electrode to the centre of the nucleus, shows that if the right tip of the nucleus is in equilibrium, its left tip cannot be in equilibrium and always shifts towards the edge of the electrode. However, the main conclusion is that at b=a the value of the intensity factor $K(a) = 2K^E/\pi$ for the right edge of the nucleus turns out to be independent of its size. Here, $K^E=Q/(2\epsilon(\pi R)^{1/2})$, Q is the linear charge of the electrode, and 2R is its width. Consequently, if condition (19) is met, nuclei of arbitrarily small size resulting from thermal fluctuations do not annihilate, but can grow, lowering the thermodynamic potential G of the system. This means the fundamental possibility of stable subcritical growth of repolarization nuclei in the vicinity of the electrode edges.

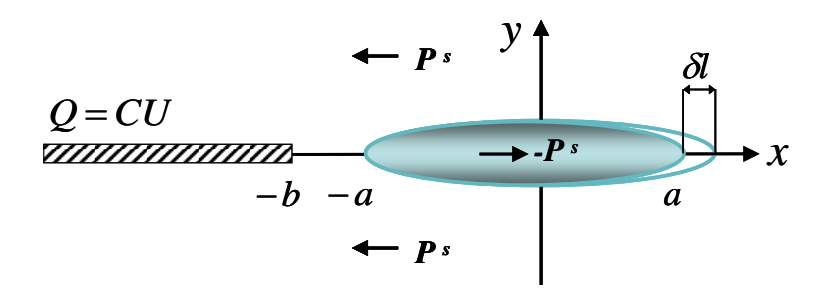


Fig. 3. A sketch of a 180° repolarization nucleus of length 2a near the edge x = -b of a thin planar electrode occupying the region $-2R - b \le x \le -b$

Conclusions

Stable subcritical growth of repolarization nuclei, which doesn't require thermal activation, becomes possible due to the lack of dependence of electric energy release on the nucleus size. This growth regime is provided by specific behaviour of the non-uniform electric field near electrode edges. Since the electric field decreases with the distance r from the electrode edge as $1/\sqrt{r}$, the electric free energy released by the domain expansion is fully consumed by the newly formed domain wall surfaces whatever nucleus size is. This effect is very similar to the microcrack formation mechanism by arrested dislocation pile-ups (Zener-Mott-Stroh model), where elastic energy release turns out to be independent of crack size [19–21].

References

- 1. Chen IW, Wang Y. Activation field and fatigue of (Pb,La)(Zr, Ti)O3 thin films. *Applied Physics Letters*. 1999; 75(26): 4186–4188.
- 2. Du X, Chen IW. Frequency spectra of fatigue of PZT and other ferroelectric thin films. *Materials Research Society Symposium Proceedings*. 1998; 493: 311–316.
- 3. Nam SM, Kil YB., Wada S, Tsurumi T. Domain switching kinetics of lead zirconate titanate thin films. Japanese. *Journal of Applied Physics*. 2003; 42(12B): L1519–L1522.

25 A.Yu. Belov

4. Tsurumi T, Num SM, Kil YB, Wada S. High frequency measurements of P-E hysteresis curves of PZT thin films. *Ferroelectrics*. 2001; 259(1): 43–48.

- 5. Jung DJ, Dawber M, Scott JF, Sinnamon LJ, Gregg J.M. Switching dynamics in ferroelectric thin films: an experimental survey. *Integrated Ferroelectrics*. 2002: 48(1): 59–68.
- 6. Mulaosmanovic H, Ocker J, Muiller S, Schroeder U, Muiller J, Polakowski P, Flachowsky S, van Bentum R, Mikolajick T, Slesazeck S. Switching kinetics in nanoscale hafnium oxide based ferroelectric field-effect transistors. *ACS Appl. Mater. Interfaces.* 2017, 9(4), 3792–3798.
- 7. Borowiak AS, Garcia-Sanchez A, Mercone S. Nucleation and growth domain limits in ferroelectric polycrystalline thin films. In: 2016 Joint IEEE International Symposium on the Applications of Ferroelectrics/European Conference on Application of Polar Dielectrics/Piezoelectric Force Microscopy Workshop (ISAF/ECAPD/PFM). Darmstadt, Germany: IEEE; 2016. p.1–4.
- 8. Belov AY. 1/E² Law: Solution of the unsolved problem in the physics of ferroelectrics. *JETP Letters*. 2018; 108(4): 221–225.
- 9. Chen IW, Wang I. A domain wall model for relaxor ferroelectrics. Ferroelectrics. 1998;206(1): 245-263.
- 10. Belov AY, Kreher WS, Nicolai M. The evaluation of activation parameters for ferroelectric switching in in soft PZT ceramics. *Ferroelectrics*. 2009; 391(1): 42–50.
- 11. Belov AY, Kreher WS. Creep in soft PZT: the effect of internal fields. Ferroelectrics. 2009; 391(1): 12–21.
- 12. Belov AY, Kreher WS. Micromechanics of ferroelectrics: from domain walls to piezoceramic devices. *Ferroelectrics*. 2007;351(1): 79–87.
- 13. Belov AY. Fast polarization reversal in polycrystalline ferroelectric thin films: the origin of size effects. *Ferroelectrics*. 2019; 544(1): 27–32.
- 14. Belov AY. The growth condition for ferroelectric domains of a subcritical size. Ferroelectrics. 2022;590(1): 19–26.
- 15. Barenblatt GI. Flow, Deformation and Fracture. New York: Cambridge University Press; 2014.
- 16. Kosevich AM, Boiko VS. Dislocation theory of the elastic twinning of crystals. *Soviet Physics Uspekhi*. 1971;14(3): 286-316.
- 17. Boyko VS. Kezerashvili RY. Twinning in nanocrystalline materials. *Physics Letters A*. 2012;376(10-11): 1058-1061.
- 18. Boyko VS, Garber RI, Kosevich AM. Reversible Crystal Plasticity. New York: AIP Press; 1994.
- 19. Stroh AN. A theory of the fracture of metals. Advances in Physics. 1957;6(24): 418-465.
- 20. Stroh AN. The formation of cracks as a result of plastic flow. Proc. R. Soc. Lond. A. 1954;223(1154): 404-414.
- 21. Indenbom VL. Dislocations and Internal Stresses. In: Indenbom VL, Lothe J. (eds.) *Elastic Strain Fields and Dislocation Mobility*. Amsterdam: North-Holland; 1992. p.1-174.

About Author

Alexander Yu. Belov 🗓 Sc

Candidate of Physico-Mathematical Sciences,

Senior Researcher (Kurchatov Institute National Research Centre, Moscow, Russia)

Senior Researcher (Federal Scientific Research Center "Crystallography and photonics" of Russian Academy of Sciences, Moscow, Russia)

Submitted: August 1, 2023 Revised: November 8, 2023 Accepted: November 23, 2023

Moment-membrane theory of elastic cylindrical shells as a continual model of deformation of a single-layer carbon nanotube

S.H. Sargsyan [™],

Shirak State University, Gyumri, Armenia

Author to whom correspondence should be addressed: s_sargsyan@yahoo.com

ABSTRACT

One of the key tasks in the study of two-dimensional nanomaterials (fullerenes, nanotubes, graphene) is to explore their mechanical properties: bending, vibrations, and stability. For the study of such problems, it is essential to construct both microscopic and macroscopic models of the deformation behavior of such materials. Based on the three-dimensional moment theory of elasticity, the moment-membrane theory of elastic cylindrical shells is constructed as a continual model of deformations of a single-layer carbon nanotube. The axisymmetric deformation of an elastic cylindrical shell is studied, and numerical results are presented. Further, a moment-membrane technical theory of elastic cylindrical shells is constructed, on the basis of which the stability of the initially axial compressed state of a carbon nanotube is studied, and the critical load value is numerically determined.

KEYWORDS

carbon nanotube • continual model • moment-membrane theory of cylindrical shells axisymmetric statics problem • stability problem • critical load value

Acknowledgements. The work was carried out under contract N: 10-12/23-I/SHSU funded by the Science Committee of RA.

The article was prepared based on the report presented at the Symposium "Micromechanics of Functional Materials" at the XIII All-Russian Congress on Theoretical and Applied Mechanics.

Citation: Sargsyan SH. Moment-membrane theory of elastic cylindrical shells as a continual model of deformation of a single-layer carbon nanotube. *Materials Physics and Mechanics*. 2024;52(1): 26–38. http://dx.doi.org/10.18149/MPM.5212024_3

Introduction

The emergence of two-dimensional nanomaterials (fullerene [1], carbon nanotube [2], graphene [3]) has resulted in a need to construct continual models which enable the study of their deformations.

In [4–7], the consideration of the moment interaction between atoms in the crystal lattices of two-dimensional nanomaterials (and other nano-objects) has been justified. Also, the three-dimensional moment theory of elasticity (with independent fields of displacements and rotations) has been established as a continual model for deformations of the considered nanomaterials.

Studies [4–7] have naturally led to a topical problem concerning the construction of a model of thin plates or shells that can adequately describe the deformations of two-dimensional nanomaterials, based on the three-dimensional moment theory of elasticity.

We note that the general model of constructing the models of thin shells and plates based on the moment theory of elasticity are developed in [8,9], where a detailed review of the works in the field are presented. The general remark to these models is that the six elastic constants of the material based on the moment theory of elasticity have not been defined in them.

In this case we note that a new approach has been taken in [10] for the construction of an adequate model of two-dimensional nanomaterials based on the moment theory of elasticity.

In [10], the corresponding one-dimensional continual-beam model has been constructed, based on the study of the general deformation of a linear atomic chain, when the force interaction between its atoms is non-central and a moment interaction is in place. Considering the crystal graphene lattice, in the cell of its periodicity, by replacing interatomic interactions with the indicated beam model, a discrete-continual model of a graphene is constructed. Further, by passing the limit, a continual linear model of its deformation is constructed. In the same paper, it is stated that the constructed model of a graphene is completely identical to the so-called moment-membrane theory of elastic thin plates [11,12]. By comparing the two models, all elastic constants of the indicated theory of plates are numerically determined (through the physical parameters of the discrete model of a graphene). It is evident that the constructed moment-membrane linear theory of elastic thin plates (a) - plane stress state, (b) - transverse bending) with certain elastic constants is a continual model of graphene deformations ((a) - for its deformation in its own plane, (b) - for its transverse bending from its own plane). This opens a new avenue for studying various applied deformation problems of statics, dynamics and stability of a graphene sheet.

It is important to note that the main feature of the moment-membrane theory of elastic plates is the property of a uniform distribution of displacements, free rotations, stresses and moment stresses along the thickness of the plate. The property is characteristic for a thin membrane (it is no coincidence that in many publications (for example [13]), the term 'graphene membrane' is used for a 'graphene').

Considering that a single-layer carbon nanotube is an extended structure in the form of a hollow cylinder (consisting of one graphite layer or a graphene rolled into a tube [14], with a hexagonal organization of carbon atoms), it is appropriate to develop the ideas of works [10-12] and construct a moment-membrane theory of elastic cylindrical shells as a continual model of deformation of a single-layer carbon nanotube.

Main hypotheses. Kinematic model of deformations of moment-membrane theory of cylindrical shells. Equations of strain compatibility

As a basis, we will consider equations and boundary conditions of the three-dimensional moment linear theory of elasticity with independent fields of displacements and rotations [15] in the region of a cylindrical shell with thickness 2h. A cylindrical coordinate system x, θ, z is considered, where x, θ represent the lines of the main curvatures of the middle surface of the shell (z=0), and the rectilinear axis z is directed along the normal to this surface. In this case, for Lame coefficients of the middle surface, we take: $A_1 = 1, A_2 = R$.

To study the deformations of a single-layer carbon nanotube, below, based on the three-dimensional moment theory of elasticity, as well as based on certain hypotheses, we will consider the basic equations of the moment-membrane theory of elastic cylindrical shells.

28 S.H. Sarqsyan

The hypotheses adopted below can be considered as kinematic and static:

1. The essence of the kinematic hypothesis is the assumption about the constancy of all components of the displacement and free rotation vectors along the coordinate z (i.e., their uniform distribution over the thickness of the shell):

$$V_i = u_i(x, \theta), \ V_3 = w(x, \theta), \ \omega_i = \Omega_i(x, \theta), \ \omega_3 = \Omega_3(x, \theta), \ i = 1, 2.$$
 (1)

- 2. In the physical relations of the moment theory of elasticity [15], stresses σ_{33} , σ_{3i} and moment stresses μ_{33} , μ_{3i} can be neglected with respect to σ_{ii} , σ_{i3} , μ_{ii} , μ_{i3} (i = 1,2).
- 3. It is accepted that the shell is thin $\left(\frac{2h}{R} << 1\right)$.

We note that the formulated hypotheses correspond to the initial approximation of the result of the asymptotic method of integration of the three-dimensional boundary value problem of the moment elasticity theory in a thin shell region [16,17].

Based on hypotheses (1) and (3), from the corresponding geometric relations of the moment theory of elasticity [15] (in the case of cylindrical coordinates) for the components of the tensors of deformations and bending torsions, we have:

$$\gamma_{11}(x,\theta,z) = \Gamma_{11}(x,\theta), \quad \gamma_{22}(x,\phi,z) = \Gamma_{22}(x,\phi), \quad \gamma_{12}(x,\phi,z) = \Gamma_{12}(x,\phi), \\
\gamma_{21}(x,\phi,z) = \Gamma_{21}(x,\phi), \quad \gamma_{13}(x,\phi,z) = \Gamma_{13}(x,\phi), \quad \gamma_{23}(x,\phi,z) = \Gamma_{23}(x,\phi), \\
\chi_{11}(x,\phi,z) = k_{11}(x,\phi), \quad \chi_{22}(x,\phi,z) = k_{22}(x,\phi), \quad \chi_{12}(x,\phi,z) = k_{12}(x,\phi), \\
\chi_{21}(x,\phi,z) = k_{21}(x,\phi), \quad \chi_{13}(x,\phi,z) = k_{13}(x,\phi), \quad \chi_{23}(x,\phi,z) = k_{23}(x,\phi), \\
\chi_{31} = \chi_{32} = \chi_{33} = 0, \quad \gamma_{31} = \gamma_{32} = \gamma_{33} = 0,$$
(2)

where

$$\Gamma_{11} = \frac{\partial u_1}{\partial x}, \quad \Gamma_{22} = \frac{1}{R} \frac{\partial u_2}{\partial \theta} + \frac{w}{R}, \quad \Gamma_{12} = \frac{\partial u_2}{\partial x} - \Omega_3, \quad \Gamma_{21} = \frac{1}{R} \frac{\partial u_1}{\partial \theta} + \Omega_3, \\
\Gamma_{13} = \frac{\partial w}{\partial x} + \Omega_2, \quad \Gamma_{23} = \frac{1}{R} \frac{\partial w}{\partial \theta} - \frac{u_2}{R} - \Omega_1, \\
k_{11} = \frac{\partial \Omega_1}{\partial x}, \quad k_{22} = \frac{1}{R} \frac{\partial \Omega_2}{\partial \theta} + \frac{\Omega_3}{R}, \quad k_{12} = \frac{\partial \Omega_2}{\partial x}, \quad k_{21} = \frac{1}{R} \frac{\partial \Omega_1}{\partial \theta}, \\
k_{13} = \frac{\partial \Omega_3}{\partial x}, \quad k_{23} = \frac{1}{R} \frac{\partial \Omega_3}{\partial \theta} - \frac{\Omega_2}{R}. \tag{3}$$

Here Γ_{11} , Γ_{22} , Γ_{12} , Γ_{21} , Γ_{13} , Γ_{23} -are components of deformation tensor, k_{11} , k_{22} , k_{12} , k_{21} , k_{13} , k_{23} -components of the bending-torsion tensor in the moment-membrane theory of thin cylindrical shells.

Based on Eqs. (1)-(3), it is easy to verify that the components of the displacement and free rotation vectors, the components of the deformation and bending-torsion tensors are constant by zcoordinate functions (i.e. they are all uniformly distributed over the thickness of the cylindrical shell).

It should be noted that Eqs. (1)-(3) determine the kinematic model of deformations in the moment-membrane theory of thin cylindrical shells.

Twelve quantities Γ_{11} , Γ_{22} , Γ_{12} , Γ_{21} , Γ_{13} , Γ_{23} , k_{11} , k_{22} , k_{12} , k_{21} , k_{13} , k_{23} are expressed through six functions $u_1, u_2, w, \Omega_1, \Omega_2, \Omega_3$ by Eq. (3). These twelve quantities are interconnected by six equations, which are called the equations of strain compatibility of the middle surface in the moment-membrane theory of thin cylindrical shells (which can be obtained from Eq. (3), excluding the quantities $u_1, u_2, w, \Omega_1, \Omega_2, \Omega_3$):

$$\frac{1}{R} \frac{\partial \Gamma_{11}}{\partial \theta} - \frac{\partial \Gamma_{21}}{\partial x} + k_{13} = 0, \quad \frac{\partial \Gamma_{22}}{\partial x} - \frac{1}{R} \frac{\partial \Gamma_{12}}{\partial \theta} - \frac{\Gamma_{13}}{R} - k_{23} = 0,
\frac{\partial \Gamma_{23}}{\partial x} - \frac{1}{R} \frac{\partial \Gamma_{13}}{\partial \theta} + \frac{\Gamma_{12}}{R} + k_{11} + k_{22} = 0,
\frac{1}{R} \frac{\partial k_{11}}{\partial \theta} - \frac{\partial k_{21}}{\partial x} = 0, \quad \frac{\partial k_{22}}{\partial x} - \frac{1}{R} \frac{\partial k_{12}}{\partial \theta} - \frac{k_{13}}{R} = 0,
\frac{\partial k_{23}}{\partial x} - \frac{1}{R} \frac{\partial k_{13}}{\partial \theta} + \frac{k_{12}}{R} = 0.$$
(4)

Unit forces and moments of the moment-membrane theory of elastic cylindrical shells. Elasticity relations. Equilibrium equations

We consider an element, with the lengths of the arcs of the shell middle surface, extracted from the shell by normal sections drawn in the direction of the curvature lines. In these sections, there are tangential normal σ_{11} , σ_{22} , tangential tangents σ_{12} , σ_{21} and transverse tangents stresses σ_{13} , σ_{23} , as well as corresponding moment stresses μ_{11} , μ_{22} , μ_{12} , μ_{21} , μ_{23} , which will be distributed uniformly over the thickness of the shell. This is easy to verify if we consider the physical relations of the moment theory of elasticity [15], hypothesis (2) and geometric relations (2)-(3):

$$\begin{split} &\sigma_{11} = \frac{E}{1-\nu^2}(\Gamma_{11} + \nu \Gamma_{22}), \quad \sigma_{22} = \frac{E}{1-\nu^2}(\Gamma_{22} + \nu \Gamma_{11}), \quad \sigma_{12} = (\mu + \alpha)(\Gamma_{12} + \eta_1 \cdot \Gamma_{22}), \\ &\sigma_{21} = (\mu + \alpha)(\Gamma_{21} + \eta_1 \cdot \Gamma_{12}), \quad \sigma_{13} = \tilde{G} \cdot \Gamma_{12}, \quad \sigma_{23} = \tilde{G} \cdot \Gamma_{23}, \quad \eta_1 = \frac{\mu - \alpha}{\mu + \alpha}, \\ &\mu_{11} = (\gamma + \varepsilon)[(1 + 2\eta_2)k_{11} + \eta_2 \cdot k_{22}], \\ &\mu_{22} = (\gamma + \varepsilon)[(1 + 2\eta_2)k_{22} + \eta_2 \cdot k_{11}], \quad \eta_2 = \frac{\gamma - \varepsilon}{\gamma + \varepsilon}, \\ &\mu_{12} = (\gamma + \varepsilon)(k_{12} + \eta_2 \cdot k_{21}), \\ &\mu_{21} = (\gamma + \varepsilon)(k_{21} + \eta_2 \cdot k_{12}), \\ &\mu_{13} = B \cdot k_{13}, \quad \mu_{23} = B \cdot k_{23}, \end{split}$$
 (6)

$$E, \ \nu, \ \mu = \frac{E}{2(1+\nu)}, \ \alpha, \ \tilde{G} = \frac{4\mu\alpha}{\mu+\alpha}, \ \gamma, \ \varepsilon, \ \beta = \frac{\gamma-\varepsilon}{\gamma+\varepsilon} 2\gamma, \ B = \frac{4\gamma\varepsilon}{\gamma+\varepsilon}$$

are the elastic constants of the moment theory of elasticity for two-dimensional nanomaterials.

Now, instead we introduce integral characteristics - forces and moments - statically equivalent to the components of the stress tensor and the moment stress tensor (6). Considering the thinness of the shell, we have:

$$T_{11} = \int_{-h}^{h} \sigma_{11} dz = 2 \sigma_{11} h, \quad T_{22} = \int_{-h}^{h} \sigma_{22} dz = 2 \sigma_{22} h, \quad S_{12} = \int_{-h}^{h} \sigma_{12} dz = 2 \sigma_{12} h,$$

$$S_{21} = \int_{-h}^{h} \sigma_{21} dz = 2 \sigma_{21} h, \quad N_{13} = \int_{-h}^{h} \sigma_{13} dz = 2 \sigma_{13} h, \quad N_{23} = \int_{-h}^{h} \sigma_{23} dz = 2 \sigma_{23} h,$$

$$L_{11} = \int_{-h}^{h} \mu_{11} dz = 2 \mu_{11} h, \quad L_{22} = \int_{-h}^{h} \mu_{22} dz = 2 \mu_{22} h, \quad L_{12} = \int_{-h}^{h} \mu_{12} dz = 2 \mu_{12} h,$$

$$L_{21} = \int_{-h}^{h} \mu_{21} dz = 2 \mu_{21} h, \quad L_{13} = \int_{-h}^{h} \mu_{13} dz = 2 \mu_{13} h, \quad L_{23} = \int_{-h}^{h} \mu_{23} dz = 2 \mu_{23} h.$$

$$(8)$$

With the help of Eq. (6), as well as Eq. (8), we obtain the physical relations of elasticity of the moment-membrane theory of cylindrical shells:

$$T_{11} = \tilde{E}_*(\Gamma_{11} + \nu \cdot \Gamma_{22}), \quad T_{22} = \tilde{E}_*(\Gamma_{22} + \nu \cdot \Gamma_{11}),$$

$$S_{12} = D_2(\Gamma_{12} + \eta_1 \cdot \Gamma_{21}), \quad S_{21} = D_2(\Gamma_{21} + \eta_1 \cdot \Gamma_{12}), \quad N_{13} = D_1 \cdot \Gamma_{13},$$

$$N_{23} = D_1 \cdot \Gamma_{23}, L_{11} = D'[(1 + 2\eta_2)k_{22} + \eta_2 \cdot k_{11}], \quad L_{22} = D'[(1 + 2\eta_2)k_{22} + \eta_2 \cdot k_{11}],$$

$$L_{12} = D'(k_{12} + \eta_2 \cdot k_{21}), \quad L_{21} = D'(k_{21} + \eta_2 \cdot k_{12}), L_{13} = B_* \cdot k_{13}, \quad L_{23} = B_* \cdot k_{23},$$
where

$$E_* = 2Eh, \ \tilde{E}_* = \frac{E_*}{1-v^2}, \ D_2 = (\mu + \alpha) \cdot 2h, \ D_1 = 2\tilde{G}h, \ D' = (\gamma + \varepsilon) \cdot 2h, \ B_* = 2Bh.$$
 (10)

It should be noted that expressions (10) represent the stiffness characteristics of the moment-membrane theory of elastic cylindrical shells, the numerical values of which (in the current form) are determined in [10].

30 S.H. Sargsyan

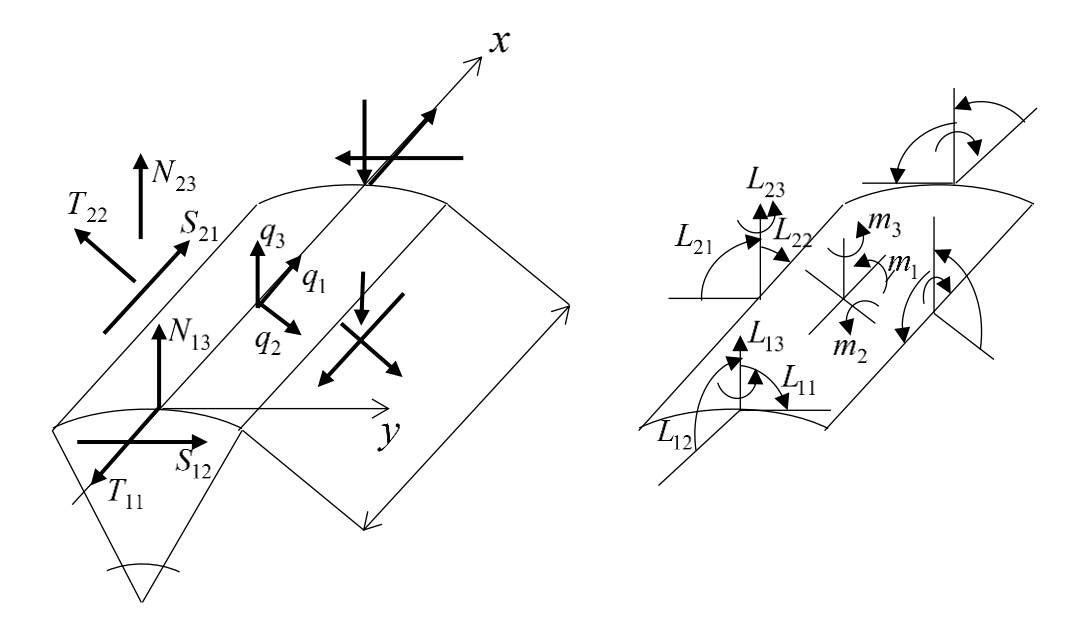


Fig. 1. Forces and moments acting on the shell element

We now consider the equilibrium of an element of the middle surface of a cylindrical shell (Fig. 1), loaded with internal forces, moments and an externally distributed load. Based on the condition that the main vector and the main moment of the indicated forces, acting on the element, are equal to zero and after switching to scalar equations, the six equilibrium equations of the moment-membrane theory of elastic thin cylindrical shells are obtained:

$$\frac{\partial T_{11}}{\partial x} + \frac{1}{R} \frac{\partial S_{21}}{\partial \theta} = -q_1, \quad \frac{1}{R} \frac{\partial T_{22}}{\partial \theta} + \frac{\partial S_{12}}{\partial x} + \frac{N_{23}}{R} = -q_2,
\frac{T_{22}}{R} - \frac{\partial N_{13}}{\partial x} - \frac{1}{R} \frac{\partial N_{23}}{\partial \theta} = q_3,
\frac{\partial L_{11}}{\partial x} + \frac{1}{R} \frac{\partial L_{21}}{\partial \theta} + N_{23} = -m_1, \quad \frac{1}{R} \frac{\partial L_{22}}{\partial \theta} + \frac{\partial L_{12}}{\partial x} + \frac{L_{23}}{R} - N_{13} = -m_2,
\frac{L_{22}}{R} - \frac{\partial L_{13}}{\partial x} - \frac{1}{R} \frac{\partial L_{23}}{\partial \theta} - (S_{12} - S_{21}) = m_3,$$
(11)

where $q_k(x,\phi)$, $m_k(x,\phi)$, k=1,2,3 are surface density components of externally distributed forces and moments.

Geometric relations (3), elasticity relations (9) and equilibrium equations (11) are the basic equations of the moment-membrane theory of elastic thin cylindrical shells, at the same time, the basic equations of the continual model of deformations of a single-layer carbon nanotube.

By substituting geometric relations (3) into elasticity relations (9) and into the obtained equilibrium equations (11) (at $m_k = 0$, k = 1,2,3), we reduce the problem to a resolving system of six differential equations with respect to generalized displacements $u_i, w, \Omega_i, \Omega_3, i = 1,2$, the order of which is twelve:

$$\tilde{L}_{11}u_{1} + \tilde{L}_{12}u_{2} + \tilde{L}_{13}w + \tilde{L}_{14}\Omega_{1} + \tilde{L}_{15}\Omega_{2} + \tilde{L}_{16}\Omega_{3} = -\frac{q_{1}}{\tilde{E}_{*}},
\tilde{L}_{21}u_{1} + \tilde{L}_{22}u_{2} + \tilde{L}_{23}w + \tilde{L}_{24}\Omega_{1} + \tilde{L}_{25}\Omega_{2} + \tilde{L}_{26}\Omega_{3} = -\frac{q_{2}}{\tilde{E}_{*}},
\tilde{L}_{31}u_{1} + \tilde{L}_{32}u_{2} + \tilde{L}_{33}w + \tilde{L}_{34}\Omega_{1} + \tilde{L}_{35}\Omega_{2} + \tilde{L}_{36}\Omega_{3} = \frac{q_{3}}{\tilde{E}_{*}},
\tilde{L}_{41}u_{1} + \tilde{L}_{42}u_{2} + \tilde{L}_{43}w + \tilde{L}_{44}\Omega_{1} + \tilde{L}_{45}\Omega_{2} + \tilde{L}_{46}\Omega_{3} = 0,
\tilde{L}_{51}u_{1} + \tilde{L}_{52}u_{2} + \tilde{L}_{53}w + \tilde{L}_{54}\Omega_{1} + \tilde{L}_{55}\Omega_{2} + \tilde{L}_{56}\Omega_{3} = 0,
\tilde{L}_{61}u_{1} + \tilde{L}_{62}u_{2} + \tilde{L}_{63}w + \tilde{L}_{64}\Omega_{1} + \tilde{L}_{65}\Omega_{2} + \tilde{L}_{66}\Omega_{3} = 0,$$
(12)

where the coefficients \tilde{L}_{km} are partial differential operators in the following form:

$$\begin{split} \tilde{L}_{11} &= \frac{\partial^{2}}{\partial x^{2}} + \frac{D_{2}}{E_{*}} \frac{1}{R^{2}} \frac{\partial^{2}}{\partial \theta^{2}}, \quad \tilde{L}_{12} = \tilde{L}_{21} = \left(\nu + \frac{D_{2}\eta_{1}}{\tilde{E}_{*}}\right) \frac{1}{R} \frac{\partial^{2}}{\partial x \partial \theta}, \quad \tilde{L}_{13} = \tilde{L}_{31} = \frac{\nu}{R} \frac{\partial}{\partial x}, \\ \tilde{L}_{14} &= \tilde{L}_{41} = 0, \quad \tilde{L}_{15} = \tilde{L}_{51} = 0, \quad \tilde{L}_{16} = \tilde{L}_{61} = \frac{D_{2}}{\tilde{E}_{*}} (1 - \eta_{1}) \frac{1}{R} \frac{\partial}{\partial \theta}, \\ \tilde{L}_{22} &= \frac{D_{2}}{\tilde{E}_{*}} \frac{\partial^{2}}{\partial x^{2}} + \frac{1}{R^{2}} \frac{\partial^{2}}{\partial \theta^{2}} - \frac{D_{2}}{\tilde{E}_{*} R^{2}}, \quad \tilde{L}_{23} = \tilde{L}_{32} = \frac{1}{R} \left(1 + \frac{D_{1}}{\tilde{E}_{*}}\right) \frac{1}{R} \frac{\partial}{\partial \theta}, \\ \tilde{L}_{24} &= \tilde{L}_{42} = -\frac{D_{1}}{\tilde{E}_{*}}, \quad \tilde{L}_{25} = \tilde{L}_{52} = 0, \quad \tilde{L}_{26} = \tilde{L}_{62} = -\frac{D_{2}}{\tilde{E}_{*}} (1 - \eta_{1}) \frac{\partial}{\partial x}, \\ \tilde{L}_{33} &= -\frac{D_{1}}{\tilde{E}_{*}} \left(\frac{\partial^{2}}{\partial x^{2}} + \frac{1}{R^{2}} \frac{\partial^{2}}{\partial \theta^{2}}\right), \quad \tilde{L}_{34} = \tilde{L}_{43} = \frac{D_{1}}{\tilde{E}_{*}} \cdot \frac{1}{R} \frac{\partial}{\partial \theta}, \\ \tilde{L}_{35} &= \tilde{L}_{53} = -\frac{D_{1}}{\tilde{E}_{*}} \frac{\partial}{\partial x}, \quad \tilde{L}_{36} = \tilde{L}_{63} = 0, \quad \tilde{L}_{44} = \frac{D'(1 + 2\eta_{2})}{\tilde{E}_{*}} \frac{\partial^{2}}{\partial x^{2}} + \frac{D'}{\tilde{E}_{*}} \cdot \frac{1}{R^{2}} \frac{\partial^{2}}{\partial \theta^{2}} - \frac{D_{1}}{\tilde{E}_{*}}, \\ \tilde{L}_{45} &= \tilde{L}_{54} = \frac{2D'\eta_{2}}{\tilde{E}_{*}} \cdot \frac{1}{R} \frac{\partial^{2}}{\partial x \partial \theta}, \quad \tilde{L}_{46} = \tilde{L}_{64} = \frac{D'\eta_{2}}{\tilde{E}_{*} R^{2}} \frac{\partial}{\partial x'}, \\ \tilde{L}_{55} &= \frac{D'}{\tilde{E}_{*}} \frac{\partial^{2}}{\partial x^{2}} + \frac{D'(1 + 2\eta_{2})}{\tilde{E}_{*}} \cdot \frac{1}{R^{2}} \frac{\partial^{2}}{\partial \theta^{2}} - \left(\frac{B_{*}}{\tilde{E}_{*} R^{2}} + \frac{D_{1}}{\tilde{E}_{*}}\right), \\ \tilde{L}_{56} &= \tilde{L}_{65} &= \left[\frac{D'(1 + 2\eta_{2})}{\tilde{E}_{*} R} + \frac{B_{*}}{\tilde{E}_{*} R}\right] \cdot \frac{1}{R} \frac{\partial}{\partial \theta}, \\ \tilde{L}_{66} &= -\frac{B_{*}}{\tilde{E}_{*}} \cdot \frac{\partial^{2}}{\partial x^{2}} - \frac{B_{*}}{\tilde{E}_{*}} \cdot \frac{1}{R^{2}} \frac{\partial^{2}}{\partial \theta^{2}} + \left[\frac{2D_{2}(1 - \eta_{1})}{\tilde{E}_{*}} + \frac{D'(1 + 2\eta_{2})}{\tilde{E}_{*} R^{2}}\right]. \end{split}$$

When solving specific problems, this system should be attached by boundary conditions, the total number of which is equal to six at each of the ends x = 0, and x = l of the shell (l is the length of the shell), as well as periodicity conditions (due to a closed shell that is considered).

Potential energy of deformation of the middle surface. The principle of possible displacements in the moment-membrane theory of elastic thin cylindrical shells. Boundary conditions

In accordance with the general relations of the three-dimensional moment theory of elasticity [15], by applying the expression for the potential energy of the deformation of a shell which we consider a three-dimensional body and, further, by applying Eq. (2) for the components of the deformations and bending-torsion tensors, as well as Eq. (8) and hypothesis (3), the potential energy of deformation in the moment-membrane theory of elastic thin cylindrical shells will be expressed as follows:

$$U_{0} = \frac{1}{2} \iint_{(s)} (T_{11} \cdot \Gamma_{11} + T_{22} \cdot \Gamma_{22} + S_{12} \cdot \Gamma_{12} + S_{21} \cdot \Gamma_{21} + N_{13} \cdot \Gamma_{13} + N_{23} \cdot \Gamma_{23} + L_{11} \cdot k_{11} + L_{22} \cdot k_{22} + L_{12} \cdot k_{12} + L_{21} \cdot k_{21} + L_{13} \cdot k_{13} + L_{23} \cdot k_{23}) R dx d\theta,$$

$$(14)$$
where (s) -is an area of the middle surface.

If the expressions for forces and moments are used with the help of elasticity relations (9), the surface density of the potential energy of the deformation of the moment-membrane theory of elastic thin cylindrical shells will be expressed as follows:

$$W_{0} = \frac{1}{2} \langle \tilde{E}_{*} (\Gamma_{11}^{2} + \Gamma_{22}^{2} + 2\nu \cdot \Gamma_{11} \cdot \Gamma_{22}) + D_{2} (\Gamma_{12}^{2} + \Gamma_{21}^{2} + 2\eta_{1} \cdot \Gamma_{12} \cdot \Gamma_{21}) + D_{1} (\Gamma_{13}^{2} + \Gamma_{23}^{2}) + D' \{ [(1 + 2\eta_{2})(k_{11}^{2} + k_{22}^{2}) + 2\eta_{2}k_{11}k_{22}] + (k_{12}^{2} + k_{21}^{2} + 2\eta_{2}k_{12}k_{21})] \} + B_{*} (k_{13}^{2} + k_{23}^{2}) \rangle.$$

$$(15)$$

Using the law of elasticity (9), it is easy to verify that:

$$T_{11} = \frac{\partial W_0}{\partial \Gamma_{11}}, \dots, S_{21} = \frac{\partial W_0}{\partial \Gamma_{21}}, \dots, L_{12} = \frac{\partial W_0}{\partial k_{12}}, \dots$$

$$\tag{16}$$

Thus, the function W_0 can be considered as an elastic potential of forces and moments.

In all cases, when there is an elastic potential, the principle of possible displacements is valid. According to the principle, the actual state of equilibrium of an elastic body differs from adjacent geometrically possible states in that for any infinitely

32 S.H. Sargsyan

small possible displacements from the equilibrium position, the variation of the total energy of the system is equal to zero.

If we write the principle of possible displacements of the shell, considering it as a three-dimensional body [15], applying formulas for displacements and rotations (1), components of bending deformation and bending-torsion tensors (2), stresses and moment stresses (6), the equation of the principle of possible displacements of the moment-membrane theory of elastic thin cylindrical shells will be obtained:

$$\iint_{(s)} (T_{11} \cdot \delta \Gamma_{11} + T_{22} \cdot \delta \Gamma_{22} + S_{12} \cdot \delta \Gamma_{12} + S_{21} \cdot \delta \Gamma_{21} + N_{13} \cdot \delta \Gamma_{13} + N_{23} \cdot \delta \Gamma_{23} + L_{11} \cdot \delta k_{11} + L_{22} \cdot \delta k_{22} + L_{12} \cdot \delta k_{12} + L_{21} \cdot \delta k_{21} + L_{13} \cdot \delta k_{13} + L_{23} \cdot \delta k_{23}) R dx d\theta - \delta A_0 = 0,$$
(17)

where δA_0 is the work of external forces and moments on possible displacements and rotations δu_1 , δu_2 , δw , $\delta \Omega_1$, $\delta \Omega_2$, $\delta \Omega_3$:

$$\delta A_{0} = \iint_{(s)} (q_{1} \cdot \delta u_{1} + q_{2} \cdot \delta u_{2} + q_{3} \cdot \delta w + m_{1} \cdot \delta \Omega_{1} + m_{2} \cdot \delta \Omega_{2} + m_{3} \cdot \delta \Omega_{3}) R dx d\theta -
- \iint_{\theta_{0}} (\bar{T}_{11} \cdot \delta u_{1} + \bar{S}_{12} \cdot \delta u_{2} + \bar{N}_{13} \cdot \delta w + \bar{L}_{11} \cdot \delta \Omega_{1} + \bar{L}_{12} \cdot \delta \Omega_{2} + \bar{L}_{13} \cdot \delta \Omega_{3}) \Big|_{x=0} R d\theta +
+ \iint_{\theta_{0}} (\bar{T}_{11} \cdot \delta u_{1} + \bar{S}_{12} \cdot \delta u_{2} + \bar{N}_{13} \cdot \delta w + \bar{L}_{11} \cdot \delta \Omega_{1} + \bar{L}_{12} \cdot \delta \Omega_{2} + \bar{L}_{13} \cdot \delta \Omega_{3}) \Big|_{x=1} R d\theta.$$
(18)

Due to the independence of the variations δu_1 , δu_2 , δw , $\delta \Omega_1$, $\delta \Omega_2$, $\delta \Omega_3$, from the variational equation (17), the equilibrium equations (11) follow as Euler equations, and static boundary conditions of the moment-membrane theory of elastic thin closed cylindrical shells follow as natural boundary conditions:

$$T_{11} = \bar{T}_{11}, \ S_{12} = \bar{S}_{12}, \ N_{13} = \bar{N}_{13}, \ L_{11} = \bar{L}_{11}, \ L_{12} = \bar{L}_{12}, \ L_{13} = \bar{L}_{13}, \ \text{at } x = 0, x = l.$$
 (19)

The boundary conditions in generalized displacements will be as follows:

$$u_1(x,\theta) = \bar{u}_1(x,\theta), \; u_2(x,\theta) = \bar{u}_2(x,\theta), \; w(x,\theta) = \bar{w}(x,\phi),$$

$$\Omega_1(x,\theta) = \bar{\Omega}_1(x,\theta), \ \Omega_2(x,\theta) = \bar{\Omega}_2(x,\theta), \ \Omega_3(x,\theta) = \bar{\Omega}_3(x,\theta), \text{ at } x = 0, x = l.$$

As noted, the order of the resolving system of Eq. (12) of the moment-membrane theory of cylindrical shells is equal to twelve, therefore six boundary conditions of the type (19) or (20) must be set on each edge of a closed cylindrical shell. There may also be mixed boundary conditions (for example, hinge support conditions).

Axisymmetric deformation of a cylindrical shell

Due to symmetry, we accept $u_2=0$, $\Omega_1=0$, $q_2=0$. Quantities u_1 , w, Ω_2 , Ω_3 will depend only on the coordinate x.

The resolving system for axisymmetric deformation with respect to u_1, w, Ω_2 takes the following form:

$$\frac{d^{2}u_{1}}{dx^{2}} + \frac{v}{R}\frac{dw}{dx} = -\frac{q_{1}}{\tilde{E}_{*}}, \frac{D_{1}}{\tilde{E}_{*}}\frac{d^{2}w}{dx^{2}} - \frac{w}{R^{2}} - \frac{v}{R}\frac{du_{1}}{dx} + \frac{D_{1}}{\tilde{E}_{*}} \cdot \frac{d\Omega_{2}}{dx} = -\frac{q_{3}}{\tilde{E}_{*}}, \frac{d^{2}\Omega_{2}}{dx^{2}} - \left(\frac{D_{1}}{D'} + \frac{B_{*}}{D' \cdot R^{2}}\right)\Omega_{2} - \frac{D_{1}}{D'} \cdot \frac{dw}{dx} = 0.$$
(21)

We note that for the axisymmetric problem we also obtain $\Omega_3 \equiv 0$. Further, a case is considered when $q_1 = 0$. In that case, from the first equation of system (21) we obtain: $\frac{du_1}{dx} + \frac{v}{R}w = C_0 = const.$ (22)

This means that $T_{11}=const.$ To be specific, we take $T_{11}=0$, i.e.

$$\frac{du_1}{dx} = -\frac{v}{R}w. ag{23}$$

Instead of system (21) we obtain:
$$\frac{d^2w}{dx^2} - \frac{E_*}{D_1R^2}w + \frac{d\Omega_2}{dx} = -\frac{q_3}{D_1}, D' \cdot \frac{d^2\Omega_2}{dx^2} - \left(\frac{B_*}{R^2} + D_1\right)\Omega_2 - D_1\frac{dw}{dx} = 0.$$
 (24)

From the equations of this system the following formula is obtained for Ω_2 :

$$\left(\frac{B_*}{R^2} + D_1\right)\Omega_2 = D'\left(-\frac{d^3w}{dx^3} + \frac{E_*}{D_1R^2} \cdot \frac{dw}{dx} - \frac{1}{D_1}\frac{dq_3}{dx}\right) - D_1\frac{dw}{dx}.$$
 (25)

Using Eqs. (24) and (25), we arrive at the solution of the following inhomogeneous fourth-order differential equation for w:

$$\frac{d^4w}{dx^4} - \left(\frac{E_*}{D_1R^2} + \frac{B_*}{D'R^2}\right)\frac{d^2w}{dx^2} + \frac{E_*}{D'\cdot D_1R^2}\left(\frac{B_*}{R^2} + D_1\right)w = \frac{1}{D'D_1}\left(\frac{B_*}{R^2} + D_1\right)q_3 - \frac{1}{D_1}\frac{d^2q_3}{dx^2}.$$
(26)

Further, a case is considered when
$$q_3 = const.$$
 In that case, instead of Eq. (26) we obtain:
$$\frac{d^4w}{dx^4} - \left(\frac{E_*}{D_1R^2} + \frac{B_*}{D'R^2}\right)\frac{d^2w}{dx^2} + \frac{E_*}{D'\cdot D_1R^2}\left(\frac{B_*}{R^2} + D_1\right)w = \frac{1}{D'D_1}\left(\frac{B_*}{R^2} + D_1\right)q_3. \tag{27}$$

It is easy to see that a particular solution of Eq. (27) is:

$$\widetilde{w} = \frac{q_3 R^2}{E_*}. (28)$$

Let us consider a specific example, where a carbon nanotube, when the ends x = 0, x = l are hinge supported, is loaded with a uniformly distributed normally applied surface load q_3 . The boundary conditions in this case will be:

$$w\Big|_{\substack{x=0\\x=l}} = 0, \frac{\partial \Omega_2}{\partial x}\Big|_{\substack{x=0\\x=l}} = 0.$$
 (29)

The initial data has the following meanings: $q_3 = 10 \text{ nN/nm}^2$, R = 10 nm, l = 100 nm. The stiffness characteristics of a nanotube are expressed numerically as follows [10]: $E_* = 287 \frac{\text{nN}}{\text{nm}}$; $B_* = 0.505 \text{ nN} \cdot \text{nm}$, $D_1 = 86 \frac{\text{nN}}{\text{nm}}$, $D' = 0.415 \text{ nN} \cdot \text{nm}$.

The general solution of differential Eq. (27) (considering Eq. (28)) has the form: $w(x) = 3.484 + e^{-1.15x}(C_1 \cos 1.14x + C_2 \sin 1.14x) + e^{1.15x}(C_3 \cos 1.14x + C_4 \sin 1.14x)$, where C_1 , C_2 , C_3 , C_4 are constants.

With the help of boundary conditions (29), by determining the constants of integration, the solution of the stated problem will finally be expressed as follows: $w(x) = 3.484 + e^{-1.15x}(-3.484\cos 1.14x - 0.03\sin 1.14x)$ (nm).

The maximum deflection of the nanotube is obtained at x = 50 nm, w_{max} .

Technical theory of cylindrical shells

The integration of the system of differential equations of a cylindrical shell into generalized displacements based the moment-membrane theory (12) is a complex task, therefore, the resolving toolkit of the theory of cylindrical shells (similar to the classical theory of cylindrical shells [18,19]) should involve equations that are simpler in structure and provide sufficient accuracy in applied calculations.

Such a simplified (technical) version of the theory of a cylindrical shell (the shell in this case has zero Gaussian curvature) is built on the basis of the following assumptions: a) following members in equilibrium equations (11) can be neglected: in the second one (as in the classical case) $\frac{N_{23}}{R}$, in the fifth one - $\frac{L_{23}}{R}$ and in the sixth one - $\frac{L_{22}}{R}$;

b) following members in the geometrical relations (3) can be neglected: for $\Gamma_{23} - \frac{u_2}{R}$ (as in the classical case); $k_{23} - \frac{\Omega_2}{R}$; $k_{22} - \frac{\Omega_3}{R}$.

In view of the above facts, the main relations of the theory of a cylindrical shell (3), Eq. (11) can be written as follows:

Equilibrium equations:

Equitibrium equations.

$$\frac{\partial T_{11}}{\partial x} + \frac{1}{R} \frac{\partial S_{21}}{\partial \theta} = -q_1, \quad \frac{1}{R} \frac{\partial T_{22}}{\partial \theta} + \frac{\partial S_{22}}{\partial x} = -q_2, \quad \frac{T_{22}}{R} - \frac{\partial N_{13}}{\partial x} - \frac{1}{R} \frac{\partial N_{23}}{\partial \theta} = q_3, \\
\frac{\partial L_{11}}{\partial x} + \frac{1}{R} \frac{\partial L_{21}}{\partial \theta} + N_{23} = -m_1, \quad \frac{1}{R} \frac{\partial L_{22}}{\partial \theta} + \frac{\partial L_{12}}{\partial x} - N_{13} = -m_2, \\
\frac{\partial L_{13}}{\partial x} + \frac{1}{R} \frac{\partial L_{23}}{\partial \theta} + (S_{12} - S_{21}) = -m_3.$$
(30)

34 S.H. Sargsyan

Geometrical relations:

Geometrical relations:

$$\Gamma_{11} = \frac{\partial u_1}{\partial x}, \quad \Gamma_{22} = \frac{1}{R} \frac{\partial u_2}{\partial \theta} + \frac{w}{R}, \quad \Gamma_{12} = \frac{\partial u_2}{\partial x} - \Omega_3, \\
\Gamma_{21} = \frac{1}{R} \frac{\partial u_1}{\partial \theta} + \Omega_3, \quad \Gamma_{13} = \frac{\partial w}{\partial x} + \Omega_2, \quad \Gamma_{23} = \frac{1}{R} \frac{\partial w}{\partial \theta} - \Omega_1, \\
k_{11} = \frac{\partial \Omega_1}{\partial x}, \quad k_{22} = \frac{1}{R} \frac{\partial \Omega_2}{\partial \theta}, \quad k_{12} = \frac{\partial \Omega_2}{\partial x}, \quad k_{21} = \frac{1}{R} \frac{\partial \Omega_1}{\partial \theta}, \quad k_{13} = \frac{\partial \Omega_3}{\partial x}, \quad k_{23} = \frac{1}{R} \frac{\partial \Omega_3}{\partial \theta}.$$
(31)

We add the elasticity relations (9) to the equilibrium equations (30) and geometric relations (31).

From the geometric relations (31), by eliminating displacements u_1, u_2 , we arrive at the following equations for the continuity of deformations:

$$\frac{\partial \Gamma_{21}}{\partial x} - \frac{1}{R} \frac{\partial \Gamma_{11}}{\partial \theta} - k_{13} = 0, \frac{1}{R} \frac{\partial \Gamma_{12}}{\partial \theta} - \frac{\partial \Gamma_{22}}{\partial x} + k_{23} = -\frac{1}{R} \frac{\partial w}{\partial x}.$$
 (32)

It should be mentioned that equations $\frac{1}{R}\frac{\partial k_{11}}{\partial \theta} = \frac{\partial k_{21}}{\partial x}$, $\frac{\partial k_{22}}{\partial x} = \frac{1}{R}\frac{\partial k_{12}}{\partial \theta}$ and $\frac{1}{R}\frac{\partial k_{13}}{\partial \theta} = \frac{\partial k_{23}}{\partial x}$ are automatically satisfied.

Let us consider a more essential case of loading the cylindrical shell, when $q_3 = q$, $q_1 = q_2 = m_1 = m_2 = m_3 = 0$.

Introducing auxiliary functions
$$\Phi_1$$
 and Φ_2 by formulas:

$$T_{11} = \frac{1}{R} \frac{\partial \Phi_1}{\partial \theta}, S_{21} = -\frac{\partial \Phi_1}{\partial x}, T_{22} = \frac{\partial \Phi_2}{\partial x}, S_{12} = -\frac{1}{R} \frac{\partial \Phi_2}{\partial \theta},$$
(33)

the first two equilibrium equations (30) are identically satisfied.

Let us consider the sixth equilibrium equation from the system (30):

$$\frac{\partial L_{13}}{\partial x} + \frac{1}{R} \frac{\partial L_{23}}{\partial \theta} + (S_{12} - S_{21}) = 0. \tag{34}$$

Function ψ is introduced by formulas:

$$L_{13} = \frac{\partial \psi}{\partial x}, L_{23} = \frac{1}{R} \frac{\partial \psi}{\partial \theta}. \tag{35}$$

By considering Eq. (33) for S_{12} and S_{21} , as well as by satisfying Eq. (34), we arrive at the equality:

$$\frac{\partial}{\partial x} \left(\frac{\partial \psi}{\partial x} + \Phi_1 \right) = \frac{1}{R} \frac{\partial}{\partial \theta} \left(\Phi_2 - \frac{1}{R} \frac{\partial \psi}{\partial \theta} \right). \tag{36}$$

Now, if we introduce the function ϕ according to the formulas:

For efforts
$$T_{11}$$
, T_{22} , S_{12} , S_{21} and moments L_{13} , L_{23} , we finally have:
$$T_{11} = \frac{1}{R^2} \frac{\partial^2 \phi}{\partial \theta^2} - \frac{1}{R} \frac{\partial^2 \psi}{\partial x \partial \theta}, \quad T_{22} = \frac{\partial^2 \phi}{\partial x^2} + \frac{1}{R} \frac{\partial^2 \psi}{\partial x \partial \theta},$$

$$S_{21} = -\frac{1}{R} \frac{\partial^2 \phi}{\partial x \partial \theta} + \frac{\partial^2 \psi}{\partial x^2}, \quad S_{12} = -\frac{1}{R} \frac{\partial^2 \phi}{\partial x \partial \theta} - \frac{1}{R^2} \frac{\partial^2 \psi}{\partial \theta^2},$$

$$L_{13} = \frac{\partial \psi}{\partial x}, \quad L_{23} = \frac{1}{R} \frac{\partial \psi}{\partial \theta}.$$
(38)

For the indicated forces and moments, by applying Eq. (38), as noted above, the first two and the sixth equilibrium equations from the system (30) are identically satisfied. As a result of the replacement of forces and moments through generalized displacements w, Ω_1, Ω_2 and functions ϕ and ψ , the other three equations from the system (30), with the help of Eq. (38), take the form:

$$\frac{1}{R} \left(\frac{\partial^2 \phi}{\partial x^2} + \frac{1}{R} \frac{\partial^2 \psi}{\partial x \partial \theta} \right) - D_1 \Delta w - D_1 \left(\frac{\partial \Omega_2}{\partial x} - \frac{1}{R^2} \frac{\partial \Omega_1}{\partial \phi} \right) = q,$$

$$\Delta \Omega_1 + 2\eta_2 \frac{\partial}{\partial x} \left(\frac{\partial \Omega_1}{\partial x} + \frac{1}{R} \frac{\partial \Omega_2}{\partial \theta} \right) + \frac{D_1}{D'} \left(\frac{1}{R} \frac{\partial w}{\partial \theta} - \Omega_1 \right) = 0,$$

$$\Delta \Omega_2 + 2\eta_2 \frac{1}{R} \frac{\partial}{\partial \theta} \left(\frac{1}{R} \frac{\partial \Omega_2}{\partial \theta} + \frac{\partial \Omega_1}{\partial x} \right) - \frac{D_1}{D'} \left(\frac{\partial w}{\partial x} + \Omega_2 \right) = 0,$$
(39)

$$\Delta(\cdot) = \frac{\partial^2(\cdot)}{\partial x^2} + \frac{1}{R^2} \frac{\partial^2(\cdot)}{\partial \theta^2}.$$
 (40)

Now the angles of free rotation Ω_1 and Ω_2 will be represented as follows [19-21]:

$$\Omega_1 = -\frac{1}{R} \frac{\partial G}{\partial \theta} + \frac{\partial \chi}{\partial x}, \ \Omega_2 = \frac{\partial G}{\partial x} + \frac{1}{R} \frac{\partial \chi}{\partial \theta}, \tag{41}$$

where G and χ are auxiliary functions to be determined.

By substituting Eq. (41) into the second and third equations from the system (39), it is easy to see that for the function χ we arrive at the solution of the following Helmholtz equation:

$$\Delta \chi - \tilde{k}^2 \cdot \chi = 0, \tag{42}$$

where

$$\tilde{k}^2 = \frac{D_1}{D'(1+2\eta_2)}. (43)$$

To determine the function G, we obtain the following equation:

$$G = -\frac{1}{D_1}(D'\Delta w + D_1 w) + \frac{D'}{D_1^2}(\Delta'_k \phi + \Delta''_k \psi) - \frac{D'}{D_1^2}q.$$
(44)

In addition, if the second equation from the system (39) is differentiated with respect to the operator $\frac{1}{R}\frac{\partial}{\partial\theta}$, while the third one- with respect to $\frac{\partial}{\partial x}$, the second equation is subtracted from the obtained first equality, by using the first equation from system (39), we arrive at the following equation:

$$D'\Delta\Delta w + \frac{1}{R}\left(1 - \frac{D'}{D_1}\Delta\right)\left(\frac{\partial^2 \phi}{\partial x^2} + \frac{1}{R}\frac{\partial^2 \psi}{\partial x \partial \theta}\right) = q - \frac{D'}{D_1}\Delta q. \tag{45}$$

Thus, instead of system (39), we have obtained a system of two Eqs. (45) and (42), which contain four functions w, ϕ , ψ , χ . We will turn to two equations of continuity of deformations (32), by substituting in them the inverse relations of elasticity (9), which express Γ_{11} , Γ_{22} , Γ_{12} , Γ_{21} through forces T_{11} , T_{22} , S_{12} , and by using Eq. (38), instead of the equations of compatibility of deformations (32), we obtain the following equations:

$$\frac{\partial}{\partial x} (l_*^2 \Delta - 1) \psi - \frac{B_*}{E_*} \cdot \frac{1}{R} \frac{\partial \Delta \phi}{\partial \theta} = 0,$$

$$\frac{1}{R} \frac{\partial}{\partial \theta} (l_*^2 \Delta - 1) \psi + \frac{B_*}{E_*} \cdot \frac{\partial \Delta \phi}{\partial x} = B_* \frac{1}{R} \frac{\partial w}{\partial x},$$
(46)

where

$$l_*^2 = \frac{B_*(\mu_* + \alpha_*)}{4\mu_* \alpha_*}. (47)$$

Eq. (45), in conjunction with Eqs. (42) and (46), will form a complete system of equations for determining four functions w, ϕ , ψ , χ :

$$D'\Delta\Delta w + \frac{1}{R} \left(1 - \frac{D'}{D_1} \Delta \right) \left(\frac{\partial^2 \phi}{\partial x^2} + \frac{1}{R} \frac{\partial^2 \psi}{\partial x \partial \theta} \right) = q - \frac{D'}{D_1} \Delta q,$$

$$\frac{\partial}{\partial x} (l_*^2 \Delta - 1) \psi - \frac{B_*}{E_*} \cdot \frac{1}{R} \frac{\partial \Delta \phi}{\partial \theta} = 0, \quad \frac{1}{R} \frac{\partial}{\partial \theta} (l_*^2 \Delta - 1) \psi + \frac{B_*}{E_*} \cdot \frac{\partial \Delta \phi}{\partial x} = B_* \frac{1}{R} \frac{\partial w}{\partial x},$$

$$\Delta \gamma - \tilde{k}^2 \gamma = 0.$$
(48)

The system of resolving equations of the moment-membrane technical theory (48) lends itself to further simplifications.

Based on the second and third equations of system (48), it is easy to obtain the following equation:

$$\Delta\Delta\phi = E_* \frac{1}{R} \frac{\partial^2 w}{\partial x^2}. \tag{49}$$

If we consider the first and third equations of system (48), it will be possible to express the mixed derivative of the function ψ through functions w and ϕ :

$$\frac{1}{R} \left(\frac{1}{R} \frac{\partial^2 \psi}{\partial x \partial \theta} \right) = -D' c_0 \Delta \Delta w - \frac{c_0}{R} \cdot \frac{\partial^2 \phi}{\partial x^2} + \frac{1}{R} \cdot \frac{D'}{D_1} \cdot \frac{c_0}{a_0} \Delta \frac{\partial^2 \phi}{\partial x^2} + \frac{d_0}{R^2} B_* \cdot \frac{d^2 w}{dx^2} + c_0 q - c_0 \frac{D'}{D_1} \Delta q,$$
where

$$c_0 = \frac{l_*^2}{l_*^2 - \frac{D}{D_*}}, \quad d_0 = \frac{\frac{D}{D_1}}{l_*^2 - \frac{D}{D_*}}, \quad a_0 = \frac{l_*^2}{l_*^2 - \frac{B_*}{E_*}}.$$
 (51)

36 S.H. Sargsyan

The substitution of Eq. (50) into the first equation of system (48), will result in the following system of equations, instead of the system of equations (48):

$$D'\Delta\Delta w - D'c_{0}\left(1 - \frac{D'}{D_{1}}\Delta\right)\Delta\Delta w - \frac{d_{0}}{R}\left(1 - \frac{D'}{D_{1}}\Delta\right)\frac{\partial^{2}\phi}{\partial x^{2}} + \frac{1}{R}\cdot\frac{D'}{D_{1}}\cdot\frac{c_{0}}{a_{0}}\left(1 - \frac{D'}{D_{1}}\Delta\right)\Delta\frac{\partial^{2}\phi}{\partial x^{2}} + \frac{1}{R}\cdot\frac{D'}{D_{1}}\cdot\frac{c_{0}}{a_{0}}\left(1 - \frac{D'}{D_{1}}\Delta\right)\Delta\frac{\partial^{2}\phi}{\partial x^{2}} + \frac{1}{R}\cdot\frac{D'}{D_{1}}\Delta\frac{\partial^{2}\phi}{\partial x^{2}} - \frac{1}{R}\cdot\frac{\partial^{2}\phi}{\partial x^{2}} - \frac{\partial^{2}\phi}{\partial x^{2}}$$

Accepting,

$$w = \Delta \Delta F, \ \phi = \frac{E_*}{R} \cdot \frac{\partial^2 F}{\partial x^2}, \tag{53}$$

we identically satisfy the second equation of system (52). From the first equation of system (52), we obtain a tenth-order equation with respect to the new potential function F. As a result, instead of system (52), we arrive at the following twelfth-order system of two equations for the functions F and χ :

$$D'\Delta\Delta\Delta\Delta F - D'c_{0}\left(1 - \frac{D'}{D_{1}}\Delta\right)\Delta\Delta\Delta\Delta F - \frac{d_{0}}{R^{2}}E_{*}\left(1 - \frac{D'}{D_{1}}\Delta\right)\frac{\partial^{4}F}{\partial x^{4}} + \frac{1}{R^{2}}\cdot\frac{c_{0}}{a_{0}}\cdot\frac{D'}{D_{1}}\cdot E_{*}\left(1 - \frac{D'}{D_{1}}\Delta\right)\Delta\frac{\partial^{4}F}{\partial x^{4}} + \frac{d_{0}}{R^{2}}B_{*}\left(1 - \frac{D'}{D_{1}}\Delta\right)\Delta\Delta\frac{\partial^{2}F}{\partial x^{2}} = -d_{0}\left(1 - \frac{D'}{D_{1}}\Delta\right)q + c_{0}\frac{D'}{D_{1}}\left(1 - \frac{D'}{D_{1}}\Delta\right)\Delta q, \ \Delta\chi - \tilde{K}^{2}\chi = 0.$$

$$(54)$$

If a closed cylindrical shell is hinged at the ends $x=0,\ x=l,$ it can be shown that in this particular case of boundary conditions, we have:

$$\chi \equiv 0. \tag{55}$$

In that case, the problem is reduced to solving one equation of the tenth order with respect to the function *F*:

$$D'\Delta\Delta\Delta\Delta F - D'c_{0}\left(1 - \frac{D'}{D_{1}}\Delta\right)\Delta\Delta\Delta\Delta F - \frac{d_{0}}{R^{2}}E_{*}\left(1 - \frac{D'}{D_{1}}\Delta\right)\frac{\partial^{4}F}{\partial x^{4}} + \frac{1}{R^{2}}\cdot\frac{c_{0}}{a_{0}}\cdot\frac{D'}{D_{1}}\cdot E_{*}\left(1 - \frac{D'}{D_{1}}\Delta\right)\Delta\frac{\partial^{2}F}{\partial x^{2}} + \frac{d_{0}}{R^{2}}B_{*}\left(1 - \frac{D'}{D_{1}}\Delta\right)\Delta\Delta\frac{\partial^{2}F}{\partial x^{2}} = -d_{0}\left(1 - \frac{D'}{D_{1}}\Delta\right)q + c_{0}\frac{D'}{D_{1}}\left(1 - \frac{D'}{D_{1}}\Delta\right)\Delta q.$$
(56)

We note that the simplified version of the moment-membrane technical theory of a cylindrical shell presented here can be used for studying various static problems for a carbon nanotube, in particular, for studying problems of its stability.

Stability of an axially compressed closed cylindrical shell according to the moment-membrane theory (axisymmetric problem)

Let us present the basic equations necessary for studying the stability of a cylindrical shell according to the moment-membrane theory.

We consider a case when a closed cylindrical shell is under the action of a uniform axial compression (the main momentless state). For stability problems, the general equations of the technical theory of a cylindrical shell must be supplemented with terms that consider subcritical forces in the shell.

In this case, in the first equation from the system (48), instead q we take a "fictitious" transverse load:

$$q = -p_1 \frac{\partial^2 w}{\partial x^2},\tag{57}$$

where p_1 is the axial force that occurs in the shell before buckling. The specified system will take the form (further we consider the case when the ends x = 0, x = l of the cylindrical shell are hinge supported, i.e. $\chi \equiv 0$):

$$D'\Delta\Delta w + \frac{1}{R} \left(1 - \frac{D'}{D_1} \Delta \right) \left(\frac{\partial^2 \phi}{\partial x^2} + \frac{1}{R} \frac{\partial^2 \psi}{\partial x \partial \theta} \right) = -p_1 \frac{\partial^2 w}{\partial x^2} + \frac{D'}{D_1} p_1 \Delta \frac{\partial^2 w}{\partial x^2},$$

$$\frac{\partial}{\partial x} (l_*^2 \Delta - 1) \psi - \frac{B_*}{E_*} \cdot \frac{1}{R} \frac{\partial \Delta \phi}{\partial \theta} = 0, \quad \frac{1}{R} \frac{\partial}{\partial \theta} (l_*^2 \Delta - 1) \psi + \frac{B_*}{E_*} \cdot \frac{\partial \Delta \phi}{\partial x} = B_* \frac{1}{R} \frac{\partial w}{\partial x}.$$
(58)

Repeating the steps of the previous paragraph, instead of Eq. (58) we obtain:

$$D'\Delta\Delta w - D'c_{0}\left(1 - \frac{D'}{D_{1}}\Delta\right)\Delta\Delta w - \frac{d_{0}}{R}\left(1 - \frac{D'}{D_{1}}\Delta\right)\frac{\partial^{2}\phi}{\partial x^{2}} + \frac{1}{R}\cdot\frac{D'}{D_{1}}\cdot\frac{c_{0}}{a_{0}}\left(1 - \frac{D'}{D_{1}}\Delta\right)\Delta\frac{\partial^{2}\phi}{\partial x^{2}} + \frac{1}{R}\cdot\frac{D'}{D_{1}}\cdot\frac{c_{0}}{a_{0}}\left(1 - \frac{D'}{D_{1}}\Delta\right)\Delta\frac{\partial^{2}\phi}{\partial x^{2}} + \frac{1}{R}\cdot\frac{D'}{D_{1}}\Delta\frac{\partial^{2}\phi}{\partial x^{2}} + \frac{1}{R}\cdot\frac{D'}{D_{1}}\Delta\frac{\partial^{2}\phi}{\partial x^{2}} + \frac{1}{R}\cdot\frac{D'}{\partial x^{2}}\Delta\frac{\partial^{2}\phi}{\partial x^{2}} + \frac{1}{R}\cdot\frac{D'}{\partial x^{2}}\Delta\frac{\partial^{2}\phi}{$$

Based on the second equation from system (59), when studying the stability of a cylindrical closed shell, we arrive at the solution of the following 10th order equation with respect to w:

$$D'\Delta\Delta\Delta\Delta w - D'c_{0}\left(1 - \frac{D'}{D_{1}}\Delta\right)\Delta\Delta\Delta\Delta w - \frac{d_{0}}{R^{2}}E_{*}\left(1 - \frac{D'}{D_{1}}\Delta\right)\frac{\partial^{4}w}{\partial x^{4}} + \frac{E_{*}}{R^{2}}\cdot\frac{D'}{D_{1}}\cdot\frac{c_{0}}{a_{0}}\left(1 - \frac{D'}{D_{1}}\Delta\right)\Delta\frac{\partial^{4}w}{\partial x^{4}} + \frac{d_{0}}{dx^{4}} + \frac{d_{0}}{dx^{4}}B_{*}\left(1 - \frac{D'}{D_{1}}\Delta\right)\Delta\Delta\frac{\partial^{2}w}{\partial x^{2}} = p_{1}d_{0}\left(1 - \frac{D'}{D_{1}}\Delta\right)\Delta\Delta\frac{\partial^{2}w}{\partial x^{2}} - p_{1}c_{0}\frac{D'}{D_{1}}\left(1 - \frac{D'}{D_{1}}\Delta\right)\Delta\Delta\Delta\frac{\partial^{2}w}{\partial x^{2}}.$$
(60)

If the curved surface of the shell remains axisymmetric after buckling, the deflection wdepends only on the coordinate x, and Eq. (60) looks as follows:

$$\left[\frac{D'^{2}c_{0}}{D_{1}} - p_{1}c_{0}\left(\frac{D'}{D_{1}}\right)^{2}\right]\frac{\partial^{10}w}{\partial x^{10}} + \left[D' - D'c_{0} - \frac{1}{R^{2}}\left(\frac{D'}{D_{1}}\right)^{2}\frac{c_{0}}{a_{0}}E_{*} - B_{*}\frac{d_{0}\cdot D'}{R^{2}\cdot D_{*}} + p_{1}(d_{0} + c_{0})\frac{D'}{D_{1}}\right]\frac{\partial^{8}w}{\partial x^{8}} + \left[\frac{d_{0}\cdot E_{*}}{R^{2}}\frac{D'}{D_{1}} + \frac{E_{*}}{R^{2}}\frac{D'}{D_{1}}\frac{c_{0}}{a_{0}} + \frac{d_{0}}{R^{2}}B_{*} - p_{1}d_{0}\right]\frac{\partial^{6}w}{\partial x^{6}} - \frac{d_{0}\cdot E_{*}}{R^{2}}\frac{\partial^{4}w}{\partial x^{4}} = 0.$$
(61)

Based on the homogeneous differential Eq. (61), we consider the problem of determining the critical force of a carbon nanotube uniformly compressed in the axial direction.

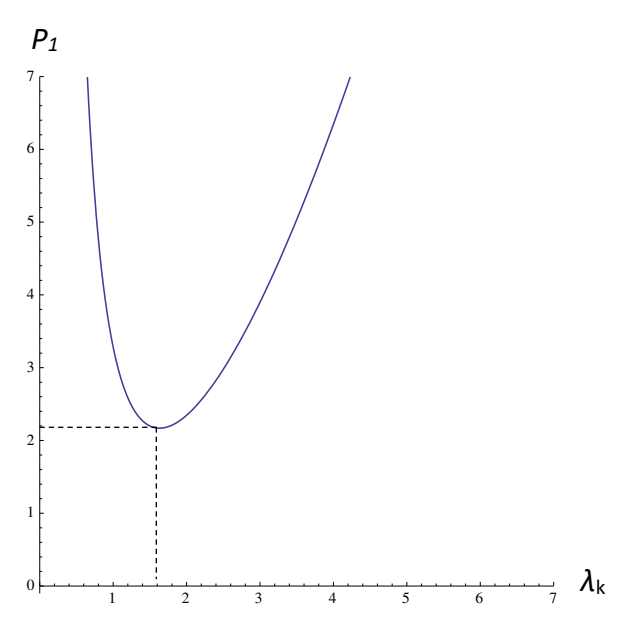


Fig. 2. Graphic definition of the critical force as a result of $p_1(\lambda_k)$ dependency minimization

Assuming deflection $w(x) = f \sin \lambda_k x$, f = const, $\lambda_k = \frac{\pi k}{l}$, k = 1,2,3,..., by satisfying the boundary conditions of hinge support at x = 0, x = l, we obtain (here the data of paragraph 5 of this paper are used): $p_1 = \frac{140072 + 1249,43\lambda_k^2 + 20257,1\lambda_k^4 + 82,93\lambda_k^6}{(48805 + 435,34\lambda_k^2 + 0,964\lambda_k^4)\lambda_k^2}$

Let us determine the smallest (critical) value of the compressive force. Equating to zero the derivative of p_1 by λ_k : $\frac{dp_1}{d\lambda_k}=0$, after determining the corresponding value for λ_k , for the critical force we obtain the following numerical value: $p_{cr}=2.169\frac{\rm nN}{\rm nm}$. This result is also substantiated graphically, by constructing a dependence graph $p_1(\lambda_k)$ (Fig. 2).

38 S.H. Sargsyan

Conclusion

Based on the three-dimensional moment linear theory of elasticity, with the application of the hypotheses' method, the basic equations, relations and boundary conditions of the moment-membrane theory of elastic cylindrical shells are constructed, which is interpreted as a continual model of the deformation behavior of a single-layer carbon nanotube. The resolving equations of the moment-membrane technical theory of elastic cylindrical shells are also constructed. The constructed continual theories of a cylindrical shell open new possibilities for studying various applied problems of the mechanical behavior of a single-walled carbon nanotube.

As particular problems, in an axisymmetric formulation, the problems of the static bending of a single-layer carbon nanotube and the problem of the stability of its initial axial compressed state have been studied.

References

- 1. Kroto HW, Heath JR, O'Brien SC, Curl RF, Smalley RE. C60: Buckminsterfullerene. Nature. 1985;318(6042): 162 163.
- 2. lijima S. Helical microtubules of graphitic carbon. *Nature*. 1991;354(6348): 56–58.
- 3. Geim AK, Novoselov KS. The Rise of Graphene. Nature Materials. 2007;6(3): 183-191.
- 4. Ivanova EA, Krivtsov AM, Morozov NF. Derivation of macroscopic relations of the elasticity of complex crystal lattices taking into account the moment interactions at the microlevel. *Applied Mathematics and Mechanics*. 2007;71(4): 543–561.
- 5. Berinskii IE, Ivanova EA, Krivtsov AM, Morozov NF. Application of moment interaction to the construction of a stable model of graphite crystal lattice. *Mechanics of Solids*. 2007;42(5): 663–671.
- 6. Kuzkin VA, Krivtsov AM. Description for mechanical properties of graphene using particles with rotational degrees of freedom. *Doklady Physics*. 2021;56(10): 527 530.
- 7. Berinsky IE. *Modern problems of mechanics. Mechanical properties of covalent crystals.* St. Petersburg: Publishing house of Politekhn. University; 2014. (In-Russian)
- 8. Eremeev VA, Zubov LM. Mechanics of elastic shells. Moscow: Nauka; 2008. (In-Russian)
- 9. Eremeev V, Altenbach H. Basics of Mechanics of Micropolar Shells. In: *Shell-like structures. Advanced Theories and Application. CISM. Internat. Center for Mechanical Sciences*. Springer; 2017. p.63–111.
- 10. Sargsyan SH. Beam and Continual Models for Deformations of Two-dimensional Nanomaterials. *Physical Mesomechanics*. 2022;25(4): 373–384.
- 11. Sargsyan SH. A Moment-Elasticity Thin Shell Model for Shear-Plus-Rotation Deformation. *Physical Mesomechanics*. 2021;24(2): 140–145.
- 12. Sargsyan SH. Variation Principles of Moment-Membrane Theory of Shells. Moscow University Mechanics Bulletin. 2022;77(1):1–11.
- 13. Kvashnin AG, Sorokin PB, Kvashnin DG. Theoretic Investigation of Mechanical Properties of Graphene Membranes by Means of Molecular Mechanics. *Journal of Siberian Federal University. Mathematics & Physics*: 2009;2(4): 426–431.
- 14. Baimova YA, Mulyukov RR. Graphene, nanotubes and other carbon nanostructures Moscow: RAN; 2018. (In-Russian)
- 15. Nowacki W. Theory of Asymmetric Elasticity. Oxford: Pergamon; 1986.
- 16. Sargsyan SH. Boundary-value problems of the asymmetric theory of elasticity for thin plates. *Journal of Applied Mathematics and Mechanics*. 2008;72(1): 77–86.
- 17. Sargsyan SH. The theory of micropolar thin elastic shells. Journal of Applied Mathematics and Mechanics. 2012;76(2): 235–249.
- 18. Vlasov VZ. General theory of shells. Moscow: GITTL; 1949. (In-Russian)
- 19. Pelekh BL. Theory of shells with finite shear rigidity. Kyiv: Nauka dumka; 1973. (In-Russian)
- 20. Morozov NF. Mathematical Problems of the Theory of Cracks. Moscow: Nauka; 1984. (In-Russian)
- 21. Mindlin RD. Influence of moment stresses on stress concentrations. Sat. per. foreign articles. Mechanics. 1964;88: 115–128.

About Author

Samvel H. Sargsyan 📵 Sc

Doctor of Physical and Mathematical Sciences Professor (Shirak State University, Gyumri, Armenia) Submitted: November 3, 2023

Revised: November 30, 2023

Accepted: December 9, 2023

Emission of lattice dislocations from triple junctions of grain boundaries in high-temperature ceramics with amorphous intercrystalline layers

M.Yu. Gutkin, D N.V. Skiba , D

Institute for Problems in Mechanical Engineering RAS, St. Petersburg, Russian Federation

[™] nikolay.skiba@gmail.com

ABSTRACT

A theoretical model of a mechanism of plastic deformation in high-temperature ceramic materials containing amorphous intercrystalline layers (AILs) is suggested. Within the model, the plastic deformation is realized due to the nucleation and the development of inclusions of a liquid-like phase in the AILs and the glide of lattice dislocations emitted from the triple junctions of the AILs that contain the liquid-like phase inclusions. In the exemplary case of high-temperature α -Al₂O₃ ceramics with AILs, the temperature dependences of the critical stresses for the formation of a liquid-like phase nucleus, for the lattice dislocation emission and for the lattice dislocation glide in a wide range of the deformation temperatures from 300 to 1500 K are calculated. The critical values of the external shear stress and the deformation temperature, at which the glide of the emitted lattice dislocations in the grain interior becomes energetically favorable, are determined.

KEYWORDS

high-temperature ceramics • amorphous intercrystalline layers • liquid-like phase inclusions lattice dislocations • deformation temperature

Acknowledgements. The authors gratefully appreciate the Russian Science Foundation for financial support of this study (grant N^2 23-19-00236).

Citation: Gutkin MYu, Skiba NV. Emission of lattice dislocations from triple junctions of grain boundaries in high-temperature ceramics with amorphous intercrystalline layers. *Materials Physics and Mechanics*. 2024;52(1): 39-48. http://dx.doi.org/10.18149/MPM.5212024_4

Introduction

It is well known that high-temperature ceramic materials and composites have high strength, hardness and wear resistance, maintaining these characteristics at elevated temperatures [1–3]. These unique properties depend on the deformation behavior of intercrystalline boundaries. According to experimental data [4–6], the grain boundaries in the ceramic materials with covalent chemical bonding (Al_2O_3 , SiC, Si_3N_4 , etc.) often contain amorphous intercrystalline layers (AILs), which have an approximately constant thickness (of the order of several nanometers). The experimental observations of the nucleation and the evolution of the AILs are difficult due to their small size that stimulated the development of analytical theoretical models [7–9] and computer modeling [10–13] of the deformation behavior of intercrystalline boundaries.

In particular, in the works [10-12] on computer modeling of amorphous silicon, it was shown that the material is divided into two phases: a solid-like matrix and regions of a liquid-like phase. According to these models [10-12], the liquid-like phase regions are the carriers of plastic deformation in amorphous silicon and their volume fraction increases

40 M.Yu. Gutkin, N.V. Skiba

under mechanical loading. Also, the authors of the work [11] came to the conclusion that a similar mechanism of plastic deformation can operate in other amorphous materials with covalent bonds.

Based on the results of computer modeling [10–12], a mechanism of plastic deformation in nanoceramics with AILs through the nucleation and evolution of liquid-like inclusions in the grain boundaries under the action of an external shear stress was considered in analytical theoretical models [7–9]. The plastic shear within the liquid-like inclusions and their elastic fields and energies were modeled by gliding dislocation loops [7,8] and dislocation dipoles [9] with increasing Burgers vectors. Within the framework of these models, the achievement of a certain critical value by the external shear stress led to the formation of a liquid-like nucleus that grew in size and filled the entire grain boundary between the adjacent triple junctions. Also, in theoretical works [8,9], two cases of further development of plastic deformation in the nanoceramics with AILs were considered: (i) due to the nucleation of nanocracks on the liquid-like phase inclusions and the propagation of these nanocracks in the neighboring AILs [8], and (ii) due to liquid-like phase inclusions overcoming the triple junctions of the AILs and penetrating into a neighboring AIL [9].

The main aim of this work is to propose the third possible scenario for the development of plastic deformation in the high-temperature ceramics with AILs due to the nucleation and the extension of the liquid-like phase inclusions in the AILs with the subsequent emission of lattice dislocations from the triple junctions of the AILs and the glide of these dislocations into the bulk of a neighboring grain. As a result of this model, the critical values of the external shear stress that are required for the formation of a liquid-like nuclei, for the lattice dislocation emission from the triple junctions, and for the lattice dislocation glide in the grain interiors in a wide temperature range in the exemplary case of a high-temperature α -Al $_2$ O $_3$ ceramics with the AILs are estimated and discussed in detail.

Model

Within the framework of the approach used in the model [9], a ceramic sample consists of crystallites divided by the AILs (Fig. 1(a)). Consider an individual AIL AC with length L and width h, in which acts the maximum shear stress $\tau = \sigma/2$ resulting from the application of an external mechanical tensile stress σ (Fig. 1(b)).

According to the works [8,9], a nucleus of a liquid-like phase of length l starts to form in the AIL when the external shear stress reaches a certain critical value $\tau = \tau_{c1}$ (Fig. 1(b)). This nucleus of the liquid-like phase is a carrier of the plastic shear s that is modeled by an edge dislocation dipole with the variable Burgers vectors $\pm \mathbf{s}$ ($\pm s$ -dislocation dipole) and the arm l (Fig. 1(b)). Under the action of the external shear stress $\tau \geq \tau_{c1}$, the nucleus grows and transforms into an inclusion of length l, which corresponds to the length of AIL AC, with a simultaneous increase in the plastic shear value l0, which is described by an increase in the strength of the l1-l2-dislocation dipole to a certain value l3 (Fig. 1(c)). As a result, the defect structure is characterized by a dipole of superdislocations with Burgers vectors l2-l3-superdislocation dipole) and arm l3 (Fig. 1(c)).

Further, it is assumed that, under the combine action of the external shear stress $\tau \geq \tau_{c2}$ and the stress field of the $\pm B$ -superdislocation dipole, a lattice dislocation (LD) with the Burgers vector \mathbf{b} (b-LD) is emitted from triple junction C of the AlLs into the adjacent grain interior under the angle α to AC plane (Fig. 1(d)). Here τ_{c2} denotes a critical value of the external shear stress τ , at which the emission of the LD becomes energetically favorable. Upon reaching a critical stress τ_{c3} that determines the shear stress required to overcome the Peierls barrier, the emitted LD can glide over the distance p along its easy slip plane (Fig. 1(d)). In the model, the p-LD emission is modeled by the formation of a LD dipole with the Burgers vectors $\pm \mathbf{b}$ ($\pm p$ -LD dipole) (Fig. 1(d)). It is worth noting that a similar model was invented long ago by Pozdnyakov and Glezer [14] although without thorough examination.

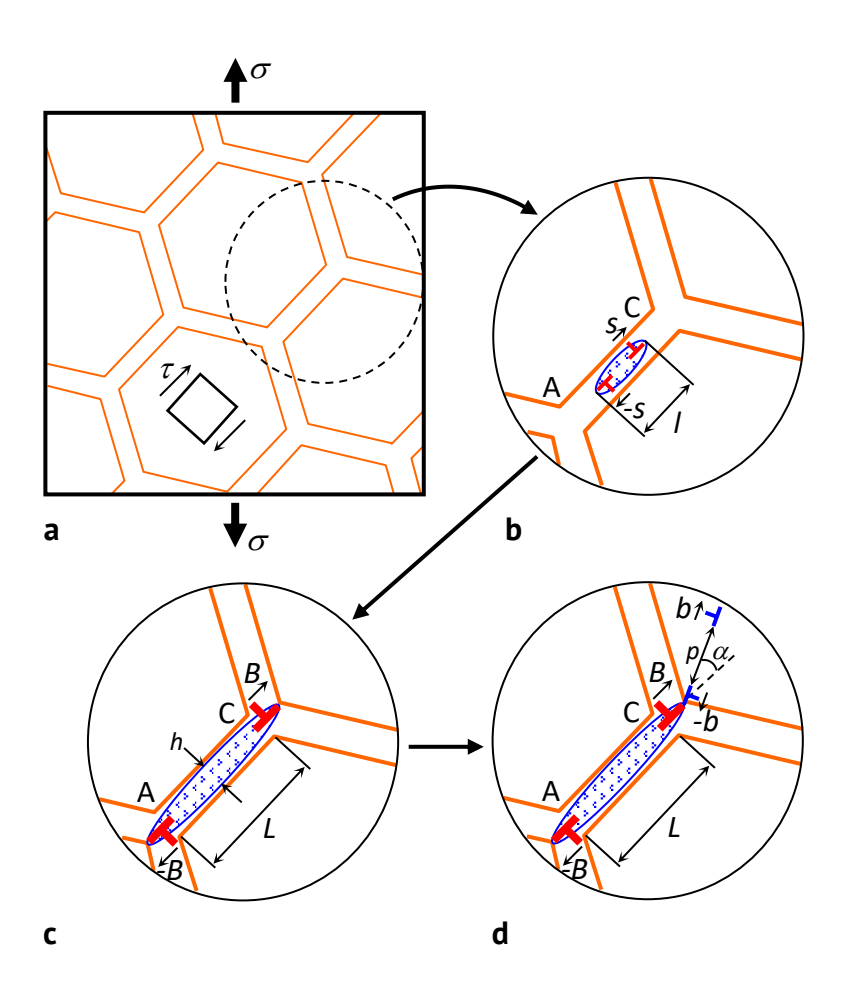


Fig. 1. A two-dimensional model of the plastic deformation of ceramics with AlLs.
(a) Model of a ceramic sample with AlLs under mechanical tensile stress σ.
(b) An individual AlL AC with a nucleus of the liquid-like phase, modeled by an ellipsoidal inclusion that contains an edge dislocation dipole with growing Burgers vectors ±s. (c) Growth of the liquid-like phase inclusion with the dipole of superdislocations with Burgers vectors ±b to the size L. (d) Emission of a lattice dislocation with the Burgers vector b from triple junction C of the AlLs into an adjacent grain under the angle α to AC plane and the dislocation glide in the grain interior over the distance p

Thus, it is assumed that the glide of LDs emitted from the triple junctions of AILs can provide the development of plastic deformation in the case when further evolution of the liquid-like inclusions is suppressed.

42 M.Yu. Gutkin, N.V. Skiba

Results

Consider the energy characteristics of the formation of a liquid-like phase nucleus in AIL AC, which contains a $\pm s$ -dislocation dipole with variable Burgers vectors (Fig. 1(a-c)).

The change in the total energy of the system ΔW that characterizes the formation of the $\pm s$ -dislocation dipole surrounded by a region of the liquid-like phase is given by [9]:

$$\Delta W = E_d + \Delta H S - \tau \, s p, \tag{1}$$

where E_d is the strain energy of the $\pm s$ -dislocation dipole; ΔH is the excess enthalpy of the liquid-like phase in comparison with the solid-like phase, and S is the cross-sectional area of the liquid-like phase nucleus.

The strain energy E_d of the $\pm s$ -dislocation dipole reads [15,16]:

$$E_d = Ds^2 \ln \frac{l - r_c}{r_c},\tag{2}$$

where $D = G/[2\pi(1-\nu)]$, G is the shear modulus, ν is the Poisson ratio, $r_c \approx s$ is the cutoff radius of the elastic field of the $\pm s$ -dislocation dipole at the dislocation lines.

According to the work [9], the cross-sectional area S = lh, where $h \approx ka$ is the transverse size of the liquid-like phase nucleus, k = (2...4)a, a is the average interatomic distance within the AIL.

As a result, Eq. (1) for the energy change ΔW can be rewritten as follows:

$$\Delta W = \frac{Gs^2}{2\pi(1-\nu)} \ln \frac{l-r_c}{r_c} + H \, lka - \tau \, sp. \tag{3}$$

With using Eq. (3), the maps of the energy change ΔW in the normalized coordinates s/a and l/a in the exemplary case of high-temperature α -Al₂O₃ ceramics at the different deformation temperatures T = 300 and 1500 K were calculated. To the best of our knowledge, no studies have been carried out until now to calculate the parameters characterizing the liquid-like phase in AILs in the α -Al₂O₃ ceramics. Therefore, in the first approximation, it is assumed that the elastic moduli of the liquid-like phase are approximately equal to those of the solid-like phase $(G_i = G_m = G, v_i = v_m = v)$, weakly depend on the deformation temperature, and have the following values: G = 169 GPa and v = 0.23 [17,18]. Also, in the absence of the calculations of the enthalpy values for the liquid-like phase, one can use the estimate $\Delta H_i \approx 1.5 \Delta H_m$. This is motivated by the case of amorphous silicon (Si), in which the enthalpy of the liquid-like phase is approximately 1.5 times greater than the enthalpy of the solid-like phase both at low (T = 300 K) and high (T = 1000 K) temperatures [7]. Following the experimental work [19], the enthalpy ΔH_m of the solid-like phase is 10 kJ/mol at T = 300 K and 152.27 kJ/mol at T = 1500 K. As a result, the excess enthalpy $\Delta H = \Delta H_i - \Delta H_m \approx 0.05$ eV/at. at T = 300 K and 0.79 eV/at. at T = 1500 K. The average interatomic distance a in AlLs, the magnitude of the LD Burgers vector b in the grain, and the transverse size h of the liquid-like phase nucleus in an AIL were chosen as follows, respectively: $a \approx 0.19$ nm, $b \approx 0.27$ nm [17], and $h \approx 2a$. The angle α was taken as the average angle α = 22° between 0 and 45° that correspond to the maximum and minimum levels of the external shear stress τ , respectively.

The results of numerical calculations of the maps of energy change ΔW in the normalized coordinates s/a and l/a are shown in Fig. 2(a) for the low deformation temperature (T = 300 K) and Fig. 2(b) for the high deformation temperature (T = 1500 K). In both the cases, the energy maps were built for the critical value τ_{c1} of the external shear stress τ , which characterizes the barrier-free formation of the liquid-like phase nucleus and

is approximately equal to 5.5 GPa for T = 300 K and 10.2 GPa for T = 1500 K. In these maps, the transition to the barrier-free regime of the nucleation of the liquid-like phase nucleus corresponds to the zero level (ΔW = 0) contours touching the straight line l = 2a that corresponds to the initial size of the liquid-like nucleus (Fig. 2). The arrows in Fig. 2, drawn from the nucleation point along the line of the maximum gradient of the function $\Delta W(s, l)$, indicate the evolution of both the liquid-like nucleus and $\pm s$ -dislocation dipole in the space (s, l) under the critical stress τ_{c1} . As follows from Fig. 2, at both the low and high deformation temperatures, an increase in the length l of the liquid-like nucleus is accompanied by a corresponding increase in the strength s of the dislocation dipole, which reaches the value $s \approx 2.5a$ at t = 300 K (Fig. 2(a)) and t = 300 K (Fig. 2(b)) when t = 100a. Using these relations, one can express the strength t = 1500 K.

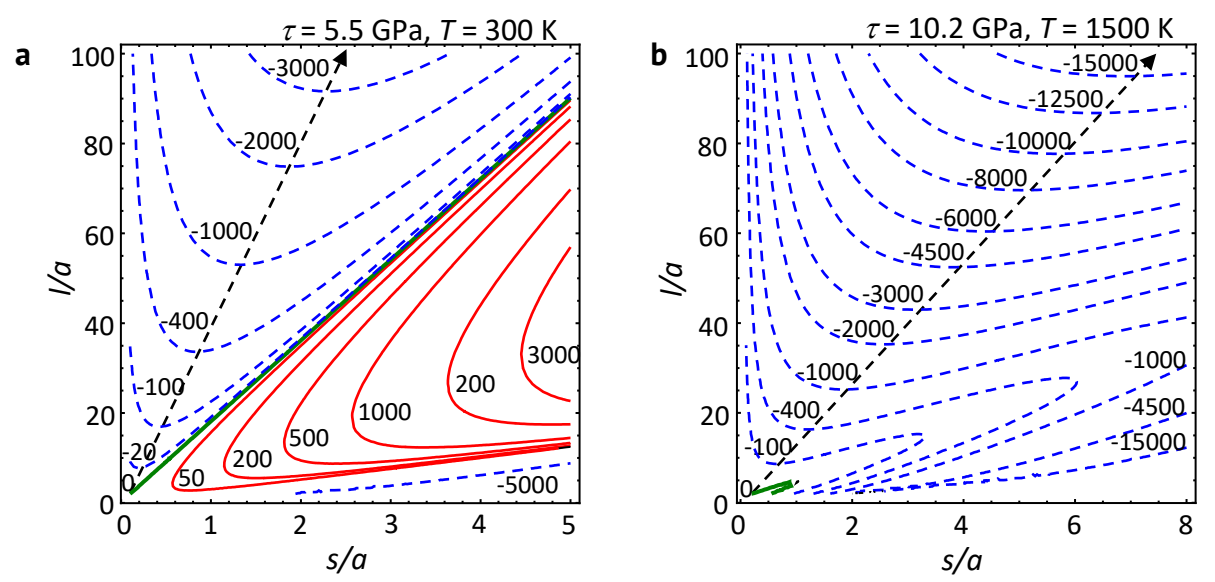


Fig. 2. Contour maps of the energy change ΔW (in units of eV/nm) in the space of the normalized strength s/a and the normalized arm l/a of the $\pm s$ -dislocation dipole at the deformation temperature T = (a) 300 and (b) 1500 K, and at the external shear stress τ = (a) 5.5 and (b) 10.2 GPa

Let us consider now the energy characteristics that correspond to the LD emission from the triple junction of AlLs at point C (Fig. 1(d)). It is assumed that, under the action of the external shear stress $\tau \geq \tau_{c1}$, the liquid-like phase inclusion fills entire AlL AC, thus increasing in size to the length l = L, and the $\pm s$ -dislocation dipole (modeling the plastic shear associated with the growth of the liquid-like phase inclusion) is transformed into the $\pm B$ -superdislocation dipole (Fig. 1(c)).

The process of the LD emission is specified by the energy change $\Delta W_b = W_{b2} - W_{b1}$, where W_{b1} and W_{b2} are the energies of the system in the initial state, before the b-LD emission (Fig. 1(c)), and in its current state, after the b-LD emission and glide over a distance p (Fig. 1(d)), respectively. Such a transformation of the defect system is energetically favorable if $\Delta W_b < 0$.

The energy change ΔW_b (per unit length of the *b*-LD) can be written as follows: $\Delta W_b = E_b + E_{int} - \tau b p$, (4)

44 M.Yu. Gutkin, N.V. Skiba

where E_b is the self energy of the $\pm b$ -LD dipole, E_{int} is the interaction energy between the $\pm B$ -superdislocation dipole and the $\pm b$ -LD dipole, and p is the distance moved by the emitted b-LD in the grain interior.

The self energy E_b of the $\pm b$ -LD dipole is given by [15,16]:

$$E_b = Db^2 \left(ln \frac{p - r_b}{r_b} + 1 \right), \tag{5}$$

where $r_b \approx b$.

The interaction energy E_{int} is calculated by a standard method [15,16] as the work spent to generate the $\pm b$ -LD dipole in the stress field of the $\pm B$ -superdislocation dipole. After some algebra, it reads:

$$E_{int} = \frac{DBb}{2} \left(\cos \alpha \left(\ln \frac{L^2 + p^2 + 2Lp\cos\alpha}{L^2 + b^2 + 2Lb\cos\alpha} - 2\ln\frac{p}{b} \right) - \frac{2Lp\sin^2\alpha}{L^2 + p^2 + 2Lp\cos\alpha} + \frac{2Lb\sin^2\alpha}{L^2 + b^2 + 2Lb\cos\alpha} \right). \tag{6}$$

Using Eqs. (4)-(6), the dependence of the energy change ΔW_b on the distance p was calculated for different values of the external shear stress τ and the size L of the liquid-like phase inclusions. The numerical calculation of the dependences $\Delta W_b(p)$ was carried out at the same values of the system parameters as before, in calculating the energy maps $\Delta W(s, l)$ shown in Fig. 2 in the exemplary case of the high-temperature α -Al₂O₃ ceramics with AlLs. The strength B of the $\pm B$ -superdislocation dipole was chosen equal to $\approx 0.025L$ at T = 300 K and $\approx 0.075L$ at T = 1500 K. The dependences $\Delta W_b(p)$ are shown in Figs. 3 and 4 for different values of the size L of the liquid-like phase inclusion: L = 5 (Figs. 3(a) and 4(a)), 10 (Figs. 3(b) and 4(b)), 15 (Figs. 3(c) and 4(c)), and 20 nm (Figs. 3(d) and 4(d)).

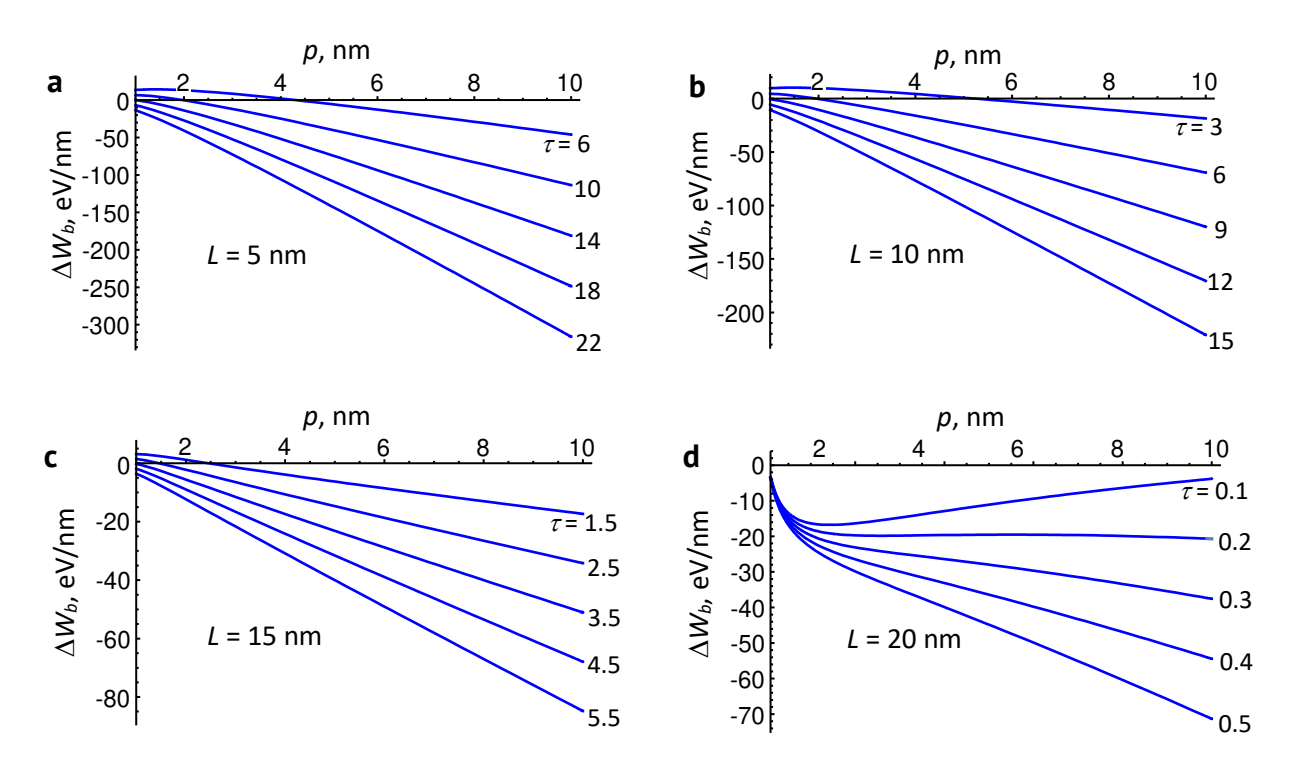


Fig. 3. Dependence of the energy change ΔW on the distance p at various values of the external shear stress τ (shown at curves in units of GPa) for different sizes L = (a) 5, (b) 10, (c) 15 and (d) 20 nm, in the case of low deformation temperature T = 300 K

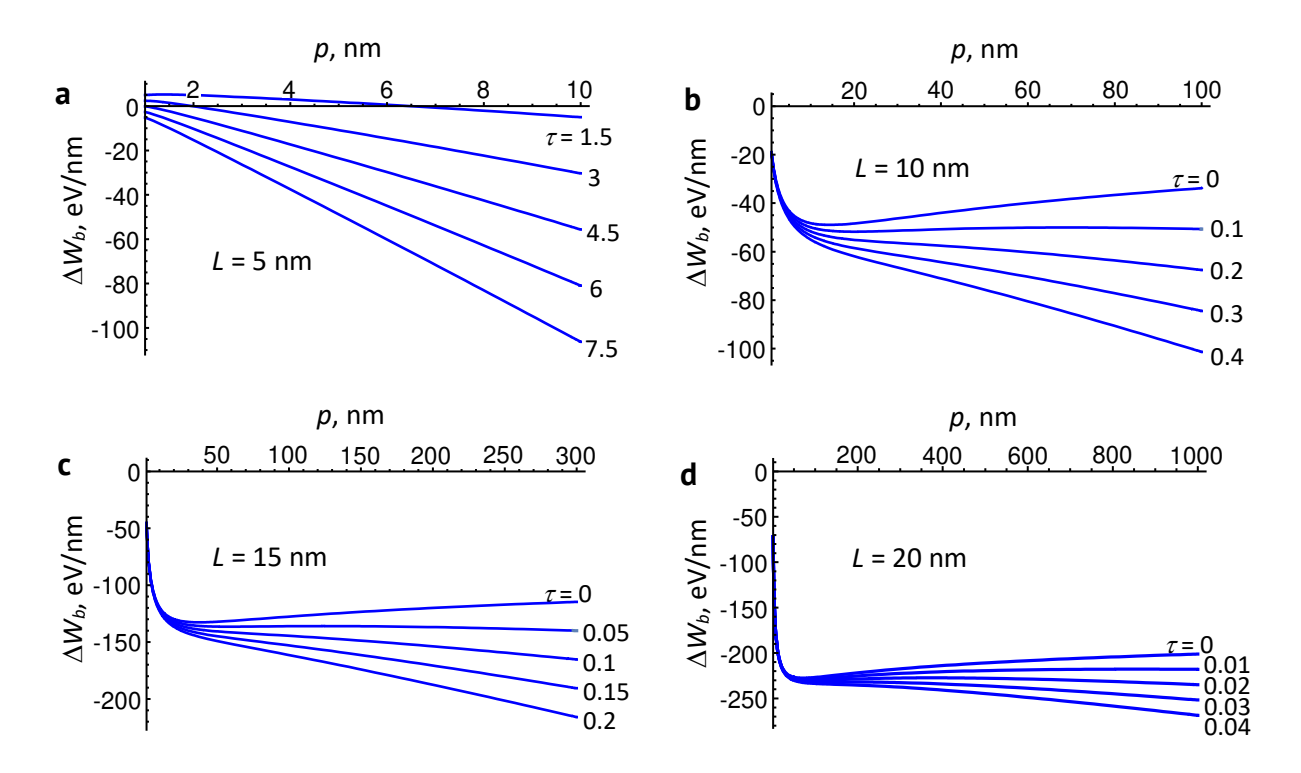


Fig. 4. Dependence of the energy change ΔW on the distance p at various values of the external shear stress τ (shown at curves in units of GPa) for different sizes L = (a) 5, (b) 10, (c) 15 and (d) 20 nm, in the case of high deformation temperature T = 1500 K

The emission of the LD and its subsequent glide in the grain interior is energetically favorable, if the energy change ΔW_b is negative at the initial point of the LD emission (when $p\approx 1$ nm) and then monotonously decreases with the distance p. In these circumstances, the critical stress τ_{c2} that is the minimum stress required for the emission of a LD from the triple junction of the AILs, can be calculated from the conditions $\Delta W_b \le 0$ at p=1 nm and $\partial \Delta W_b / \partial p < 0$ at p>1 nm that guarantee the barrier-less emission of the LD.

As can be seen from the dependences $\Delta W_b(p)$ in Figs. 3 and 4, the critical stress τ_{c2} increases with a decrease in the length L of the liquid-like phase inclusion and a decrease in the deformation temperature T. For example, τ_{c2} = 14, 9, 3.5 and 0.3 GPa at T = 300 K (Fig. 3), and 4.5, 0.2, 0.1 and 0.03 GPa at T = 1500 K (Fig. 4) for the size L = 5, 10, 15 and 20 nm, respectively. The critical stresses τ_{c2} for other deformation temperatures in the range from 300 to 1500 K were determined in a similar way.

During its slip in the grain interior, the LD is subject to resistance from the crystal lattice that is characterized by the Peierls barrier. In this case, the LD slip becomes possible when the external shear stress τ reaches a certain critical value τ_{c3} that is required to overcome the Peierls barrier. The Peierls barrier depends on the temperature and decreases with an increase in it. Thus, the critical stress τ_{c3} also decreases with an increase in the temperature. The temperature dependences of the critical stresses τ_{c3b} and τ_{c3p} for the basal and prismatic slip, respectively, in α -Al₂O₃ ceramics were found in experiments [20]. They are given by the following formulas [20]:

$$\tau_{c3b} = \tau_{0b} e^{-0.0052 \, T},\tag{7}$$

$$\tau_{c3p} = \tau_{0p} e^{-0.0026T},\tag{8}$$

where τ_{c0b} = 109 GPa and τ_{c0p} = 9 GPa.

46 M.Yu. Gutkin, N.V. Skiba

With Eqs. (3)-(8), one can calculate the temperature dependences of the critical stresses τ_{c1} , τ_{c2} , and τ_{c3} . The resulting curves $\tau_{c1}(T)$, $\tau_{c2}(T)$, and $\tau_{c3}(T)$ are shown in Fig. 5 for different values of the size L of the liquid-like phase inclusion: L=5 (Fig. 5(a)), 10 (Fig. 5(b)), 15 (Fig. 5(c)), and 20 nm (Fig. 5(d)). Within the model, the emission of LDs can occur only after the formation of a liquid-like phase inclusion. Therefore, the LD generation becomes energetically favorable if the conditions $\tau \geq \tau_{c1}$ and $\tau \geq \tau_{c2}$ are satisfied. In turn, the realization of the LD slip in the grain interior along its easy slip plane becomes possible if the conditions $\tau \geq \tau_{c3p}$ and/or $\tau \geq \tau_{c3b}$ are satisfied. Regions I and II correspond to the values of the external shear stress τ and the deformation temperature T, at which the glide of the LD along the basal (region I) and prismatic (region II) slip planes is possible (Fig. 5). As is seen from Fig. 5, the regions I and II expand with an increase in the size L of the liquid-like phase inclusions until this size reaches 15 nm and then rest constant in area.

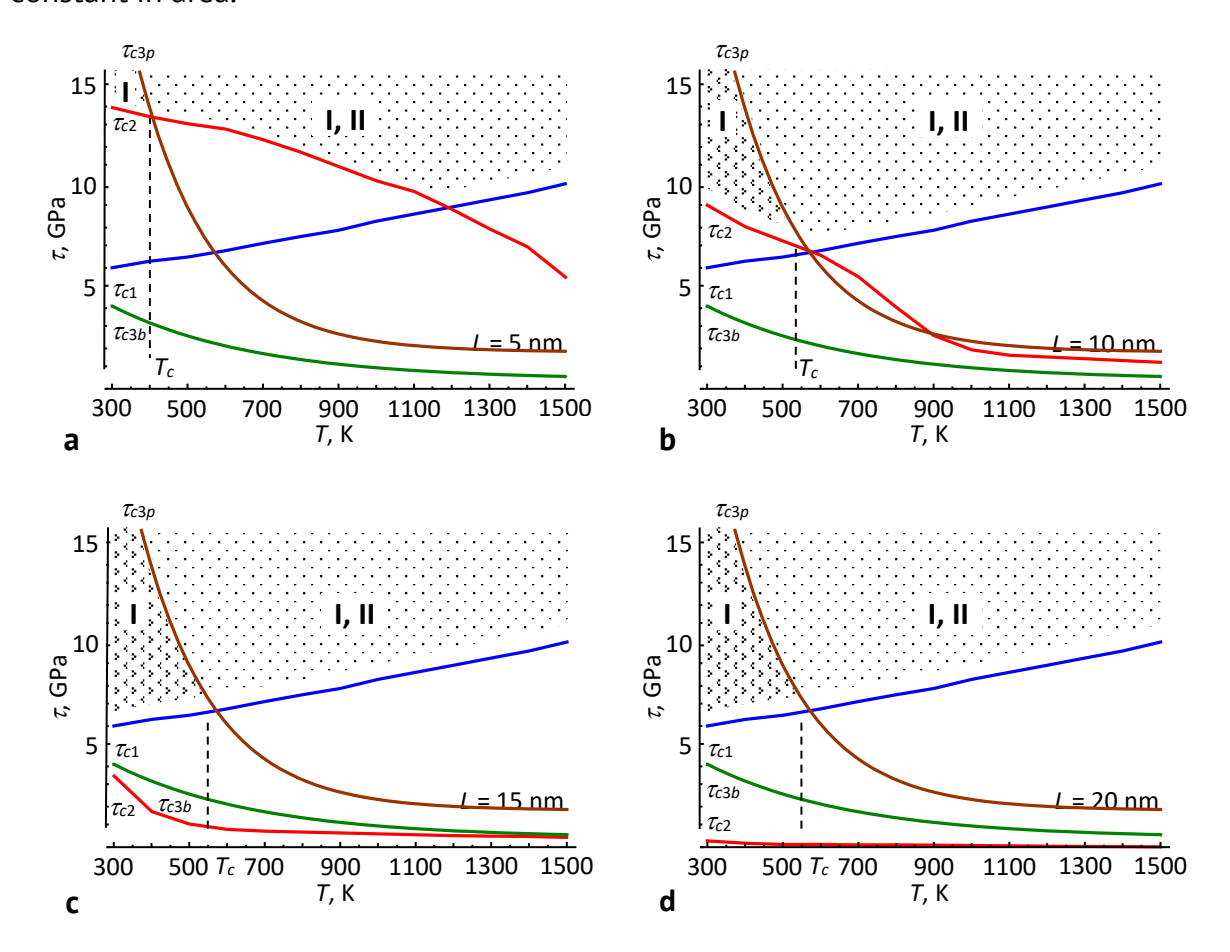


Fig. 5. Dependences of the critical stresses τ_{c1} , τ_{c2} and τ_{c3} on the deformation temperature T for different values of the liquid-like phase inclusion size L = (a) 5, (b) 10, (c) 15, and (d) 20 nm. Regions I and II correspond to the basal and prismatic plane slip, respectively

It should be noted that, as follows from Fig. 5, there is a certain critical deformation temperature T_c , below which the basal plane slip is possible at lower values of the external shear stress τ than those needed for the prismatic plane slip. When $T > T_c$, both the basal and prismatic slip systems are expected to be activated under the same shear stress $\tau \ge \max\{\tau_{c1}, \tau_{c2}\}$. The critical deformation temperature T_c increases with an increase

in the size L of the liquid-like phase inclusion up to a certain value $T_c \approx 550$ K, which is achieved at the size L = 15 nm in our exemplary case of the α -Al₂O₃ ceramics (Fig. 5(c)), while then it does not change with increasing L (Fig. 5(d)). As a result, the critical deformation temperature values vary with small L (when $5 \le L \le 15$ nm) in the range of $400 < T_c < 550$ K (Fig. 5).

Conclusions

Thus, a theoretical model of a new mechanism of plastic deformation in the high-temperature ceramics with amorphous intercrystalline layers over a wide temperature range is developed. Within the model, the plastic deformation of a ceramic sample has two stages.

At the first stage, the plastic deformation occurs due to the generation and the evolution of nuclei of the liquid-like phase in amorphous intercrystalline layers under the action of the external shear stress. This mechanism of plasticity works until the liquid-like phase inclusions reach the nearest obstacles that, in the case of nanoceramics, are the nearest triple junctions of amorphous intercrystalline layers.

At the second stage, the plastic deformation of the nanoceramic sample develops due to the emission of lattice dislocations from the liquid-like phase inclusions, inhibited by the triple junctions of amorphous intercrystalline layers, followed by the dislocation glide in the grain interior.

The energy characteristics of the generation of the liquid-like phase nuclei in the amorphous intercrystalline layers and the emission of the lattice dislocations from the triple junctions of amorphous intercrystalline layers containing the liquid-like phase inclusions are calculated. In the exemplary case of a high-temperature α -Al₂O₃ nanoceramics, the critical stresses for the formation of a liquid-like phase nucleus, for the emission of the lattice dislocations from the triple junctions of amorphous intercrystalline layers, and for the lattice dislocation glide along the basal and prismatic slip planes are calculated in dependence on the deformation temperature. The temperature dependences of these critical stresses are plotted for different sizes of the liquid-like phase inclusion. The ranges of the values of the external shear stress and the deformation temperature, at which the glide of the emitted lattice dislocations in the grain interior is energetically favorable, are determined. It is shown that there is a certain critical deformation temperature, below which the basal plane slip is more preferable than the prismatic plane slip. In the exemplary case of the high-temperature α-Al₂O₃ nanoceramics with amorphous intercrystalline layers, the critical deformation temperature increases from 400 to 550 K, when the size of the liquid-like phase inclusion increases from 5 to 15 nm, and then remains constant when this size grow further.

Thus, the plastic deformation of the high-temperature nanoceramics can effectively occurs through the emission of lattice dislocations from the triple junctions of amorphous intercrystalline layers at elevated temperatures.

48 M.Yu. Gutkin, N.V. Skiba

References

1. Zhang D, Yu R, Feng X, Guo X, Yang Y, Xu X. Enhanced mechanical properties of Al_2O_3 nanoceramics via low temperature spark plasma sintering of amorphous powders. *Materials*. 2023;16(16): 5652.

- 2. Wang LY, An L, Zhao J, Shimai S, Mao XJ, Zhang J, Liu J, Wang SW. High-strength porous alumina ceramics prepared from stable wet foams. *J. Adv. Ceram.* 2021;10: 852–859.
- 3. Cheng M, Liu H, Zhao B, Huang C, Yao P, Wang B. Mechanical properties of two types of Al₂O₃/TiC ceramic cutting tool material at room and elevated temperatures. *Ceramics International*. 2017;43(16): 13869–13874.
- 4. Zhang ZL, Sigle W, Koch CT. Dynamic behavior of nanometer-scale amorphous intergranular film in silicon nitride by in situ high-resolution transmission electron microscopy. *Journal of the European Ceramic Society*. 2011;31(9):1835–1840.
- 5. Subramaniam A, Koch CT, Cannon RM, Rühle M. Intergranular glassy films: An overview. *Materials Science and Engineering A*. 2006;422(1-2): 3–18.
- 6. Kleebe HJ. Structure and chemistry of interfaces in Si_3N_4 ceramics studied by transmission electron microscopy. *Journal of the Ceramic Society of Japan*. 1997;105(1222): 453–475.
- 7. Gutkin MYu, Ovid'ko IA. A composite model of the plastic flow of amorphous covalent materials. *Physics of the Solid State*. 2010;52(1): 58–64.
- 8. Gutkin MYu, Ovid'ko IA. Plastic flow and fracture of amorphous intercrystalline layers in ceramic nanocomposites. *Physics of the Solid State*. 2010;52(4): 718–727.
- 9. Gutkin MYu, Mikaelyan KN. A model of strain hardening in nanoceramics with amorphous intercrystalline layers. *Physics of Complex Systems*. 2021;2(2): 51–60.
- 10. Demkowicz MJ, Argon AS. High-density liquidlike component facilitates plastic flow in a model amorphous silicon system. *Physical Review Letters*. 2004;93(2): 025505.
- 11. Demkowicz MJ, Argon AS. Liquidlike atomic environments act as plasticity carriers in amorphous silicon. *Physical Review B*. 2005;72(24): 245205.
- 12. Demkowicz MJ, Argon AS, Farkas D, Frary M. Simulation of plasticity in nanocrystalline silicon. *Philosophical Magazine*. 2007;87(28): 4253–4271.
- 13. Mo YF, Szlufarska I. Simultaneous enhancement of toughness, ductility, and strength of nanocrystalline ceramics at high strain-rates. *Applied Physics Letters*. 2007;90(18): 181926.
- 14. Pozdnyakov VA, Glezer AM. Structural mechanisms of fracture of nanocrystalline materials. *Physics of the Solid State*. 2005;47(5): 817–824.
- 15. Skiba NV. Crossover from deformation twinning to lattice dislocation slip in metal–graphene composites with bimodal structures. *Crystals*. 2020;10(1): 47.
- 16. Gutkin MYu, Skiba NV, Orlova TS. Grain-boundary nanoprecipitates-mediated mechanism of strengthening in Al-Cu-Zr alloy structured by high-pressure torsion. *Materials Physics and Mechanics*. 2022;50(3): 431–438.
- 17. Smithells CJ, Brands EA. Metals reference book. London: Butter-worths; 1976.
- 18. Munro RG. Evaluated material properties for a sintered α -alumina. *Journal of the American Ceramic Society*. 1997;80(8): 1919–1928.
- 19. Archer DG. Thermodynamic properties of synthetic sapphire (α -Al₂O₃), standard reference material 720 and the effect of temperature-scale differences on thermodynamic properties. *Journal of Physical and Chemical Reference Data*. 1993;22(6): 1441–1453.
- 20. Choi S-M, Awaji H. Nanocomposites a new material design concept. *Science and Technology of Advanced Materials*. 2005;6(1): 2–10.

About Authors

Mikhail Yu. Gutkin D Sc

Doctor of Physical and Mathematical Sciences

Head of Department, Principal Researcher (Institute for Problems in Mechanical Engineering RAS, St. Petersburg, Russia)

Nikolay V. Skiba Sc

Doctor of Physical and Mathematical Sciences Leading Researcher (Institute for Problems in Mechanical Engineering RAS, St. Petersburg, Russia) Submitted: October 11, 2023

Revised: December 11, 2023

Accepted: February 13, 2024

Analytical description of the Bauschinger effect using experimental data and the generalized Masing principle

S.I. Feoktistov, [©] I.K. Andrianov [™], [©]

Komsomolsk-na-Amure State University, Komsomolsk-on-Amur, Russia

Author to whom correspondence should be addressed: ivan_andrianov_90@mail.ru

ABSTRACT

The research is devoted to the problem of obtaining an analytical expression for the dependence of stresses on strains during unloading and subsequent loading by the reverse sign force, taking into account the Bauschinger effect. The assessment of the deformed state was carried out using the use of Hencky strains. The mathematical model was developed under the assumption of a cyclically ideal material. To process the experimental data, the generalized Masing principle was applied, which is used to describe the ideal Bauschinger effect. On the basis of experimental data for the 45HGMA material, curves of changes in the coefficients of the Bauschinger effect were obtained using the least squares method. The results obtained showed sufficient convergence with experimental data. The results of the study can be used in solving elastic-plastic problems for various processes of alternating loading using the deformation theory of plasticity, when a description of the deformation diagram of the material is required, using the analytical dependence of stresses on strains according to the hypothesis of a single curve.

KEYWORDS

Bauschinger effect • generalized Masing principle • deformation diagram • alternating loading stress • logarithmic strain

Acknowledgements. The research was carried out with the financial support of the "Council for Grants of the President of the Russian Federation for state support of young Russian scientists and state support of leading scientific schools of the Russian Federation" within the framework of a scholarship under the project SP-2200.2022.5 "Development of models and algorithms for calculating plastic shaping of blanks of stamping production".

Citation: Feoktistov SI, Andrianov IK. Analytical description of the Bauschinger effect using experimental data and the generalized Masing principle. *Materials Physics and Mechanics*. 2024;52(1): 49–59. http://dx.doi.org/10.18149/MPM.5212024_5

Introduction

The issues of determining stresses and strains in the presence of finite areas of plastic strains, in cases where external loads are applied once, are currently well studied, especially in the framework of deformation theory and in the theory of ideal plasticity. However, in engineering practice, numerous cases can be found when external forces are applied repeatedly (including with a sign change) and the behavior of the elastic-plastic system differs significantly from the case of a single loading.

If, during the first loading, plastic strains occurred in the entire body or in some of its finite areas, then after the removal of external forces, it will not return to its original state, certain residual strains and stresses will occur in it. With subsequent loading by an arbitrary system of forces, the body will behave differently than in the case of its loading from the initial state. For example, if a sample, previously stretched beyond the elastic limit, is compressed, then plastic strains will appear at a lower axial load value than at the previous stretching. The elastic limit during subsequent compression decreases to a

50 S.I. Feoktistov, I.K. Andrianov

greater extent, the higher the stress of the previous stretching was. Similar changes are observed in the case of stretching after pre-compression. Hysteresis loops are also observed during unloading and re-stretching. This behavior of the material is called the Bauschinger effect.

The first successful attempt to explain the Bauschinger effect and the hysteresis loops observed during repeated loading was made by G. Masing, who proceeded from the fact that individual grains in a polycrystalline body, due to their different orientations and the anisotropy of crystals, have different mechanical characteristics and deform differently [1]. He proposed an interesting scheme of elastic-plastic deformation of a sample made of polycrystalline material, which is quite fully described in the work of Moskvitin V.V. [1]. The Masing model or principle is widely used by various authors in the analysis of alternating and cyclic loading [2–4].

According to the analysis of the current state of the research issue, most of the scientific works aimed at studying the Bauschinger effect are of an applied nature, in particular, taking into account the Bauschinger effect during experimental research was considered in [5]. Experimental studies of the behavior of the material, as well as its hardening under cyclic loading are reflected in [6,7]. The issues of deformation under cyclic loading, alternating loading in the case of loading and unloading were studied in [8–11]. Dynamic models of elastic-plastic deformation, which were studied in the works [12,13], also seem to be very relevant in recent years. Taking into account the Bauschinger effect is important for fatigue failure problems, as well as for the analysis of damage accumulation in the case of isotropic and kinematic hardening, to which the works are devoted [14–17].

In addition, the complexity of the study of the Bauschinger effect is due to the need to take into account the nonlinearity of the deformation process. Some issues of plastic deformation under the nonlinear hardening law require the use of numerical research methods, some aspects of the analytical description of the plastic behavior of the material are considered in [18]. Also, the problem of solving problems of nonlinear plasticity was considered in [19–21]. The deformation hardening that occurs in this case is important for assessing the ultimate deformations, which is noted in [22].

Taking into account the Bauschinger effect is also used in problems of elastic-plastic deformation in the calculation of residual stresses. The effect of the Bauschinger effect on the picture of the residual stress-strain state is analyzed in [23,24].

In this article, we will consider an important issue for the analytical description of the Bauschinger effect of obtaining an expression of the stress – strain dependence during unloading and subsequent loading by the reverse sign force. To do this, we will use the generalized Masing principle [1].

Generalized Masing principle

The results of theoretical studies made it possible for Masing to suggest that the curve of repeated alternating loading coincides with the corresponding curve at the first loading, but constructed in axes with a doubled scale and reverse direction. This assumption will be called the Masing principle [1]. If, at the first loading, the stresses and the corresponding strains are connected by the equation:

$$\sigma^{(1)} = \Phi(e),\tag{1}$$

then according to the Masing principle, the stress differences $\bar{\sigma} = \sigma' - \sigma^{(2)}$ and the strain differences $\bar{e} = e' - e$ satisfy the equation (Fig. 1) [1]:

$$\bar{\sigma} = 2\Phi\left(\frac{\bar{e}}{2}\right),\tag{2}$$

$$\sigma^{(2)} = \sigma' - 2\Phi\left(\frac{e' - e}{2}\right),\tag{3}$$

where $\sigma^{(1)}$ – equation relating stresses and Hencky strains at the first loading in the coordinate system (σ, e) ; $\bar{\sigma}$ – equation describing the curve of repeated alternating loading in the coordinate system $(\bar{\sigma}, \bar{e})$; $\sigma^{(2)}$ – equation relating stresses and strains under repeated alternating loading in the coordinate system (σ, e) ; σ' ν ν ν ν - maximum stresses and strains obtained during the first loading.

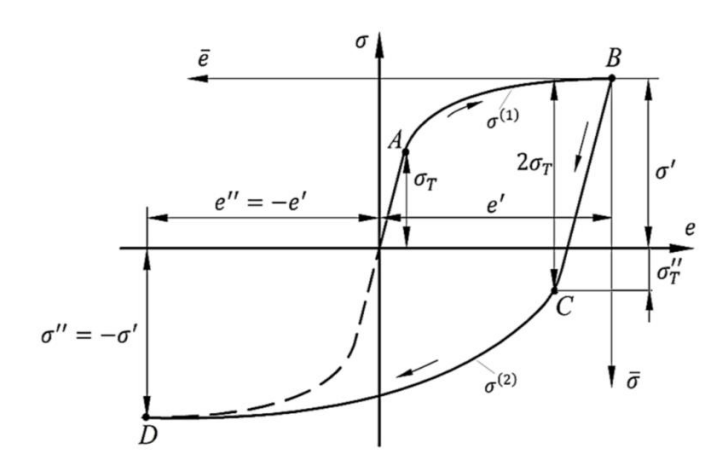


Fig. 1. Diagram of repeated alternating deformation of Masing [1]

If the diagram of the behavior of the material under the first loading (1) is known, then Eq. (3) relates the stresses $\sigma^{(2)}$ and the corresponding deformations e under repeated alternating loading. It should be noted that if the maximum stresses σ' and strains e' were reached during the first loading, then with repeated loading in the opposite direction, the yield strength is determined by the equation (Fig. 1) [1]:

$$\sigma_T^{\prime\prime} = 2\sigma_T - \sigma^{\prime}. \tag{4}$$

Thus, if, after stretching to a plastic state, the sample is unloaded and then compressed, then the yield strength decreases, and, as follows from Eq. (4), the sum of the absolute values of the maximum tensile stress and the new yield strength during compression is equal to twice the yield strength of the undeformed material. In this case, the Bauschinger effect is usually called ideal [25] and a classical hysteresis loop is observed.

Let us consider the important question for the analytical description of the Bauschinger effect of obtaining an expression of the stress – strain dependence during unloading and subsequent loading by the force of the reverse sign. The difficulties encountered in this case are due to the fact that, unlike the primary deformation curve, when the stress $\sigma^{(1)}$ is a function of only e, with repeated loading, the stress $\bar{\sigma}$ is a function not only of \bar{e} , but also, as experiments have shown, depends on the parameter e' – the maximum strain obtained during the first loading.

52 S.I. Feoktistov, I.K. Andrianov

As one of the possible generalizations of the Masing principle, the assumption is introduced that the deformation curve under alternating loading coincides with the curve of the previous loading $\sigma^{(1)} = \Phi(e)$, but with a change in scale α_e times along the strain axis and α_σ times along the stress axis, and in the general case α_e and α_σ can be functions of the preceding deformation at $e' \geq e_T$: $\alpha_e = \alpha_e(e')$, $\alpha_\sigma = \alpha_\sigma(e')$ [1]. In this case (Fig. 1):

$$\bar{\sigma} = \alpha_{\sigma} \Phi\left(\frac{\bar{e}}{\alpha_{e}}\right),\tag{5}$$

or

$$\sigma^{(2)} = \sigma' - \alpha_{\sigma} \Phi\left(\frac{e' - e}{\alpha_e}\right). \tag{6}$$

The functions $\alpha_e(e')$ and $\alpha_\sigma(e')$ are called Masing functions and they must satisfy certain conditions. If the stretching and compression curves of the source material coincide with each other, then for $e' = e_T$ there should be [1]:

$$\alpha_e(e_T) = 2, \ \alpha_\sigma(e_T) = 2. \tag{7}$$

If we take into account the deformation anisotropy of elastic constants, then before the appearance of plastic strains during repeated alternating loading:

 $\bar{\sigma} = \bar{E}(e') \, \bar{e},$

where $\bar{E}(e')$ – variable modulus of elasticity, depending on the previous strain. In this case, according to [1]:

$$\bar{\sigma} = \alpha_{\sigma} E \frac{\bar{e}}{\alpha_{e}}, \qquad \frac{\alpha_{\sigma}}{\alpha_{e}} = \frac{\bar{E}(e')}{E}.$$
 (8)

Therefore, if the function of changing the Young's variable modulus $\bar{E}(e')$ is known, then from experiments on alternating loading it remains to determine only one function depending on the parameter $e' - \alpha_e(e')$. If the deformation anisotropy of elastic constants is not taken into account, then $\bar{E}=E$. In this case, according to [1] it follows from Eq. (8) that:

$$\alpha_{\sigma}(e') = \alpha_{e}(e') = \alpha(e'). \tag{9}$$

As experimental data [26] show, the changes in the Young's modulus under alternating loading are insignificant and, as calculations show, these changes are commensurate with the errors in determining elastic constants, which is introduced by the hypothesis of incompressibility of the material. In the future, when considering alternating loading, we will not take into account the anisotropy of elastic constants.

Definition of Masing functions

The Bauschinger effect is defined as a decrease in the yield strength of a material under compression as a result of previous tensile strain. The majority of researchers agree that the degree of preliminary strain has a significant impact on the Bauschinger effect [27,28]. To quantify the Bauschinger effect, we take the ratio of the yield strength $\sigma_T''(e')$ observed during compression to the maximum stress in the previous loading σ' (Fig. 1).

We call it the coefficient of the Bauschinger effect and denote β_T :

$$\beta_T = \beta_T(e') = \frac{\sigma_T''(e')}{\sigma'(e')},\tag{10}$$

where e' – the maximum strain obtained during the first loading; $\sigma'(e')$ – the maximum stress corresponding to this strain.

In accordance with the generalized Masing principle, by analogy with Eq. (4), we can write $\sigma_T''(e') = \alpha(e')\sigma_T - \sigma'(e')$, or taking into account Eq. (10):

$$\alpha = \alpha(e') = \frac{\sigma'(e')}{\sigma_T} (1 + \beta_T(e')). \tag{11}$$

Determination of the Masing function based on experimental data

For the calculations, we take the experimental results presented in [29]. In this work, the results of tests on steels of grades St3, SHL-4 (10HCND), 09G2 and on alloy steels having $\sigma_{0.2} = 600 \div 1200$ MPa are presented. The research was carried out by the method of "probing". The sample was loaded to a certain specified strain, determined by the residual strain $\varepsilon_{\mathrm{long}}^{\mathrm{res}}$ and the stress σ^D , then unloading and loading of the opposite sign was carried out to a residual strain of 0.2 %, determined by the stress $\sigma_{0.2}^{\rm C}$. Then the direct loading was repeated until the next level of the specified strain was reached, "probing" was carried out again, etc. The Bauschinger effect in this case was characterized by the ratio $\sigma_{0,2}^{\mathbb{C}}/\sigma^{D}$ and we will denote it $\beta_{0,2}^{D}$.

To display the test results on the deformation diagram (σ_i, e_i) we will use the hypothesis of a single curve, put forward by Ludwik and described in a scientific work [25], and recalculate relative strains into logarithmic, and conditional stresses into true stresses according to the formulas: $\varepsilon^D = \left(\varepsilon_{long}^{res} + \frac{\sigma^D}{\epsilon}\right)$, $e_i' = ln(1 + \varepsilon^D)$, $\sigma_i' = \sigma^D (1 + \varepsilon^D)$, $\sigma_{i0.2}'' = \sigma_{0.2}^{\rm C} \left(1 - \left(0.002 + \frac{\sigma_{0.2}^{\rm C}}{E} \right) \right)$.

Calculations have been carried out for 45HGMA steel, which has $\sigma_{0.2} = 800$ MPa, which corresponds to the data given in [29]. The calculation results are presented in Table 1.

Table 1. Steel $\sigma_{0,2} = 800$ MPa (45HGMA - GOST 4543-2016)								
ϵ_{long}^{res}	ϵ^D	e_i'	σ^D , MPa	σ'_i , MPa	$\sigma_{0,2}^{C}$, MPa	$\sigma_{i0,2}^{\prime\prime}$, MPa	$\beta_{0,2}^D = \frac{\sigma_{0,2}^C}{\sigma^D}$	$\beta_{0,2} = \frac{\sigma''_{i0,2}}{\sigma'_i}$
0.0022	0.0061	0.0061	825	830.1	675	671.5	0.82	0.81
0.0072	0.0113	0.0112	863	872.8	488	485.9	0.57	0.56
0.0140	0.0182	0.0181	888	904.2	450	448.1	0.51	0.50
0.0216	0.0259	0.0256	900	923.3	425	423.3	0.47	0.46
0.0288	0.0332	0.0327	925	955.7	438	436.2	0.47	0.46
0.0358	0.0402	0.0394	925	962.2	400	398.4	0.43	0.41
0.0432	0.0477	0.0466	938	982.7	413	411.4	0.44	0.42
0.0504	0.0549	0.0534	938	989.5	425	423.3	0.45	0.43
0.0572	0.0617	0.0598	938	995.8	425	423.3	0.45	0.43
0.0644	0.0689	0.0666	938	1002.6	388	386.5	0.41	0.39
0.0716	0.0761	0.0733	938	1009.4	388	386.5	0.41	0.38
0.0800	0.0845	0.0811	938	1017.2	425	423.3	0.45	0.42
0.0858	0.0902	0.0864	925	1008.4	400	398.4	0.43	0.40

To describe the deformation diagram of the material, we apply a linear-power approximation [30] in the form:

$$\sigma_{i} = \Phi(e_{i}) = \begin{cases} Ee_{i}, & \text{if } e_{i} \leq e_{iT} \\ A(e_{i} - e_{0i})^{n}, & \text{if } e_{i} > e_{iT} \end{cases}$$
(12)

54 S.I. Feoktistov, I.K. Andrianov

where σ_i – intensity of stresses; e_i – intensity of Hencky strain; e_{iT} – the value of the strain intensity corresponding to the transition point of the linear dependence to the power-law (yield strength); e_{0i} – the magnitude of the displacement of the power function along the strain axis; $A \bowtie n$ – power function parameters.

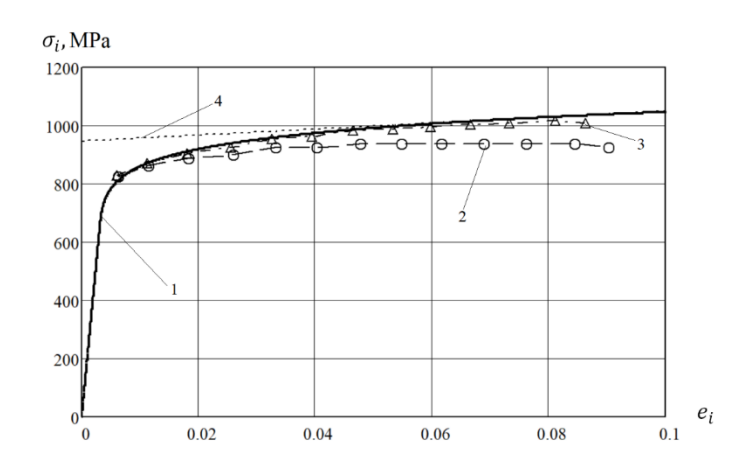


Fig. 2. Approximation of the deformation diagram of 45XGMA steel (E=210000 MPa, e_{iT} = 0.00367, σ_{iT} =771.14 MPa, A =1301.29 MPa, n =0.0933) and experimental data for steel $\sigma_{0,2}$ =800 MPa (Table 1): 1 – diagram constructed according to equation (12); 2 – diagram of conditional stresses σ_i^D ; 3 – diagram of true stresses σ_i^C ; 4 – tangent, characterizing the property of the deformation diagram of the III kind [30]

Figure 2 shows the results of the approximation of the 45HGMA steel deformation diagram and experimental data. As you can see, the results match quite well. In the case of approximation of the deformation diagram by Eqs. (5), (6), and (12), taking into account Eq. (9), will be written as:

$$\bar{\sigma}_{i} = \alpha(e_{i}')\Phi\left(\frac{\bar{e}_{i}}{\alpha(e_{i}')}\right) = \begin{cases} \alpha(e_{i}')E\left(\frac{\bar{e}_{i}}{\alpha(e_{i}')}\right), & \text{if } 0 \leq \bar{e}_{i} \leq \alpha(e_{i}')e_{iT} \\ \alpha(e_{i}')A\left(\frac{\bar{e}_{i}}{\alpha(e_{i}')} - e_{0i}\right)^{n}, & \text{if } \bar{e}_{i} > \alpha(e_{i}')e_{iT} \end{cases}$$

$$(13)$$

and

$$\sigma_{i}^{(2)} = \sigma_{i}'(e_{i}') - \alpha(e_{i}')\Phi\left(\frac{(e_{i}' - e_{i})}{\alpha(e_{i}')}\right) =$$

$$= \begin{cases}
\sigma_{i}'(e_{i}') - \alpha(e_{i}')E\left(\frac{(e_{i}' - e_{i})}{\alpha(e_{i}')}\right), & \text{if } e_{i}' \ge e_{i} \ge e_{i}' - \alpha(e_{i}')e_{iT} \\
\sigma_{i}'(e_{i}') - \alpha(e_{i}')A\left(\frac{(e_{i}' - e_{i})}{\alpha(e_{i}')} - e_{0i}\right)^{n}, & \text{if } e_{i} < e_{i}' - \alpha(e_{i}')e_{iT}
\end{cases}$$
(14)

where σ'_i и e'_i – accordingly, the intensity of stresses and the intensity of strains obtained during the first loading.

To determine the Masing function $\alpha(e')$, we use the Eq. (11), replacing, in accordance with the hypothesis of a single curve e' and $\sigma'(e')$ on e'_i and $\sigma'_i(e'_i)$:

$$\alpha(e_i') = \frac{\sigma_i'(e_i')}{\sigma_T} (1 + \beta_T(e_i')). \tag{15}$$

According to the available experimental data, we obtained the Bauschinger effect coefficient (Table 1) $\beta_{0,2}(e'_i) = \sigma''_{i0,2}/\sigma'_i$. To analytically describe the Bauschinger effect

using Masing functions (15), we need to determine the Bauschinger effect coefficient $\beta_T(e_i') = \sigma_{iT}''/\sigma_i'$.

If we determine the difference between $\sigma''_{i0.2}$ and σ''_{iT} , then we can obtain an equation connecting β_T and $\beta_{0.2}$:

$$\beta_T(e_i') = \frac{\sigma_{iT}''}{\sigma_i'} = \frac{\sigma_{i0,2}''}{\sigma_i'} - \frac{\left(\sigma_{i0,2}'' - \sigma_{iT}''\right)}{\sigma_i'} = \beta_{0,2}(e_i') - \frac{\left(\sigma_{i0,2}'' - \sigma_{iT}''\right)}{\sigma_i'}.$$
(16)

Considering that $(\sigma''_{i0,2} - \sigma''_{iT}) = (\overline{\sigma}_{i0,2} - \overline{\sigma}_{iT})$ we define $\overline{\sigma}_{iT}$ and $\overline{\sigma}_{i0,2}$ when unloading and subsequent loading of the opposite sign in accordance with Eq. (13):

$$\bar{\sigma}_{iT} = \alpha(e_i')\Phi\left(\frac{\bar{e}_{iT}}{\alpha(e_i')}\right) = \alpha(e_i')E\left(\frac{\bar{e}_{iT}}{\alpha(e_i')}\right) = E\bar{e}_{iT},\tag{17}$$

$$\bar{\sigma}_{i0,2} = \alpha(e_i')\Phi\left(\frac{\bar{e}_{i0,2}}{\alpha(e_i')}\right) = \alpha(e_i')A\left(\frac{\bar{e}_{i0,2}}{\alpha(e_i')} - e_{0i}\right)^n,\tag{18}$$

where \bar{e}_{iT} \bowtie $\bar{e}_{i0.2}$ – strains corresponding to the stress $\bar{\sigma}_{iT}$ and $\bar{\sigma}_{i0.2}$ when describing the deformation diagram by the function (12).

Thus, it is possible to write

$$(\sigma_{i0.2}^{"} - \sigma_{iT}^{"}) = \alpha(e_i^{'}) A \left(\frac{\bar{e}_{i0.2}}{\alpha(e_i^{'})} - e_{0i}\right)^n - E\bar{e}_{iT}.$$
(19)

Moreover, $\bar{e}_{iT} = \alpha(e'_i)e_{iT}$, and $\bar{e}_{i0,2}$ is determined numerically from the equation:

$$\alpha(e_i') A \left(\frac{\bar{e}_{i0.2}}{\alpha(e_i')} - e_{0i} \right)^n = E(\bar{e}_{i0.2} - 0.002). \tag{20}$$

It follows from Eqs. (16), (19), and (20) that the function $\beta_T(e_i')$ depends on $\alpha(e_i')$. Since initially the value of the Masing function is not known, we take $\alpha(e_i') = 2$ for calculations in the first approximation, as for the ideal Bauschinger effect. Next, using Eqs. (16) and (18), we determine the Masing function $\alpha(e_i')$ by Eq. (15).

As calculations show, in the first approximation, the values of $\sigma_{i0,2}^{(2)}$ calculated by Eq. (14) differ significantly from the values of $\sigma_{i0,2}^{\prime\prime}$ obtained experimentally (Table 1). In this case, the average arithmetic error of determining $\sigma_{i0,2}^{(2)}$ is 9.5 %, and the maximum is 20.7 %. To improve the result, a second approximation is carried out. In this case, the Masing function $\alpha(e_i')$ obtained in the first approximation is substituted into Eqs. (19), (20) and using Eqs. (15) and (16), the Masing function $\alpha(e_i')$ is refined in the second approximation.

Figure 3 shows the functions $\beta_T = \beta_T(e_i')$ and $\beta_{0.2} = \beta_{0.2}(e_i')$ obtained in the second approximation by processing experimental data. Since the Bauschinger effect begins to manifest itself only after the e_{iT} yield stress deformations or the $e_{i0,2}$ conditional yield stress deformations are reached during the first loading, the graphs of the function $\beta_T = \beta_T(e_i')$ and $\beta_{0.2} = \beta_{0.2}(e_i')$ were constructed in such a way that $\beta_T = \beta_T(e_{iT}) = 1$ and $\beta_{0.2} = \beta_{0.2}(e_{i0.2}) = 1$. In addition, when constructing the curve $\beta_T(e_i')$, the experimental points $\beta_{0.2}(e_i')$ shifted not only along the ordinate axis down by an amount $(\overline{\sigma}_{i0.2} - \overline{\sigma}_{iT})$, but also along the abscissa axis to the left by an amount $(\overline{e}_{i0.2} - \overline{e}_{iT})$.

56 S.I. Feoktistov, I.K. Andrianov

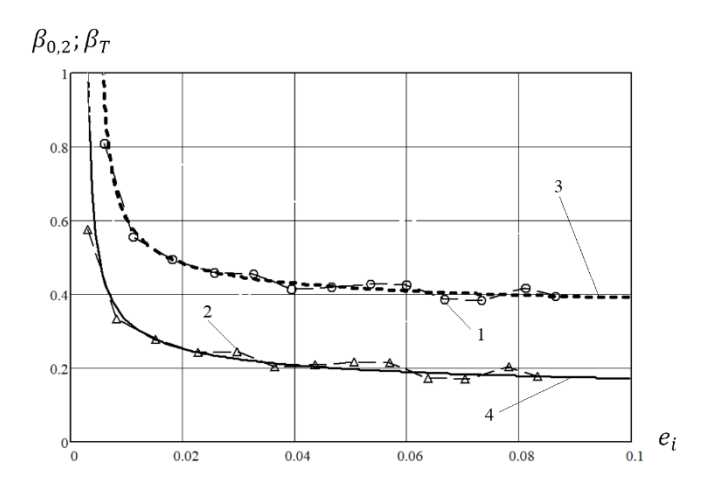


Fig. 3. Curves of changes in the coefficients of the Bauschinger effect $\beta_{0.2} = \beta_{0.2}(e_i')$ and $\beta_T = \beta_T(e_i')$ obtained on the basis of processing experimental data (Table 1) and approximation by equations of the form (21): 1 – experimental values $\beta_{0,2}$ (Table 1); 2 – β_T values obtained by processing experimental data; 3 – function $\beta_{0.2} = \beta_{0.2}(e_i')$; 4 – function $\beta_T = \beta_T(e_i')$

To approximate the curves obtained experimentally, an equation of the form $\beta(e'_i) = a/(e'_i + b)^c + d$ was used. Provided that the curve passes through a given point $(e'_i 0; \beta 0)$, the equation will take the form:

$$\beta(e_i') = \frac{a}{(e_i' + b)^c} - \frac{a}{(e_i'0 + b)^c} + \beta 0.$$
(21)

In our case $\beta 0=1$ and $e_i'0=e_{i0.2}$ when determining $\beta_{0.2}(e_i')$ and $e_i'0=e_{iT}$ when determining $\beta_{\rm T}(e_i')$. The coefficients a,b and c were determined from the given points by the least squares method.

After determining the Bauschinger coefficient $\beta_T = \beta_T(e_i')$, by the Eq. (15) we determine the Masing function $\alpha = \alpha(e_i')$. Figure 4 shows graphs of these functions, constructed from experimental data and according to the Eq. (15).

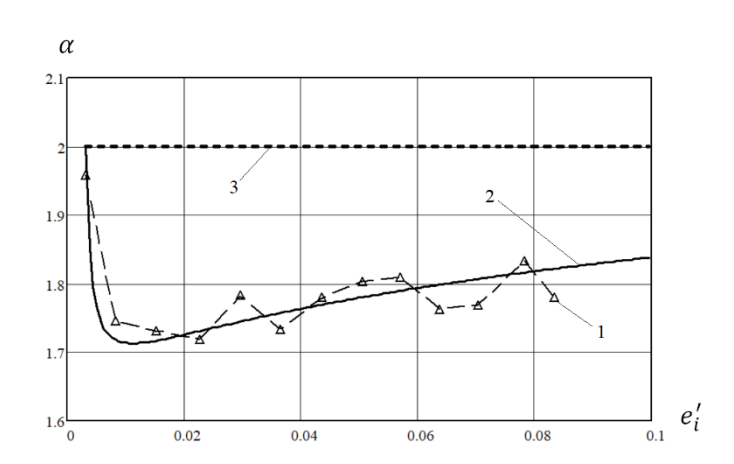


Fig. 4. The Masing function $\alpha = \alpha(e_i')$, determined by experimental data and by Eq. (15): 1 – the values of α obtained by processing experimental data; 2 – the function $\alpha = \alpha(e_i')$, obtained by Eq. (15); 3 – the values of the Masing function for an ideal Bauschinger effect, $\alpha = \alpha(e_i') = 2 = \text{const}$

Figure 5 shows diagrams of deformation of 45HGMA steel under reverse loading. The loading diagram was constructed using Eq. (12). Diagrams of unloading and further loading of the opposite sign were constructed on the basis of the generalized Masing principle according to Eq. (14) using the resulting Masing function shown in Fig. 4. As can be seen from the comparison of the calculation results with experimental data on the definition of $\sigma''_{i0.2}$, good convergence is obtained. The average arithmetic error of determining $\sigma^{(2)}_{i0.2}$ is 4.8 %, and the maximum is 15.1 %. Moreover, the greatest error is observed for the initial loading stage at $e'_i < 0.01$, which corresponds to the descending branch of the graph $\alpha = \alpha(e'_i)$ (Fig. 4). In addition, a comparison of the results obtained with the calculated data for the ideal Bauschinger effect shows (Fig. 4) that the application of the generalized Masing principle allows get more accurate results.

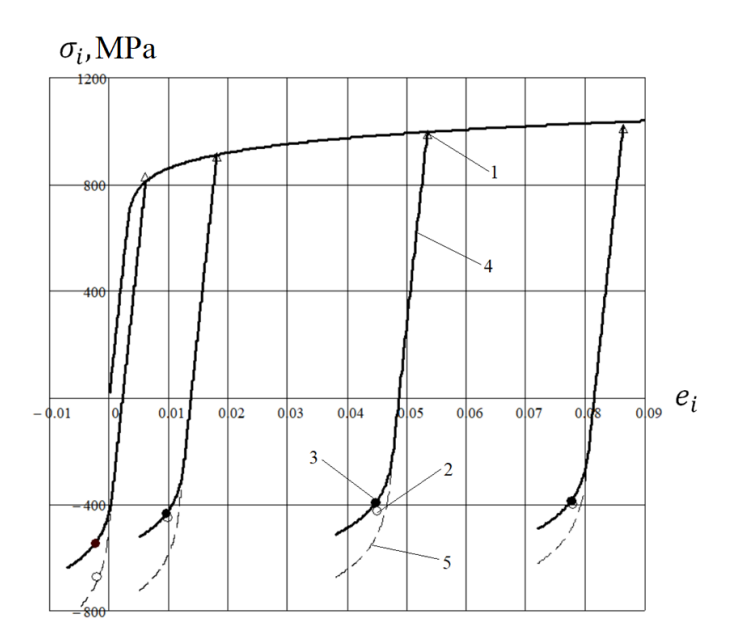


Fig. 5. Diagrams of deformation of 45HGMA steel under reverse loading: $1 - \exp(\sigma_i)$ and $1 - \exp(\sigma_i)$ are initial loading level σ_i ; $1 - \exp(\sigma_i)$ and $1 - \exp(\sigma_i)$ are initial loading level $1 - \exp(\sigma_i)$ and $1 - \exp(\sigma_i)$ are initial loading level $1 - \exp(\sigma_i)$ and $1 - \exp(\sigma_i)$ are initial loading level $1 - \exp(\sigma_i)$ and $1 - \exp(\sigma_i)$ are initial loading level $1 - \exp(\sigma_i)$ and $1 - \exp(\sigma_i)$ are initial loading level $1 - \exp(\sigma_i)$ and $1 - \exp(\sigma_i)$ are initial loading level $1 - \exp(\sigma_i)$ and $1 - \exp(\sigma_i)$ are initial loading level $1 - \exp(\sigma_i)$ and $1 - \exp(\sigma_i)$ are initial loading level $1 - \exp(\sigma_i)$ and $1 - \exp(\sigma_i)$ are initial loading level $1 - \exp(\sigma_i)$ and $1 - \exp(\sigma_i)$ are initial loading level $1 - \exp(\sigma_i)$ and $1 - \exp(\sigma_i)$ are initial loading level $1 - \exp(\sigma_i)$ and $1 - \exp(\sigma_i)$ are initial loading level $1 - \exp(\sigma_i)$ and $1 - \exp(\sigma_i)$ are initial loading level $1 - \exp(\sigma_i)$ and $1 - \exp(\sigma_i)$ are initial loading level $1 - \exp(\sigma_i)$ and $1 - \exp(\sigma_i)$ are initial loading level $1 - \exp(\sigma_i)$ and $1 - \exp(\sigma_i)$ and $1 - \exp(\sigma_i)$ are initial loading level $1 - \exp(\sigma_i)$ and $1 - \exp(\sigma_i)$ are initial loading level $1 - \exp(\sigma_i)$ and $1 - \exp(\sigma_i)$ are initial loading level $1 - \exp(\sigma_i)$ and $1 - \exp(\sigma_i)$ are initial loading level $1 - \exp(\sigma_i)$ and $1 - \exp(\sigma_i)$ are initial loading level $1 - \exp(\sigma_i)$ and $1 - \exp(\sigma_i)$ are initial loading level $1 - \exp(\sigma_i)$ and $1 - \exp(\sigma_i)$ are initial loading level $1 - \exp(\sigma_i)$ and $1 - \exp(\sigma_i)$ are initial loading level $1 - \exp(\sigma_i)$ and $1 - \exp(\sigma_i)$ are initial loading level $1 - \exp(\sigma_i)$ and $1 - \exp(\sigma_i)$ are initial loading level $1 - \exp(\sigma_i)$ and $1 - \exp(\sigma_i)$ are initial loading level $1 - \exp(\sigma_i)$ and $1 - \exp(\sigma_i)$ and $1 - \exp(\sigma_i)$ are initial loading level $1 - \exp(\sigma_i)$ and $1 - \exp(\sigma_i)$ and $1 - \exp(\sigma_i)$ are initial loading level $1 - \exp(\sigma_i)$ and $1 - \exp(\sigma_i)$ are initial loading level $1 - \exp(\sigma_i)$ and $1 - \exp(\sigma_i)$ and $1 - \exp(\sigma_i)$ are initial loading level $1 - \exp(\sigma_i)$ and $1 - \exp(\sigma_i)$ are initial loading level $1 - \exp(\sigma_i)$ and $1 - \exp(\sigma_i)$ are initial loading level $1 - \exp(\sigma_i)$ and $1 - \exp(\sigma_i)$ and $1 - \exp(\sigma_i)$ ar

3 – calculated data on the definition of $\sigma^{(2)}_{i0.2}$ under reverse loading; 4 – calculated diagrams of forward and reverse loading; 5 – calculated diagrams of reverse loading for the ideal Bauschinger effect

Conclusion

The possibility of an analytical description of the Bauschinger effect using experimental data allows us to obtain good convergence of the results and conclude that the generalized Masing principle can be applied in the study of various alternating loading processes.

In general, the question of the behavior of the material in the plastic region during repeated compression requires separate experimental studies, but to solve problems when repeated plastic strains are insignificant, it is possible to successfully apply the generalized Masing principle to describe the Bauschinger effect. Such tasks include, for example, calculations related to the determination of the stress-strain state and residual stresses during autofrettage of thick-walled pipes and high-pressure vessels.

58 S.I. Feoktistov, I.K. Andrianov

References

1. Moskvitin VV. *Plasticity under variable loads*. Moscow: Publishing House of Moscow State University; 1965. (In-Russian)

- 2. Pisarenko GS, Mozharovsky NS. *Equations and boundary value problems of the theory of plasticity and creep. Reference manual.* Kiev: Nauk. Dumka; 1981. (In-Russian)
- 3. Shinkin V. Bauschinger Effect, Masing Principle and Hencky Theorem for Bending Moment at Repeated Alternating-Sign Bending of Steel Sheet. *Materials Science Forum*. 2022;1052: 346-351.
- 4. Miryala M, Chauhan H, Murakami M, Saitoh T, Segawa K, Kamada K, Skelton R, Maier H, Christ H. The Bauschinger effect, Masing model and the Ramberg-Osgood relation for cyclic deformation in metals. *Materials Science and Engineering: A.* 1997;238(2): 377-390.
- 5. Shchedrin AV, Ul'yanov VV, Skoromnov VM, Bekaev FF. Bauschinger effect in complex machining methods. *Russian Engineering Research*. 2008;28(8): 797-799.
- 6. Motova YA, Nikitina NY. Experimental investigation by ultrasound of engineering materials behavior under the cyclic loading. *Materials Physics and Mechanics*. 2016;28(1-2): 43-47.
- 7. Kravchenko GN. Influence of Cyclic Loading on the Effectiveness of Repeated Shot Hardening. *Russian Engineering Research*. 2022;42(4): 365-369.
- 8. Mahato JK, De PS, Sarkar A. Effect of prestrain and stress rate on Bauschinger effect of monotonically and cyclically deformed ofhc copper. In: XVII International Colloquium on Mechanical Fatigue of Metals (ICMFM17), Verbania, 25–27 June 2014. 2014. p.368-375.
- 9. Adigamov PR, Andreev PA, Rogacheva SO. Manifestation of the Bauschinger effect in alternating deformation. *Izvestiya*. *Ferrous Metallurgy*. 2022;65(7): 455-466. (In Russian)
- 10. Savchenko VG, Babeshko ME. Technique of Allowing for Plastic Strains Under Unloading in Thermoplasticity Problems for Axisymmetric Bodies. *International Applied Mechanics*. 2019;55(4): 416-425.
- 11. Castro E Sousa AD, Hartloper AR, Lignos DG. Cyclic Metal Plasticity Model Parameters with Limited Information: Constrained Optimization Approach. *Journal of Engineering Mechanics*. 2021;147(7): 04021035.
- 12. Hwan AD, Hwan DV, Samsonova VI. Hardening of thin-walled cylindrical racks by plastic deformation. *Forging and stamping production. Processing of materials under pressure*. 2019;1: 14-17.
- 13. Makarov PV. The Model of Dynamic Stress Relaxation of Elastoplastic Materials. *Russian Physics Journal*. 2021;63(11): 1876-1884.
- 14. Andrianov IK. Minimization of dies volume using uniform distribution of hollows in the conditions of multi-cycle fatique dependence on temperature. *CIS Iron and Steel Review.* 2022;23: 33-38.
- 15. Kroon MA. Rubin MB. Simple Scalar Directional Hardening Model for The Bauschinger Effect Compared With a Tensorial Model. *Journal of Mechanics of Materials and Structures*. 2020;15(4): 510-539.
- 16. Fedorenkov DI, Kosov DA, Tumanov AV. Methodology for determining constants and parameters of the damage accumulation model with isotropic and kinematic hardening. *Physical Mesomechanics*. 2022;25(6): 63-74.
- 17. Temis YM. Mathematical simulation of low cycle fatigue of high-loaded engine parts. *Propulsion and Power Research*. 2018;7(4): 277-287.
- 18. Shinkin VN. Analytical description of metal plasticity at shift. CIS Iron and Steel Review. 2020;19: 66-70.
- 19. Zemlyanushnova NY, Porokhin AA, Zemlyanushnov NA. Stress-strain state of the valve spring in an auto engine during plastic hardening. *Russian Engineering Research*. 2016;36(7): 535-540.
- 20. Shen J, Wei X, Kraposhin VS, Vekshin BS. High cold plastic deformation of die steel 4Kh5VF1S subjected to hardening and tempering. *Metal Science and Heat Treatment*. 2012;53(9-10): 503-504.
- 21. Domichev K, Petrov A, Steblyanko P. Mathematical model shear lines for plastic deformation. *The Scientific Heritage*. 2021;61: 54-56.
- 22. Zheng M, Li Z. Strain-hardening effect on critical strain assessment of pipe plastic bending at buckling. *Materials Physics and Mechanics*. 2020;44(1): 48-60.
- 23. Abashkin EE, Burenin AA, Zhilin SG. Modeling of residual stress distribution in a welded joint. *Physics and Mechanics of Materials*. 2019;42(5): 671-689.
- 24. Aleksandrov S, Lyamina E, Yeau-Ren NG. Influence of the Bauschinger effect on the distribution of residual stresses in a thin hollow hyperbolic disc under external pressure. *Materials Science Forum*. 2019;972: 105-110.
- 25. Malinin NN. Applied theory of plasticity and creep. Moscow: Mashinostroenie; 1975. (In-Russian)

- 26. Perl M, Perry J. An Experimental-Numerical Determination of the Three-Dimensional Autofrettage Residual Stress Field Incorporating Bauschinger Effects. *Journal of Pressure Vessel Technology*. 2006;128(2): 173-178.
- 27. Adigamov RR, Andreev VA, Rogachev SO, Fedotov ES, Khadeev GE, Yusupov VS, Adigamov PR. Bauschinger effect during alternating deformation. *Izvestiya. Ferrous Metallurgy*. 2022;65(7):455-466. (In Russian)
- 28. Pykhtunova SV. On the issue of the Baushinger effect. *Quality in Materials Processing*. 2015;1(3): 75-77. (In-Russian)
- 29. Nigmatullin VI. Experimental investigation of the effect of preliminary plastic deformation on the behavior of structural steels under reverse loading. *Transactions of the Krylov State Research Centre*. 2011;60: 119-132. (In Russian)
- 30. Andrianov IK, Feoktistov SI. Fundamentals of constructing deformation diagrams taking into account the compressibility of the material and the Bauschinger effect. Komsomolsk-on-Amur: KnAGU; 2022. (In-Russian)

About Authors

Sergey I. Feoktistov D Sc

Doctor of Technical Sciences
Professor (Komsomolsk-na-Amure State University, Komsomolsk-on-Amur, Russia)

Ivan K. Andrianov 📵 Sc

Candidate of Technical Sciences, Associate Professor (Komsomolsk-na-Amure State University, Komsomolsk-on-Amur, Russia) Submitted: November 7, 2023

Revised: November 19, 2023

Accepted: December 8, 2023

Green's function molecular dynamics method for contact mechanics with a viscoelastic layer

V.G. Petrenko ¹, I.U. Solovyov ¹, E.V. Antonov ^{1 \infty},

L.M. Dorogin ¹,

Y. Murugesan ²

ABSTRACT

Advanced technological and engineering solutions involve usage of complex tribological systems. There is a demand for precise and computationally efficient methods to describe such systems. The aim of this study is to develop a computationally efficient method to solve the problem of deformation of a two-layer system using the Green's function molecular dynamics (GFMD) technique. We consider a viscoelastic layer attached to an elastic halfspace and derive a constitutive equation in Fourier space from the corresponding elastic solution. This third-order equation is numerically integrated by the backward Euler method, and a quasi-static solution is found through the fast inertial relaxation engine (FIRE) optimization algorithm. The method is illustrated with a simple model of indentation by a rigid cylinder. Using this method, contact area and pressure were calculated as a function of time for various shear modulus values.

KEYWORDS

boundary element method • viscoelasticity • contact mechanics • computational method • contact area

Acknowledgements. The work was supported by the Ministry of Science and Higher Education of the Russian Federation (Project 075-15-2021-1349).

Citation: Petrenko VG, Solovyov IU, Antonov EV, Dorogin LM, Murugesan Y. Green's function molecular dynamics method for contact mechanics with a viscoelastic layer. *Materials Physics and Mechanics*. 2024;52(1): 60-68. http://dx.doi.org/10.18149/MPM.5212024_6

Introduction

Tribology is one of the oldest sciences, yet even after the hundreds years of research it remains not completely understood. Tribology of viscoelastic materials is becoming more and more important as technology moves forward: there is a large class of new rubberlike materials which have a wide range of innovative implementations in engineering, microelectronics, microbiology. Therefore, when modelling such systems, it is necessary to include an accurate description of the response of the viscoelastic material. The contact of a rigid rough surface with a viscoelastic halfspace was investigated in the work of Bugnicourt et al. [1]. In their work, the contact problem was numerically solved through a combination of the backward Euler method and conjugate gradient optimization. A viscoelastic model utilizing Green's function molecular dynamics (GFMD) and a semianalytical solution with improved accuracy instead of the backward Euler method was developed in [2] and applied to the quasi-static indentation and rolling of a rigid cylinder on a frictionless viscoelastic halfspace. GFMD [3] is a boundary element method based on the fast Fourier transform and molecular dynamics energy minimization that simulates the response of an elastic body to an external force. GFMD has been used in simulations of rough elastic contacts [4], bodies of finite height [5], atomistic systems [3], viscoelastic

¹ ITMO University, St. Petersburg, Russia

² University of Padova, Padua, Italy

[™] evantonov@itmo.ru

halfspaces [6] and adhesive viscoelastic roughness contact [7]. Recently, GFMD was accelerated with the fast inertial relaxation engine (FIRE) algorithm, resulting in speedups of one order of magnitude [8].

Contact mechanics models are used in many applications [9–11]. Sometimes contact mechanical systems can be represented by semi-infinite bodies. That, however, is not always the case [12]. There are systems that require a consideration of the layer's thickness, such as power transmission belts [13], seismic energy dissipation systems [14], electroadhesive devices [15], multi-layer structure [16], biomedical applications [17], coatings etc. In these situations, one should take into consideration the surface layer on top of the main half-space [18]. With further modification that concept can be used in investigation of adhesion of viscoelastic polymers depending on various factors, such as temperature, environment [19], blending [20] or molecular cross-linking density [21].

In this work we study the indentation of a viscoelastic layer of finite thickness bonded to an elastic halfspace. The paper is organized as following. In section "Methods", a constitutive equation is derived, following which, the methodology to obtain a numerical solution is explained. In section "Result and Discussion", using the newly developed model, the results for the indentation of a cylindrical punch onto a viscoelastic material are shown and discussed.

Methods

Consider a viscoelastic layer with stress σ and strain ε . Let $s = \sigma - (1/3) \operatorname{tr}(\sigma) I$ be the stress deviator, and let $e = \varepsilon - (1/3) \operatorname{tr}(\varepsilon) I$ be the strain deviator. Assume that viscoelasticity of the layer is described by the following equation [22]:

$$s(t) = \int_{-\infty}^{t} G(t - t')\dot{e}(t')dt', \tag{1}$$

where t is the time and G(t) is the time-dependent shear modulus. The complex shear modulus $G(\omega)$ is then defined by

$$G(\omega) = i\omega \int_0^\infty G(t)e^{-i\omega t} dt', \tag{2}$$

so that

$$s(\omega) = 2G(\omega)e(\omega),\tag{3}$$

where $s(\omega) = \int e^{-i\omega t} s(t) dt$, $e(\omega) = \int e^{-i\omega t} e(t) dt$, and ω is the angular frequency.

The complex shear modulus in the Zener model [22] is given by

$$G(\omega) = (G_0 + i\omega\tau G_{\infty}) \times (1 + i\omega\tau)^{-1},\tag{4}$$

where τ is the relaxation time, $G_0 = \lim_{\omega \to 0} G(\omega)$ is the low-frequency shear modulus, and $G_\infty = \lim_{\omega \to \infty} G(\omega)$ is the high-frequency shear modulus. The time-dependent shear modulus takes the form:

$$G(t) = G_0 + (G_{\infty} - G_0)e^{-t/\tau}.$$
 (5)

Substituting Eq. (4) in Eq. (3) and applying an inverse Fourier transform, we obtain: $s(t) + \tau \dot{s}(t) = 2G_0 e(t) + 2\tau G_\infty \dot{e}(t)$. (6)

For an elastic halfspace with shear modulus G and Poisson ratio v the relation between normal surface stress $\sigma(x)$ and normal surface displacement u(x) is [23]:

$$u(x) = -\frac{1-\nu}{2\pi G} \int \frac{\sigma(x')}{|x-x'|} dx'. \tag{7}$$

After taking the Fourier transform, we can write:

$$u(q) = M(q)\sigma(q), \tag{8}$$

where $u(q) = \int u(x) e^{-ix \cdot q} dx$, $\sigma(q) = \int \sigma(x) e^{-ix \cdot q} dx$, q is the wavevector, q = |q|, and

$$M(q) = -\frac{1-\nu}{Ga}. (9)$$

Consider an elastic layer of thickness d with shear modulus G and Poisson ratio vattached to an elastic halfspace with shear modulus G_{bulk} and Poisson ratio v_{bulk} . Equation (9) becomes (see [24]):

$$M(q) = -\frac{1-\nu}{Gq}S(q),\tag{10}$$

$$S(q) = \frac{1 + 4mqde^{-2qd} - mne^{-4qd}}{1 - (m + n + 4mq^2d^2)e^{-2qd} + mne^{-4qd}},$$
(11)

where

$$m = (G/G_{\text{bulk}} - 1) \times (G/G_{\text{bulk}} + 3 - 4\nu)^{-1},$$
 (12a)

$$m = (G/G_{\text{bulk}} - 1) \times (G/G_{\text{bulk}} + 3 - 4\nu)^{-1},$$

$$n = 1 - \frac{4(1-\nu)}{1 + (G/G_{\text{bulk}})(3 - 4\nu_{\text{bulk}})}.$$
(12a)

In the limiting case where the halfspace is rigid ($G_{\text{bulk}} = \infty$), Eq. (11) reduces to:

$$S(q) = \frac{(3-4\nu_0)\sinh(2qd)-2qd}{(3-4\nu_0)\cosh(2qd)+2(qd)^2-4\nu_0(3-2\nu_0)+5},$$
(13)

while for a free layer ($G_{\text{bulk}} = 0$), Eq. (11) reduces to:

$$S(q) = \frac{\sinh(2qd) + 2qd}{\cosh(2qd) - 2(qd)^2 - 1}.$$
(14)

Assume the layered solid is incompressible. Then $v = v_{\text{bulk}} = 0.5$ and Eq. (12) simplify to:

$$m = n = (G - G_{\text{bulk}})/(G + G_{\text{bulk}}). \tag{15}$$

Due to the elastic-viscoelastic correspondence principle, a solution to our viscoelastic problem can be derived from the elastic solution by replacing G with the complex shear modulus $G(\omega)$. Substituting Eq. (4) in Eq. (15) gives:

$$n = \frac{(G_0 + i\omega\tau G_{\infty})/(1 + i\omega\tau) - G_{\text{bulk}}}{(G_0 + i\omega\tau G_{\infty})/(1 + i\omega\tau) + G_{\text{bulk}}} = \frac{(G_0/G_{\text{bulk}} - 1) + i\omega\tau (G_{\infty}/G_{\text{bulk}} - 1)}{(G_0/G_{\text{bulk}} + 1) + i\omega\tau (G_{\infty}/G_{\text{bulk}} + 1)} = \frac{a_0 + sa_1}{a_2 + sa_3},$$
(16)

where

$$s = i\omega \tau$$
, (17a)

$$a_0 = G_0/G_{\text{bulk}} - 1,$$
 (17b)

$$a_1 = G_{\infty}/G_{\text{hulk}} - 1,\tag{17c}$$

$$a_2 = G_0/G_{\text{bulk}} + 1,\tag{17d}$$

$$a_3 = G_{\infty}/G_{\text{bulk}} + 1. \tag{17e}$$

We define:

$$r = e^{-2qd}, (18a)$$

$$b_0 = -2(1+2(qd)^2), (18b)$$

$$b_1 = 4qd, (18c)$$

and write Eq. (11) as:

$$S(q) = \frac{1 + 4nqde^{-2qd} - (ne^{-2qd})^2}{1 - (2n + 4n(qd)^2)e^{-2qd} + (ne^{-2qd})^2} = \frac{1 + b_1nr - (nr)^2}{1 + b_0nr + (nr)^2}.$$
(19)

Substituting Eq. (16) gives:

$$S(q,\omega) = \frac{1+b_1((a_0+sa_1)/(a_2+sa_3))r - (((a_0+sa_1)/(a_2+sa_3))r)^2}{1+b_0((a_0+sa_1)/(a_2+sa_3))r + (((a_0+sa_1)/(a_2+sa_3))r)^2} = \frac{(a_2+sa_3)^2 + b_1(a_0+sa_1)(a_2+sa_3)r - ((a_0+sa_1)r)^2}{(a_2+sa_3)^2 + b_0(a_0+sa_1)(a_2+sa_3)r + ((a_0+sa_1)r)^2} = \frac{c_{1,1} + c_{2,1}s + c_{3,1}s^2}{c_{1,0} + c_{2,0}s + c_{3,0}s^2},$$
(20)

where

$$c_{0,k} = 0, (21a)$$

$$c_{1,k} = a_2^2 + a_0 a_2 b_k r + (-1)^k a_0^2 r^2, (21b)$$

$$c_{2,k} = 2a_2a_3 + (a_1a_2 + a_0a_3)b_kr + (-1)^k 2a_0a_1r^2,$$
(21c)

$$c_{3,k} = a_3^2 + a_1 a_3 b_k r + (-1)^k a_1^2 r^2, (21d)$$

$$c_{4,k} = 0.$$
 (21e)

For k = 0, 1. Using Eqs. (4), (9), and (20) gives:

$$M(q,\omega) = -\frac{S(q,\omega)}{2G(\omega)q} = -\frac{1}{2q} \frac{1+s}{G_0+sG_\infty} \frac{c_{1,1}+c_{2,1}s+c_{3,1}s^2}{c_{1,0}+c_{2,0}s+c_{3,0}s^2} = \frac{1}{2q} \frac{c_{1,1}+(c_{1,1}+c_{2,1})s+(c_{2,1}+c_{3,1})s^2+c_{3,1}s^3}{G_0c_{1,0}+(G_0c_{2,0}+G_\infty c_{1,0})s+(G_0c_{3,0}+G_\infty c_{2,0})s^2+G_\infty c_{3,0}s^3}.$$
(22)

Substituting this in Eq. (8), we have:

$$\sum_{k=0}^{3} \left(c_{k+1,1} + c_{k,1} \right) s^{k} \sigma(q, \omega) = -2q \sum_{k=0}^{3} \left(c_{k+1,0} G_{0} + c_{k,0} G_{\infty} \right) s^{k} u(q, \omega).$$
 (23)

An inverse Fourier transform is applied to obtain the constitutive equation:

$$\sum_{k=0}^{3} \left(c_{k+1,1} + c_{k,1} \right) \tau^{k} \partial_{t}^{k} \sigma(q,t) = -2q \sum_{k=0}^{3} \left(c_{k+1,0} G_{0} + c_{k,0} G_{\infty} \right) \tau^{k} \partial_{t}^{k} u(q,t). \tag{24}$$

Consider the limiting case where the elastic halfspace is infinitely rigid, i.e.,

$$G_{\text{bulk}} = \infty$$
. Then $-a_0 = -a_1 = a_2 = a_3 = 1$ and:

$$1 - b_k r + (-1)^k r^2 = c_{1,k} = c_{2,k}/2 = c_{3,k}.$$
 (25)

For k = 0, 1 so that the left-hand side operator of Eq. (24) is:

$$\sum_{k=0}^{3} \left(c_{k+1,1} + c_{k,1} \right) (\tau \partial_t)^k = c_{1,1} + (c_{1,1} + c_{2,1}) (\tau \partial_t) + \left(c_{2,1} + c_{3,1} \right) (\tau \partial_t)^2 + c_{3,1} (\tau \partial_t)^3 = (1 - b_1 r - r^2) (1 + 3(\tau \partial_t) + 3(\tau \partial_t)^2 + (\tau \partial_t)^3) = (1 - b_1 r - r^2) (1 + \tau \partial_t)^3,$$
(26)

while the right-hand side operator is:

$$-2q\sum_{k=0}^{3} (c_{k+1,0} G_0 + c_{k,0} G_\infty) (\tau \partial_t)^k = -2q(1 - b_0 r + r^2)(G_0 + (2G_0 + G_\infty)(\tau \partial_t) + (G_0 + 2G_\infty)(\tau \partial_t)^2 + G_\infty(\tau \partial_t)^3) = -2q(1 - b_0 r + r^2)(G_0 + G_\infty \tau \partial_t)(1 + \tau \partial_t)^2.$$
(27)

After removing the common factor $(1 + \tau \partial_t)^2$, we get the equation:

$$\sigma(q,t) + \tau \dot{\sigma}(q,t) = -2q \frac{1 - b_0 r + r^2}{1 - b_1 r - r^2} \left(G_0 u(q,t) + G_\infty \tau \dot{u}(q,t) \right). \tag{28}$$

If the viscoelastic layer is infinitely thick, i.e., $d = \infty$, then Eq. (28) reduces to:

$$\sigma(q,t) + \tau \dot{\sigma}(q,t) = -2q \left(G_0 u(q,t) + G_\infty \tau \dot{u}(q,t) \right), \tag{29}$$

which was obtained and integrated semi-analytically by van Dokkum et al. [2]. Note that the same semi-analytical integration scheme may be used to solve Eq. (28).

Assume the layered solid is indented by rigid punch with a trajectory h(x,t). The time is discretized into time points $0, \Delta t, 2\Delta t,...$ and the surface of the layered solid u(x,t) is discretized with n grid points $x_0, x_1, ..., x_{n-1}$. Overlap of the punch and the layered solid is not allowed $(u(x_i,t) \le h(x_i,t))$. Also, it is assumed that at the bottom of the elastic solid being approximated by the elastic halfspace the displacements are fixed at zero. Then, since the layered solid is incompressible, the mean surface displacement is zero $(\sum_{i=0}^{n-1} u(x_i,t)=0)$.

To numerically solve Eq. (24) for σ the $\partial_t^k u$ are approximated with finite differences and used to compute the input to the backward Euler method. An alternative might be to solve Eq. (24) semi-analytically [25] for improved convergence properties. The equilibrium displacement field at a given time is found by solving an energy minimization problem via FIRE-based GFMD [8].

If $u(q,t-4\Delta t)$, $u(q,t-3\Delta t)$, $u(q,t-2\Delta t)$, and $u(q,t-\Delta t)$ have been found, then $\sigma(q,t)$ can be shown to be a linear function of u(q,t). Thus, the slopes and the intercepts of the linear functions may be precomputed before the minimization. (Note that the displacements could be shifted to eliminate the intercepts.)

The fast Fourier transform and its inverse are denoted by *FFT* and *IFFT*. The pseudocode is as follows:

- 0 set up the trajectory of the punch h(t)
- set displacements u(t) to zero for t < 0
- $2 t \leftarrow 0$
- 3 be solver \leftarrow (backward Euler solver of (24) for σ)
- 4 while true
- 5 $a \leftarrow \text{(slopes of } \sigma \text{ from } be \text{ solver)}$
- b ← (intercepts of σ from be_solver)
- use FIRE-based GFMD to find u(t) such that the energy corresponding to the force IFFT ($a \odot FFT(u(t)) + b$) is minimal subject to $\sum_{j=0}^{n-1} u(x_j, t) = 0$ and $u(t) \le h(t)$, where
 - O is elementwise product
- 8 $rhs \leftarrow$ (new values of the right-hand side of (24) computed from $u(t 3\Delta t)$, $u(t 2\Delta t)$, $u(t \Delta t)$, u(t) using finite differences)
- 9 update be solver with rhs
- 10 $t \leftarrow t + \Delta t$

Results and Discussion

We consider indentation by a rigid punch in two dimensions. The punch is periodic in the *x* direction with period *L* and its trajectory is defined by:

$$h(x,t) = \frac{R}{2} \left(\frac{x}{R}\right)^2 + \frac{-h_0 L}{\tau} \cdot \begin{cases} 0, & \text{for } t < 0 \\ t, & \text{for } 0 \le t < \tau, \\ \tau, & \text{for } t \ge \tau \end{cases}$$
 (30)

for $-1/2 \le x/L \le 1/2$, where h_0L is the maximum indentation depth and R is the radius of curvature at x=0. A schematic of the system is shown in Fig. 1. The relative contact area is defined as $\tilde{a}=a/L$, and the dimensionless pressure is defined as $\tilde{p}=p(2G_0)$, where p is the mean normal contact stress. The numerical results are obtained for $G_{\text{bulk}}/G_0=1$, $G_{\infty}/G_0=10$, G

The relative contact area and the dimensionless pressure as functions of time for $G_{\infty} = G_{\text{bulk}}$ and d/L = 0, 1/32, 1/16, 1/8, 1/4, ∞ are presented in Figs. 2. At time $t \approx 0$ the responses are approximately the same. This is because the coating is responding with the high-frequency modulus $G_{\infty} = G_{\text{bulk}}$ and the whole layered solid is behaving like a purely elastic halfspace with $G = G_{\text{bulk}}$ regardless of thickness d. As the coating thickness d/L is varied from 0 to ∞ , the relative contact area curve rises until d/L = 1/16 and then returns to the initial values. As we can see, the contact area curve is the same for d = 0 and $d = \infty$. At d = 0 the system is purely elastic, hence the contact area and pressure become constant when the punch stops at $t = \tau$. The constantness of contact area at the hold for $d = \infty$ is in accordance with the simulations by van Dokkum [5]. That $\lim_{t \to \infty} \tilde{a}(t)$ must be the same for d = 0 and $d = \infty$ follows from the corresponding elastic energy functions being equal

up to a positive constant factor. In Figure 3, the contact area and the pressure for varying hardness of the bulk layer are presented. As the bulk becomes harder, the values of the contact area curve increase up to infinite rigidity, at which point the contact area is constant at the hold. In Figure 4, the contact area and the pressure for $G_{\infty}/G_0 = 2$, 3, 5, 9, 17 are presented. As G_{∞} increases, the contact area curve goes down, while the pressure curve goes up. When $t \to \infty$, the curves approach the same response of an elastic halfspace with $G = G_0 = G_{\text{bulk}}$.

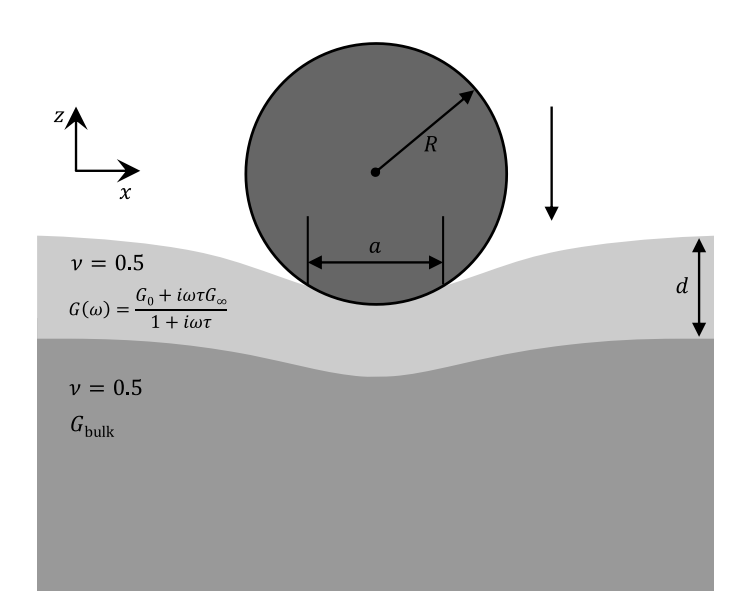


Fig. 1. Schematic of a rigid punch indenting a viscoelastically layered solid

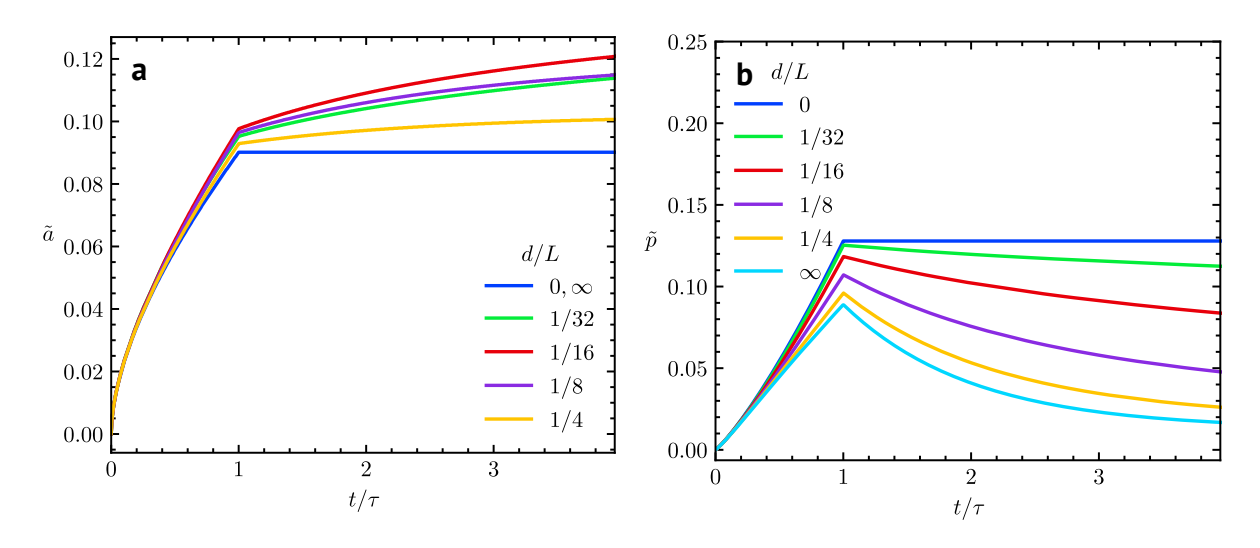


Fig. 2. The relative contact area \tilde{a} (a) and the dimensionless pressure \tilde{p} (b) as a function of the dimensionless time t/τ for $G_{\infty} = G_{\text{bulk}}$ and d/L = 0, 1/32, 1/16, 1/8, 1/4, ∞

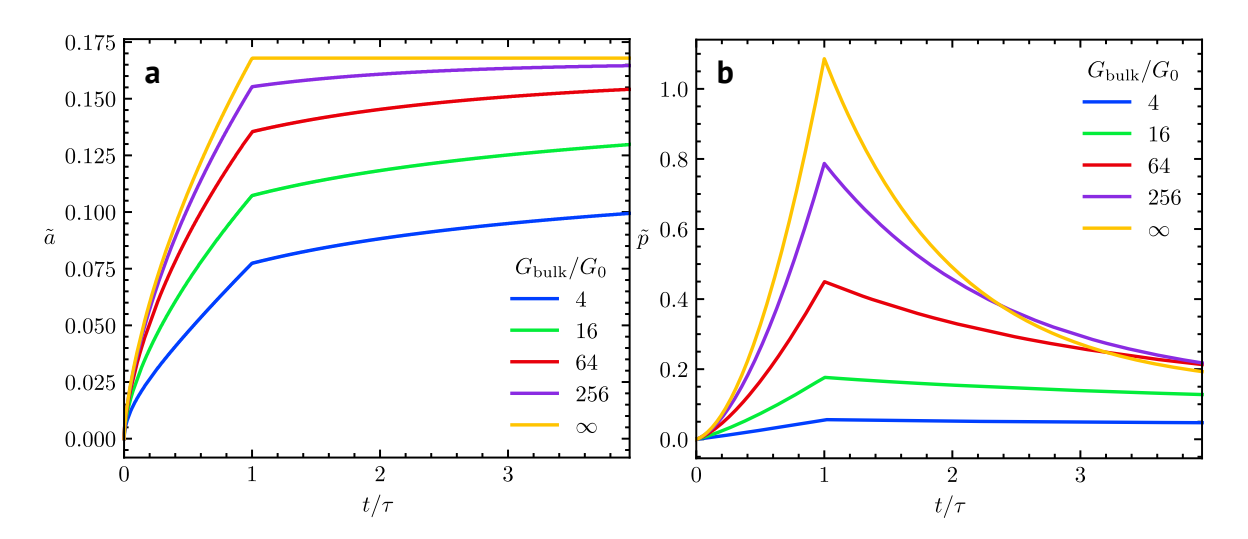


Fig. 3. The relative contact area \tilde{a} (a) and the dimensionless pressure \tilde{p} (b) as a function of the dimensionless time t/τ for $G_{\text{bulk}}/G_0 = 4$, 16, 64, 256, ∞

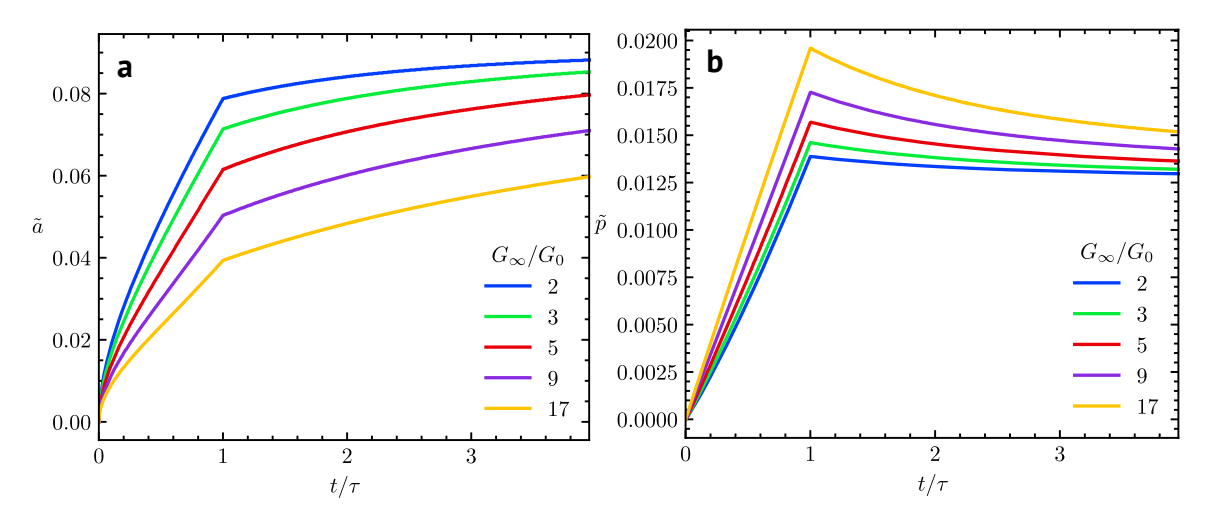


Fig. 4. The relative contact area \tilde{a} (a) and the dimensionless pressure \tilde{p} (b) as a function of the dimensionless time t/τ for $G_{\infty}/G_0 = 2, 3, 5, 9, 17$

Conclusions

There is a demand for computationally efficient methods to model tribological systems. We formulate and implement a GFMD technique to compute the response of a viscoelastic layer of finite thickness bonded to an elastic half-space. We derive a constitutive equation and solve it numerically using the backward Euler method. A quasi-static solution is found using the FIRE optimization algorithm. The developed method is applied to model indentation by a rigid punch.

The model described in the article can be used in a number of cases, for instance, electroadhesive devices, multi-layer structures, coating, and etc. Moreover, as a future development, this computational model can be extended with adhesion forces, more precise (higher orders) of viscoelastic material allowing to simulate broader range of cases.

References

- 1. Bugnicourt R, Sainsot P, Lesaffre N, Lubrecht AA. Transient frictionless contact of a rough rigid surface on a viscoelastic half-space. *Tribology International*. 2017;113: 279–285.
- 2. Dokkum JS van, Nicola L. Green's function molecular dynamics including viscoelasticity. *Modelling and Simulation in Materials Science and Engineering*. 2019;27(7): 075006.
- 3. Campañá C, Müser MH. Practical Green's function approach to the simulation of elastic semi-infinite solids. *Physical Review B*. 2006;74(7): 075420.
- 4. Prodanov N, Dapp WB, Müser MH. On the Contact Area and Mean Gap of Rough, Elastic Contacts: Dimensional Analysis, Numerical Corrections, and Reference Data. *Tribology Letters*. 2013;53(2): 433–448.
- 5. Venugopalan SP, Nicola L, Müser MH. Green's function molecular dynamics: including finite heights, shear, and body fields. *Modelling and Simulation in Materials Science and Engineering*. 2017;25(3): 034001.
- 6. Sukhomlinov S, Müser MH. On the viscous dissipation caused by randomly rough indenters in smooth sliding motion. *Applied Surface Science Advances*. 2021;6: 100182.
- 7. Pérez-Ràfols F, Van Dokkum JS, Nicola L. On the interplay between roughness and viscoelasticity in adhesive hysteresis. *Journal of the Mechanics and Physics of Solids*. 2023;170: 105079.
- 8. Zhou Y, Moseler M, Müser MH. Solution of boundary-element problems using the fast-inertial-relaxation-engine method. *Physical Review B*. 2019;99(14): 144103.
- 9. Sethi SK, Shankar U, Manik G. Fabrication and characterization of non-fluoro based transparent easy-clean coating formulations optimized from molecular dynamics simulation. *Progress in Organic Coatings*. 2019;136: 105306.
- 10. Müller C, Samri M, Hensel R, Arzt E, Müser MH. Revealing the coaction of viscous and multistability hysteresis in an adhesive, nominally flat punch: A combined numerical and experimental study. *Journal of the Mechanics and Physics of Solids*. 2023;174: 105260.
- 11. Müser MH, Dapp WB, Bugnicourt R, Sainsot P, Lesaffre N, Lubrecht TA, Persson BNJ, Harris K, Bennett A, Schulze K, Rohde S, Ifju P, Sawyer WG, Angelini T, Esfahani HA, Kadkhodaei M, Akbarzadeh S, Wu JJ, Vorlaufer G, Vernes A, Solhjoo S, Vakis AI, Jackson RL, Xu Y, Streator J, Rostami A, Dini D, Medina S, Carbone G, Bottiglione F, Afferrante L, Monti J, Pastewka L, Robbins MO, Greenwood JA. Meeting the Contact-Mechanics Challenge. *Tribology Letters*. 2017;65(4): 118.
- 12. Menga N, Afferrante L, Carbone G. Effect of thickness and boundary conditions on the behavior of viscoelastic layers in sliding contact with wavy profiles. *Journal of the Mechanics and Physics of Solids*. 2016;95: 517–529.
- 13. Zhu H, Zhu WD, Fan W. Dynamic modeling, simulation and experiment of power transmission belt drives: A systematic review. *Journal of Sound and Vibration*. 2021;491: 115759.
- 14. Zhang C, Ali A. The advancement of seismic isolation and energy dissipation mechanisms based on friction. *Soil Dynamics and Earthquake Engineering*. 2021;146: 106746.
- 15. Cao C, Sun X, Fang Y, Qin QH, Yu A, Feng XQ. Theoretical model and design of electroadhesive pad with interdigitated electrodes. *Materials & Design*. 2016;89: 485–491.
- 16. He T, Duan M, Wang J, Lv S, An C. On the external pressure capacity of deepwater sandwich pipes with inter-layer adhesion conditions. *Applied Ocean Research*. 2015;52: 115–124.
- 17. Guo S, Zhu X, Loh XJ. Controlling cell adhesion using layer-by-layer approaches for biomedical applications. *Materials Science and Engineering: C.* 2017;70: 1163–1175.
- 18. Liu L, Yu M, Lin H, Foty R. Deformation and relaxation of an incompressible viscoelastic body with surface viscoelasticity. *Journal of the Mechanics and Physics of Solids*. 2017;98: 309–329.
- 19. Chipara AC, Tsafack T, Owuor PS, Yeon J, Junkermeier CE, Van Duin ACT, Bhowmick S, Asif SAS, Radhakrishnan S, Park JH, Brunetto G, Kaipparettu BA, Galvao DS, Chipara M, Lou J, Tsang HH, Dubey M, Vajtai R, Tiwary CS, Ajayan PM. Underwater adhesive using solid–liquid polymer mixes. *Materials Today Chemistry*. 2018;9: 149–157. 20. Sethi SK, Soni L, Shankar U, Chauhan RP, Manik G. A molecular dynamics simulation study to investigate poly(vinyl acetate)-poly(dimethyl siloxane) based easy-clean coating: An insight into the surface behavior and substrate interaction. *Journal of Molecular Structure*. 2020;1202: 127342.
- 21. Jin C, Wang Z, Volinsky AA, Sharfeddin A, Gallant ND. Mechanical characterization of crosslinking effect in polydimethylsiloxane using nanoindentation. *Polymer Testing*. 2016;56: 329–336.
- 22. Popov VL. Contact mechanics and friction. 2nd ed. Berlin, Germany: Springer; 2017.
- 23. Landau LD, Pitaevskii LP, Lifshitz EM, Kosevich AM. *Theory of elasticity*. 3rd ed. Oxford, England: Butterworth-Heinemann; 1984.

- 24. Persson BNJ. Contact mechanics for layered materials with randomly rough surfaces. *Journal of Physics: Condensed Matter.* 2012;24(9): 095008.
- 25. Sorvari J, Hämäläinen J. Time integration in linear viscoelasticity—a comparative study. *Mechanics of Time-Dependent Materials*. 2010;14(3): 307–328.

About Authors

Veniamin G. Petrenko

PhD Student (ITMO University, St. Petersburg, Russia)

Ivan U. Solovyov

Engineer (ITMO University, St. Petersburg, Russia)

Evgenii V. Antonov 🗓

Engineer (ITMO University, St. Petersburg, Russia)

Leonid M. Dorogin 🗓

PhD, Assosiate Professor (ITMO University, St. Petersburg, Russia)

Yaswanth Murugesan

Engineer (University of Padova, Padua, Italy)

Accepted: November 23, 2023

Submitted: September 5, 2022 Revised: September 29, 2022

Numerical estimation of fatigue life of aluminum alloy specimen with surface defects based on stress-life approach

L.A. Almazova, DO.S. Sedova , DO.S. Sedova

St. Petersburg State University, St. Petersburg, Russia

[™] olya-sedova@mail.ru

ABSTRACT

This paper presents a numerical study for fatigue life estimation of a cylindrical specimen made of aluminum alloy under high cycle fatigue regime. The fatigue life is assessed through the stress-life approach. The sample is weakened by either a cluster of surface defects or by an equivalent defect. Two different forms of defects are considered. The load conditions are assumed to be uniaxial tension-compression with a load ratio R = 0.1. To account for non-zero mean stress the Goodman correction is used. The material properties are considered to be combined nonlinear isotropic and kinematic hardening implemented in ANSYS Workbench software.

KEYWORDS

aluminum alloy • finite element analysis • FEM • stress-strain state • corrosion pit • fatigue life • surface defect • interaction of defects • cyclic loads

Acknowledgements. This work was supported by Russian science foundation (RSF #21-19-00100).

Citation: Almazova LA, Sedova OS. Numerical estimation of fatigue life of aluminum alloy specimen with surface defects based on stress-life approach. *Materials Physics and Mechanics*. 2024;52(1): 69–80. http://dx.doi.org/10.18149/MPM.5212024 7

Introduction

Most of the metal structures are subjected to cyclic mechanical loads during their service life. Even if the applied loads never exceed the elastic limit of the material, it is possible that after a certain number of cycles failure may occur. Therefore, it is important to understand how the mechanical properties of the material degrade as a result of the gradual accumulation of damage under the influence of various stresses below the elastic limit, i.e., the fatigue life of the material.

For a correct estimation of fatigue life, it is necessary to determine the appropriate parameters of the metal in question as a result of many experiments, as well as to account for a lot of different factors affecting fatigue behavior such as surface condition, type of loading, environment conditions, etc. The literature analysis indicates that fatigue performance of structures is hard to predict since it depends on numerous parameters.

Moreover, the majority of structures always contain a certain number of defects, which, becoming stress concentrators, reduce the strength and fatigue life of the structure. For metals such local stress concentrators may often result from manufacturing process [1,2] or be induced by corrosion [3–5]. The effect of defects on fatigue strength has been widely studied for decades, nevertheless, a lot of dependencies are still unclear. It is known with reasonable accuracy about two parameters that influence fatigue limit significantly. The first of them is defect size; it was shown by many researchers that fatigue limit decreases with increasing defect size, e.g., [6–9]. The second known

70 L.A. Almazova, O.S. Sedova

characteristic is defect location: surface, subsurface or internal. Studies, comparing surface and internal defects, clearly showed that surface ones are more dangerous than internal ones, e.g., [6,10,11]. Papers, where subsurface defects were considered, showed that this type of defect location is most harmful to fatigue life [12,13]. Recent experimental research by Nadot [14] performed for different materials and various parameters shows that the defect's size, type and position are among the major parameters affecting fatigue performance. The author notes that assessing fatigue limit in the presence of a defect is indeed a challenging task where many questions are not yet answered. Including those issues of interest named the local material behaviour near defects, which may be not only elastic but also plastic, which is considered in limited research on structures weakened by defects.

The influence of single defects on the stress-strained state of structures has been studied extensively both for surface and internal defects. However, it is obvious that real materials may contain several defects, which, being in close proximity, begin to interact with each other. In particular, defects caused by production activities, namely casting defects or welding defects, corrosion pits, surface roughness, micro inclusions, dislocations, are often located close together, which leads to interaction of fields of stresses and significantly reduces the strength limit of the material [6,15].

In [3,16,17] it is noted that corrosion pits on the surface of steels and aluminum alloys have a complex shape, where the main and secondary pitting at the bottom can be conditionally distinguished. Studies carried out on the modelling of stress-deformed structures containing one corrosion defect of such a complex shape show that the influence of the additional pitting leads to a significant increase in the stress concentration coefficient [16-18].

It is worth mentioning that in situations where the defects are located in close proximity to each other, it is very difficult to determine the actual size and form of damage [11,19]. That is why research designed to find simplified forms that could approximate such complex forms of defects or sets of defects is extremely relevant. Such simplified forms are utilized in a few papers for a variety of problems, where they are usually called "equivalent" forms for the considered complex-shaped surface or internal defects or "equivalent" defects, e.g. [11,20,21].

In [22] a cluster of surface defects is approximated by a rectangle to determine the ultimate strength of a plate with randomly distributed defects. More complex approach which may be considered as multiple equivalent rectangles is used in [23]. Simplified conical, cylindrical and spherical shapes of pits are used [24] to numerically assess the ultimate strength of hull structural plate with multiple local corrosion defects. Rounded rectangles are also utilized to approximate complex-form defects or set of defects [21,25,26]. Note that in papers [21,25,26], where the defects are simplified by rounded rectangles, the rounded edge serves for avoiding singularities in finite element analysis, yet the possible effect of the different values of the rounding radius is not studied. Authors of [24,27,28] showed that the form of defects (circular, conical, elliptical or cylindrical) has a slight effect on strength of plates under different loading. However, in the mentioned papers neither the effect of varying sizes of the defect with rounded rectangle form nor the influence of complex forms of defects are not considered.

Experimental and numerical research for aluminum alloy under cyclic load is conducted in [20]. Spherical and three types of complex form artificial defects were introduced in specimens. Fatigue test results were complemented by finite element analysis conducted for geometries with two types of equivalent defect forms: spherical and elliptical. Simulations performed with elliptical defects provided better correspondence with experimental results. The possible reason for that might be that the elliptical defects account for the orientation of the defect which is extremely important for fatigue life prediction.

The impact of surface defect interaction is investigated in order to assess the high cycle fatique performance of aluminum alloy in [21]. Nonlinear hardening is used to describe the material behaviour under uniaxial cyclic load. The stress distribution around the cluster of three hemispherical defects on the surface of a cylindrical specimen is numerically calculated. Circumferential and longitudinal configurations of defects are considered as well as various defect sizes, distances between defects and applied loads. The numerical results obtained through the Crossland criterion are compared with experiments by Mu et. al. [29]. Additionally, authors [21] proposed substituting three interacting hemispherical surface defects with a single equivalent defect in the shape of a rounded rectangle. The calculated fatigue limit of the model with the equivalent defect is compared with the fatigue limit of the model with three interacting defects. It is concluded that the fatigue limit of specimens with the cluster of defects can be estimated by the finite analysis of the model with the single equivalent defect. The authors report that the fatique limit obtained using the equivalent defect is greater than with three interacting hemispherical defects, with the difference being within 7%. However, it remains unexplored whether the equivalent defect sizes proposed in [21] are optimal, and whether the suggested method can be applied to estimate the fatigue limit when defects are of complex forms [3,16,17]. These questions are addressed in the present paper.

In this paper, the fatigue life of a specimen made of aluminum alloy is assessed. Fatigue life is determined by the SN curve method. The specimen is weakened by a cluster of surface defects. Three hemispherical defects and three defects of a complex shape, where the main and secondary hemispherical pitting at the bottom can be conditionally distinguished, are considered. The defects are located in close proximity to each other so that the interaction of stress fields takes place. Three models with corresponding equivalent defects that could approximate complex forms of the considered sets of defects are constructed and analyzed. The combined nonlinear isotropic and kinematic hardening model is utilized to describe the material behaviour. The mean stress correction is used to account for the effect of non-zero mean stresses.

Fatique life assessment

The most common approaches for assessing fatigue damage under cyclic loading are a stress-life approach, a strain-life approach and fracture mechanics approach [30]. In stress-life and strain-life approaches, the number of cycles to failure is represented as a function of alternating stress and mean stress, alternating stress and R-ratio (defined as a ratio of the minimum stress value to the maximum stress value), and alternating strain and mean strain, respectively [30]. In fracture mechanics approach the rates of growing cracks are analyzed to assess fatigue life [30].

72 L.A. Almazova, O.S. Sedova

The stress-life approach is used in applications where the applied stress is essentially within the elastic range, and the material has a long cyclic life. This approach is suitable when the degree of plastic straining is negligible, as in high cycle fatigue regime (HCF), where plastic strains are relatively small and concentrated in a small area. Stress-life data is usually represented by SN curve, which is either plotted as a log-linear or a log-log plot. SN curve is obtained from constant-amplitude uniaxial cyclic tests performed for a given material for different alternating stresses with the same stress ratio R. Different SN curves are therefore generated for different R-ratios. The Basquin model is widely used to determine fatigue life in terms of stress-life in the case of uniaxial loads for multi-cycle fatigue [31]. According to this model based on fatigue curves, the difference between the minimum and maximum stresses in the cycle is linearly related to the number of cycles before the destruction [32]:

$$\sigma_a N_f^b = c, (1)$$

where N_f is the number of cycles before destruction, σ_a – stress amplitude of a symmetric loading cycle, b = const – fatigue strength exponent, c = const. For the cases where mean stress is non-zero, the load amplitude needs to be corrected before using Eq. (1). The parameters b and c depend on the material properties. Numerical parameters of the Basquin model are determined by the SN curve of the alloy considered.

The strain-life approach considers the plastic deformation that may occur during fatigue loading. This method accounts for localized yielding, which is often the case in metal components corresponding to low cycle fatigue (that is a relatively short fatigue life, usually less than 10^5 cycles). In such a case, the plastic deformation of a material may take place not only in a small area near stress concentrators.

In this research, fatigue life is assessed through the stress-life approach using Basquin's relation Eq. (1).

Mean stress correction

SN curve methods are widely used to estimate fatigue life of materials under symmetrical loading conditions, i.e., where mean stress is zero. As mentioned above, by performing multiple tests it is possible to obtain the SN curves for a considered material under different mean stress conditions. It is obvious that resources for conducting experiments are quite limited, or it may be impossible to create the necessary conditions. Thus, the case with a zero mean stress has become the one that has been most studied experimentally. Whereas, when the magnitude of loading in both directions is different, mean stress value plays a vital role in fatigue life estimation [33-35]. None-zero mean stress may decrease or increase the estimated life depending on parameters of a problem [35]. There are variety of models for the mean stress correction developed for different materials and conditions, e.g. [36-38]. Such models allow one to use the data from experiments with zero mean stress for a case where the mean stress is non-zero. The mean stress correction essentially provides the stress amplitude called equivalent amplitude (with zero mean stress) which results in the same fatigue damage as the given non-symmetric stress amplitude (with non-zero mean stress). By means of equivalent amplitude fatique life is assessed. Some of the common mean stress correction methods are the Coffin-Mason relationship [39], Morrow's mean stress approach [40] and the Smith, Watson and Topper [41]. A new model to account for the mean stress is proposed and found to be valid for different materials in [42].

One of the widely used mean stress corrections is Goodman equation [43] that is generally suitable for brittle materials [44]:

$$\frac{\sigma_a}{\sigma_{ar}} + \frac{\sigma_m}{\sigma_u} = 1,\tag{2}$$

where σ_a – is the stress amplitude, σ_m – mean stress, σ_u – ultimate tensile strength. That used to solve for σ_{ar} – equivalent amplitude of a corresponding symmetric cycle.

Smith-Watson-Topper (SWT) mean stress correction is a good choice for general use and quite accurate for aluminum alloys [41,45,46]:

$$\sigma_{ar} = \sigma_{max} \sqrt{\frac{1-R}{2}},$$
 where $\sigma_{max} = \sigma_m + \sigma_a.$ (3)

Problem formulation

The cylindrical sample of aluminum alloy either with a cluster of three corrosion defects or with a single equivalent defect is considered under HCF regime. The load conditions are assumed to be uniaxial tension-compression with R = 0.1. The problem is to numerically assess the fatigue life of a sample for various load values and different defect shapes. Mean stress correction is made by Goodman theory (Eq. (2)). The distribution of von Mises stress under static uniaxial tension is also analyzed.

Material

The paper considers the alloy AS7G06 with T6 post-thermal treatment. The chemical composition are shown in the Table 1 [29].

Table 1. Chemical composition of AS7G06

Element	Si	Mg	Fe	Cu	Mn	Ni	Zn	Pb	Ti
%	7.00	0.56	0.097	<0.015	<0.03	<0.01	<0.01	<0.003	0.13

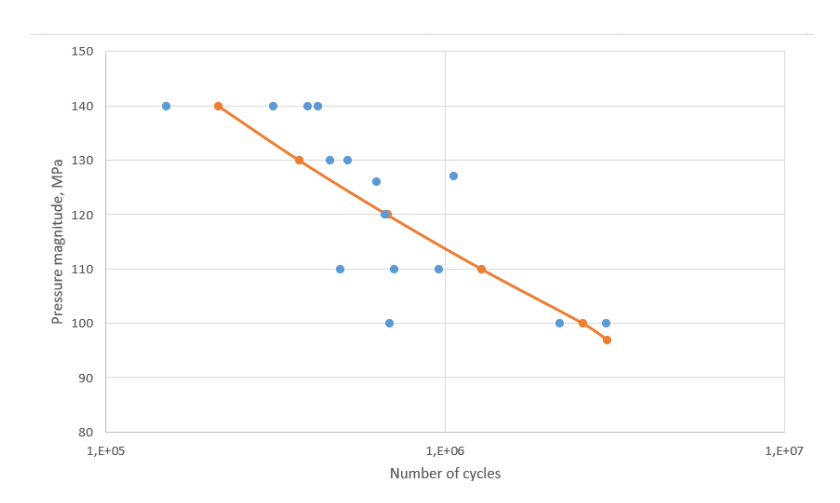


Fig. 1. SN curve for AS7G06: blue dots correspond to experimental results [29], orange curve results from fitting a set of data points with a quadratic function

74 L.A. Almazova, O.S. Sedova

The material parameters are specified in the ANSYS Workbench package in the Engineering Data section. The material behavior is described by a model with a combined nonlinear isotropic and kinematic hardening implemented in ANSYS Workbench.

Moreover, SN curve for the considered material (Fig. 1) obtained in [29] was used to find numerical parameters needed for fatigue life estimation.

Model

The geometric model was built in the ANSYS SpaceClaim package. The elementary model in question is a cylinder corresponding to the gauge part of the experimental samples either with a cluster of surface defects or with a single equivalent defect. Cylinder has a diameter 10 mm and length 20 mm. Five geometries with differently shaped defects have been constructed:

- 1. A sample with three hemispherical defects (Fig. 2(a)). All hemispherical defects are equal to each other, their radii are set to r_m = 0.32 mm. The distance between defects equals 0.1 mm.
- 2. A sample with three defects of a complex form: every defect consists of the main defect and a secondary damage at the bottom of the main one (Fig. 2(b)). Both the main and secondary damage are of a hemispherical form. All main defects are equal to each other, their radii are set to $r_m = 0.32$ mm. The distance between main defects equals 0.1 mm. All secondary defects are equal to each other and have a radius $r_s = 0.08$ mm.
- 3. A sample with one equivalent defect to approximate geometry (i). The defect is modeled as a rectangle cut with a rounded edge. The rectangle dimensions are length = $6r_m$, width = $2r_m$ and height = $\frac{r_m}{2}$, the radius of curvature of a rounded edge is $0.1r_m$.
- 4. A sample with one equivalent defect to approximate geometry (i) (Fig. 2(c)). The defect is modeled as a rectangle cut with a rounded edge. The rectangle dimensions are length = $6r_m$, width = $2r_m$ and height = $\frac{r_m}{4}$, the radius of curvature of a rounded edge is $0.1r_m$.
- 5. A sample with one equivalent defect to approximate geometry (ii) (Fig. 2(d)). The defect is modeled as a rectangle cut with a rounded edge. The rectangle dimensions are length = $6r_m$, width = $2r_m$ and height = $r_m + r_s$, the radius of curvature of a rounded edge is $0.1r_m$.

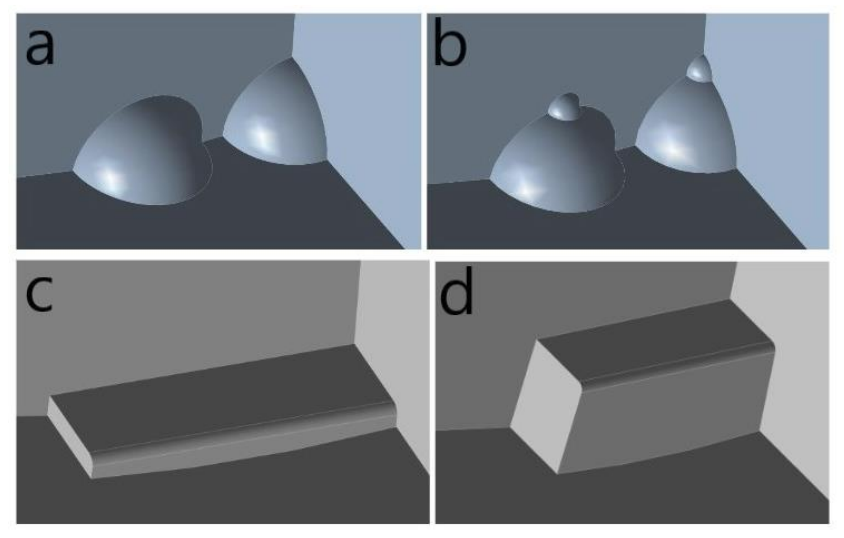


Fig. 2. Geometries with differently shaped defects

Due to symmetry, only a one fourth part of each of the considered models was constructed (see Fig. 3). It should be noted that sizes in geometry descriptions (i-v) are given for the whole elementary models. Consequently, in constructed parts with the equivalent defect (iii -v), the length and width of the defect are $3r_m$ and r_m , respectively. The height of the equivalent defect in one fourth part of each of the considered models (iii -v) remains as indicated above.

The constructed geometric models have the following boundary conditions: on the cross-section corresponding to the boundary of the gauge part of the sample, the force corresponding to the amplitude in cyclic tests is applied; the symmetry condition ("frictionless support" condition in ANSYS Workbench) acts on the cross-section planes of the quarter of the model (planes a and b in Fig. 3).

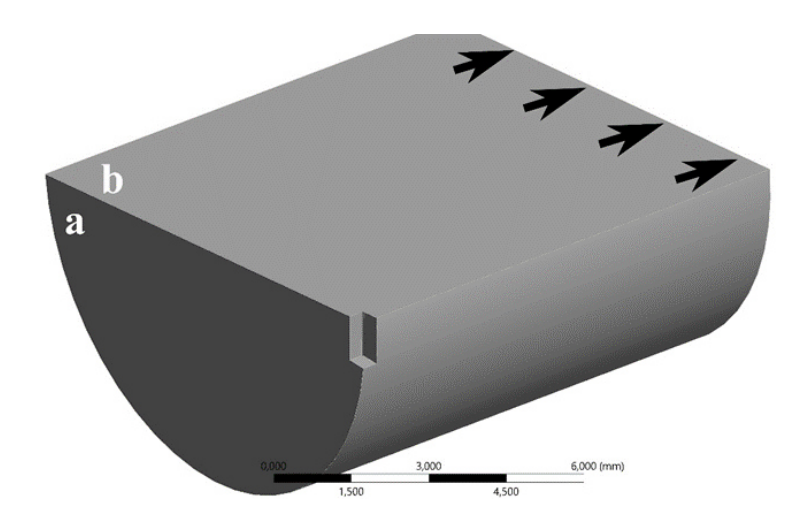


Fig. 3. A geometrical model with the equivalent-form defect: a, b – the planes with symmetry condition; arrows indicate the plane of load application and direction

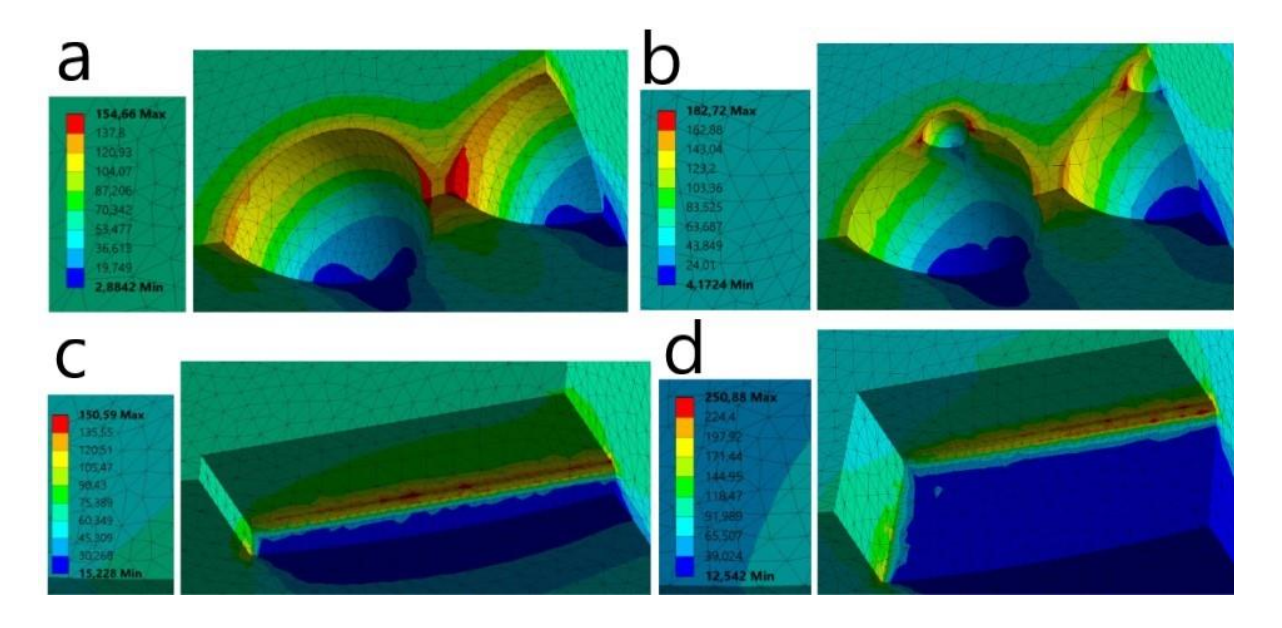


Fig. 4. Stress distribution for constructed geometries (stress values are given in MPa)

76 L.A. Almazova, O.S. Sedova

To use the finite element method, a tetrahedron mesh was constructed. Moreover, since the vicinity of the defects is a probable place of stress concentration, the face sizing method was additionally applied to the surface of the defects, allowing to set a fine grid in the specified areas (Fig. 4).

The mesh convergence study was carried out in order to ensure the accuracy of solution. With various finite element meshes, several static analysis simulations for geometry with three surface defects of a complex form (geometry (ii)) were conducted. Figure 5 shows the maximum von Mises stress corresponding to the number of elements in a certain mesh. It was found that for meshes with the number of elements over 10^6 the relative differences between results of considered simulations is less than 4 %. Therefore, for further analysis the number of elements was approximately 1.2×10^6 .

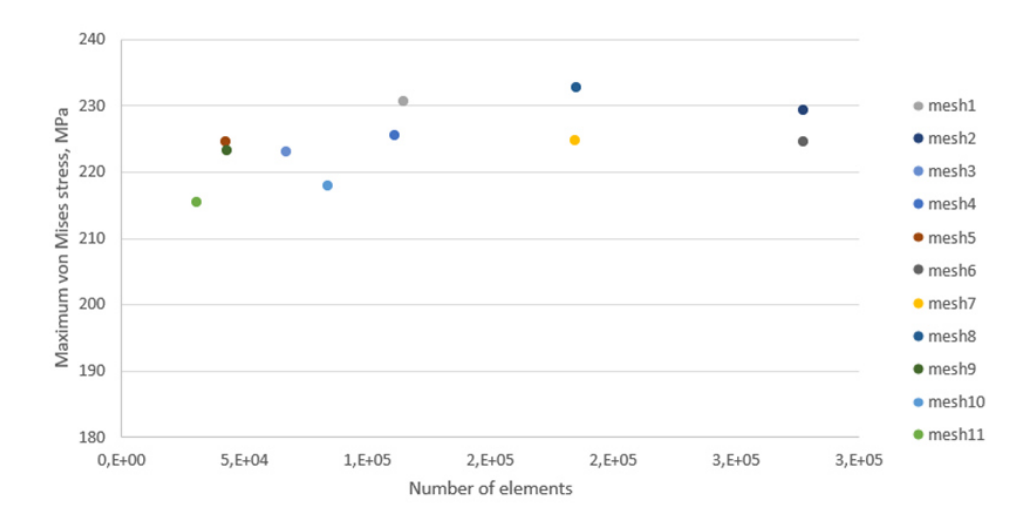


Fig. 5. Mesh convergence of maximum von Mises stress obtained with different meshes

Results

Stress distributions near the local defects for the set of geometries in question are presented in Fig. 4 for the applied static load equal to 60 MPa. They clearly demonstrate that for geometries with a cluster of three pits (i) and (ii) (Fig. 4(a,b), respectively) a significant increase in the value of the von Mises stress is observed in the presence of the secondary damage (geometry (ii), Fig. 4(b)). Note that in the case of defects of a complex shape (Fig. 4(b)), the maximum stress values are reached at the joint of the secondary defects with the main ones. For geometry (i) with three defects of a hemispherical form (without a secondary damage), the maximum of the von Mises stress is achieved at the sharp edges between the defects (Fig. 4(a)). This result is in accordance with [21,48,49].

From Fig. 4 it is seen that the difference between maximum stress values in a sample with three hemispherical pits (i, Fig. 4(a)) and a sample with equivalent defect (iv, Fig. 4(c)) is below 3 %. While the difference between values of maximum stress obtained in geometry (ii, Fig. 4(b)) with a cluster of complex-shaped pits and the geometry (v, Fig. 4(d)) with the equivalent defect is over 30 % for a considered load. Therefore, the equivalent defect (iv) provides a good approximation of a cluster of hemispherical pits (i) in terms of prediction of stress values for static analysis (Figs. 4(a,c)). At the same time, none of the considered equivalent defects (iii -v) allows to estimate the stress values near

a cluster of complex-shaped pits (ii) for static analysis. It should be noted that the difference between results obtained for a sample with three hemispherical pits (i, Fig. 4(a)) and for the equivalent defect (iii) is sufficiently more than 3 %.

The dependencies of calculated fatigue life values of constructed models (i-v) from values of applied loads at R = 0.1 with the Goodman mean stress correction (Eq. (2)) are shown in Fig. 6. It can be seen that the maximum life of geometries considered coincides, but in the case of defects of a complex shape (geometry (ii), solid orange curve) it is achieved at a maximum load of 60 MPa, while for geometry with defects of a hemispherical form without a secondary damage (geometry (i), solid blue curve) the maximum value of fatigue life is maintained up to a load of 90 MPa. In this case, the maximum load at which a structure with secondary damages (geometry (ii)) does not undergo instantaneous destruction reaches 60 MPa when for the second model (geometry (i)), it reaches 90 MPa. Thus, the presence of a secondary defect at the bottom of the main one causes a significant decrease in strength. Note that in contrast to steel and titanium alloys, aluminum alloys do not have a distinct fatigue limit. Consequently, aluminum specimens are susceptible to fatigue failure, even under minimal stress amplitudes.

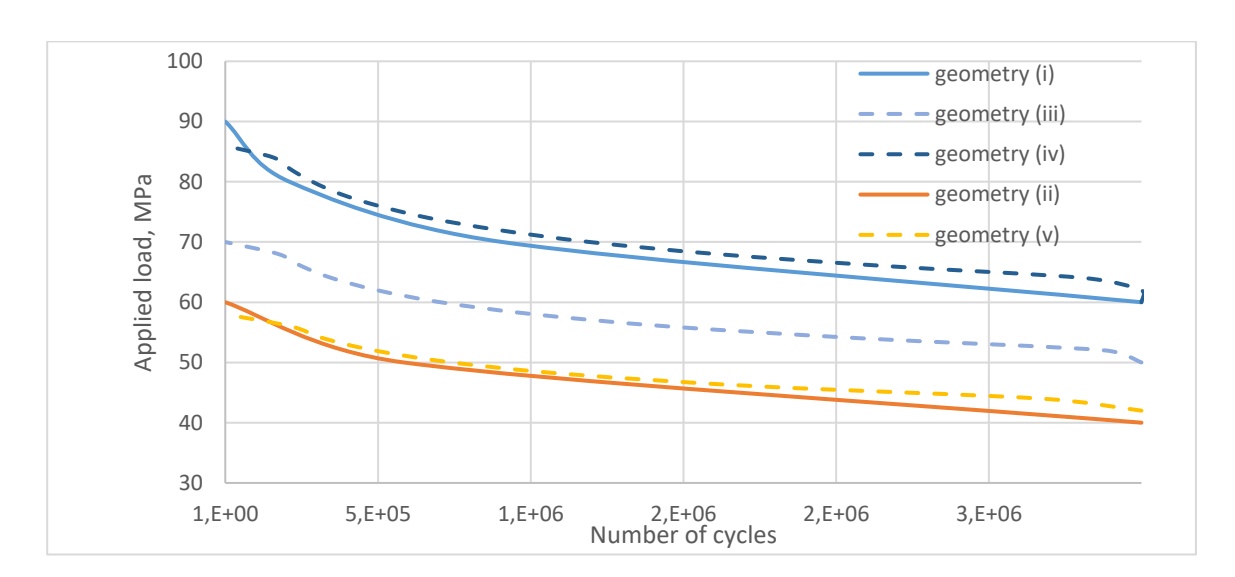


Fig. 6. Dependence of fatigue life from values of applied loads

It is seen from Fig. 6 that the curves for geometries (i) and (iv), (ii) and (v) are close to each other for all considered applied loads. However, the analysis of results showed that for a fixed load value the estimated lifetimes between geometries (i) and (iv) may reach 40 %. This difference grows with the growing applied load. For loads under 66 MPa the difference is less than 30 %. In the same way the difference between the estimated fatigue lifetimes between geometries (ii) and (v) grows as load grows, reaching 33 % at 56 MPa. For loads under 48 MPa the difference is less than 26%.

Thus, the geometries with equivalent defects (iv) and (v) provide overestimated values of calculated fatigue lifetimes up to 40 and 33 %, respectively, compared with the results of lifetimes obtained using geometries with pit clusters (i) and (ii).

78 L.A. Almazova, O.S. Sedova

Conclusions

In the paper a cylindrical sample of aluminum alloy either with a cluster of surface defects or with a single equivalent defect is considered at high cycle fatigue regime under uniaxial tension-compression load with ratio R = 0.1. Using ANSYS Workbench the fatigue life of a sample for various load values and different defect shapes is numerically assessed. Goodman mean stress correction is performed to account for non-zero mean stress. The distribution of von Mises stress under static uniaxial tension is also analyzed for different defect shapes.

It was found that the equivalent defect may be used for prediction of stress values for a specimen with a cluster of three hemispherical pits for static analysis.

It was shown that the form of surface pits plays significant role for the calculated fatigue life. Complex form of surface defects reduces fatigue strength.

The error of modelling a cluster of three pits by a single equivalent defect grows with the growing applied load for both considered shapes of pits. The assessment of fatigue life of locally corroded specimens through a single equivalent defect may provide overestimated values of fatigue lifetimes up to 40 % for a cluster of three hemispherical pits and up to 33 % for a cluster of three complex-shaped pits.

References

- 1. Wang QG, Crepeau PN, Davidson CJ, Griffiths JR. Oxide films, pores and the fatigue lives of cast aluminum alloys. *Metallurgical and Materials Transactions*. 2006;37(B): 887–895.
- 2. Biswal R, Zhang X, Syed AK, Awd M, Ding J, Walther F, Williams S. Criticality of porosity defects on the fatigue performance of wire + arc additive manufactured titanium alloy. *International Journal of Fatigue*. 2019;122: 208–217.
- 3. Genel K, Demirkol M, Gülmez T. Corrosion fatigue behaviour of ion nitrided AISI 4140 steel. *Materials Science and Engineering*. 2000;288(1): 91–100.
- 4. Co NEC, Burns JT. Effects of micro-scale corrosion damage features and local microstructure on fatigue crack initiation location. *International Journal of Fatigue*. 2021;150: 106301.
- 5. Fabas A, Monceau D, Doublet S, Put AR. Modelling of the kinetics of pitting corrosion by metal dusting. *Corros. Sci.* 2015;98: 592–604.
- 6. Murakami Y. Metal Fatique: Effects of Small Defects and Nonmetallic Inclusions. Chennai. Academic Press. 2019.
- 7. Wang ML, Yang XG, Li B, Shi DQ, Miao GL, Guo SQ, Fan YS. The dominant role of defects on fatigue behaviour of a SLM Ni-based superalloy at elevated temperature. *International Journal of Fatigue*. 2023;176: 107894.
- 8. Yang L, Cai P, Xu Z, Jin Y, Liang C, Yin F, Zhai T. A 3-D model for quantification of fatigue weak-link density and strength distribution in an A713 cast aluminum alloy. *International Journal of Fatigue*. 2017;96: 185–195.
- 9. Wu X, Schlangen E, van der Zwaag S. Linking porosity to rolling reduction and fatigue lifetime of hot rolled AA7xxx alloys by 3D X-ray computed cosmography. *Adv. Eng. Mat.* 2012;14(7): 457–463.
- 10. Serrano-Munoz I, Buffiere JY, Verdu C, Gaillard Y, Mu P, Nadot Y. Influence of surface and internal casting defects on the fatigue behaviour of A357-T6 cast aluminium alloy. *International Journal of Fatigue*. 2016;82: 361–370.
- 11. Yamashita Y, Murakami T, Mihara R, Okada M, Murakami Y. Defect analysis and fatigue design basis for Nibased Superalloy 718 manufactured by selective laser melting. *International Journal of Fatigue*. 2018;117: 485–495. 12. Pineau A, Antolovich S. D. Probabilistic approaches to fatigue with special emphasis on initiation from
- inclusions. *International Journal of Fatigue*. 2016;93: 422–434.

 13. Fan J, McDowell DL, Horstemeyer MF, Gall K. Cyclic plasticity at pores and inclusions in cast Al Si alloys.
- Engineering Fracture Mechanics. 2003;70(10): 1281–1302.

 14. Nadot Y. Fatigue from Defect: Influence of Size, Type, Position, Morphology and Loading. *International Journal of Fatigue*. 2022;154: 106531.
- 15. Leitner M, Murakami Y, Farajian M, Remes H, Stoschka M. Fatigue Strength Assessment of Welded Mild Steel Joints Containing Bulk Imperfections. *Metals*. 2018;8(5): 306.

- 16. Cerit M, Genel K, Eksi S. Numerical investigation on stress concentration of corrosion pit. *Engineering Failure Analysis*. 2009;16(7): 2467–2472.
- 17. Zhao W, Huang YF, Ye XB, Hu BR, Liu JZ, Chen LJ. Correlation between the Geometric Parameters of Corrosion Pit and Stress Concentration Factor. *Applied Mechanics and Materials*. 2013;327: 156–160.
- 18. Cerit M. Corrosion pit-induced stress concentration in spherical pressure vessel. *Thin-Walled Structures*. 2019;136: 106–112.
- 19. Beretta S, Romano S. A comparison of fatigue strength sensitivity to defects for materials manufactured by AM or traditional processes. *International Journal of Fatigue*. 2017;94: 178–191.
- 20. Rotella A, Nadot Y, Piellard M, Augustin R, Fleuriot M. Influence of defect morphology and position on the fatigue limit of cast Al alloy: 3D characterization by X-ray microtomography of natural and artificial defects. *Materials Science and Engineering: A.* 2020;785: 139347.
- 21. Ben Ahmed A, Nasr A, Bahloul A, Fathallah R. The impact of defect morphology, defect size, and SDAS on the HCF response of A356-T6 alloy. *The International Journal of Advanced Manufacturing Technology*. 2017;92(1): 1113–1125.
- 22. Ok D, Pu Y, Incecik A. Computation of ultimate strength of locally corroded unstiffened plates under uniaxial compression. *Marine Structures*. 2007;20(1–2): 100–114.
- 23. Khedmati MR, Nouri ZHME. Analytical simulation of nonlinear elastic plastic average stress average strain relationships for un-corroded/both-sides randomly corroded steel plates under uniaxial compression. *Thin-Walled Structures*. 2015;86: 132–141.
- 24. Zhang Y, Huang Y, Zhang Q. Ultimate strength of hull structural plate with pitting corrosion damnification under combined loading. *Ocean Engineering*. 2016;116: 273–285.
- 25. Tee KF, Wordu AH. Burst strength analysis of pressurized steel pipelines with corrosion and gouge defects. *Eng. Fail. Anal.* 2020;108: 104347.
- 26. Gao J, Yang P, Li X, Zhou J, Liu J. Analytical prediction of failure pressure for pipeline with long corrosion defect. *Ocean Eng.* 2019;191: 106497.
- 27. Zhao Z, Zhang H, Xian L, Liu H. Tensile strength of Q345 steel with random pitting corrosion based on numerical analysis. *Thin Wall. Struct.* 2020;148: 106579.
- 28. Huang Y, Zhang Y, Liu G, Zhang Q. Ultimate strength assessment of hull structural plate with pitting corrosion damnification under biaxial compression. *Ocean Eng.* 2010;37(17–18): 1503–1512.
- 29. Mu P, Nadot Y, Serrano-Munoz I, Chabod A. Influence of complex defect on cast AS7G06-T6 under multiaxial fatigue loading. *Engineering Fracture Mechanics*. 2014;123: 148–162.
- 30. Dowling NE. A Review of Fatigue life Prediction Methods. SAE International. 1987;96(3): 1117–1138.
- 31. Bonnand V, Chaboche JL, Cherouali H, Kanoute P, Ostoja-Kuczynski E, Vogel F. Investigation of multiaxial fatigue in the prospect of turbine disc applications: Part II, Fatigue criteria analysis and formulation of a new combined one. In: *Proc. 9th Int. Conf. of Multiaxial Fatigue and Fracture (ICMFF9)*. Parma, Italy; 2010. p.691–698.
- 32. Schijve J. (eds.) *Fatigue of Structures and Materials*. Dordrecht: Springer; 2009.
- 33. Kumbhar SV, Tayade RM. A case study on effect of mean stress on fatigue life. *International Journal of Engineering Development and Research*. 2014;2(1): 304–308.
- 34. Bader Q, Kadum E. Mean stress correction effects on the fatigue life behavior of steel alloys by using stress life approach theories. *Int. J. Eng. Technol.* 2014;10: 50.
- 35. Böhm M, Kluger K, Pochwała S, Kupina M. Application of the SN curve mean stress correction model in terms of fatigue life estimation for random torsional loading for selected aluminum alloys. *Materials*. 2020;13(13): 2985.
- 36. Dowling NE. Mean stress effects in stress-life and strain-life fatigue. SAE International. 2004;32(12): 1004–1019.
- 37. Ince A. A mean stress correction model for tensile and compressive mean stress fatigue loadings. *Fatigue & Fracture of Engineering Materials & Structures*. 2017;40(6): 939–948.
- 38. Zhu SP, Lei Q, Huang HZ, Yang YJ, Peng W. Mean stress effect correction in strain energy-based fatigue life prediction of metals. *International Journal of Damage Mechanics*. 2017;26(8): 1219–1241.
- 39. Manson SS, Halford GR. Practical implementation of the double linear damage rule and damage curve approach for treating cumulative fatigue damage. *International Journal of Fracture*. 1981;17(2): 169–192.
- 40. Morrow J. Fatique properties of metals. In: Section 3.2, Fatique Design Handbook. Society of Automotive Engineers. 1968; AE-4.
- 41. Ince A, Glinka G. A modification of Morrow and Smith Watson Topper mean stress correction models. *Fatique Fracture Engineering Material Structure*. 2011;34(1) 854–867.
- 42. Liu Y, Paggi M, Gong B, Deng C. A unified mean stress correction model for fatigue thresholds prediction of metals. *Engineering Fracture Mechanics*. 2020;223: 106787.
- 43. Goodman J. *Mechanics applied to engineering*. Longmans, Green; 1919.
- 44. Smith JO. The Effect of Range of Stress on the Fatigue Strength of Metals. Bulletin. 1942;334: 7-47.

80 L.A. Almazova, O.S. Sedova

45. Smith KN, Watson P, Topper TH. A Stress-Strain Function for the Fatigue of Metals. *Journal of Materials*. 1970;5(4):767–778.

- 46. Papuga J, Vízková I, Lutovinov M, Nesládek M. Mean stress effect in stress-life fatigue prediction reevaluated. *MATEC Web Conf.* 2018;165: 10018.
- 47. Sun J, Cheng YF. Modeling of mechano-electrochemical interaction between circumferentially aligned corrosion defects on pipeline under axial tensile stresses. *J. Petrol. Sci. Eng.* 2021;198: 108160.
- 48. Liao Y, Liu C, Wang T, Xu T, Zhang J, Ge L. Mechanical behavior analysis of gas pipeline with defects under lateral landslide. *Journal of Mechanical Engineering Science*. 2021;235(23): 6752–6766.
- 49. Almazova LA, Sedova OS. Simulation of the surface defects influence on the aluminum alloy behaviour under the cyclic load conditions. *Frontier Materials & Technologies*. 2022;1: 7–14. (In Russian)

About Authors

Liana A. Almazova 🗓 Sc

Researcher (St. Petersburg State University, St. Petersburg, Russia)

Olga S. Sedova 🗓 Sc

Candidate of Physical and Mathematical Sciences Associate Professor (St. Petersburg State University, St. Petersburg, Russia)

Accepted: February 6, 2024

Submitted: November 29, 2023

Revised: December 12, 2023

Microstructure, mechanical properties and heat resistance of AL30 piston alloy produced via electromagnetic casting

M.Yu. Murashkin ^{1 \to 1}, L.I. Zainullina ¹, M.M. Motkov ², A.E. Medvedev ¹,

V.N. Timofeev ², D N.A. Enikeev ^{1,3}, D

ABSTRACT

The paper explores the microstructure, mechanical properties and heat resistance of the piston alloy AL30 (AK12MMqN) for the first time produced via continuous casting into an electromagnetic mold (electromagnetic casting, EMC). The study demonstrates that casting into EMC allows for the formation of a homogeneous dispersed microstructure in both the peripheral and central zones of the ingot, consisting of a blend of aluminum's solid solution and eutectic, which contains lamellar silicon (Si). The volume fraction of compact primary Si particles does not exceed 1 %. In addition to Si, the aluminum matrix contains the phases of crystallization origin such as ε-Al₃Ni, π-Al₈FeMg₃Si₆, Q-Al₄Cu₂MgSi₇ and S-Al₂CuMg. The analysis of the evolution of microstructure and properties of a cast alloy after conventional heat treatment (HT) reveals that microstructural changes induced by HT lead to the AL30 alloy having mechanical properties that far exceed the properties of its counterparts obtained through traditional casting methods. The research analysis shows that mechanical properties and heat resistance of the AL30 alloy produced via EMC with subsequent T6 treatment are comparable to the deformable piston alloys such as the AK12D alloy after similar heat treatment.

KEYWORDS

piston aluminum alloy • electromagnetic casting • heat treatment • microstructure• phase composition mechanical properties • heat resistance

Acknowledgements. M.Yu.M, L.I.Z. and N.A.E. acknowledge the support from the Russian Ministry of Science and *Higher Education (state assignment FEUE-2023-0007).*

Citation: Murashkin MYu, Zainullina LI, Motkov MM, Medvedev AE, Timofeev VN, Enikeev NA. Microstructure, mechanical properties and heat resistance of AL30 piston alloy produced via electromagnetic casting. *Materials Physics and Mechanics*. 2024;52(1): 81–94. http://dx.doi.org/10.18149/MPM.5212024 9

Introduction

Most of the pistons for internal combustion (IC) engines are made of special heat-resistant aluminum piston alloys [1,2]. For example, in Russian Federation, the commonly used materials for pistons produced by permanent mold casting are the eutectic modifications of silumin alloys such as AL25(AK12M2MqN) and AL30(AK12MMqN), which after hardening heat treatment T6 (following the national standard GOST 1583-93 [3]) have the room-temperature strength in the range of 195-235 MPa [1,4]. Likewise, engine pistons abroad are generally manufactured from the M124 alloy (AlSi12CuMgNi), which is similar in chemical composition and properties to the materials produced in Russian

© M.Yu. Murashkin, L.I. Zainullina, M.M. Motkov, A.E. Medvedev, V.N. Timofeev, N.A.Enikeev, 2024. This is an open access article under the CC BY-NC 4.0 license (https://creativecommons.org/li-censes/by-nc/4.0/)

¹ Ufa University of Science and Technology, Ufa, Russia

² Siberian Federal University, Krasnoyarsk, Russia

³ Saint Petersburg State University, Saint Petersburg, Russia

m.murashkin.70@gmail.com

Federation [2]. Following the need to make the IC engines, and therefore their pistons, substantially more efficient, one of the timely research trends in this field deals with increasing the mechanical and service properties of silumin piston alloys. Due to the fact that strength, ductility and heat resistance are structure-dependent features, nowadays, much attention is focused on the formation of microstructure in piston materials, which will ensure the maximum level of properties. As is known, decreasing dendritic cell size of the aluminum solid solution, as well as the refinement of the second phases included in the eutectic may result in a higher complex of properties of cast alloys [2,5]. Nowadays, such changes in microstructure are achieved by modifying the alloy composition during casting [1,2,6–9], by using casting or powder metallurgy techniques that ensure high crystallization rates [10–12], by using various types of heat [13] and deformation treatments [14,15], including severe plastic deformation [16–18].

Recently, much attention has been focused on the fabrication of semifinished products from aluminum alloys in the form of bars of small cross-section (diameter from 8 to 12 mm) by continuous electromagnetic casting method (EMC). During EMC, intensive melt circulation in the region of ingot crystallization is implemented, which promotes the formation of a homogeneous microstructure throughout its volume, and the high cooling rate (10^3 - 10^5 K/s) ensures the formation of highly dispersed cast structures [19-22]. In addition, high cooling rate during crystallization leads to abnormal supersaturation of aluminum with alloying elements [19,20]. All the above-listed microstructural features of cast rods produced by EMC favorably influences their mechanical and service properties after various deformation or deformation-thermal treatments [19-22]. As was demonstrated recently in the work [23] on the example of the formation of the solid solution in the Al-Zn-Mg-Ca-Fe system alloy, the EMC method may be used to produce bulk cylindrical billets with a homogeneous structure in which the dendritic cell size is less than $10~\mu m$ and the second phases are less than $3~\mu m$ in size.

Herein, we study the microstructure features, mechanical properties and heat resistance of a solid cast rod from piston alloy AL30, that was for the first time produced through casting in EMC subsequently conventionally hardened by heat treatment.

Materials and Methods

The experiments were conducted on the AL30 (AK12MMgN) alloy bar with a diameter of 80 mm obtained by continuous casting in EMC at the Research and Production Center of Magnetic Hydrodynamics Ltd [24]. The alloy was produced on the basis of primary aluminum grade A85 (not less than 99.85 wt. % Al), silicon grade KR00 (not less than 99.41 wt. % Si), magnesium grade MG-95 (not less than 99.95 wt. % Mg), copper grade M00k (not less than 99.9 wt. % Cu), and alloying compositions AlNi20 and AlSr10. Prior to casting, the finished melt was degassed with argon and simultaneously treated with a special flux. Continuous casting in the EMC unit was carried out at a temperature of 750 °C and rate of 5 mm/s. Chemical composition of the peripheral and central zones of the cast rod was observed using the Bruker Q4 Tasman optical emission spectrometer and is given in Table 1. As is seen, the chemical composition of the rod obtained by casting in EMC does not change from the periphery to its central zone and fully meets the requirements of the GOST 1583-93 national standard [3].

Table 1. Chemical	composition	of the allow	1 3 1 1 1 1 1 1 1 1 1 1 1 1 1 1 1 1 1 1	%)
Table 1 . Chennical	CONDUSTRION	or the attov	ALJU (WL	/01

	Si	Cu	Mg	Ni	Fe	Ti	Cr	Mn	Zn	ΣSn, Pb
Α	13.1/13.0*	1.3/1.3	1.0/1.0	1.3/1.3	0.25/0.20		<	0.2		< 0.06
В	11-13	0.8-1.5	0.8-1.3	0.8-1.3	≤0.7		\(\)	0.2	•	≤0.06

- A chemical composition of the alloy AL30 produced by electromagnetic casting
- B chemical composition of the alloy AL30 [3]
- * chemical composition of the peripheral/central zone of the cast rod

The microstructure and properties of the cast rod were examined precisely in the peripheral (the area of these parts was determined by the data of structural analysis) and central parts of the rod. The choice of such areas for study was determined by the fact that in the process of producing the cast rod by EMC, there was observed the maximum difference in the rate of material crystallization between these areas and, therefore, the different degree of dispersion of the obtained microstructure.

One part of the samples from the peripheral and central zones of the cast rod was subjected to heat treatment (HT) T1, the other part was subjected to heat treatment T6, according to the regimes recommended in [3] for the AL30 alloy. The T1 treatment included artificial aging at a temperature of $190\,^{\circ}$ C for 12 hours (without preliminary hardening). The T6 treatment included annealing at $520\,^{\circ}$ C for up to 4 hours, quenching into water and aging at $180\,^{\circ}$ C, 6 hours.

After the T6 treatment, the AL30 alloy samples were used for the examination of heat resistance according to the method introduced in [25]. The samples were annealed at a temperature of 300 °C and 100 hours of holding time. Samples of the AK12D alloy in the T6 state were subjected to similar annealing. During annealing, intermediate measurements of hardness change after 1, 3, 5, and 24 hours of exposure were made.

HT and annealing of the samples to determine the heat resistance of the alloy were carried out in a chamber furnace Nabertherm N15/65HA.

The microstructure was examined using optical microscopy (OM), scanning and transmission electron microscopy (SEM and TEM), and X-ray diffraction analysis (XRD).

OM was performed on an Olympus QX 51 microscope. SEM was performed on a Tescan Mira scanning microscope at 10-20~kV accelerating voltage. Chemical composition of the second phases was analyzed by energy dispersive X-ray spectroscopy (EDS) using the INCA X-Act installation from Oxford instruments. SEM was performed on a JEOL JEM 2100 transmission microscope at 200 kV accelerating voltage. The samples for microstructure studies were prepared by jet electrolytic polishing of thin foils on a Tenupol-5 equipment from Struers Inc. in a solution of 20 % nitric acid and 80 % methanol at \geq -20 °C and 10-20 V voltage. ImageJ software and Grain Size software package were used to process the obtained images and quantitatively analyze the microstructure features (average dendritic cell size, average section size of the second phase within the eutectic/size of second phase particles, volume fraction of particles).

X-ray diffraction analysis of the samples was performed on a Bruker D8 Discover diffractometer using the Cu-K α -radiation. The results were used to determine the phase composition and lattice period (a) of the samples in different zones of the cast rod and after HT. The a value was calculated using the Rietveld method and MAUD software [26].

Vicker's microhardness [27] was measured using an EMCO-Test DuraScan-50 device at a load of 1 H and a dwell time of 15 s.

Mechanical properties (conditional yield stress ($\sigma_{0,2}$), ultimate tensile strength (σ_{UTS}) and elongation to failure (δ_5)) after HT were determined using the results of static tensile tests, which were performed on an Instron 5982 universal testing machine in accordance with the GOST 1497-84 national standard [28].

Results and discussion

Microstructure of the alloy after casting into EMC mold and subsequent heat treatment

Typical microstructure of the AL30 alloy in the peripheral and central parts of the cast rod produced by EMC is shown in Fig. 1(a,b). The microstructure is composed of dendrites of aluminum solid solution (α_{Al}) and the eutectic, with dispersed lamellar silicon (Si) located along the α_{Al} boundaries (Figs. 2 and 3). In addition to Si, the particles that are different in color from it were noted in the eutectic. Also, a small amount of coarse compact particles of primary Si were observed in the microstructure of the cast rod - both in the peripheral and central zones (Fig. 1(a,b)).

General view of the microstructure of the AL30 alloy obtained by casting into EMC resembles the eutectic silumins produced by conventional casting methods [1,2,4–6]. However, the size of cells and of lamellar silicon included in the eutectic, especially in the peripheral zone, indicates an unusually high cooling rate of the melt during its crystallization. Quantitative evaluation of the cross-sectional area of the bar demonstrated that the microstructure, which is characteristic of the peripheral zone (Fig. 1(a)), occupies about 20 % of its total area.

The results of quantitative analysis of microstructure in the cast rod are presented in Table 2.

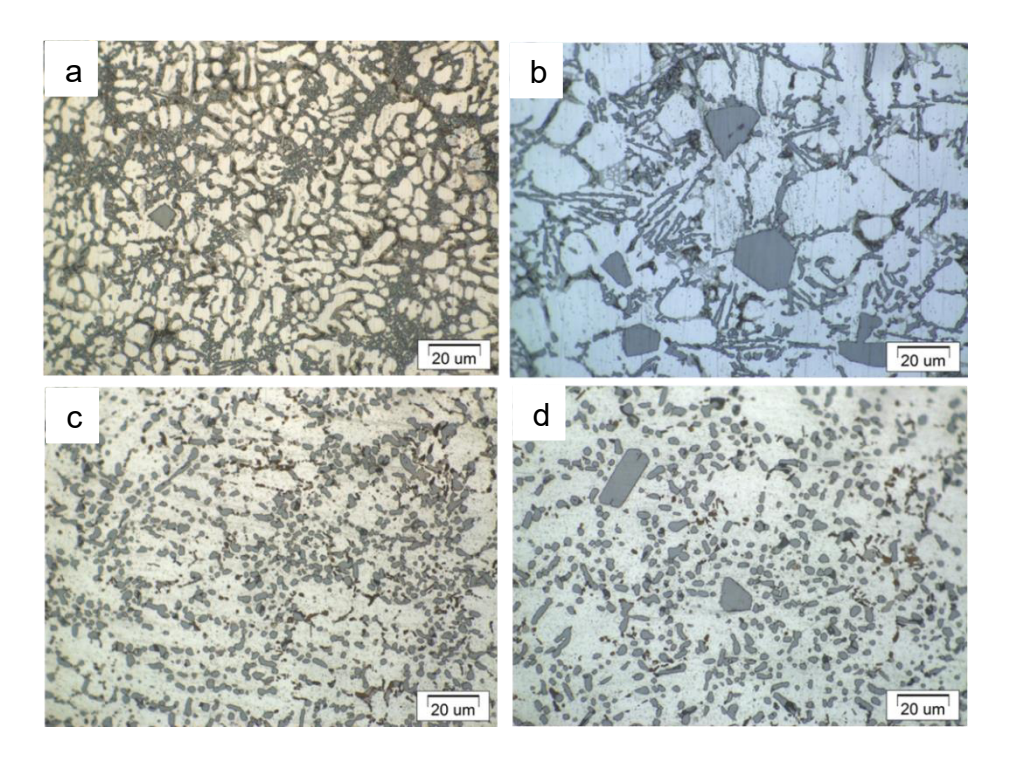


Fig. 1. Microstructure of the AL30 alloy cast rod after casting into EMC (a, b) and after T6 treatment (c, d). (a, c - peripheral zone of the rod; b, d - central zone of the rod) (OM method)

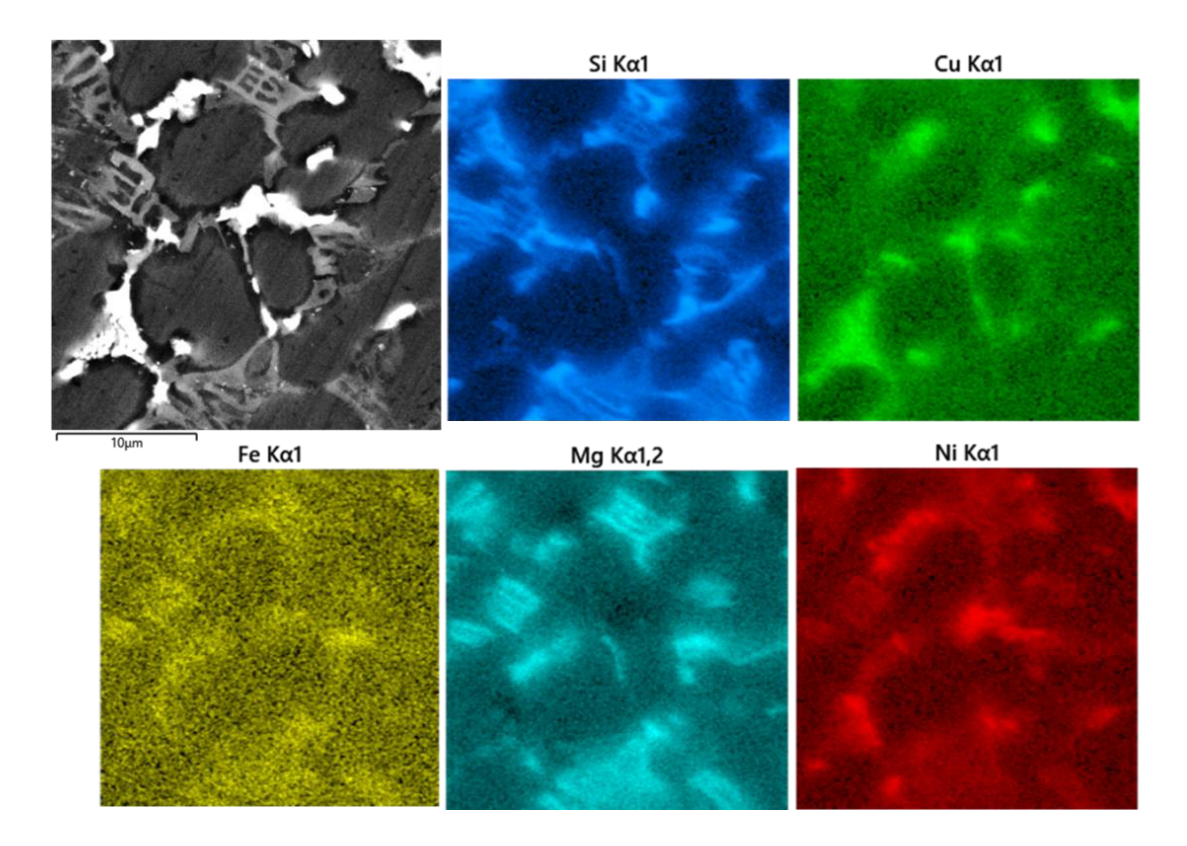


Fig. 2. Typical microstructure area in the peripheral zone of the cast rod and elemental mapping of such area (SEM)

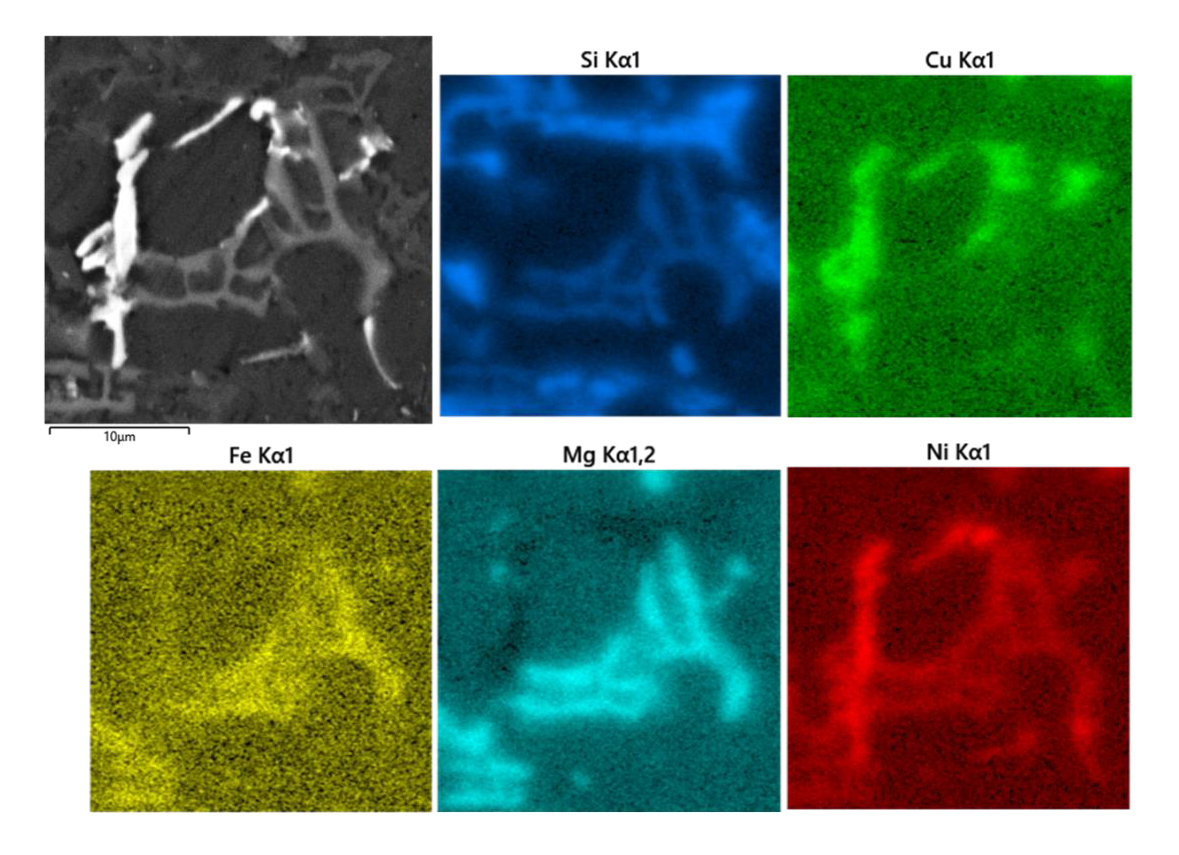


Fig. 3. Typical microstructure area in the central zone of the cast rod and elemental mapping of such area (SEM)

treatment							
State	Zone of cast rod	<i>d</i> , μm	d _{Si} , μm	<i>Q</i> _{Si} , %	<i>h</i> , μm	K_{f}	Q√, %
FMC	Periphery	7.6 ± 0.4	11.3 ± 0.5	0.3 ± 0.1	0.96 ± 0.12	-	24 ± 3
EMC	Center	16.6 ± 0.6	16.2 ± 0.4	1.1 ± 0.1	1.57 ± 0.16	-	22 ± 5
	Periphery	-	-	-	2.80 ± 0.28*	2.1	25 ± 4
Т6	Center	-	-	-	5.65 ± 1.45*	2.7	23 ± 3

Table 2. Microstructural characteristics of the alloy AL30 alloy after casting into EMC and subsequent T6 treatment

where d is an average size of dendritic cell; d_{Si} and Q_{Si} are average size and volume fraction of primary Si particles; h is average size of second phase section inside eutectic; K_f is mold ratio of second phase particles; Q_V is volume fraction of second phase particles; * average size of second phase particles

The obtained data reveals that the sizes of dendritic cells formed by α_{Al} and eutectic are more than twice smaller in the peripheral zone of the cast rod. Also in this zone, the cross-section of Si plates included in the eutectic is noticeably smaller than the crosssection of Si plates formed in the central zone. As is known, the increase in the crystallization rate (V_c) reduces not only the size of dendritic cells (d), but also the size of second phase particles [5]. At the same time, the dependence between d and V_c has a linear character on a logarithmic scale and persists up to cooling rates ≥ 108 K/s. According to this dependence, in the peripheral and central zone of the cast rod of AL30 alloy, the value V_c differs by more than an order of magnitude, constituting $\geq 10^3$ and $\leq 10^2$ K/s, respectively. It is the difference in V_c that explains the differences revealed in the microstructure (Table 2). The microstructure formed in the peripheral zone is qualitatively similar to the microstructure formed in cast billets of aluminum alloys for electrical and structural purposes, which were also obtained by casting into EMC [19-22]. The microstructure in the central zone of the cast rod is similar to the microstructure that was obtained in eutectic silumin piston alloys by casting methods, the latter providing a noticeably lower V_c [1,2,4–6]. However, considering the results of study of crystallization in a bulk rod of the alloy Al-Zn-Mq-Ca-Fe during casting into EMC, the values of V_c still remain high and may reach 600 K/s [23].

Considering the different color of particles, which is clearly visible in Figs. 1-3, the eutectic composition includes other phases in addition to Si. Distribution maps in the areas of the peripheral and central zones of the cast rod for the main alloying elements made by EDS (Fig. 2 and 3) showed the presence of Si and Mg in addition to aluminum in the dark gray plates include, and the presence of Cu, Ni and Fe in the light gray phases.

The results of X-ray phase analysis are presented in Fig. 4 and the data made it possible to determine the phase composition of the alloy. The phases ε -Al₃Ni, π -Al₈FeMg₃Si₆, Q-Al₄Cu₂MgSi₇ and S-Al₂CuMg were formed both in the peripheral and central parts of the cast rod in addition to Si during casting into EMS. The presence of these phases has been previously reported in similar silumin piston alloys [5,6,29,30].

The absence of noticeable differences in the value of lattice parameter in the peripheral and central parts of the cast rod, which constitutes 4.0487 ± 0.0001 and 4.0490 ± 0.0001 Å respectively, means that the concentration of alloying elements in α_{Al} after EMC is almost similar.

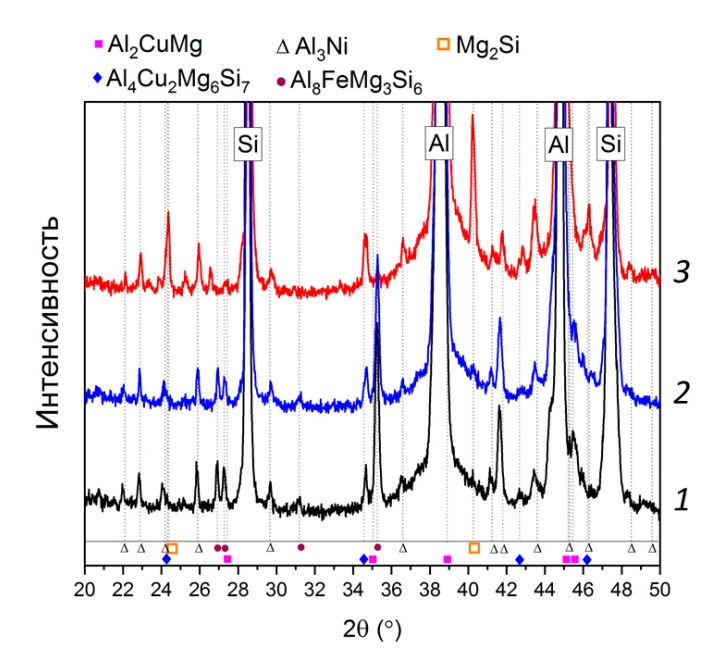


Fig. 4. X-ray profiles of the sample of AL30 alloy cast rod obtained from the peripheral (1) and central (2) zones, as well as from the central zone after T6 treatment (3) (X-ray analysis)

When T1 heat treatment was performed, the AL30 alloy samples were subjected only to artificial aging at a temperature that could not lead to significant changes in the size and morphology of the second phases [5,29]. Therefore, microstructure evolution in the cast rod was examined after T6 heat treatment. Typical images of the microstructure after such treatment in the peripheral and central parts of the rod are presented in Fig. 1(c,d), as well as in Figs. 5-7.

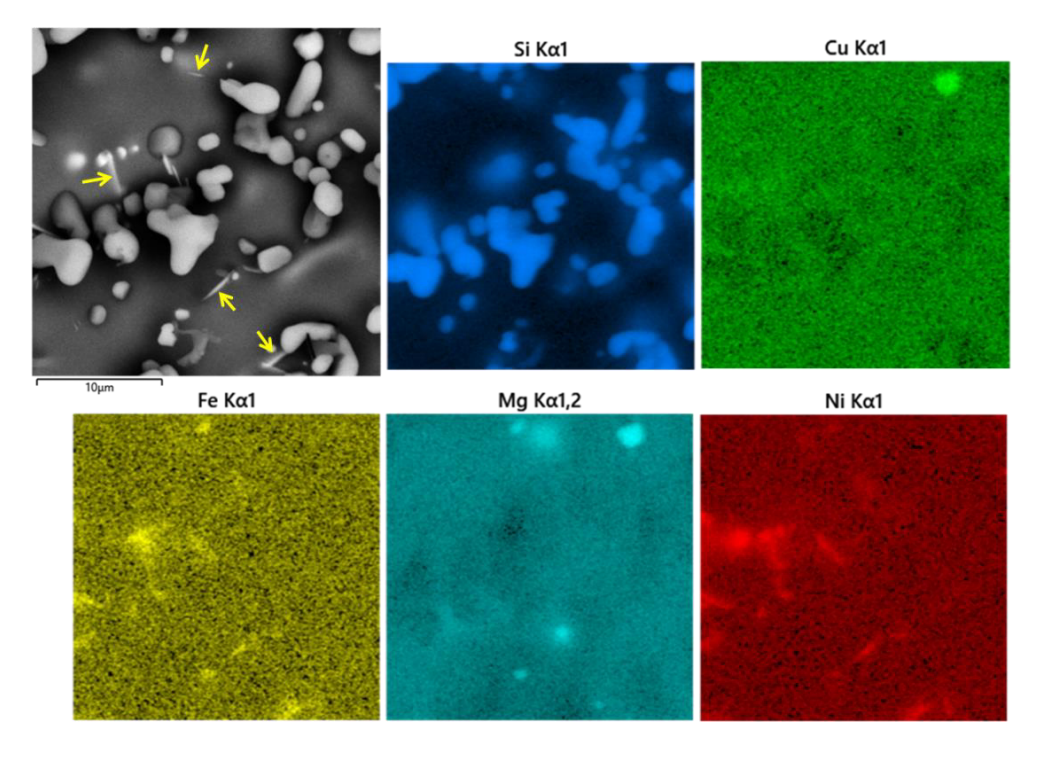


Fig. 5. Typical microstructure area in the peripheral zone of the cast rod and elemental mapping of such area (SEM)

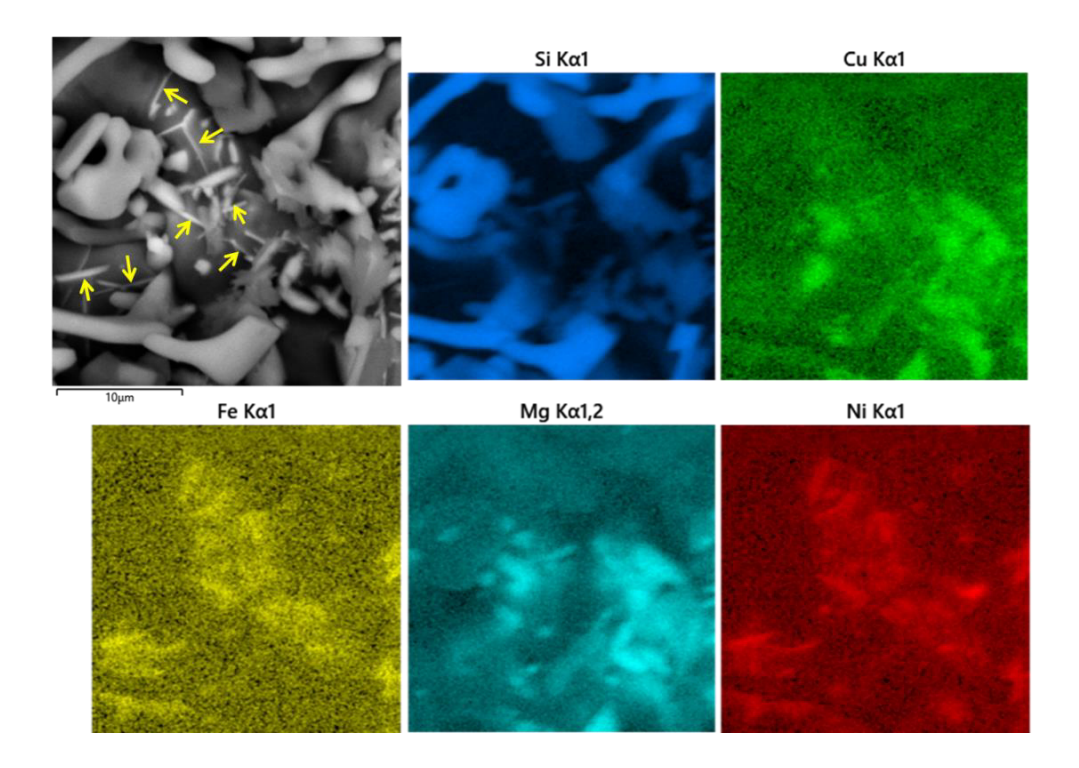


Fig. 6. Typical microstructure area in the central zone of the cast rod and elemental mapping of such area (SEM)

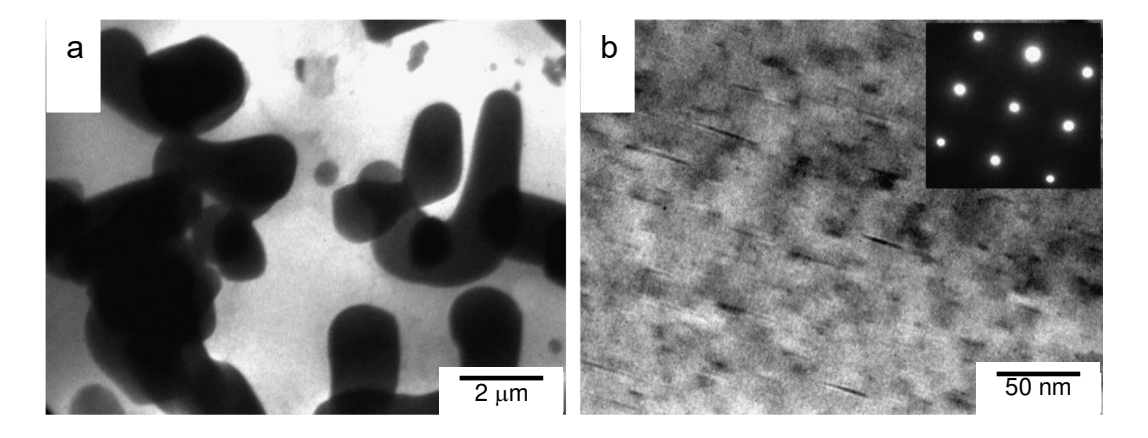


Fig. 7. Microstructure in the peripheral zone of the cast rod after T6 treatment: (a) after annealing at 520 °C and quenching; (b) after quenching and artificial aging (axis of the microdiffraction pattern zone [001]) (TEM)

As can be seen, after T6 treatment at the stage of annealing at 520 °C, fragmentation and spheroidization of lamellar Si and other phases in the eutectic occurred. In addition, the results of quantitative analysis (Table 2) demonstrate that annealing leads to coarsening of the particles (coalescence). However, there is still a noticeable difference in the particle size in the peripheral and central parts, which was noted earlier for the cast rod before HT.

In addition to the particles, whose morphology and size changed as a result of annealing at 520 °C, the microstructure of the alloy exhibits the presence of particle in the form of thin plates/needles with a smooth surface (indicated by arrows in Figs. 5 and 6), which did not undergo fragmentation. Elemental mapping showed that these particles, in addition to aluminum, include Fe and Ni. As was stated in the work [29], the particles of phases with similar morphology, which include alloying elements of a

low solubility in aluminum, possess high resistance to thermal effects. Such particles include the particles of ϵ -phase (Al₃Ni), which was possible to identify by X-ray diffraction, as well as, probably, the particles of Al₉FeNi – the presence of a small amount of such phase in the alloy is indicated by EDS results.

After the second stage of T6 treatment, which is artificial aging, the formation of rod-/plate-like particles of secondary phase is observed in the aluminum matrix, which are oriented in a strictly defined direction, have a thickness of several nanometers and a length in the range from 20 to 100 nm (Fig. 7(b)). The XRD data reveals a new welldefined diffraction peak related to the Mg₂Si phase that develops on X-ray diffraction pattern 3 (Fig. 4) after T6 heat treatment. According to [31], the particles of this phase develop after artificial ageing in the form of thin plates lying in {100}_{Al} planes, i.e., as in the image shown in Fig. 7(b). After T6 treatment, the lattice parameter of the alloy was as close as possible to that of pure aluminum (4.0507 ± 0.0001 Å). Such a change in the lattice parameter indicates the process of decomposition of α_{Al} as a result of aging and that aluminum solid solution has reached the maximum depletion of alloying elements. It is known that in silumins, as a result of heat treatment, including aging, other strengthening phases such as Al₂Cu, Al₂CuMq, and secondary Si can be formed in addition to Mq₂Si [29]. However, such phases were not detected in the examined samples in the process of microstructural analysis either by TEM or XRD. The possibility of detecting the phases of such composition might be limited by research techniques applied in the present study.

It should be noted that the microstructure that was formed in the AL30 alloy due to continuous casting into EMC and subsequent T6 heat treatment is close in its parameters to the microstructure of piston alloys with a similar chemical composition, which are used for manufacturing of semifinished products using deformation processing [14–18]. In the peripheral zone of the cast rod, in which $Vc \ge 10^3$ K/s was implemented after HT, it was possible to form a more dispersed microstructure. Similar microstructure was observed in the billets subjected to severe plastic deformation [16–18] or obtained by selective laser melting (SLM), in the process of which, as in the case of EMC casting, V_c in the range of 10^4 - 10^7 K/s is realized [11,12].

Mechanical properties of the alloy after heat treatment

Mechanical properties of the cast rod obtained by casting into EMC from the alloy AL30 and subsequent T1 and T6 heat treatment are presented in Table 3. In addition, Table 3 lists the properties of counterparts produced by conventional casting into the steel coquille (i.e., permanent mold casting) in Russian Federation [2,25] and abroad [3]. For comparison, the properties of semifinished products made of piston alloys similar in chemical composition, which were obtained using the deformation processing techniques, including severe deformation by equal-channel angular pressing (ECAP) [17], as well as by SLM technology [11,12], are also presented.

The data summarized in Table 3 from the present as well as previously carried out studies clearly demonstrate that the samples of cast rod obtained by casting into EMC from the alloy AL30 after T1 and T6 treatments are considerably superior to the mechanical properties of counterparts obtained by conventional casting. After T6

treatment the alloy AL30 demonstrates the "strength-ductility" ratio at the level of forged piston alloy M124R(AlSi12CuMgNi) [2] and alloy Al-11Si processed by ECAP [17], as well as of deformable alloy AK12D. However, its strength is found to be inferior to the alloys produced by SLM technology [11,12].

Table 3. Mechanical properties of the cast rod obtained from the alloy AL30 after conventional HT and of eutectic silumins with close chemical composition manufactured by different techniques

Alloy	State	Cast rod zone	HV	$\sigma_{ extsf{UTS}}$, MPa	$\sigma_{0.2}$, MPa	δ_5 , %
	T1	Periphery	135 ± 5	345 ± 10	250 ± 15	2.1 ± 0.3
	II	Center	139 ± 9	309 ± 5	295 ± 7	0.5 ± 0.1
AL30	T6	Periphery	150 ± 4	404 ± 5	335 ± 8	4.2 ± 0.3
(AK12MMgN)	10	Center	147 ± 9	393 ± 7	329 ± 9	2.4 ± 0.3
	T1 [3]	-	HB90	196	1	0.5
	T6 [3]	-	HB100	216	-	0.7
AL25						
(AK12M2MgN)	T6 [25]	-	-	360	1	-
M124						
(AlSi12CuMgNi)	T6 [2]	-	-	200-251	190-230	< 1
M124R						
(AlSi12CuMgNi)	T6 [2]	-	-	300-370	280-340	< 1
AK12D*	T6	-	156 ± 5	407 ± 4	387 ± 6	1.9 ± 0.2
Al-11Si	ECAP +T6 [17]	-	-	~ 390	-	~ 7
Al10SiMg	SLM [11]	-	-	475	294	2.4
Al-12Si	SLM [12]	-	-	≥ 425	≥ 275	≥ 6
* – heat treatment	and tests were carr	ied out in the fra	mework of	present study	/	

The level of properties displayed by the alloy AL30, obtained by casting into EMC and subjected to HT, is in good agreement with its microstructural features. In terms of dispersibility, the alloy AL30 is close to the alloys that undergo deformation treatment and occupies an intermediate position between the counterparts obtained by conventional casting methods and those produced by SLM technology. The increased strength of SLM-produced alloys relates to their ability to form a highly dispersed structure, which surpasses the structure resulting from casting into EMC, including the structure in the peripheral zone of the cast rod obtained from the alloy AL30. For example, as was demonstrated in the work [11], the samples of SLM-produced alloy $Al_{10}SiMg$ revealed the formation of a microstructure featuring dendritic cells of submicron scale (around 500 nm) and Si particles in the nanometer range.

Evaluation of heat resistance of the alloy after casting into EMC and subsequent heat treatment

Traditionally, pistons in IC engines are operated for extended periods (over 1000 hours) at temperatures up to and including 300 °C [1,2]. In this case, it seems important to determine the level at which the strength properties of piston materials become stable under these conditions. For this purpose, it was proposed in [25] to evaluate heat resistance by examining the piston alloys' hardness after annealing at 300 °C for 100 hours. Temperature exposure for the same period is used to determine the long-term strength of such materials.

Table 4 displays the results of evaluation of hardness change in the alloy AL30 samples after T6 heat treatment as a result of annealing at 300 °C. For comparison, the annealing treatment was performed on a sample of deformable alloy AK12D in the state T6, which has a similar chemical composition and level of mechanical properties (Table 3). In addition, Fig. 8 shows the graph of change in hardness with annealing time at 300 °C.

Table 4. Hardness of cast rod obtained from the alloy AL30 after thermal exposure at 300 °C
--

Pod zopo	Initial		Annealing time, h						
Rod zone	hardness	1	3	5	24	100			
Periphery	150 ± 4	114 ± 7	98 ± 5	89 ± 4	72 ± 4	66 ± 7			
Center	147 ± 8	115 ± 5	98 ± 4	86 ± 5	71 ± 4	68 ± 7			

As follows from Table 4 and Fig. 8, the character of hardness change is the same for the peripheral and central parts of the alloy AL30 cast rod. After 1-hour exposure at 300 °C, the sample hardness decreases by ~ 25 %, and hardness values continue to decrease significantly during 24 hours of annealing. Further increase of exposure time does not lead to considerable changes in hardness. It becomes stable at the level of ~ HV70, which is ~ 45 % of the initial hardness - after T6 heat treatment (Table 4). In the work [25], after similar annealing, the samples of alloy AL25 (AK12M2MgN) with close chemical composition, obtained by casting with crystallization under pressure and subjected to T6 treatment, demonstrated residual hardness of about 40 % of the initial hardness, and the samples of deformable alloy AK12D in the T6 state – 47 % (Fig. 8).

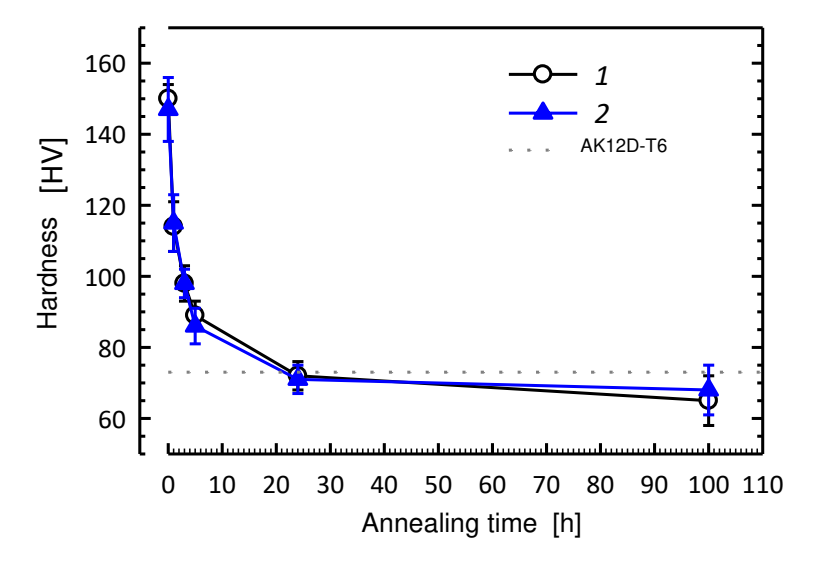


Fig. 8. Change in hardness of the alloy AL30 cast rod after T6 heat treatment with exposure time during annealing 300 °C: (1) – peripheral and (2) – central zones

Based on the analysis of the data herein and previous studies, it may be concluded that the cast rods, obtained from the alloy AL30 by casting into EMC and subsequent T6 heat treatment, exhibit heat resistance at the level of counterparts produced by casting or deformation processing. The absence of difference in the heat resistance level in different zones of the alloy AL30 cast rod might relate to the fact that the sizes of Si

particles and other secondary phases are insufficient for more pronounced stabilization of strength characteristics under extended thermal exposure (at 300 °C).

First results obtained in this study have shown that the use of continuous casting into EMC in combination with conventional HT to produce bulk billets of piston eutectic silumins makes it is possible to increase their mechanical properties while maintaining heat resistance at a high level. However, more research is needed to study the potential for further increasing the complex of properties through the formation of more homogeneous and dispersed structures (at submicron and/or nanoscale level) as well as improving the conditions of casting into EMC and HT modes.

Conclusions

- 1. The microstructure, mechanical properties and heat resistance of piston alloy AL30 (AK12MMgN), which for the first time was obtained by continuous casting into an electromagnetic mold (EMC), were studied.
- 2. It was shown that the EMC technique makes it possible to form a homogeneous dispersed microstructure comprised of a mixture of aluminum solid solution and eutectic with lamellar silicon (Si), as well as secondary phases, including ε -Al₃Ni, π -Al₈FeMg₃Si₆, Q-Al₄Cu₂MgSi₇ and S-Al₂CuMg, in both the central and peripheral regions of the bulk ingot. 3. It was established that in the alloy AL30, a microstructure formed by casting into EMC with subsequent T6 heat treatment provides the achievement of mechanical properties (σ _{0.2}, σ _{UTS} and δ ₅ not less than 330, 390 MPa and 2.5 % respectively), which are noticeably higher than the properties of its material counterparts produced by conventional casting in Russian Federation and abroad.
- 4. It was shown that the mechanical properties and heat resistance of the EMC-produced alloy AL30 with subsequent T6 heat treatment are identical to the properties of deformable piston alloys subjected to similar HT.

References

- 1. Belov NA, Belov VD, Savchenko SV. Piston silumins. Moscow: Ore and Metals; 2011. (In-Russian)
- 2. MAHLE GmbH (Ed.). Pistons and engine testing. Stuttgart, Germany: Springer; 2016.
- 3. Gosstandart of Russia. GOST 1583–93. *Alloys aluminum casting. Specifications*. 1993. (In-Russian)
- 4. Vyrubov DN, Efimov SI, Ivashchenko NA. *Internal Combustion Engines: Design and Strength Calculation of Piston and Combined Engines*. Moscow: Mashinostroenie Publishing House; 1984. (In-Russian)
- 5. Zolotorevskiy VS, Belov NA. *Metallurgy of cast aluminum alloys*. Moscow: MISIS Publishing House: 2005. (In-Russian)
- 6. Kolonakov AA, Kukharenko AV, Deev VB, Abaturova AA. Structure and Chemical Composition of the AK12MMgN Piston Alloy Fabricated Based on Various Charges. *Izvestiya*. *Non-Ferrous Metallurgy*. 2015;3: 49–55. (In-Russian)
- 7. Zhang X, Zhou Y, Zhong G, Zhang J, Chen Y, Jie W, Schumacher P, Li J. Effects of Si and Sr elements on solidification microstructure and thermal conductivity of Al–Si-based alloys. *Journal of Materials Science*. 2022;57: 6428–6444.
- 8. Ganesh K, Hemachandra Reddy K, Sudhakar Babu S, Ravikumar M. Study on microstructure, tensile, wear, and fracture behavior of A357 by modifying strontium (Sr) and calcium (Ca) content. *Materials Physics and Mechanics*. 2023;51(2): 128–139.
- 9. Kaiser MS. Effect of Solution Treatment on Age-Hardening Behavior of Al-12Si-1Mg-1Cu Piston Alloy with Trace-Zr Addition. *Journal of Casting & Materials Engineering*. 2018;2(2): 30–37.

- 10. Kumai S. Tear toughness evaluation of high-quality squeeze-cast and rheocast aluminum alloy castings. *Materials Science Forum.* 2006;519-521: 1733–1740.
- 11. Marola S, Manfredi D, Fiore G, Poletti M.G, Lombardi M, Fino P, Battezzati L. A comparison of Selective Laser Melting with bulk rapid solidification of AlSi10Mg alloy. *Journal of Alloys and Compounds*. 2018;742: 271–279.
- 12. Takata N, Liu M, Kodaira H, Suzuki A, Kobashi M. Anomalous strengthening by supersaturated solid solutions of selectively laser melted Al-Si-based alloys. *Additive Manufacturing*. 2020;33: 101152.
- 13. Sjolander E, Seifeddine S. Review. The heat treatment of Al–Si–Cu–Mg casting alloys. *Journal of Materials Processing Technology*. 2010;210: 1249–1259.
- 14. Hu HE, Wang X, Deng L. High temperature deformation behavior and optimal hot processing parameters of Al-Si eutectic alloy. *Materials Science and Engineering A*. 2013;576: 45–51.
- 15. Yu SB, Kim MS. Microstructure and High Temperature Deformation of Extruded Al-12Si-3Cu-Based Alloy. *Metals*. 2016;6: 32.
- 16. Cepeda-Jimenez CM, Garcia-Infanta JM, Zhilyaev AP, Ruano OA, Carreno F. Influence of the supersaturated silicon solid solution concentration on the effectiveness of severe plastic deformation processing in Al-7 wt.% Si casting alloy. *Materials Science and Engineering A.* 2011;528: 7938–7947.
- 17. Ma F, Takagi M, Saito N, Iwata H, Nishida Y, Suzuki K, Shigematsu I. Tensile properties of an Al-11 mass%Si alloy at elevated temperatures processed by rotary-die equal-channel angular pressing. *Materials Science and Engineering A.* 2005;408: 147–153.
- 18. Damavandi E, Nourouzi S, Rabiee SM, Jamaati R, Szpunar JA. Effect of route BC-ECAP on microstructural evolution and mechanical properties of Al–Si–Cu alloy. *Journal of Materials Science*. 2021;56: 3535–3550.
- 19. Belov N, Murashkin M, Korotkova N, Akopyan T, Timofeev V. Structure and properties of Al-0.6 Wt.%Zr wire alloy manufactured by direct drawing of electromagnetically cast wire rod. *Metals*. 2020;10(6): 769.
- 20. Belov N, Akopyan T, Korotkova N, Murashkin M, Timofeev V, Fortuna A. Structure and properties of Ca and Zr containing heat resistant wire aluminum alloy manufactured by electromagnetic casting. *Metals*. 2021;11(2): 236.
- 21. Medvedev AE, Zhukova OO, Fedotova DD, Murashkin MYu. The mechanical properties, electrical conductivity, and thermal stability of a wire made of Al–Fe alloys produced by casting into an electromagnetic crystallizer. *Frontier Materials & Technologies*. 2022;3: 96–105.
- 22. Korotkova NO, Belov NA, Timofeev VN, Motkov MM. Cherkasov S.O. Influence of Heat Treatment on the Structure and Properties of an Al-7% REM Conductive Aluminum Alloy Casted in an Electromagnetic Crystallizer. *Physics of Metals and Metallography*. 2020;121(2): 173–179.
- 23. Gamin YV, Belov NA, Akopyan TK, Timofeev VN, Cherkasov SO and Motkov MM. Effect of Radial-Shear Rolling on the Structure and Hardening of an Al-8%Zn-3.3%Mg-0.8%Ca-1.1%Fe Alloy Manufactured by Electromagnetic Casting. *Materials*. 2023;16(2): 677.
- 24. *RPC of Magnetic Hydrodynamics Ltd*. Available from: http://www.npcmgd.com [Accessed 29th November 2023]. 25. Vasenin VI. Determining the High-Temperature Strength of Aluminum Alloys. *Metallurgy of Machinery Building*. 2004;3: 38–40. (In-Russian)
- 26. Lutterotti L, Matthies S, Wenk HR, Schultz A, Richardson J. Combined texture and structure analysis of deformed limestone from time-of-flight neutron diffraction spectra. *Journal of Applied Physics*. 1997;81: 594–600. 27. International Standard Organization. ISO 6507-1:2023. *Metallic materials. Vickers hardness test. Part 1: Test method*. ISO; 2023.
- 28. Gosstandart of Russia. GOST 1497-84. Metals. Methods of tension test. 1986.
- 29. Belov NA. *Phase composition of industrial and promising aluminum alloys: monograph.* Moscow: MISIS Publishing House; 2010. (In-Russian)
- 30. Khalikova GR, Kalshchikov RV, Shvets KS, Trifonov VG. Structure and mechanical properties of aluminum alloy AK12MMgN reinforced with SiC particles. *Fundamental Problems of Modern Materials Science*. 2015;12(4): 459–463. (In-Russian)
- 31. Edwards GA, Stiller K, Dunlop GL, Couper MJ. The precipitation sequence in Al-Mg-Si alloys. *Acta Materialia*. 1998;46(11): 3893–3904.

About Authors

Maxim Yu. Murashkin 🗓 Sc

Candidate of Technical Sciences Senior Researcher (Ufa University of Science and Technology, Ufa, Russia)

Lily I. Zainullina 📵 Sc

Candidate of Technical Sciences
Associate Professor, Senior Researcher (Ufa University of Science and Technology, Ufa, Russia)

Mikhail M. Motkov (1) Sc

Candidate of Technical Sciences Senior Researcher (Siberian Federal University, Krasnoyarsk, Russia)

Andrey E. Medvedev D Sc

Candidate of Physical and Mathematical Sciences Senior Researcher (Ufa University of Science and Technology, Ufa, Russia)

Viktor N. Timofeev D Sc

Doctor of Technical Sciences Professor (Siberian Federal University, Krasnoyarsk, Russia)

Nariman A. Enikeev D Sc

Doctor of Physical and Mathematical Sciences Leading Researcher (Ufa University of Science and Technology, Ufa, Russia) Leading Researcher (Saint Petersburg State University, Saint Petersburg, Russia)

Accepted: December 26, 2023

Submitted: November 7, 2023

Revised: November 21, 2023

Influence of various friction stir processing (FSP) schemes on the microstructure and properties of AD31 aluminium alloy busbar

A.E. Medvedev ^{1 \subseteq}, \(\bar{\text{D}} \) V.V. Atroshchenko ², \(\bar{\text{D}} \) A.S. Selivanov ², \(\bar{\text{D}} \) A.R. Bogdanov ¹, M.V. Gorbatkov ³, \(\bar{\text{D}} \) Y.V. Logachev ², \(\bar{\text{D}} \) V.S. Lobachev ², \(\bar{\text{D}} \)

ABSTRACT

This paper examines the influence of various schemes for implementing friction stir processing (FSP) on the microstructure and properties of a conductive busbar made of AD31T (AA6063) aluminum alloy. In particular, the implementation of five different FSP schemes on the formation of structure and volumetric defects in the volume of the stir zone was studied. It has been shown that performing FSP at a tool rotation speed of 1120 rpm and a linear tool movement velocity of 200 mm/min ensures the absence of macroscopic defects in the volume of the stir zone. The implementation of certain FSP schemes made it possible to achieve the formation of an ultrafine-grained structure both in the near-surface layer and in the bulk of the material under study. This type of processing can be recommended as a way to increase the strength of aluminum materials without significant loss of their electrical conductivity.

KEYWORDS

friction stir processing • FSP • Al-Mg-Si • AA6063 • aluminium alloy • fine-grained structure microhardness • electrical conductivity

Acknowledgements. The authors express special gratitude to the Center for Collective Use "Nanotech" of the Federal State Budgetary Educational Institution of Higher Education "UUST".

Citation: Medvedev AE, Atroshchenko VV, Selivanov AS, Bogdanov AR, Gorbatkov MV, Logachev YV, Lobachev VS. Influence of various friction stir processing (FSP) schemes on the microstructure and properties of AD31 aluminium alloy busbar. *Materials Physics and Mechanics*. 2024;52(1): 95-107. http://dx.doi.org/10.18149/MPM.5212024_9

Introduction

Aluminium and aluminium alloys occupy a significant share in the modern metallurgical industry. Along with relative availability, one of the most important properties of aluminium alloys that determine its widespread use is its low density and good electrical conductivity, accounting for 62 % of the electrical conductivity of copper. Considering the scarcity and high cost of copper, the role of aluminium as a conductor material is steadily increasing. The undoubted advantages of aluminium include its high plasticity, thermal conductivity and heat capacity, good manufacturability, and corrosion resistance [1]. The main disadvantage of aluminium is its relatively low strength - 49 MPa. This level of properties is not sufficient for widespread industrial use, so research aimed at increasing the strength of aluminium alloys is important. One of the ways to strengthen aluminium is to create alloys based on it [2]. The general pattern of aluminium alloying is that the

© A.E. Medvedev, V.V. Atroshchenko, A.S. Selivanov, A.R. Bogdanov, M.V. Gorbatkov, Y.V. Logachev, V.S. Lobachev, 2023. Publisher: Peter the Great St. Petersburg Polytechnic University

¹ Ufa University of Science and Technology, Ufa, Russia

²LLC Attestation Center Svarka Tech. Service, Ufa, Russia

³LLC Krus-Zapad, Ufa, Russia

[™] medvedevandreyrf@gmail.com

addition of other elements, leading to an increase in the strength of the aluminium alloy, leads to a decrease in its electrical conductivity [3–5]. The need to maintain the level of electrical conductivity of pure aluminium, or to minimize its drop due to alloying, as well as the desire to reduce the cost of production of aluminium alloys, lead to minimizing the amount of additions of alloying elements without a significant loss in properties - the creation of the so-called low-alloyed alloys [6,7].

Another fundamental approach to increasing the strength of aluminium and aluminium alloys is the use of deformation methods - stamping, drawing, pressing, etc. [2]. Such methods have undoubted advantages - they are well-developed modes and conditions of deformation, stability and predictability of the results obtained. The disadvantages of such methods include the volumetric nature of the impact - deformation, as a rule, extends to the entire volume of the processed material, as well as an increase in the density of defects, which entails a drop in electrical conductivity [8]. The effect of deformation can be reduced by using local hardening methods, such as coldworking, shot peening, diamond burnishing and other similar methods [1]. A separate group of methods aimed at modifying the surface and surface layer of a material includes methods based on the effect of surface friction. These include, in particular: friction stir welding, friction stir processing, friction surfacing, friction brazing, friction transformation hardening, friction extrusion and others [9]. The most popular and commonly used in industry are friction stir welding (FSW) and friction stir processing (FSP).

Friction stir processing (FSP) is a technology aimed at changing the structure and properties of the surface and subsurface layer of materials in the solid phase [9–11]. A distinctive feature of this method is local mixing of the metal in the treated area without the formation of a liquid phase, which can lead to oxidation and burnout of the metal, as well as a decrease in its strength properties. Work aimed at studying FSP quickly showed that this method can modify the surface layer of the processed material, providing a structure and properties different from the processed material [12]. Since FSP involves processing the material in the solid phase, the main attention has been paid to soft materials, such as aluminium alloys [13], magnesium alloys [14] and copper alloys [15]. There is also a limited set of publications on FSP of titanium alloys and steels [11,16].

Research aimed at FSP of aluminium alloys aims to create permanent joints where welding is not applicable or impractical. Thus, it was shown that FSP with the imposition of tracks on the aluminium surface makes it possible to reduce the average grain size to 100–200 nm over a relatively large area, reaching an ultrafine-grained (UFG) state [17–19]. The authors propose a similar approach that makes it possible to obtain large-sized products with a UFG structure of the surface layer. The authors of [13] claim a decrease in the average grain size per one pass of FSP by more than 20 times, which led to an increase in the yield strength of the material by 2.4 times. Articles [20–22] explore methods of friction stir welding with overlap, a two-pass connection in one direction and in opposite directions, on both sides of the welded sample. These studies claim that such methods can provide good fluidity and mixing of dissimilar metals, reducing the size of grains and defects at their boundaries, and a two-pass connection can significantly increase the strength properties of the welded joint, reduce wear, and obtain minimal costs for mixing tools.

Despite a large amount of information regarding the FSP of aluminium alloys, there is depressingly little data on the effect of this processing method on the electrical conductivity of aluminium alloys. There is no data on the effect of this processing method on the level of electrical conductivity in conductive products made from aluminium alloys. This study is a continuation of works devoted to the FSP of conductive busbars made of aluminium alloy AD31 [23]. In previous work, a rational FSP mode was established, which allows, for a given geometry of the processing tool, to obtain a processed zone without volumetric defects. This paper examines five different schemes for implementing FSP, their influence on the structure and properties of busbars made of AD31T aluminium alloy.

Materials and Methods

As a research material, hot-rolled aluminium alloy plates of 10 mm thick and $200 \times 200 \text{ mm}$ in size were used. The plates were obtained in the "T" state, meaning quenching and natural aging. The chemical composition of the commercially produced AD31T alloy (AA6063 analogue) is given in Table 1.

Table 1. Chemical composition of the AD31T alloy

Concentration of the element, wt. %							
Al Si Fe Mg Mn Cu Zn							
Base material	0.410	0.390	0.390	≤ 0.035	≤ 0.035	≤ 0.035	

The processing of the material was carried out on a vertical console milling machine FSS-400, adapted for FSP, in 6 different processing schemes (Table 2). Based on the results of previous research [23], the FSP parameters were set as follows: tool rotation speed 1120 rpm, tool linear velocity 200 mm/min. During FSP, the shoulder penetration was 0.635 mm at a tool inclination angle of 3°. The tool dwelling time after immersion is 10 sec.

A sketch of the tool is shown in Fig. 1. The tool is made of steel containing 0.2 wt. % C and 13 wt. % Cr (the closest analogue is AISI 420). Before use, the tool is hardened up to 580 HB. Most authors tend not to disclose the details of the geometry of the stirring tool, however, the general recommendations for aluminium alloys are that the tool pin should be a tapered cone or a threaded one. Since the production of the threaded tool is more expensive and complex, than the production of the tapered cone tool, and tapered cone tool is proven to provide defect less structure [22,24,25], the latter type of tool was used.



Fig. 1. Schematic drawing of the stirring tool

Table 2. FSP schemes

Marking of the sample	FSP scheme description	FSP scheme depiction
225	Single linear track	
226	Two unidirectional tracks, on a single line, one from each surface (upper and lower) of the plate	
227	Two unidirectional tracks, on a single line, on top of each other, on the same surface of the plate	
228	Two counter directional tracks, on a single line, on top of each other, on the same surface of the plate	
229	Multiple unidirectional overlapping tracks on the same surface, overlap of 10 mm	
233	Multiple unidirectional overlapping tracks on the same surface, overlap of 5 mm	

X-ray control was carried out on the hardware-software complex of digital radiography "Tsifrakon". Microstructure studies were performed on an Olympus Q15OR optical microscope. For metallographic analysis, macrosections were made by cutting in the middle of the length of the stir zone (SZ) in the direction perpendicular to the processing direction. Surface finishing was carried out in a 3 % hydrofluoric acid solution to reveal the macrostructure. Microhardness (HV) was evaluated by the Vickers method on a Buehler MicroMet 5101 instrument at a load of 1 N and a holding time under load of 10 s. The microhardness (HV) value was calculated using the Omnimet Imaging System software. Microhardness was measured on transverse sections of specimens along lines parallel to the surface of the original plate. The measurements were taken at the middle of the sample thickness, and ¼ of the height from the bottom and top surfaces of the plate. When measuring the microhardness of the stir zone, the line of measurements passed through all sections of the cross-section of the FSP sample at a measurement step of 0.5 mm (about 60 measurements per line). The error value for the microhardness profiles was calculated as a standard deviation for each profile. Generally, the absolute value of the microhardness error does not exceed 5 HV. Mechanical tensile tests were carried out on samples manufactured in accordance with GOST 1497-84. Tests were carried out on flat samples with length 70 mm and cross-sectional dimensions 3 × 9 mm. The samples were cut in the direction perpendicular to the FSP treatment so that the treated area aligned with the middle of the sample. Specific electrical conductivity (ω) of the alloy samples was determined with a relative error of 2% using a VE-27NTs/4-5 eddy current electrical conductivity meter according to ASTM E1004-09. The electrical conductivity value of the samples relative to annealed copper (International Annealed Copper Standard) was calculated using Eq. (1):

$$IACS = \omega_{AI}/\omega_{Cu} \cdot 100 \, [\%], \tag{1}$$

where ω_{Al} is the experimentally determined value of the electrical conductivity of the aluminium alloy sample, ω_{Cu} is the electrical conductivity of annealed copper, equal to 58 MS/m, (MS/m stands for 10^6 S/m, siemens per meter). Since the electrical conductivity was measured at 10 points on a line located in the middle of the sample thickness.

Results and Discussion

Samples and stir zone (SZ) assessment

Images of the samples 225-233 are presented on Fig. 2. Sample 225 was produced to ensure the correctness of the chosen FSP mode [23] in appliance to the studied material, ensuring the absence of macroscopic defects in the research material. Visual attestation of the samples 226-233 shows the absence of the macroscopic defects, tunnel effect, melting and excessive material pushouts from the stir zone during FSP. Figure 2(f) on example of 233 demonstrates the placement of the tensile test samples.

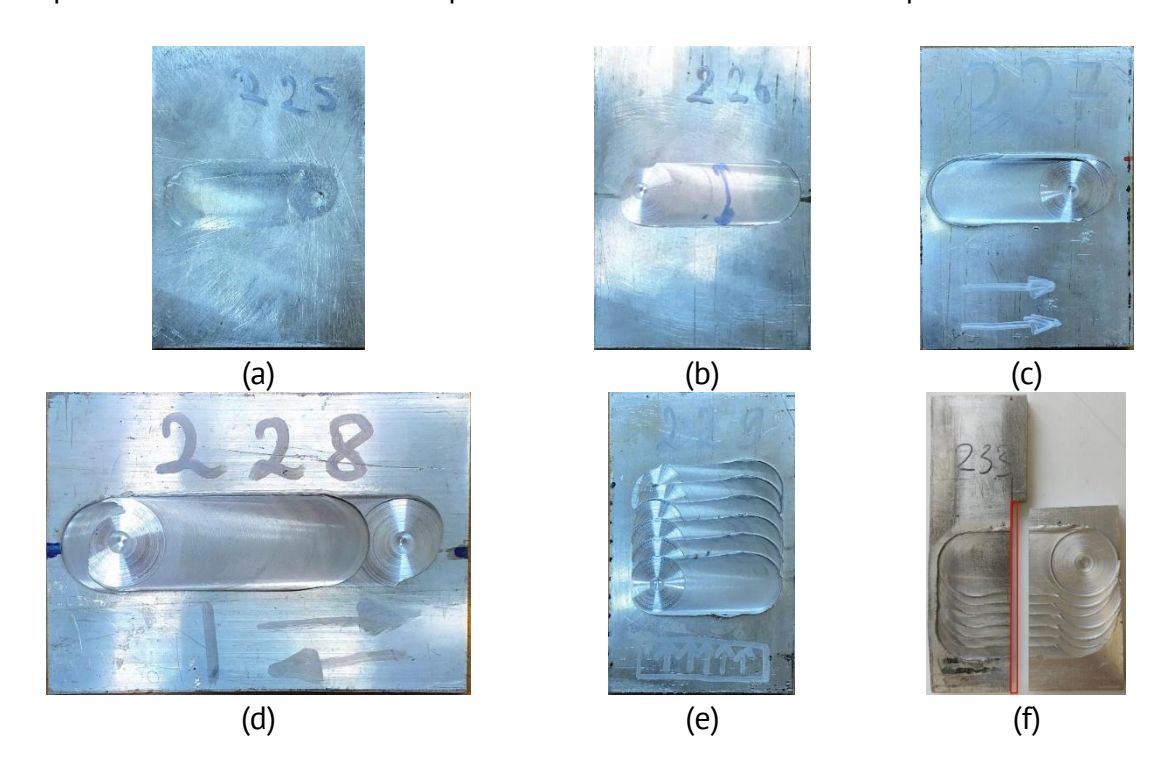


Fig. 2. Samples 225(a), 226 (b), 227 (c), 228 (d), 229 (e) and 233 (f) after FSP. Red rectangle on (f) represents the placement of the tensile test sample

The results of X-ray control of samples 225–229 and 233 are presented in Fig. 3. Each of the studied samples demonstrate the absence of the volumetric defects: tunnel defects, gas pores and other.

Since sample 225 was used as a reference one for testing the FSP conditions, it was no longer studied further.

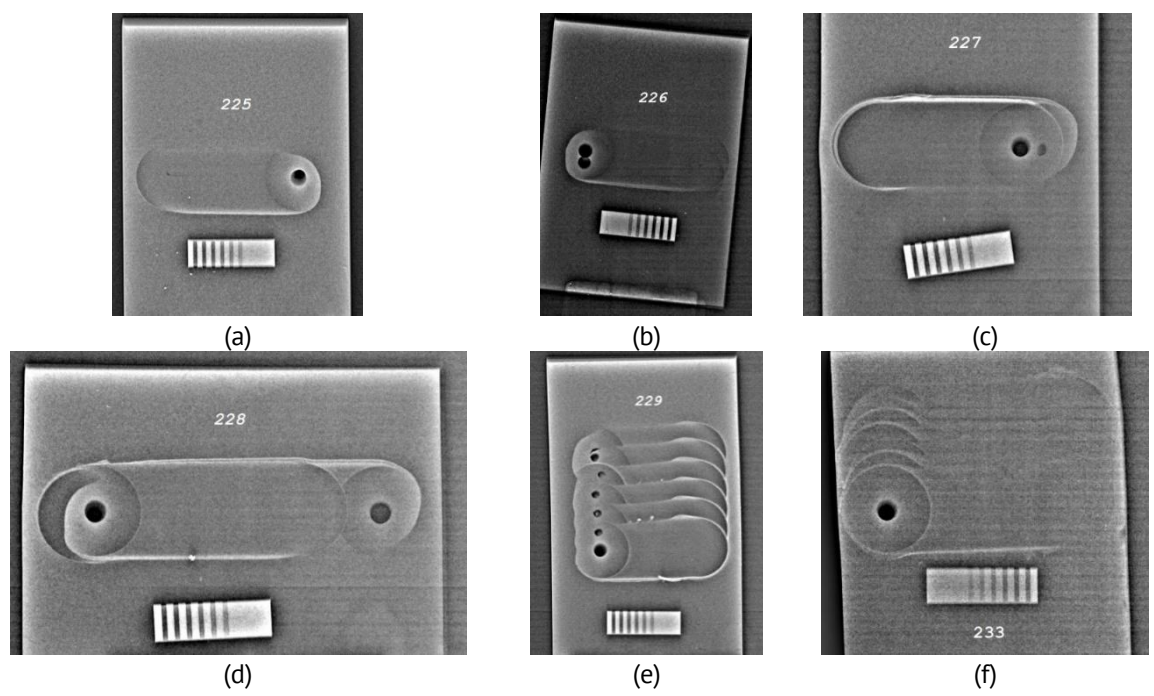


Fig. 3. Results of the X-Ray control of samples 225 (a), 226 (b), 227 (c), 228 (d), 229 (e) and 233 (f) after the FSP

Macrostructure assessment

Figure 4 shows photographs of the cross-section of samples 226-233 after FSP. As a result of FSP, a finely dispersed structure was formed in the stir zone (SZ) and the heat affected zone (HAZ) (Fig. 4). The shape and size of the HAZ is similar for samples 227–229 - it narrows towards the base of the sample due to more significant heat dissipation in the sample volume. The HAZ of samples 229 and 233 is wider than in samples 226-228 due to the overlap of the HAZ of each individual track.

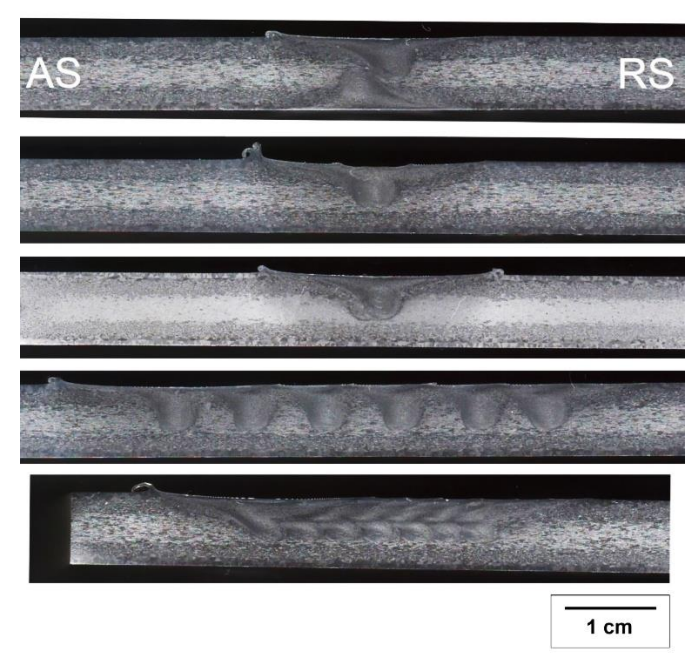


Fig. 4. Macrostructure assessment of the 226 - 233 samples (top to bottom) cross-sections. Advancing side and retreating side are marked AS and RS, correspondingly

According to macroscopy data, a busbar made of the alloy under study in the initial state is characterized by three zones - central, intermediate, and peripheral (Fig. 5). The central zone is characterized by relatively small, elongated grains with the size not exceeding 100 μ m. In the intermediate zone, grains are characterized by a larger size, ranging from 50 to 300 μ m with an average of 146 μ m, and a shape close to equiaxial. The peripheral zone consists of coarse crystals arranged in 1 or 2 rows. These coarse grains are generally presented in the shape of elongated towards the edge of the busbar grains, with the average length of 337 μ m (ranging from 130 to 740 μ m) and average width of 571 μ m (ranging from 300 to 900 μ m).

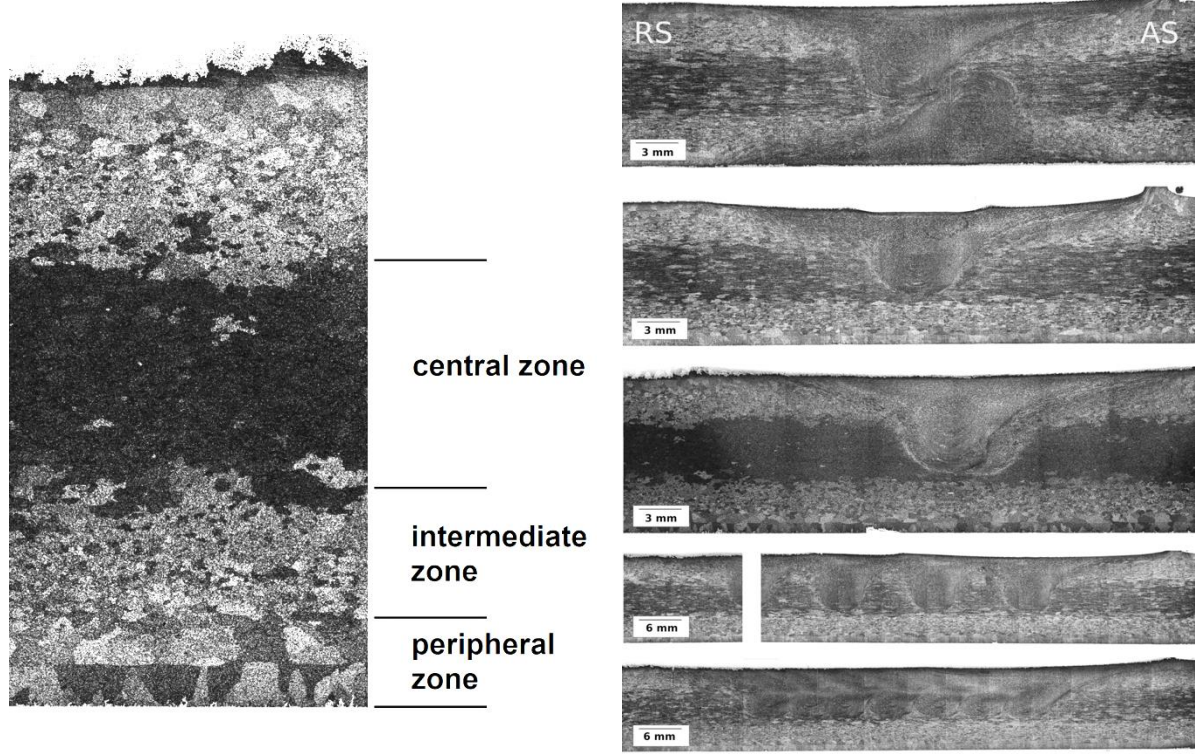


Fig. 5. Macroscopic images of the initial busbar cross section. Three zones are distinctly visible – central, intermediate, and peripheral, OM

Fig. 6. Metallographic analysis of the samples 226-233 cross sections (top to bottom), OM. Advancing side and retreating side are marked AS and RS, correspondingly

Figure 6 presents the panoramic images of the 226-233 samples. According to it, the grain size within the SZ ranges from 20 to 30 μ m with an average of 22 ± 8 μ m. The value of the average grain size is the same throughout the SZ, so the deformation could be considered uniform in the SZ. Outside the SZ, however, in the HAZ the average size of the grain is 295.35 nm, which is higher than in both intermediate and central zones of the busbar (Fig. 5). The grain growth presumably is caused by the heating inevitably accompanying the FSP process.

According to Fig. 6, in sample 226, the tracks located on different sides of the busbar did superimpose each other but were located offset. However, the SZs of both tracks influenced each other, bending the normally symmetrical shape of the SZ. In samples 227 and 228, the tracks overlapped with virtually no displacement relative to each other. If in sample 227 the directions of tool movement coincided, and the advancing side (AS) and

retreating side (RS) zones overlapped each other, increasing the heterogeneity of the thermomechanically affected zone (TMAZ), then in sample 228, during the second pass, the AS and RS zones overlapped each other, providing a symmetrical TMAZ. Sample 229 was obtained with superimposed unidirectional tracks with a tool offset of 10 mm. As it turned out, a displacement of this magnitude does not provide only partial overlap of the SZ, leaving untreated areas. In sample 233, processed according to a scheme similar to sample 229, the displacement of the tracks was 5 mm, as a result of which complete overlap of the SZ was achieved.

Microhardness and electrical conductivity assessment

Analysis of the hardness distribution curves (Fig. 7) shows that the cross-section of sample 226 is characterized by two significantly different sections: the base metal (BM), which hardness is 50-55 HV (depending on the depth of measurements relative to the surface), and the metal of the SZ, the hardness of which is on average 10–15 % higher. There is also a noticeable decrease in hardness at the boundary of the SZ, between the BM and the TMAZ, caused by recovery processes as a result of thermal effects. Microhardness values increase in the center of the SZ, since due to a greater degree of deformation, the contribution of grain boundary and dislocation strengthening increases as well.

The microhardness profiles of samples 226-228 are largely similar, however, there are certain differences. In sample 226, there was no exact overlap of the SZ core, as a result of which the TMAZ of the second track partially overlapped the SZ core of the first track, leading to softening - the maximum microhardness in sample 226 does not reach 60 HV, which is the minimum value for samples 226-228 (Fig. 7(a)). The microhardness values for the upper, middle, and lower zones of the sample are almost completely identical, which indicates the absence of hardening in the surface zone. Also, the microhardness values completely coincide in the center of the sample - between the centers of the SZ cores.

In sample 227, in which unidirectional tracks were superimposed, an increase in microhardness is observed throughout the entire SZ and TMAZ, and the hardness values for the upper and middle layers of the sample turned out to be higher than for the lower layer (Fig. 7(b)). The multidirectionality of the tracks in sample 228 caused the strengthening of the lower layer, in addition to an increase in microhardness in the upper and middle layers of the sample (Fig. 7(c)). In general, the increase in microhardness in sample 228 is less pronounced, most likely due to the overlap of the HAZ from multidirectional tool passes.

The nature of the microhardness profiles for samples 229 and 233 is different from samples 226-228. In sample 229, the microhardness of the surface layer turned out to be higher than in the base material, since the overlap of the SZ core is located just near the surface. The microhardness of the lower layer of the busbar increases slightly, but the change is insignificant. The microhardness profile of the middle layer has a sawtooth character, corresponding to alternating SZs (Figs. 4-6). The growth of microhardness in the upper and middle zones of sample 233 is more pronounced than in sample 229, and, in general, the hardening in sample 233 is greater than in sample 229. A characteristic feature of sample 233 is a sharp decrease in microhardness at the boundary of the zone - where the overlaps of the SZs, and this decrease is most noticeable in the upper and middle layers of the sample.

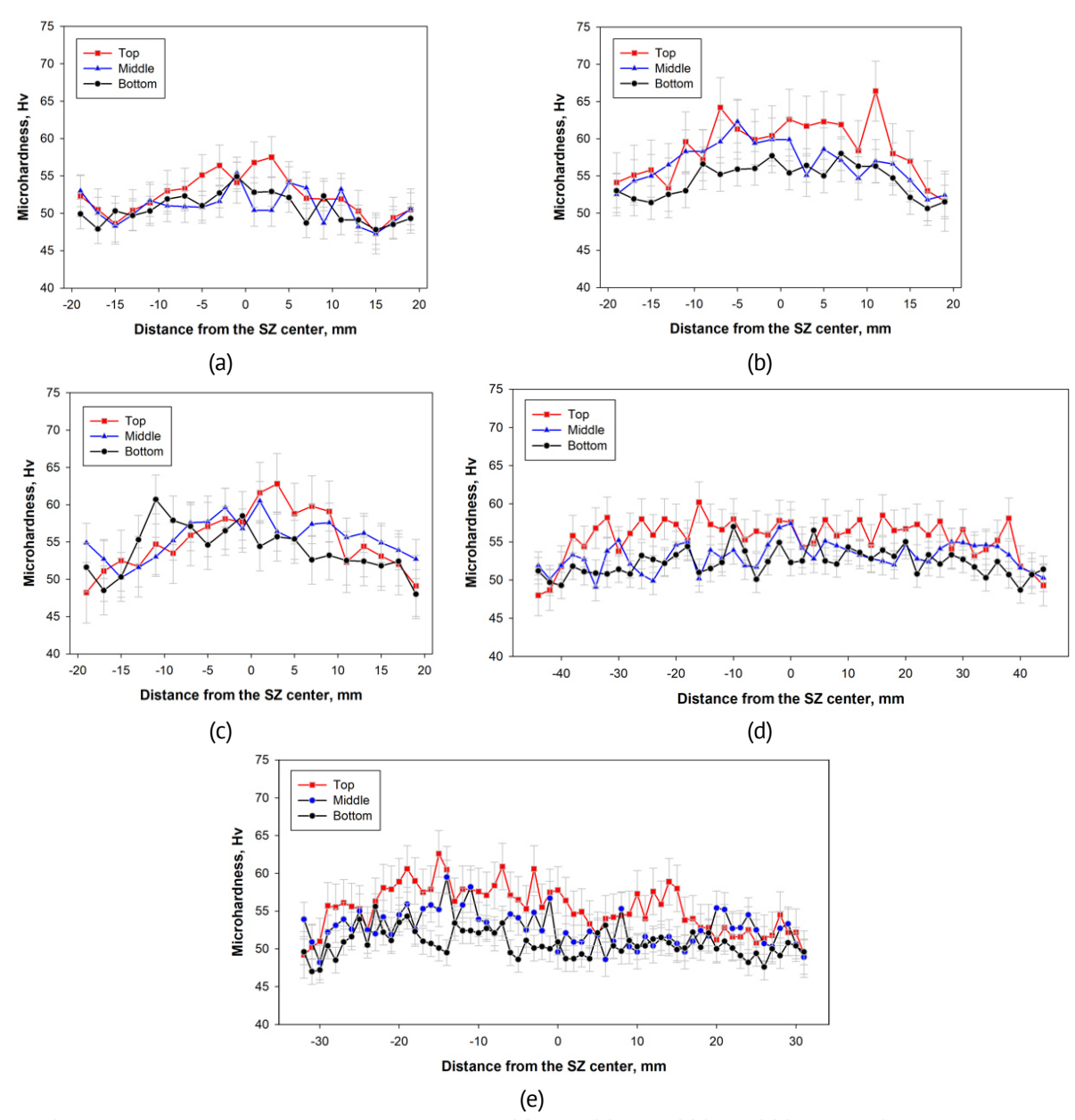


Fig. 7. Microhardness profiles for the samples 226 (a), 227 (b), 228 (c), 229 (d) and 233 (e). For all samples advancing side (AS) is on the right and retreating side (RS) is on the left

Figure 8 shows the electrical conductivity profiles of the samples. Based on the results of measuring the electrical conductivity of the SZ and TMAZ, the average value of the electrical conductivity of the BM was 28.8–29.1 MS/m.

The change in resistivity value for each sample is different from the others. Thus, in sample 226, there is a noticeable decrease in electrical conductivity in the SZ and TMAZ (Fig. 8(a)), and an increase beyond them. According to Fig. 8(a), a relatively small increase in microhardness is observed in the sample SZ, which correlates with a decrease in electrical conductivity. Near the SZ, an increase in electrical conductivity is observed, probably as a result of recovery processes. The behavior of electrical conductivity in samples 227 and 228 correlates with changes in microhardness - for example, the microhardness in the SZ of sample 227 is higher, and the electrical conductivity is lower than in the SZ of sample 228. The electrical conductivity values to the left and right of

the SZ and TMAZ in sample 228 are higher than in sample 227 are and are located symmetrically due to the overlap of the AS and RS zones from each tool pass.

Just like microhardness, the electrical conductivity profiles in samples 229 and 233 are different from the electrical conductivity profiles for samples 226-228. In general, the electrical conductivity of the TMAZ of the sample 229 corresponds to the electrical conductivity of the BM, except for areas at the edge of the SZ. The electrical conductivity of sample 233 is higher almost throughout its entire length than in the base material, and decreases only at the edge of the SZ (Fig. 8(f)).

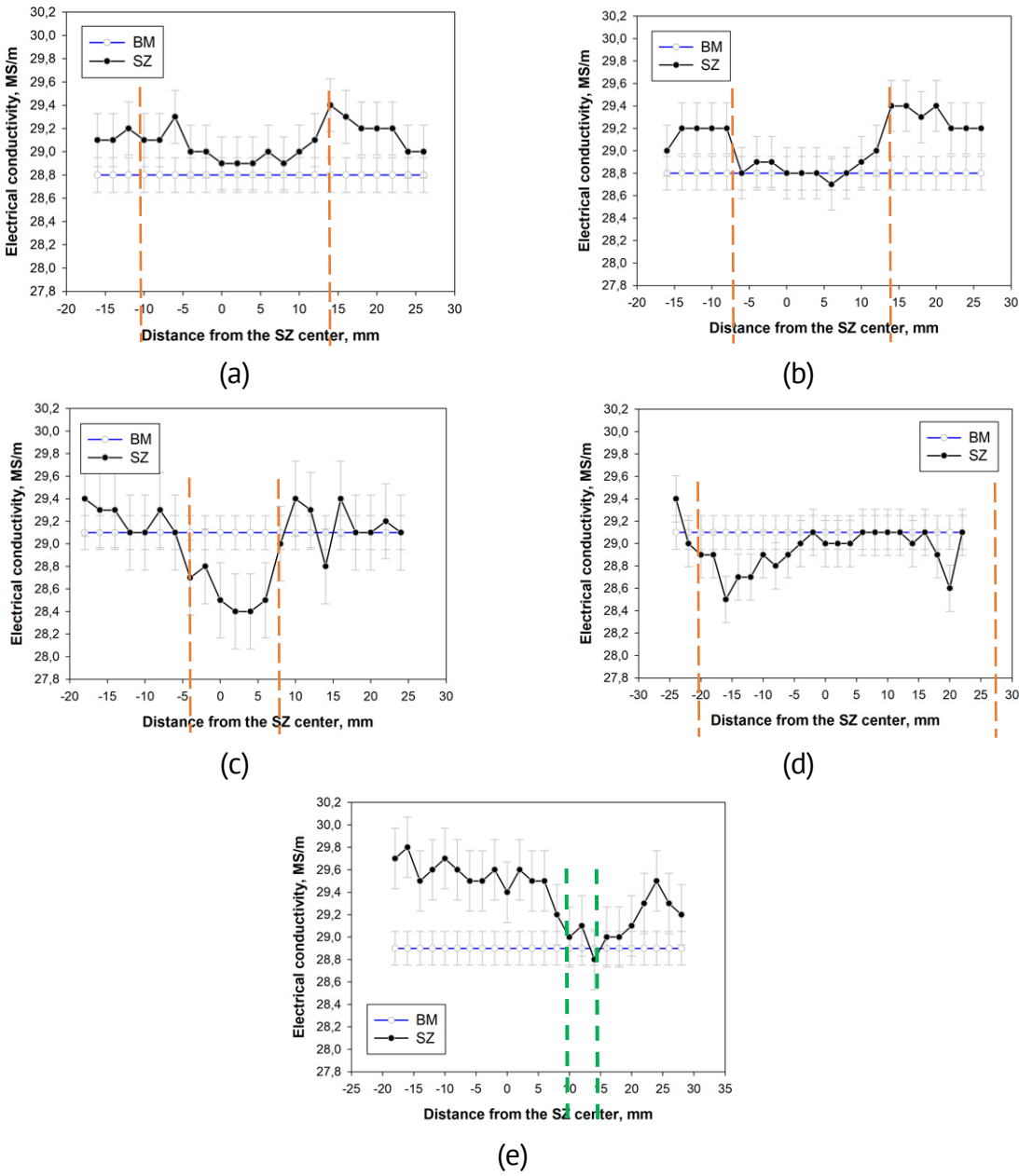


Fig. 8. Electrical conductivity profiles for samples 226 (a), 227 (b), 228 (c), 229 (d) and 233 (e). Orange dashed lines mark the edges of the SZ. For the sample 233 (e) green dashed lines mark the start and the end of the SZ edge. For all samples advancing side (AS) is on the right and retreating side (RS) is on the left

Figure 9 shows the engineering stress-strain curves of samples made from workpieces of states 226-233. All states are characterized by ductile fracture and have comparable values of the yield strength (UTS) (70-80 MPa), ultimate tensile strength (140-160 MPa) and ductility (16-18 %). The sawtooth sections of the tensile curves indicate alternating localization of deformation and its relaxation.

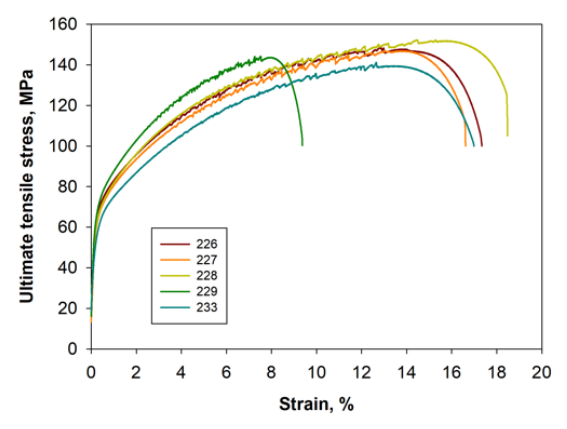


Fig. 9. Engineering strain-stress curves for the 226-233 samples



Fig. 10. Fractures tensile tests samples of the 226-233 (top to bottom) samples

Figure 10 presents the fractured tensile tests samples of the 226-233 states. Judging by these images, all samples failed outside the FSP region. Firstly, this indicates the strengthening effect of FSP, and secondly, the absence of defects introduced by FSP. On samples 226, 227 and 228 it is clearly visible that the localization of deformation occurred on both sides of the SZ. The wavy relief of localized deformation zones confirms the assumption of alternating localization and relaxation of deformation during tensile tests.

In this study, the implementation of various FSP schemes was carried out for two purposes: the first group of samples (226–228) was obtained for the purpose of testing the linear FSP regime, the second (229, 233) was obtained for the purpose of modifying the structure and properties in a certain volume of the sample. It is known that during FSP a number of processes might occur: plastic deformation, recovery, static and dynamic recrystallization, formation and decomposition of a solid solution, phase transformations [25-28]. All or some of these processes can occur simultaneously, forming different structures in the section of the SZ and TMAZ. However, judging by the results of the study, processes aimed at increasing the mechanical strength in the SZ predominate in the modes used. Despite the fact that in aluminium alloys an increase in electrical conductivity and electrical conductivity are considered competing properties [29], in this case it was possible to achieve an increase in microhardness (Fig. 7) and ultimate tensile strength (Fig. 9) in the SZ without a decrease, and in some cases - with increasing the electrical conductivity (Fig. 8). The results allow us to assert that for alloys of the Al-Mg-Si system (possibly for other thermally hardenable aluminium alloys as well), the given FSP processing modes allow obtaining a defect-free linear processing zone characterized by increased hardness, strength and electrical conductivity relative to the base material (226-228), as well as modifying a volume of material of a certain depth, which is also characterized by increased hardness, strength and electrical conductivity relative to the base material (229, 233).

Conclusions

In this work, five FSP schemes were implemented, three of them along a line, two along a surface, in the same process conditions: linear tool velocity of 200 mm/min and tool rotation speed of 1120 rpm. The authors have drawn the following conclusions:

- 1. Proposed FSP schemes implemented on a 10 mm thick conductive busbar made of commercial aluminium alloy AD31T (Al-Mg-Si system, analogue of AA6063) provided a defect-free structure.
- 2. Due to the implementation of each scheme in the volume of the treated area, due to plastic deformation, a decrease in the average grain size occurred, accompanied by hardening and a decrease in electrical conductivity. In thermally affected areas, located on the periphery of the stir zone, reverse processes occurred.
- 3. During mechanical tests, the destruction of samples of all proposed FSP schemes occurred outside the FSP zone, accompanied by alternating localization and relaxation of deformation.
- 4. Based on the research carried out, to create permanent connections of conductive aluminium busbars, it is recommended to use scheme 227 (parallel unidirectional passes with complete overlap of the second pass on the first), for strengthening treatment of the surface and near-surface layer scheme 233 (parallel unidirectional passes of the tool, with overlapping tracks by 5 mm at a given tool configuration).

References

- 1. Polmear I, StJohn D, Nie JF, Qian M. Light Alloys: Metallurgy of the Light Metals. 5th ed. Butterworth-Heinemann; 2017.
- 2. Verma RP, Kumar Lila M. A short review on aluminium alloys and welding in structural applications. *Mater. Today Proc.* 2021;46: 10687–10691.
- 3. Valiev RZ, Murashkin M, Sabirov I. A nanostructural design to produce high-strength Al alloys with enhanced electrical conductivity. *Scr. Mater.* 2014;76: 13–16.
- 4. Murashkin MY, Sabirov I, Medvedev AE, Enikeev NA, Lefebvre W, Valiev RZ, Sauvage X. Mechanical and electrical properties of an ultrafine grained Al-8.5wt. % RE (RE=5.4wt.% Ce, 3.1wt.% La) alloy processed by severe plastic deformation. *Mater. Des.* 2016;90: 433–442.
- 5. Orlova TS, Mavlyutov AM, Bondarenko AS, Kasatkin IA, Murashkin MY, Valiev RZ. Influence of grain boundary state on electrical resistivity of ultrafine grained aluminium. *Philosophical Magazine*. 2016;96(23): 2429–2444.
- 6. Belov N, Murashkin M, Korotkova N, Akopyan T, Timofeev V. Structure and properties of Al-0.6 Wt.%Zr wire alloy manufactured by direct drawing of electromagnetically cast wire rod. *Metals*. 2020;10(6): 769.
- 7. Belov N, Akopyan T, Korotkova N, Murashkin M, Timofeev V, Fortuna A. Structure and properties of ca and zr containing heat resistant wire aluminum alloy manufactured by electromagnetic casting. *Metals*. 2021;11(2): 236.
- 8. Murashkin MY, Sabirov I, Sauvage X, Valiev RZ. Nanostructured Al and Cu alloys with superior strength and electrical conductivity. *J. Mater. Sci.* 2016;51(1): 33–49.
- 9. Nicholas ED. Friction Processing Technologies. Welding in the World. 2003;47(11): 2–9.
- 10. Mishra RS, De PS, Kumar N. Friction Stir Processing. In: *Friction Stir Welding and Processing*. Cham: Springer; 2014. p.259–296.
- 11. Ma ZY. Friction stir processing technology: A review. Metall. Mater. Trans. A. 2008;39: 642-658.
- 12. Kurt A, Uygur I, Cete E. Surface modification of aluminium by friction stir processing. *J. Mater. Process. Technol.* 2011;211(3): 313–317.
- 13. Yadav D, Bauri R. Effect of friction stir processing on microstructure and mechanical properties of aluminium. *Materials Science and Engineering A*. 2012;539: 85–92.
- 14. Wang W, Han P, Peng P, Zhang T, Liu Q, Yuan SN, Huang LY, Yu HL, Qiao K, Wang KS. Friction Stir Processing of Magnesium Alloys: A Review. *Acta Metall. Sin. (Engl. Lett.)*. 2020;33: 43–57.
- 15. Isa MSM, Moghadasi K, Ariffin MA, Raja S, bin Muhamad MR, Yusof F, Jamaludin MF, Yusoff NB, Ab Karim S, Recent research progress in friction stir welding of aluminium and copper dissimilar joint: a review. *Journal of Materials Research and Technology*. 2021;15: 2735–2780.
- 16. Hajian M, Abdollah-Zadeh A, Rezaei-Nejad SS, Assadi H, Hadavi SMM, Chung K, Shokouhimehr M. Microstructure and mechanical properties of friction stir processed AISI 316L stainless steel. *Mater. Des.* 2015;67: 82–94.

- 17. SuJQ, Nelson TW, Sterling CJ. Friction stir processing of large-area bulk UFG aluminum alloys. *Scr. Mater.* 2005;52(2):135–140. 18. Su JQ, Nelson TW, Sterling CJ. Microstructure evolution during FSW/FSP of high strength aluminum alloys. *Materials Science and Engineering A.* 2005;405(1–2): 277–286.
- 19. Su JQ, Nelson TW, Sterling CJ. A new route to bulk nanocrystalline materials. *J. Mater. Res.* 2003;18(8): 1757–1760. 20. Liyakat NA, Veeman D. Improvement of mechanical and microstructural properties of AA 5052-H32 TIG weldment using friction stir processing approach. *Journal of Materials Research and Technology*. 2022;19: 332–344.
- 21. Sharma V, Gupta Y, Kumar BVM, Prakash U. Friction Stir Processing Strategies for Uniform Distribution of Reinforcement in a Surface Composite. *Materials and Manufacturing Processes*. 2016;31(10): 1384–1392.
- 22. Sarmadi H, Kokabi AH, Seyed Reihani SM. Friction and wear performance of copper-graphite surface composites fabricated by friction stir processing (FSP). *Wear*. 2013;304(1-2):1-12.
- 23. Medvedev AE, Atroshchenko VV, Selivanov AS, Bogdanov AR, Gorbatkov MV, Logachev YV, Lobachev VS, Sadrislamov AR. The influence of friction stir processing on the microstructure and properties of the AD31T alloy. *Materials Physics and Mechanics*. 2023;51(4): 38-49.
- 24. Memon S, Paidar M, Ojo OO, Cooke K, Babaei B, Masoumnezhad M. The role of stirring time on the metallurgical and mechanical properties during modified friction stir clinching of AA6061-T6 and AA7075-T6 sheets. *Results Phys.* 2020;19:103364.
- 25. Wakchaure K, Thakur A. Mechanical and microstructural characteristics of underwater friction stir welded AA 6061-T6 joints using a hybrid GRA-artificial neural network approach. *Materials Physics and Mechanics*. 2023;51(1): 119–141.
- 26. Soleymani S, Abdollah-Zadeh A, Alidokht SA. Microstructural and tribological properties of ultra fine grained hybrid composite produced by friction stir processing. *Materials Physics and Mechanics*. 2013;17: 6–10.
- 27. Lebaal N, Chamoret D, Schlegel D, Folea M. Thermal modelling of friction stir process (FSP) and identification parameters. *Materials Physics and Mechanics*. 2017;32: 14–20.
- 28. Mimmi A, Merzoug M, Ghazi A, Dellal N. Mechanical behavior of structures welded with friction stir lap welding process. *Materials Physics and Mechanics*. 2023;51(2): 151–163.
- 29. GENC M, Eloi P, Blandin JJ, Pascal C, Donnadieu P, De Geuser F, Lhuissier P, Desrayaud C, Martin G. Optimization of the strength vs. conductivity trade-off in an aluminium alloy designed for laser powder bed fusion. *Materials Science and Engineering: A.* 2022;858: 144139.

About Authors

Andrey E. Medvedev D Sc

Candidate of Physical and Mathematical Sciences Senior Researcher (Ufa University of Science and Technology, Ufa, Russia)

Valery V. Atroshchenko (1) Sc

Doctor of Technical Sciences

Head of Chair of Modern Methods of Welding and Structural Control (LLC Attestation Center Svarka Tech. Service, Ufa, Russia)

Aleksey S. Selivanov 🗓 Sc

Candidate of Technical Sciences

Head of Scientific and Technical Department (LLC Attestation Center Svarka Tech. Service, Ufa, Russia)

Albert R. Bogdanov

Bachelor Student (Ufa University of Science and Technology, Ufa, Russia)

Mikhail V. Gorbatkov (1) Sc

Engineer (LLC Krus-Zapad, Ufa, Russia)

Yury V. Logachev D Sc

Head of Research and Development Institute (LLC Attestation Center Svarka Tech. Service, Ufa, Russia)

Vladislav S. Lobachev (1) Sc

Engineer (LLC Attestation Center Svarka Tech. Service, Ufa, Russia)

Submitted: September 7, 2023 Revised: November 18, 2023 Accepted: February 8, 2024

Role of heat treatment on mechanical and wear characteristics of Al-TiC composites

- ¹ Department of Mechanical Engineering, R L Jalappa Institute of Technology, Karnataka, India
- ² Jawaharlal Nehru University, New Delhi, India
- [™] gowrishankartp01@gmail.com

ABSTRACT

The aim of this work is to explore the mechanical and wear properties of Al-TiC composites synthesized through liquid metallurgy technique. Al6061 was the matrix material used and Titanium carbide (TiC) is the reinforcement material. The composites were fabricated by adding TiC of 3, 6, 9 and 12 wt. % to Al6061. Thermal processing was used on the produced composite specimens to accomplish solutionization at 530 °C for a period of 8 hours and quenched in three different medias like air, water and ice. The effect of heat treatment and quenching media was evaluated in the research. In order to validate the effect of heat treatment as cast samples also studies for its wear properties. Results outcomes shows the better mechanical and wear characteristics compare to composites that haven't been heat treated. Also, superior mechanical and wear characteristics of composites are produced by ice quenching compare to air and water quenching. Wear out samples are investigated through SEM to study the mechanism of wear. Microstructure study was made, and it reveals good bond between matrix and reinforcement material.

KEYWORDS

Al6061 • TiC • liquid metallurgy • SEM • wear • hardness • mechanical properties

Citation: Gowrishankar TP, Sangmesh B. Role of heat treatment on mechanical and wear characteristics of Al-TiC composites. *Materials Physics and Mechanics*. 2024;52(1): 108–117. http://dx.doi.org/10.18149/MPM.5212024_10

Introduction

Due to the enhanced performance, MMCs have recently grown in popularity and have begun to replace traditional materials in a number of engineering fields. Due to their fundamental advantages like exceptional stiffness, strength, low density, light weight, resistance to corrosion, and resistance to wear, numerous industrial applications employ MMCs, including those in the automotive, aerospace, and military sectors [1-4]. Al-based MMCs are among the kinds of MMCs that are most commonly used because of their superior mechanical and tribological characteristics. The quantity, scope, composition, and weight distribution of reinforcements are just a few of the many variables affecting the characteristics of these AMCs. Al6061 is one of the many series of aluminium that are readily available and is a popular matrix substance used in the manufacture of MMCs due to its high corrosion resistance, weldability, and machinability. Alumina, TiC, silicon carbide, Boran carbide, and other materials are frequently employed as reinforcements when Al 6061 is used to create composites that enhance a variety of mechanical qualities [3,5-8]. These particles specifically improve Al6061's mechanical and wear resistance. MMCs can be produced using a variety of methods, including the PM process, liquid phase fabrication vacuum casting, squeeze form technology, compo casting, and stir casting, and more. Because it is easy to

[©] T.P. Gowrishankar, B. Sangmesh, 2024.

obtain, simple to manufacture, and more affordable than other production procedures, the most common technique used to make AMCs is stir casting [8-12].

The majority of the basic materials have unusual properties. Because of some intrinsic traits and attributes that may not be suited for ordinary uses, the majority of them that are currently available may not be physically viable for many engineering purposes. As a result, materials are frequently thermally treated to increase their strength, making them physically and structurally viable for a larger range of industrial uses. The heat treatment procedure has the potential to change the microstructure of AMCs, strengthening its mechanical attributes. The solution treatment step of the thermal treatment procedure is followed by the quenching in different medias. Literature reveals that heat treatment positively affects the properties of composites. There is a wealth of information on metal alloys with an aluminium foundation that contain alumina, silicon carbide, boron carbide, and magnesia, however there aren't many experiments on titanium carbide particles. Although the type of reinforcement and the synergistic effect of heat treatment both significantly influence the ultimate mechanical properties of composites, little is known about the heat treatment of Al-based composites. As a result, using the liquid metallurgical approach, composites have been created in the current experiment by adding TiC particles to the Al6061 matrix. Analysis of the effects of heat treatment and quenching media on the performance of Al6061-TiC MMCs is the main goal of the study. TiC of 0-12 wt. % added to Al6061 in a stage of 3 wt. % were used in the testing. Mechanical and wear properties were then assessed and contrasted with the composites that hadn't been heated. On hardness and wear qualities, studies and reports on the effects of heat treatment and quenching medium were made.

Materials and Methods

Due to the accessibility and ease of use, the stir casting approach has been used to create MMCs that contain Al6061 and TiC at concentrations of 0-12 wt. %. Al6061 was the matrix material used in the current study. Properties and chemical composition of Al60631 was shown in Tables 1 and 2. TiC particles with a size range of 10-20 µm are utilised as reinforcement in the ongoing research work to produce composite. Properties of TiC was shown in Table 3. In a stage of 3 wt. %, TiC particles were blended at a rate of 0-12 wt. % to Al6061. Utilising a CNC machine, samples for various testing have been prepared using the created composites. To find the distribution of TiC particles across the matrix material and quantify wear behaviour, a microstructure investigation of produced sample specimens was done. In order to determine the configuration of composites, energy dispersive spectroscopy (EDS) and optical microscope were also used. Scanning electron microscopy (SEM) analysis is made to study the mechanism of wear. Therefore, they are contrasted with the basic alloy material in order to support the experimental results.

In the beginning, known quantities of Al6061 alloy rods were put into the graphite crucible and then into the electric furnace. At 850 °C, the alloy was melted and fine vortices began to form as a result of mechanical stirring. In order to increase the degree of wetting, in a different container, preheating of the TiC particles was carried out at 700 °C. The preheated TiC was then put into a furnace containing molten Al6061 alloy after being stirred to create a fine vortex. A steady feeding rate and an electric stirrer

speed of 450 rpm were used during the addition of reinforcement. By moving the molten metal from the crucible into the cavity of the mould at room temperature, the metal was given time to solidify. The same procedure was repeated for various TiC fractions, including 3, 6, 9, and 12 wt. %. Table 4 displays the configurations of the MMCs used in the ongoing research work.

Table 1. Properties of Al6061

Properties	Values
Density, g/cm ³	2.70
Melting point, °C	585.00
Tensile strength, MPa	124.00
Yields strength, MPa	55.00
Young's modulus, GPa	68.00
Poison's ratio	0.33
Thermal conductivity, W/mK	180.00
Shear strength, MPa	83.00

Table 2. Configuration of Al6061 by wt. %

Constituents	Mg	Cu	Fe	Cr	Si	Mn	Ti	Zn	Al
Percentage	1.1500	0.2750	0.1060	0.2010	0.5800	0.0014	0.1300	0.2500	Balance

Table 3. Properties of titanium carbide

Properties	Values
Formula	TiC
Density, g/cm ³	4.93
Size mesh	325
Purity, %	99.10
Melting point, °C	3155.00
Vickers hardness, VH	3200.00
UTS, MPa	240.00
Compressive strength, MPa	3700.00

Table 4. Composite configuration

Specimen	Composite
A	Al6061
В	Al6061+3 wt% TiC
С	Al6061+6 wt% TiC
D	Al6061+9 wt% TiC
E	Al6061+12 wt% TiC

To create the specimens, the designed composites were machined on a CNC machine. In order to analyse the physical and microstructural characteristics that match the test rig standards. To find the scattering of reinforcing particles in an alloy, the optical metallurgical microscope was used in the microstructural examination. The samples were polished for microstructure analysis, and the polished surface was etched using the conventional metallographic procedure. The samples were polished using the conventional metallographic method in order to examine their microstructure, and the polished surface was etched with Keller's reagent.

By using a weight of 500 g and a dwell time of 15 s, the Vickers' hardness tester was utilised to determine the microhardness of produced MMCs. For data reproducibility, three trials were conducted for each test condition in order to reduce experimental error and uncertainty. The outcome is determined using the value's arithmetic average. The average value from the dataset, a standard deviation of one on either side, is used to plot the graphs. Utilising a pin on disc device, composites have had their wear rate assessed. A force of 30 N, a velocoty of 100 rpm, and a sliding distance of 1000 m are used to measure the wear rates. The specimens were created in accordance with ASTM (G99-05) requirements for a length of 30 mm and a diameter of 8 mm. Figure 1 shows the sample that was utilised to test the wear properties. At the same time, the coefficient of friction (COF) of aluminium and its composites was also observed. SEM was used to do a morphological analysis on worn-out samples in order to investigate the wear mechanism.



Fig. 1. Wear test specimens

Heat treatment has been applied to the produced composites. The heat treatment for solutionizing was carried out in a muffle furnace. Al6061 and Al6061-TiC composites that have been cast are first given an 8-hour solutionizing treatment in a muffle furnace at a temperature of 530 °C, followed by an immediate quenching in three distinct media, like air, water and ice. In order to evaluate how heat treatment and quenching media affect composites, the microstructural and wear behaviour of both heat-treated and non-heated MMCs were examined.

Results and discussion

Examination of microstructure

In the current study, hybrid MMCs are created by combining Al6061 with micron-sized TiC particles. With the aid of an optical microscope, a morphological study has been carried out to look at the dispersion of reinforcing materials into Al6061. The corresponding optical micrographs of Al6061 with 0–12 % TiC particles are shown in Fig. 2. The accurate and uniform dispersion of TiC particles over the matrix alloy is shown in Fig. 2. A homogenous dispersion of reinforcing elements has been seen in optical micrographs. Due to the swirling effect created during the production process, this has happened. Additionally, the key factor for the homogenous dispersion of TiC in alloy is the existence of a component of magnesium in the matrix alloy [13–16].

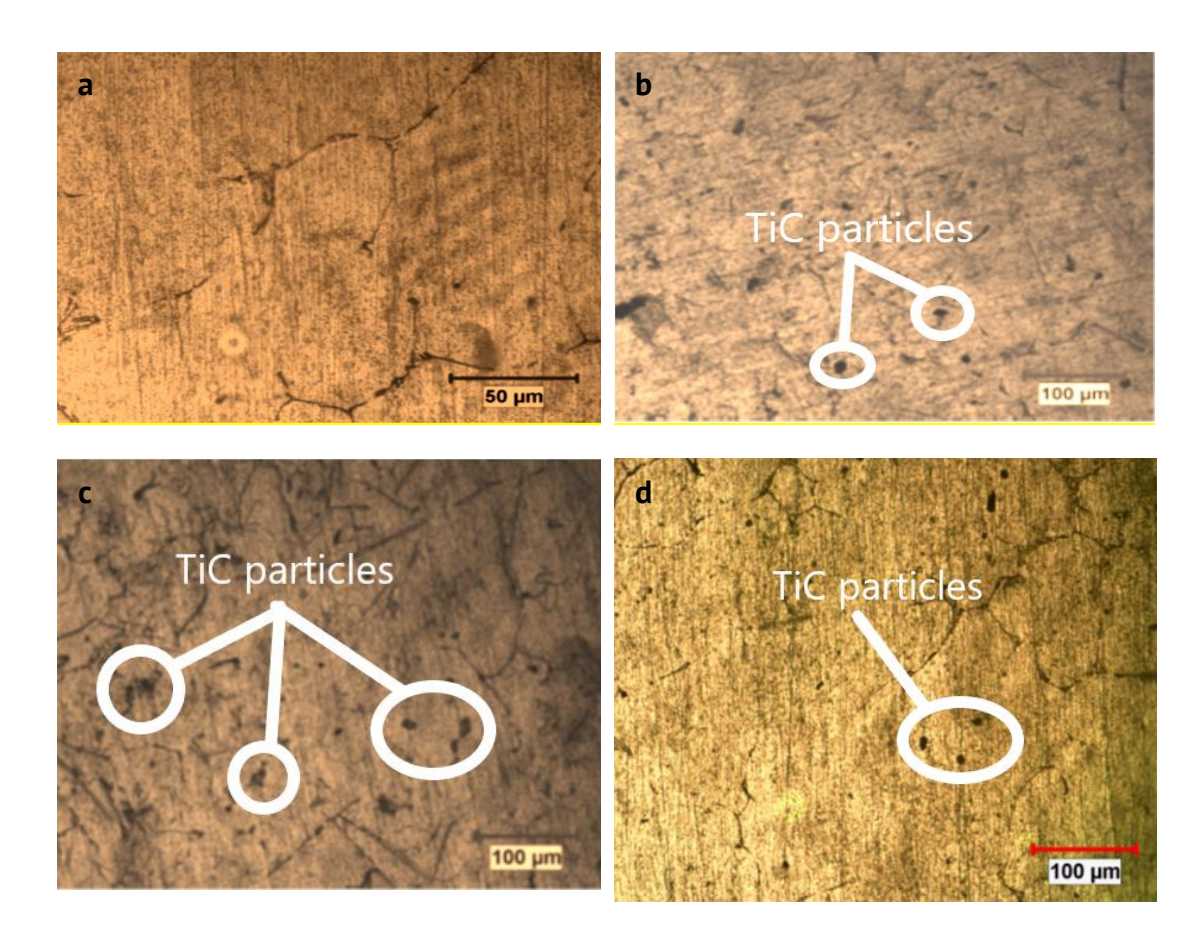


Fig. 2. Microstructure of composites (a) Al6061, (b) Al6061+3 % TiC, (c) Al6061+6 % TiC, (d) Al6061+9 % TiC

The EDS spectrum of generated MMCs, which is shown in Fig. 3, identifies the presence of the elements used in the current investigation to create composites. The incorporation of TiC reinforcements has been noticed in the EDS spectrum's Ti and C elements. The presence of all the components predicted in the paper was confirmed by the Al6061's high intensity peak that was also seen in the spectrum.

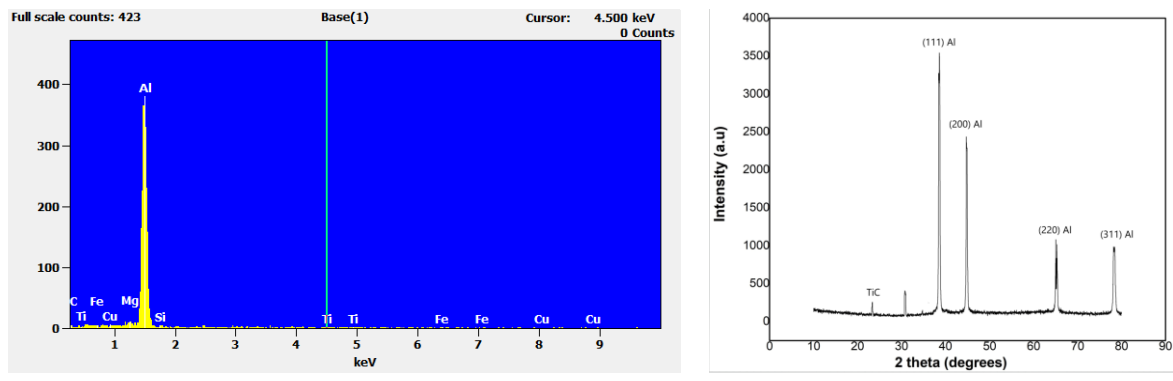


Fig. 3. EDS spectrum of composites

Fig. 4. XRD pattern of composites

An appropriate sample was created in accordance with the guidelines in order to perform the X-ray diffraction study. Figure 4 depicts an X-ray diffraction (XRD) pattern for the provided material to illustrate its quality and attest to the presence of the constituent elements used to construct the present composite material. Figure 4 displays multiple

peaks for Al6061 and TiC particulates at the same time as well as peaks at (111), (200), and (220). Due to Al's low sterility and TiC's higher purity, this occurs. This is likewise a result of the Al and TiC particulates samples being oriented in the (111), (200), and (220) planes. After comparing the experimental peaks attained and the standard peaks, components such as Al and TiC were found. TiC reinforcement is present in the ongoing study, according to the X-ray diffraction results.

Hardness

The hardness of the produced composites is assessed using the Vickers' hardness tester. The microhardness of composites without and with heat treatment condition is shown in Fig. 5. Studies demonstrate that hardness is significantly increased when TiC is added to Al alloy. Up to 9 weight percent, adding TiC to Al6061 results in an increase in hardness; after that, it decreases. Composites lose hardness as a result of reinforcement agglomeration caused by increased TiC buildup in the matrix alloy. Similar outcomes were attained for all of the case studies involving both heat-untreated and heat-treated composites. Additionally, studies are conducted to determine how heat treatment and quenching media affect the hardness of produced composites. By solutionizing heat treating composites and immediately quenching them in air, water, or ice, the hardness of the material is significantly increased. This is because Al and its composites have been solutionized, allowing the highest concentration of the hardening solute to dissolve into solution. Additionally, quenching media influences how hard composites are. For Al+9%TiC composites that were ice quenched, a higher hardness was achieved. The hardness and mechanical qualities of composites can be increased through quick quenching, which produces a saturated solution. Because of this, ice-quenched composites have superior mechanical properties compare to air and water quenched composites. When compared to unheated Al alloy, ice-quenched Al+9%TiC composites show a hardness improvement of about 43 %. Similar kind of outcomes is seen in [17-23].

Wear

The wear rate of composites was investigated using a pin on the disc wear tester with a load of 30 N, a velocity of 100 rpm, and a sliding length of 1000 m. Figure 6 illustrates how quickly composite materials wear down with and without heat treatment. The findings indicate that the volume loss per unit distance decreases as TiC reinforcement are added to the Al6061 alloy. Increasing the weight fraction of TiC in Al alloy reduces the rate at which composites wear out. This decrease in composite wear rate is seen up until the inclusion of 9 wt. % TiC; however, TiC concentration above 9 wt. % causes an increase in wear rate. This is due to the fact that an agglomeration with a greater TiC concentration in Al alloy can be seen in the microstructure. It has been discovered that the wear rate of composite materials can be decreased by mixing hard TiC particles with Al6061.

Additionally, it is evident that heat treatment has a favourable impact on composites capacity to resist abrasion. Wear resistance of composites is improved by solutionizing heat treatment at 530 °C for 8 hours, followed by rapid quenching in three distinct mediums. In all the examples that were examined, it was found that the addition of TiC particles decreased the composites' rate of wear up to 9 wt. % of TiC. The

solutionizing process causes the intermetallic phase of Mg and Si to develop, which is harder than Al and exhibits better wear resistance compare to un heat treated composites. The impact of the quenching medium on the composites' wear rate was also researched. For all quenching media examined, such as air, water, and ice, the wear rate of aluminium alloy and its composites reduces.

It was discovered that Al6061 and its composites wear down at the least rate when the composites are ice quenched compare to air and water. Compared to air and water quenching, the ice quenching procedure produces composites with superior wear resistance since the composites cool down more quickly following solutionizing treatment. Intermetallic precipitations from the extremely saturated solid solution will not be able to form during the quenching process due to the fast cooling. Minimum wear rate is observed for Al+9 % TiC for all cases tested. When compared to unheated Al6061 alloy, wear resistance for ice quenched Al+9 % TiC composites was found to be improved by about 62 %. Results are familiar in the work [24–26].

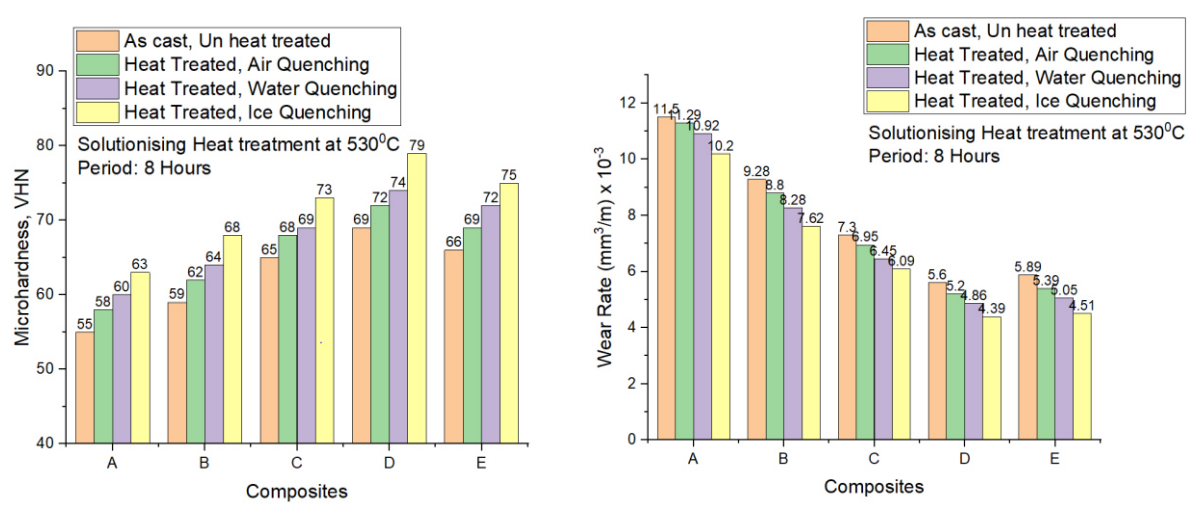


Fig. 5. Microhardness of composites

Fig. 6. Wear rate of composites

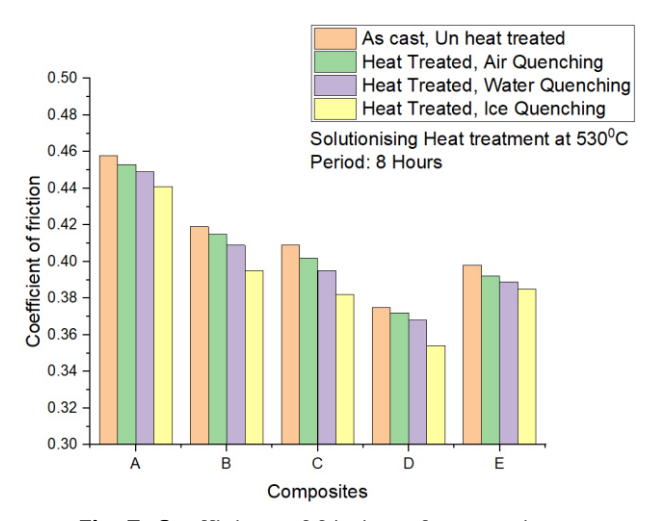


Fig. 7. Coefficient of friction of composites

Coefficient of friction

The typical coefficient of friction for composites is shown in Fig. 7. It is amply demonstrated that adding TiC lowers the coefficient of friction. When compared to unreinforced Al6061 alloy, the coefficient of friction (COF) of composites is lower. For Al6061 alloy, a high COF was seen, while reinforced composites showed a low COF. COF was found minimum for Al+9 % TiC. As a result of the harder TiC reinforcement sharing its strength with the Al alloy, the addition of TiC boosts the COF of the alloy. Additionally, solutionizing heat treatment is seen to significantly improve composites' COF. For all evaluated examples of heat treatment Al+9 % TiC composites, COF is shown to be low. It was also looked at how quenching mediums affected COF and discovered that COF of composites decreased across the board. When Al6061 and its composites are ice quenched, the COF of the composites decreases at the least rate when compared to air and water, it was found. Comparing ice quenched Al+9 % TiC to unheated Al alloy, COF drops by about 23 %.

Figure 8 displays the SEM micrographs of the worn-out surfaces acquired under a load of 30 N at a speed of 100 rpm. The composites wear down more quickly as a result of the accumulation of harder TiC particles and an oxide layer between the pin and the disc. The samples' surfaces are all marked with scratches and grooves, as seen in the figure. Furthermore, the particles separate from the outer layer of the samples as a result of plastic deformation, which shows that the composites' surface adhesive has worn down. Researchers [27–30] have made similar observations. According to the research, the presence of hard ceramic particles enhances the wear properties of composites, increasing the wear resistance of MMCs.

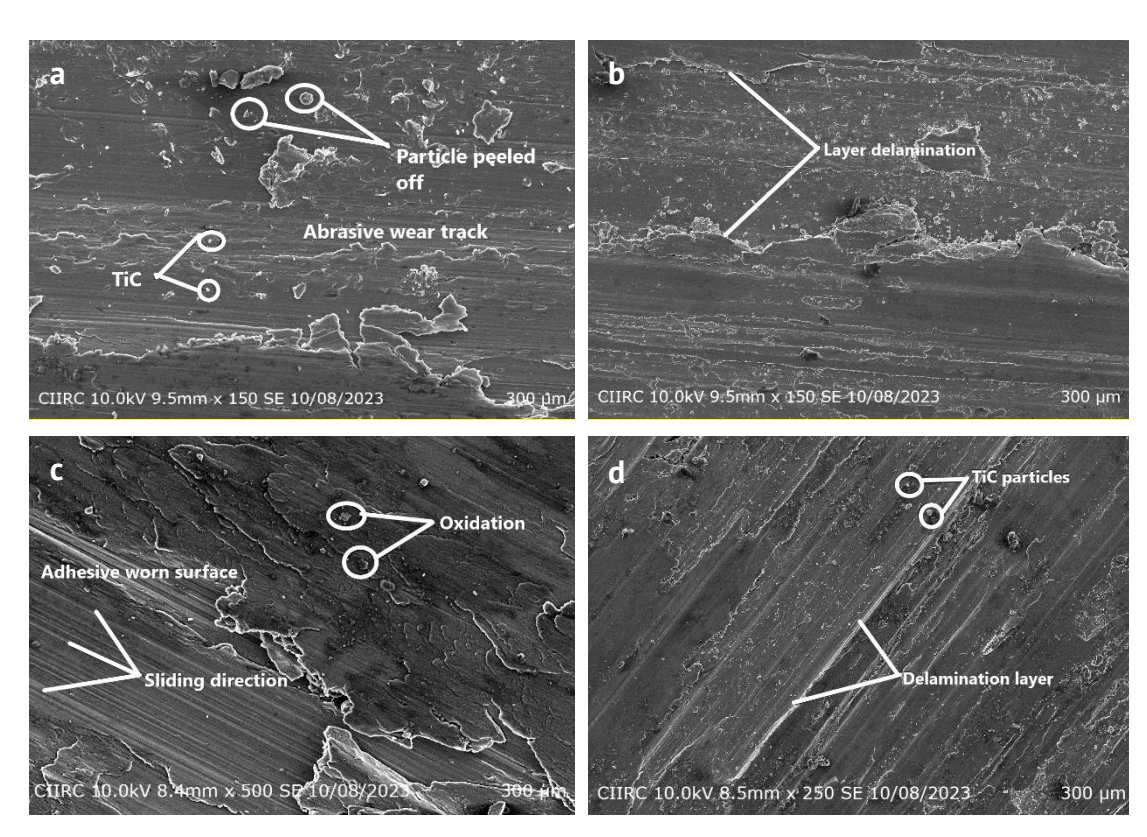


Fig. 8. SEM worn out surfaces of composites (a) Al6061+3%TiC, (b) Al6061+6%TiC, (c) Al6061+9%TiC, and (d) Al6061+12%TiC

Conclusions

- 1. Analysis of the role of thermal treatment and quenching media for Al6061 mixed with TiC MMCs is the main goal. To create composites, the stir casting technique was used, and the microstructure examination revealed a uniform distribution of reinforcements.
- 2. The EDS spectrum further supports the existence of study-related reinforcements.
- 3. The microhardness of composite materials increases up to a TiC content of 9 wt. % in an Al alloy; after that, it declines.
- 4. The hardness of composites is also influenced by heat treatment and the quenching media. The composites that have undergone ice quenching and contain 9 wt. % TiC are the toughest.
- 5. The addition of TiC to the Al alloy significantly reduces the wear rate of composite materials. For all of the evaluated scenarios, Al+9 % TiC composites showed the lowest wear rate.
- 6. The heat treatment and quenching medium has a considerable impact on the alloy and its composites' wear behaviour.
- 7. Ice quenched composites exhibits superior wear resistance compare to air and water quenched composites.

References

- 1. Prabhudev MS, Kori SA. Dry sliding wear characteristics of Al-7Si-0.3Mg alloy with minor additions of magnesium at high temperature. *Tribology Materials, Surfaces & Interfaces*. 2022;16(1): 2–9.
- 2. Arunprasath K, Amuthakkannan P, Vijayakumar M, Sundarakannan R, Selwin M, Kavitha S, Singh Lavish Kumar. Effect of Mechanical Properties of AL7075/Mica Powder Hybrid Metal Matrix Composite. *Materials Physics and Mechanics*. 2023;51(1): 142–150.
- 3. SB Boppana, S Dayanand, MRA Kumar, Kumar V, Aravinda T. Synthesis and characterization of nano graphene and ZrO2 reinforced Al 6061 metal matrix composites. *Journal of Materials Research and Technology*. 2020;9(4):7354–7362.
- 4. Gireesh CH, Prasad KGD, Ramji K, Vinay PV. Mechanical Characterization of Aluminium Metal Matrix Composite Reinforced with Aloe vera powder. *Materials Today: Proceedings*. 2018;5(2): 3289–3297.
- 5. Gowrishankar TP, Manjunatha LH, Sangmesh B. Mechanical and wearbehaviour of Al6061 reinforced with graphite and TiC hybrid MMC's. *Materials Research Innovations*. 2019;24(3): 179–185.
- 6. Baradeswaran A, Perumal AE. Wear and mechanical characteristics of Al 7075/graphite composites. *Composites Part B: Engineering*. 2014;56: 472–476.
- 7. Mandri AD, Colombo DA, Brühl SP, Dommarco RC. Sliding friction and wear behaviour of ion nitrided and TiN coated AISI 4140 steel. *Tribology Materials, Surfaces & Interfaces*. 2022;16(4): 373–383.
- 8. Gowrishankar TP, Manjunatha LH, Sangmesh B. Heat treatment and its effect on mechanical and wear properties of Al6061/Gr/TiC hybrid MMCs. *Int. J. Microstructure and Materials Properties*. 2020;15(4): 316–331.
- 9. Ahamed A, Khan ARA. Effect of Heat Treatment on Slurry Erosive Wear Behaviour of Al 6061 Based Composites. *International Journal of Applied Science and Engineering*. 2018;15(1): 71–82.
- 10. Gobalakrishnan B, Lakshminarayanan PR, Varahamoorthi R. Combined Effect of TiB₂ Particle Addition and Heat Treatment on Mechanical Properties of Al6061/TiB2 In-Situ Formed MMCs. *Journal of Advanced Microscopy Research*. 2017;12(3): 230–235.
- 11. Chandra BT, Shankar HSS. Effect of Heat Treatment on Dry Sand Abrasive Wear Behavior Of Al7075-Albite Particulate Composites. *Materials Today: Proceedings*. 2018;5(2): 5968–5975.
- 12. Kumar A, Gautam RK, Tyagi R. Dry sliding wear characteristics of in situ synthesized Al-TiC composites. *Composite Interfaces*. 2016;23(6): 469–480.
- 13. Chen JP, Gu L, He GJ. A review on conventional and nonconventional machining of SiC particle-reinforced aluminium matrix composites. *Advances in Manufacturing*. 2020;8: 279–315.
- 14. Rajesh S, Suresh S, Nithyananth SB, Sivakumar S, Prabhusubramaniam S. Influence and Wear Characteristics of TiC Particle in Al6061 Metal Matrix Composites. *International Journal of Applied Engineering Research*. 2018;13(9): 6514–6517

- 15. Dwivedi SP, Kumar A. Development of graphite and alumina reinforced aluminium based composite material. *Materials Today Proceedings*. 2021;34(3): 825–828.
- 16. Rajkeerthi E, Satyanarayan CP, Jaivignesh M, Pradeep N, Hariharan P. Effect of heat treatment on strength of aluminium matrix composites. *Mater Today Proc.* 2021;46: 4419-4425.
- 17. Viswanatha BM, Kumar MP, Basavarajappa S, Kiran TS, Kanchiraya S. Effect of heat treatment and ageing on microstructure for hypoeutectic Al-7Si alloy and hybrid metal matrix composites. *International Journal of Engineering, Science and Technology.* 2021;13(4): 1–11.
- 18. Karuppusamy T, Velmurugan C, Thirumalaimuthukumaran M. Experimental study on the mechanical properties of heat treated aluminium composites. *Mater. Res. Express.* 2019;6(9): 096552
- 19. Ravikumar M, Reddappa HN, Suresh R, Reddy MS. Experimental studies of different quenching media on mechanical and wear behavior of Al7075/SiC/Al2O3 hybrid composites. *Frattura ed Integrità Strutturale*. 2020;15(55): 20–31.
- 20. Ganesh K, Hemachandra Reddy K, Sudhakar Babu S, Ravikumar M. Study on microstructure, tensile, wear, and fracture behavior of A357 by modifying strontium (Sr) and calcium (Ca) content. *Materials Physics and Mechanics*. 2023;51(2):128–139.
- 21. Kumaraswamy J, Kumar V, Purushotham G. Evaluation of the microstructure and thermal properties of (ASTM A 494 M grade) nickel alloy hybrid metal matrix composites processed by sand mold casting. *International Journal of Ambient Energy*. 2022;43(1): 4899–4908,
- 22. Anil KC, Veena TR, Purushotham G, Kumar S. Investigating the mechanical properties of Al 7075 alloy for automotive applications: synthesis and analysis. *Evergreen*. 2023;10(3): 1286–1295.
- 23. Purushotham G, Hemanth J. Study of Physico-Chemical Properties of Monel M-35-1 Nickel Alloy-Fused Silica Metal Matrix Composite for Marine Application. *Indian Journal of Advances in Chemical Science*. 2016;4(3): 235–240. 24. Ravikumar M, Suresh R. Study on mechanical and machinability characteristics of n-Al2O3/SiC-reinforced Al7075
- composite by design of experiment technique. *Multiscale and Multidiscip. Model. Exp. and Des.* 2023;6: 747–760.
- 25. Ravikumar M, Chethana KY, Vinod BR, Suresh R. Nano sizedSiC Gr particulates reinforced Al7075 hybrid composite: Experimental studies and analysis of quenching agents. *Jurnal Tribologi*. 2023;38: 82–99. 26. Ravikumar M, Reddappa HN, Suresh R, Gangadharappa M. Effect of Heat Treatment on Tensile Strength of
- Al7075/Al203/SiCp Hybrid Composite by Stir Casting Technique. *Materials Today: Proceedings*. 2018;5(10). 22460–22465.
- 27. Fattahi Z, Sajjadi SA, Babakhani A, Saba F. Ni–Cr matrix composites reinforced with nano and micron sized surface-modified zirconia: Synthesis, microstructure and mechanical properties. *Journal of Alloys and Compounds*. 2020;817:15275.
- 28. Reddy KSK, Kannan M, Karthikeyan R, Laxman B. Evaluation of thermal and mechanical properties of Al7475 alloy reinforced with SiC and graphite. *Materials Today: Proc.* 2020;26(2): 2691–2696
- 29. Harish RS, Reddy S, Kumaraswamy J. Wear characterization of Al7075 Alloy hybrid composites. *Metallurgical and Materials Engineering*. 2022;28(2): 291–303.
- 30. Zielinska M, Yavorska M, Porêba M, Sieniawski J. Thermal properties of cast nickel based superalloys. *Archives of Materials Science and Engineering*. 2010;44(1): 35–38.

About Authors



T.P. Gowrishankar 🔟 Sc

PhD, Assistant Professor (Departrment of Mechanical Engineering, RL Jalappa Institute of Technology, Karnataka, India)



B. Sangmesh 🔟 Sc

PhD, Associate Professor (Jawaharlal Nehru University, New Delhi, India)

Submitted: May 11, 2022 Revised: September 6, 2022 Accepted: February 28, 2023

Influence of aging on fatigue strength of carbon fiber reinforced plastics

A.R. Arutyunyan [™] 🗓

St. Petersburg State University, St. Petersburg, Russia

[™] belov@crys.ras.ru

ABSTRACT

Various composite materials are implemented in aircraft, rocket and automobile construction, shipbuilding, railway transport, tidal power and others due to their high strength to weight ratio, superior fatigue strength, and design flexibility. These materials are used in critical areas of engineering practice, so this makes their long-term aging and fatigue characteristics of paramount importance. At the same time, the characteristics of these materials essentially changed after long-term operation. Thus, investigations of aging of these materials are much needed. Experimental studies on alternation of cyclic loading, climatic and thermal aging were conducted to study the characteristics of unidirectional carbon fiber reinforced plastic of the T107/ON190/R132436 mark. Experimental results shown a significant hardening during cyclic experiments, which considerably depends on the aging program.

KEYWORDS

composite materials • carbon fiber reinforced plastics • degradation • climatic aging • deformation aging • fatigue strength Citation: Arutyunyan AR. Influence of aging on fatigue strength of carbon fiber reinforced plastics. *Materials Physics and Mechanics*. 2024;52(1): 118–125. http://dx.doi.org/10.18149/MPM.5212024_11

Introduction

Polymers and polymer-based composite materials are being intensively implemented in almost all areas of industry and construction: in aircraft, rocket and automotive construction, shipbuilding, railway transport, agricultural machinery production, tidal power, as well as in the production of sports equipment. These materials have a high strength-to-weight ratio, superior fatigue strength and design flexibility. Considered applications frequently have a very high performance demand, making the long-term characteristics of polymer and composite materials of paramount importance. At the same time, they were subjected to degradation due to environmental factors, including light, temperature, stress, and others. During the aging, the degradation of polymer and composite materials leads to significant changes of their physical and mechanical properties [1–5].

Polymer and polymer-based composite materials are usually tested for a long time in a liquid medium at certain temperature conditions. This method of evaluation of polymer and composite materials service conditions is termed as hygrothermal aging. Hygrothermal aging at high temperature accelerates the aging process. The natural seawater, distilled water, tap water, demineralized water, alkaline and acid environment, saline solution and any other chemical based applications can be used as aging agents. The effect of aging on the mechanical properties of the fiber reinforced plastics under various environmental factors and loading conditions was investigated in [6-18].

In the study [6], the flexure, tensile and compressive behavior of the hygrothermal aged carbon fiber reinforced epoxy composite was studied as a function of the absorbed moisture content. Composite specimens were aged by immersing them in the natural seawater at 60°C for different time intervals. The flexure, tensile and compressive strength of the material showed an inverse correlation with the absorbed moisture content, whereas the elastic modulus showed negligible correlation. Similarly, the tensile and flexure failure strain showed an inverse relationship with the absorbed moisture content.

The paper [7] was focused on the effect of hygrothermal aging on the mechanical properties of mixed short fibre/woven composite materials in different environments, i.e. moisture and temperature, for different durations. The seawater is the most aggressive medium that makes materials less resistant than distilled water and makes them brittle. The obtained results, follows that the presence of water in the composite material causes a deterioration of the mechanical properties. The penetration of water or moisture is through the outer surface of the composite within the structure. The fibers do not absorb the solvent, while the matrix is capable of absorbing them through the free volume and the micro-cavities. The water interacts with the matrix, with the reinforcement and the interfacial zones, which can in particular degrade the bonds and thus causes an irreversible degradation of the properties of the composite. In addition, the material undergoes the effect of plasticization, i.e. a modification of the structure, which can result in the simultaneous decrease of the plasticity threshold or damage. The temperature has a negative influence on the resistance of materials. A sharp drop in mechanical properties as follows: 67 % of the elastic stress, 59 % the ultimate stress and 18 % of the elastic modulus is observed during a long duration of temperature (one year). In some cases (1 month), the temperature serves to improve the properties of the material deformations due to the hardening of the material. Indeed, the increase in temperature induces, in general, a softening of the materials and a decrease of the yield point.

To characterize the durability of carbon fiber reinforced plastics (CFRP) and glassy fiber reinforced plastics (GFRP) composites to hygrothermal environment a comprehensive experimental work was carried out in [8]. Composites were directly placed in water at 80°C for accelerated hygrothermal treatment. Moisture absorbed during hygrothermal ageing improved the impact properties of CFRP composites. After absorbing 3.149 wt. % of moisture, the peak contact force of CFRP laminates during impact test increased by 20.60 %. After hygrothermal treatment (in 80 °C water for 912 h), the strength of GFRP composites decreased by 28.53 %. For GFRP laminates, the peak contact force during impact test decreased by 33.44 %. After removing the moisture absorbed, the tensile strength of CFRP composites was recovered to 95.75 % of its original value. The strength retention rate of GFRP composites was only 74.65 %. The modulus of glass fibers and GFRP composites remained nearly unchanged. In contrast, their tensile strength decreased significantly. Growth of surface flaws is considered as the main mechanism for the decrease in strength of glass fibers in the current investigation.

The effect of seawater immersion on the durability of glass- and carbon-fiber reinforced polymer composites was experimentally investigated in [9]. The materials studied were glass/polyester, carbon/polyester, glass/vinyl ester and carbon/vinyl ester composites used in marine structures. When immersed in seawater at a temperature of 30°C for over two years, the composites experienced significant moisture absorption and

120 A.R. Arutyunyan

suffered chemical degradation of the resin matrix and fiber/matrix interphase region. This degraded the flexural modulus and strength of the composites, although the mode I interlaminar fracture toughness was only marginally affected by immersion.

In the study [10] the aging of an epoxy resin and its CFRP composites in water, acidic, and alkaline solutions at different temperatures was explored. The tensile tests revealed that degradation adversely affected the tensile strength, although the tensile modulus values did not significantly decrease throughout the aging study. According to the thermal and mechanical analysis, degradation occurred in a higher rate as the exposure temperature is higher. In general, from the thermal and mechanical analysis it was observed the rate of degradation is accelerated at elevated temperature and is obvious in acidic conditions. The degradation of the composite materials can be attributed to the deterioration of the resin matrix and debonding at the fiber-resin interface. This damage was visible in the morphological analysis. By correlating the experimental data and prediction results, it can be concluded that the CFRP composite materials may need to be developed further to withstand acidic media and ensure a longer service life.

The effect of specimen thickness on the water absorption and flexural strength of wet lay-up CFRP laminates immersed in distilled water or alkaline solution was investigated in the study [11]. The water uptakes and flexural strength retentions of wet lay-up CFRP laminates were greatly affected by the adopted specimen thicknesses. For CFRP laminates conditioned in distilled water or alkaline solution up to a duration of 180 days, the water uptake decreased in the early stage of immersion and increased in the later stage of immersion with the increase of specimen thickness. Meanwhile, the flexural strength retention generally increased as the specimen thickness increased.

Two different quasi-static crushing tests have been performed in [12] to investigate the effects of humid ageing on the crashworthiness behaviors of the CFRP polymer laminates. Four different types of specimens made from T700/M21 and Cytec woven CFRP materials were placed in a humidity-controlled chamber at 90 % relative humidity (RH) and 80 °C until they reach saturation before performing the crushing tests. From the result obtained, the behavior of the force-displacement curves, crushing morphologies and damage mechanisms between humid ageing specimens and the same specimens are very similar. Nevertheless, in terms of ply mean crushing stress analysis it is quantitatively proven that there are drops nearly to 10 % on the CFRP laminates have been exposed to the humidity environment.

The results of studying the climatic aging of aviation polymer composite materials (PCMs) performed over the last 5-8 years was analyzed in [13]. These results expand the understanding of the mechanisms of the physicochemical transformations under the influence of aggressive environmental factors. The new information is useful in assessing the expected effects of changing the most common deformation-strength parameters of PCMs with allowance for the type of material, the measured mechanical index, the exposure time, and climatic conditions. If the results of selective measurements of the strength or the elastic moduli of a particular material fall out of a general trend, this is the basis for taking into account possible methodological errors in measurements. The traditional control of changing one or several mechanical properties at room temperature is insufficient to characterize the climatic resistance of PCMs. To plan climatic tests of new

promising PCMs, one can take into account in advance that the ultimate bending strength changes most strongly and the bending elastic modulus is the most stable property.

Investigation of the water uptake and interlaminar shear strength behavior of CFRP laminates after ageing was performed in [14]. Distilled water, 1.0 % saline solution and pH \approx 4.0 \pm 0.2 acidic solution were prepared to treat the samples for 12 weeks. Short beam shear tests were performed to evaluate the interlaminar shear strength (ILSS). The experimental results show that saline and acidic solution can reduce the water uptake capacity of CFRP laminate compared with distilled water. Delamination in layer and between layers and fiber-matrix interface debonding were the main environmental damages. After 12 weeks of ageing, the ILSS reduction of specimens aged in acidic solution had the largest reduction (21.52 %), followed by saline solution (15.65 %), and distilled water had the smallest reduction (10.59 %). However, there was an increase in ILSS at the early acidic and saline ageing, while a stable in distilled water ageing, which may be a new way to strengthen the CFRP in future. It was also found, that the ILSS degraded nonlinearly with the increasing of water uptake of matrix. The results would quide the application of CFRP in engineering filed.

In the paper [15], the tension-tension (T-T) and tension-compression (T-C) fatigue properties and static strength of hygrothermal aged laminates were investigated. A tensile and compressive strength reduction of laminates is observed. Based on run-out specimen data, an average 18 % reduction in fatigue strength was shown. The damage initiation and fatigue life reduction of aged specimens were higher in T-C loading as compared to T-T loading.

Experiments on accelerated aging of carbon/epoxy and glass/epoxy laminates in an artificial seawater environment with 3.5 % salinity were carried out at 60 °C for 45 days [16]. Mechanical experiments including tensile and 3-point bending tests were conducted on the reference/dry and aged standard specimens at room temperature and at 60 °C. The loss in the mechanical properties including tensile and flexural strength of carbon/epoxy and glass/epoxy laminates at 60 °C and ambient temperature is observed.

The work [17] is devoted to investigation of the static and fatigue three-point bending behavior of the carbon fiber reinforced polymer laminates. Two types of layup (unconstrained and constrained) under the dry and hygrothermal aged conditions were considered. Fatigue behavior was investigated at two stress ratios of 0.1 and 0.5. The effective flexure strength, modulus and failure strain of both constrained and unconstrained laminates degraded due to hygrothermal aging. The degradation degree depends on the aging duration. Aging significantly reduces the fatigue life of the unconstrained laminate at both stress ratios. The reduction in the fatigue limit due to aging is considerably at the high stress ratio than at the low stress ratio. The greater degradation of the aged unconstrained and constrained laminates at high stress ratio is responsible for diminishing the stress ratio effect.

The aim of the paper [18] was to investigate the combined effects of seawater ageing and fatigue loading on the bearing performance and failure mechanism of CFRP/CFRP single-lap bolted joints. The bolted joints with an interference fit size of 1.15 % were prepared and then immersed in artificial seawater (50°C-3.5% NaCl solution) for 7 months. After that, fatigue loads were further applied to the unaged and aged joints. Finally, single-lap bearing tests were carried out to evaluate the bearing performance of

122 A.R. Arutyunyan

seawater aged and fatigue load treated joints. The experimental results showed that the ultimate bearing load of joints suffered the single effect of seawater ageing decreased exponentially with the increase of ageing time, while the joints suffered the combined effect of seawater ageing and fatigue loading decreased linearly. Moreover, compared with the single effect joints, the bearing capacity of combined effect joints showed a significant improvement. Furthermore, the failure mechanism of single effect joints was mainly the shearing fracture in bearing zones and the failure mechanism of combined effect joints was changed to be delamination in bearing zones. Those findings can provide an effective support during the use of CFRP/CFRP bolted joints for marine applications. Treated the joints with fatigue loads is an alternative method to improve the bearing performance of CFRP/CFRP bolted joints. However, it is very necessary to further explore the effect of fatigue loading parameters (load peak, load ratio and fatigue cycles) on the bearing performance of CFRP/CFRP bolted joints, which will make us have a deeper understanding of the fatigue loads.

In this work, experimental studies on the alternation of cyclic loading and climatic and thermal aging were conducted to study the fatigue strength change of carbon fiber reinforced plastics.

Materials and Methods

Specimens of unidirectional carbon fiber reinforced plastic (CFRP) of the T107/ON190/R132436 mark with a length of 250 mm, a working length of 140 mm, a width of 15 mm and a thickness of 0.8-1 mm we used in tension and fatigue experiments. The geometry and dimensions of specimens and tabs are shown on Fig. 1.

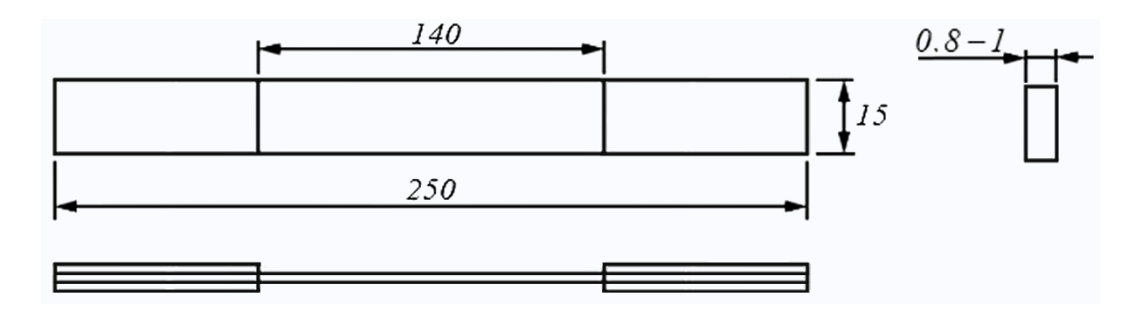


Fig. 1. Geometry and dimensions of specimens and tabs (mm)

The experiments on tension were performed on a tearing test machine TINIUS OLSEN H10K-T. Fatigue experiments were carried out on a desktop fatigue servo hydraulic test machine Si-Plan SH-B. Aging at evaluated and low temperatures were conducted correspondingly in a muffle furnace Nabertherm N40E and in a standard freezer.

Experiments on tension of CFRP specimens

Experiments on tension of CFRP specimens with a rate of 1 mm/min were conducted. The obtained tension stress-strain diagram is shown on Fig. 2.

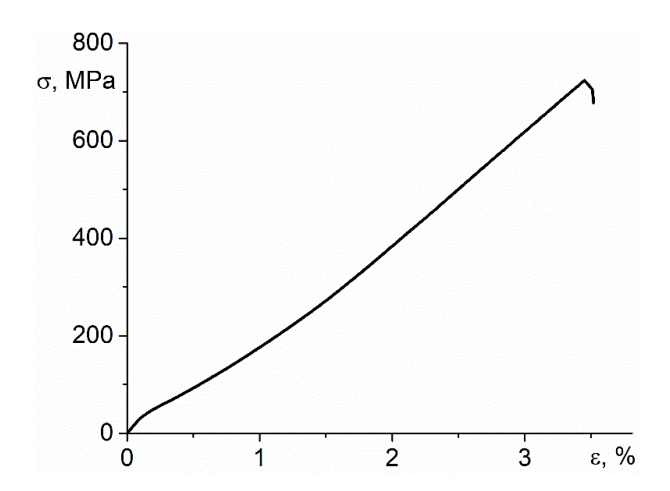


Fig. 2. Tension stress-strain diagram of CFRP specimens of the T107/ON190/R132436 mark

From Fig. 2 it can be seen that the tension stress-strain diagram has a shape close to a straight line, which is observed in experiments for various polymer composite materials [6,15,19-20].

Influence of climatic and deformation aging on fatigue strength of CFRP specimens

Cyclic experiments of CFRP specimens with constant amplitude were conducted with a sinusoidal variation in stress 6 = 337 MPa (0.45 of the ultimate tensile strength), stress ratio R = 0 and a loading frequency of 20 Hz. Thus, the average number of cycles N to fracture was determined to be 696 119 cycles.

To study the effect of climatic and deformation aging on fatigue strength, the following experimental programs were used.

Program 1. Specimens were tested up to 0.4 N cycles at noted loading parameters; placed in a muffle furnace at 120°C for 2 hours; aged in laboratory conditions for 3 months, and then tested to fracture.

Program 2. Specimens were tested up to 0.4 N cycles at noted loading parameters; placed in distilled water at room temperature, then frozen at temperature -16° C and kept in ice for 2 days; then unfrozen and kept in distilled water for 3 weeks; aged in laboratory conditions for 3 months and then tested to fracture.

Program 3. Specimens were placed in distilled water at room temperature, then frozen at temperature -16° C and kept in ice for 2 days; then unfrozen and kept in distilled water for 3 weeks; aged in laboratory conditions for 3 months and then tested to fracture.

The results of the influence of climatic and deformation aging on the cyclic strength of CFRP specimens according to programs 1-3 are presented in Table 1.

According to the obtained results, a significant hardening during cyclic experiments is observed, which considerably depends on the aging program. Therefore, for the case of cyclic loading and aging of specimens at elevated temperatures, the number of cycles

124 A.R. Arutyunyan

to fracture increased by more than two times, compared to specimens without aging. For the case of cyclic loading and aging of specimens at low temperatures, it is increased by more than 5 times. For specimens not subjected to initial cyclic loading, but aged at negative temperatures, it is increased by more than 9 times, compared to specimens without aging.

Table 1. Effect of climatic and deformation aging on the cyclic strength of CFRP specimens at 6 = 337 MPa, stress ratio R = 0 and loading frequency of 20 Hz according to various programs

	Without aging	Aging				
	Without aging	Program 1	Program 2	Program 3		
Average number of cycles to fracture N	696 119	1 789 977	3 791 257	6 295 671		
N/N _{without aging}	1	> 2	> 5	> 9		

Conclusions

To study the changes in deformation and strength characteristics of unidirectional carbon fiber reinforced plastic of the T107/ON190/R132436 mark, experiments on alternation of cyclic loading and climatic and thermal aging were conducted. The specimens were aged according to several programs, including the alternation of cyclic loading, thermal and natural aging. According to the experimental results, a significant hardening during cyclic experiments is observed, which considerably depends on the aging program. For the case of cyclic loading and aging of specimens at elevated and low temperatures, the number of cycles to fracture increased by a factor of more than 2 and 5, respectively, compared to specimens without aging. For specimens not subjected to initial cyclic loading, but aged at negative temperatures it is increased by more than 9 times, compared to unaged specimens.

References

- 1. Mc Keen L. The Effect of Long Term Thermal Exposure on Plastics and Elastomers. 4th Ed. Elsevier; 2021.
- 2. Mills N, Jenkins M, Kukureka S. Plastics. Microstructure and Engineering Applications. 4th Ed. Elsevier; 2019.
- 3. Narain R. (ed.) Polymer Science and Nanotechnology. Fundamentals and Applications. Elsevier; 2020.
- 4. Crawford R, Martin P. Plastics Engineering. 4th Ed. Elsevier; 2019.
- 5. Davies P, Rajapakse YDS. (eds.) *Durability of Composites in a Marine Environment 2, Solid Mechanics and Its Applications*. Springer; 2018.
- 6. Rajaram AN, Boay CG, Srikanth N. An empirical model to predict the strength degradation of the hygrothermal aged CFRP material. *Composite Structures*. 2020;236: 111876.
- 7. Mansouri L, Djebbar A, Khatir S, Wahab MA. Effect of hygrothermal aging in distilled and saline water on the mechanical behaviour of mixed short fibre/woven composites. *Composite Structures*. 2019;207: 816–825.
- 8. Zhong Y, Cheng M, Zhang X, Hu H, Cao D, Li S. Hygrothermal durability of glass and carbon fiber reinforced composites A comparative study. *Composite Structures*. 2019;211: 134–143.
- 9. Kootsookos A, Mouritz AP. Seawater durability of glass- and carbon-polymer composites. *Composites Science and Technology*. 2004;64(10-11): 1503–1511.
- 10. Uthaman A, Xian G, Thomas S, Wang Y, Zheng Q, Liu X. Durability of an Epoxy Resin and Its Carbon Fiber-Reinforced Polymer Composite upon Immersion in Water, Acidic, and Alkaline Solutions. *Polymers*. 2020;12(3): 614. 11. Zhang X, Wang Y, Wan B, Cai G, Qu Y Effect of specimen thicknesses on water absorption and flexural strength of CFRP laminates subjected to water or alkline solution immersion. *Construction and Building Materials*. 2019;208: 314. 12. Israr HA, Wong KJ, Rivallant S. Experimental and numerical investigation of humid ageing effects on
- CFRP laminates crashworthiness behaviours. *International Journal of Crashworthiness*. 2019;26(1): 87–98.

- 13. Kablov EN, Startsev VO. Climatic Aging of Aviation Polymer Composite Materials: I. Influence of Significant Factors. *Russian Metallurgy (Metally)*. 2020;4: 364–372.
- 14. Li H, Zhang K, Cheng H, Wu T. Water uptake and mechanical evolution behavior of carbon fiber reinforced plastic under saline and acidic environments. *Mater. Res. Express.* 2019;6(10): 105349.
- 15. Behera A, Dupare P, Thawre MM, Ballal A. Effects of hygrothermal aging and fiber orientations on constant amplitude fatigue properties of CFRP multidirectional composite laminates. *International Journal of Fatigue*. 2020;136: 105590.
- 16. Ghabezi P, Harrison N. Mechanical behavior and long-term life prediction of carbon/ epoxy and glass/epoxy composite laminates under artificial seawater environment. *Materials Letters*. 2020;261: 127091.
- 17. Rajaram AN, Boay CG, Srikanth N. Influence of stress ratio and stress concentration on the fatigue behaviour of hygrothermal aged multidirectional CFRP composite laminate. *International Journal of Fatigue*. 2020;137: 105651.
- 18. Zhang K, Li H, Cheng H, Luo B, Liu P. Combined effects of seawater ageing and fatigue loading on the bearing performance and failure mechanism of CFRP/CFRP single-lap bolted joints. *Composite Structures*. 2020;234: 111677.
- 19. Reis PNB, Ferreira JAM, Costa JDM, Richardson MOW. Fatigue life evaluation for carbon/epoxy laminate composites under constant and variable block loading. *Composites Science and Technology*. 2009;69(2):154–160.
- 20. Autar KK. Mechanics of composite materials. Boca Raton: Taylor & Francis Group; 2006.

About Author

Alexander R. Arutyunyan 📵 Sc

Candidate of Physical and Mathematical Sciences Senior Researcher (St. Petersburg State University, St. Petersburg, Russia) Submitted: August 8, 2023 Revised: September 6, 2023 Accepted: December 28, 2023

Influence of glass fibers on the physico-mechanical and performance properties of rubber based on general and special purpose caoutchoucs

E.N. Egorov , ID N.I. Kol'tsov,

I.N. Ulyanov Chuvash State University, Cheboksary, Russia

[™] enegorov@mail.ru

ABSTRACT

The effect of glass fibers (GF) on the rheometric (vulcanization) characteristics of the rubber compound, physico-mechanical, performance and dynamic properties of vulcanized rubber based on general and special purpose caoutchoucs for rail fastenings has been studied. It is shown that with the introduction of GF into the rubber compound, an increase in the minimum torque and the time of the onset of vulcanization is observed. An increase in the content of GF in the rubber compound leads to an increase in elastic-strength properties, hardness, a decrease in tear resistance and changes in physico-mechanical parameters, hardness of vulcanizates after daily thermal aging in air and after exposure to standard SZhR-1 liquid. GF contribute to an increase in the mechanical loss factor and the storage modulus of vulcanizates. It was found that the rubber compound containing 12.0 phr, has improved technological properties, and vulcanizates based on it are characterized by increased physico-mechanical, performance and dynamic parameters.

KEYWORDS

glass fibers • caoutchoucs • rubber • rheometric, physico-mechanical, performance and dynamic properties **Citation:** Egorov EN, Kol'tsov NI. Influence of glass fibers on the physico-mechanical and performance properties of rubber based on general and special purpose caoutchoucs. *Materials Physics and Mechanics*. 2024;52(1): 126–131. http://dx.doi.org/10.18149/MPM.5212024_12

Introduction

It is known [1-4] that fibrous fillers are used to improve the physical, mechanical and operational properties of rubbers. One of these fillers are glass fibers (GF) [5-10], which can increase the strength, incombustibility, heat resistance, and aggressive resistance of various materials [11-21]. The influence of GF on the physico-mechanical properties of rubbers based on siloxane [22], chloroprene [23], natural [24], and nitrile butadiene [25] caoutchoucs was studied in [22–25]. It was shown in [22] that adding 10.0 wt. % of GF in the composition of silicone rubber resulted in an increase in tensile strength by more than 26 % compared to a vulcanizate containing no GF. In [23-25] an increase in strength parameters is also shown when GF are introduced into rubber. It was found in [26] that the maximum results for testing mechanical properties were obtained from a sample of natural rubber vulcanizate with 8 wt. % GF, whose tensile strength and hardness were 57 and 32 % higher than rubber without GF. It was shown in [27] that the addition of GF modified with the capping agent Si69 (bis-[y-(triethoxysilyl)propyl]tetrasulfide) in an amount of 5.0 wt. % in the rubber composition based on styrene butadiene rubber led to a significant increase in tensile strength by 37 %. In this regard, it is of interest to study the influence of GF on the rheometric characteristics of the rubber compound, physico-mechanical, performance 127 E.N. Egorov, N.I. Kol'tsov

and dynamic properties of vulcanized rubber based on general and special purpose caoutchoucs used for the manufacture of rail fastening gaskets.

Materials and Methods

The combination of isoprene SKI-3, α -methylstyrene-butadiene SKMS-30ARK, and nitrile-butadiene SKN-2655 caoutchoucs served as the polymer base of the studied rubber compound. In addition to rubbers, the rubber compound contained the following ingredients: vulcanizing agents - sulfur, N,N'-dithiodimorpholine, tetramethylthiuram disulfide; vulcanization accelerator - N-cyclohexyl-2-benzothiazolesulfenamide; vulcanization activators - zinc oxide, stearic acid; antioxidants - acetonanil N, protective wax ZV-P, N-isopropyl-N'-phenyl-para-phenylenediamine; softeners - rosin, industrial oil I-12A; fillers - kaolin, carbons black N 220 and P 514, silicon dioxide Zeosil 1165 MP and trans-polynorbornene; scorch retarder - N-nitrosodiphenylamine.

The rubber compound was made on laboratory rolls LB 320 160/160 at a temperature of the surface of the rolls of 60–70 °C with a mixing cycle of 25 min. The vulcanization (curing) characteristics of the rubber compound were studied on a Mon Tech MDR 3000 Basic rheometer at 143 °C for 40 min in accordance with ASTM D2084-79. Rubber compound samples for determination of physico-mechanical properties were vulcanized at a temperature of 143 °C for 20 min in a P-V-100-3RT-2-PCD type vulcanizing press. Elasticstrength properties were determined according to GOST 270-75; hardness - according to GOST 263-75; tear resistance - according to GOST 262-93; change in tensile strength, elongation at break and hardness after thermal aging in air - according to GOST 9.024-74; change in tensile strength, elongation at break and hardness after exposure to standard oil liquid SZhR-1 - according to GOST 9.030-74 (method B); change in mass after exposure to aggressive media (water, industrial oil I-20A, standard oil liquid SZhR-3) - according to GOST 9.030-74 (method A). The dynamic characteristics (mechanical loss factor and storage modulus) of the rubber compound vulcanizates were studied on a Metravib VHF 104 dynamo-mechanical analyzer. The GF of Limited Liability Company Glassteks were staples with a cutting length of 4.5 mm, an elementary fiber diameter of 11 µm, a density of 2.66 g/cm³, a refractive index of 1.566, and an elastic modulus of 80 GPa.

Results and Discussion

First, the rheometric (vulcanization) characteristics of a rubber compound containing GF in an amount from 3.0 to 20.0 phr (parts per hundred parts of rubber) were studied at 143 °C, the results of which are given in Table 1.

As can be seen from Table 1, with an increase in the content of GF to 12.0 phr the maximum torque of the rubber compound remains practically unchanged. However, with a further increase in the content of GF, the maximum torque, as well as the minimum torque, of the rubber compound increases, leading to a deterioration in its technological properties and poor processability by extrusion and calendering methods. Thus, the optimal content of GF is 12.0 phr.

able 1. Variants and medinetric properties of the rubber compound								
Ingredient,		Variants of the rubber compound						
indicators	1	2	3	4	5	6	7	8
GF, phr	-	3.0	6.0	9.0	12.0	15.0	18.0	20.0
Rheometric properties of the rubber compound								
<i>M</i> _H , dN·m	18.20	18.24	18.26	18.18	18.30	18.41	19.37	20.94
<i>M</i> _L . dN·m	2.95	3.07	3.16	3.24	3.33	3.48	3.75	4.03
t _s . min	4.47	4.82	4.92	4.96	4.99	5.17	5.34	5.58
<i>t</i> ₉₀ . min	15.33	15.32	15.34	15.31	15.33	15.48	15.69	15.97

Table 1. Variants and rheometric properties of the rubber compound

Note: M_H is the maximum torque; M_L is the minimum torque; t_s is the curing scorch time; t_{90} is the optimum curing time.

Table 2. Physico-mechanical properties of vulcanizates

Indicators		Variants of the rubber mixture						
	1	2	3	4	5			
f_{100} , MPa	5.4±0.2	6.2±0.2	6.4±0.2	6.5±0.3	7.2±0.3			
$f_{\rm p}$, MPa	13.4±0.5	13.5±0.5	13.5±0.5	13.7±0.5	13.9±0.6			
ε,, %	340±13	410±16	380±15	390±15	350±14			
H, units Shore A	74±1	72±1	73±1	74±1	76±1			
B, kN/m	50±2	53±2	48±2	47±2	46±2			

Note: f_{100} is the modulus stress at 100% elongation; f_p is the tensile strength; ε_p is the elongation at break; H is the hardness; B is the tear resistance.

Subsequently, we investigated the physico-mechanical, performance and dynamic properties of vulcanizates containing up to 12.0 phr GF. The results of studying the physico-mechanical properties of vulcanizates (modulus stress at 100 % elongation, tensile strength, elongation at break, hardness and tear resistance) are presented in Table 2.

From the data in Table 2 it follows that an increase in the content of GF in the composition of the rubber compound contributes to an increase in the tensile strength, elongation at break, hardness and a decrease in the tear resistance of vulcanizates. These indicators increase to a GF content of 12.0 phr, the excess of which, as noted above, leads to a deterioration in the technological properties of the rubber compound and the associated physico-mechanical properties of the vulcanizates.

The results of studying the performance properties (changes in physico-mechanical parameters) of vulcanizates after thermal aging in air and exposure to standard hydrocarbon liquid SZhR-1 at a temperature of 100 °C for 24 hours are given in Table 3.

From the data in Table 3 shows that with an increase in the content of GF, there is a decrease in changes in the physico-mechanical parameters of vulcanizates after daily aging in air and in SZhR-1. The least changes in these indicators has vulcanizate, including 12.0 phr GF.

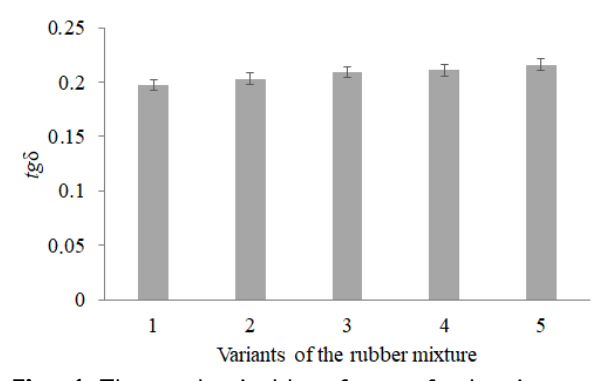
Table 3 also shows the results of a study of the change in the mass of vulcanized rubbers after soaking in water, industrial oil I-20A and SZhR-3 at 23 °C for 24 hours. As can be seen, an increase in the content of GF leads to a decrease in the change in the mass of vulcanizates. The smallest changes in the mass of vulcanizates in the studied aggressive environments are characterized by vulcanizate containing also 12.0 phr including GF.

129 E.N. Eqorov, N.I. Kol'tsov

Table 3	Performance	nroperties	of rubber	mixture	vulcanizates
Table J.	renonnance	טו טטכו נוכז	oi iubbei	IIIIXLUIC	vultariizates

Indicators	Variants of the rubber mixture						
	1	2	3	4	5		
Change in physico-mechanical properties of vulcanizates after air aging							
$\Delta f_{\rm p}$, %	-21.5±0.8	-23.9±0.9	-35.6±1.4	-20.9±0.8	-15.2±0.6		
$\Deltaarepsilon_{ m p}$, %	-35.3±1.4	-31.2±1.2	-32.1±1.3	-33.3±1.3	-28.6±1.1		
ΔH , units Shore A	+2.0±1.0	+2±1	+4±1	+4±1	+4±1		
Change in phys	co-mechanical pi	roperties of vulca	anizates after ex	posure to SZhF	R-1		
Δf _p , %	-45.9±1.8	-41.5±1.7	-38.9±1.6	-35.2±1.4	-30.4±1.2		
$\Deltaarepsilon_{ m p}$, %	-29.5±1.2	-30.5±1.2	-27.8±1.1	-23.9±0.9	-18.6±0.7		
ΔH , units Shore A	-16±1	-12±1	-12±1	-12±1	-10±1		
Change in the mass of vulcanizates in various environments							
Δm (water), %	0.64±0.01	0.59±0.01	0.51±0.01	0.46±0.01	0.41±0.01		
Δm (I-20A), %	6.97±0.10	6.31±0.09	5.97±0.08	5.11±0.07	4.89±0.07		
Δ <i>m</i> (SZhR-3), %	12.10±0.18	11.76±0.17	10.71±0.16	9.83±0.15	8.65±0.13		

Note: Δf_p , $\Delta \varepsilon_p$, Δm – relative changes in tensile strength, elongation at break and mass; ΔH is the difference in hardness after and before holding in an aggressive environment.



Figs. 1. The mechanical loss factor of vulcanizates

Fig. 2. Storage modulus of vulcanizates

A quantitative measure for assessing the dynamic (vibration-damping) properties of polymer materials, including vulcanized rubber, are the values of the mechanical loss tangent (tg δ) and the storage modulus (*E*') [28–30]. For the resulting vulcanizates, the dynamic properties were studied: the mechanical loss factor $tg\delta$ (Fig. 1) and the storage modulus *E*' (Fig. 2) in the "tension-compression" mode at a frequency of 1000 Hz, a degree of deformation of 0.01 % and a temperature of 30 °C.

From Figs. 1 and 2, it can be seen that the introduction of GF into the rubber compound contributes to an increase in both dynamic parameters. It is known [30-34] that as the mechanical loss factor of polymers (vulcanized rubbers) increases, their vibration-damping properties increase.

The highest value of $tg\delta$, and, consequently, good dynamic properties is characterized by the vulcanizate of the fifth variant containing 12.0 phr GF.

Conclusions

The influence of GF on the properties of vulcanized rubber based on general and special purpose caoutchoucs has been studied. It has been shown that with a GF content of up to 12.0 phr, the rubber compound has satisfactory technological properties and can be well processed by injection and calendering methods. The physico-mechanical properties of vulcanizates increase to the same content of GF in the rubber compound, the excess of which leads to their reduction due to deteriorating technological properties. The best performance properties are characterized by a vulcanizate that has the greatest physico-mechanical properties, i.e. vulcanizate containing 12.0 phr of GF. This is consistent with the well-known statement that most rubbers with high physico-mechanical properties are also characterized by increased performance properties. The same vulcanizate has improved dynamic properties, which is associated with the previously noted good processability (manufacturability) and the resulting homogeneous structure of the rubber compound used to produce it. Thus, for the manufacture of gaskets for rail fastenings, rubber containing 12.0 phr of GF can be recommended.

References

- 1. Rane AV, Krishnan Kanny VK, Thomas S. Partial Replacement of Carbon Black by Rice Hulls and Soy Short Fibres as Fillers in Natural Rubber Composites: Effect on Mechanical Properties. In: *Biopolymers and Biomaterials*. Apple Academic Press; 2018. p.163–214.
- 2. Brum Dutra da Rocha E, de Sousa AMF, Furtado CRG. Properties Investigation of novel nitrile rubber composites with rockwool fibers. *Polymer Testing*. 2020;82: 106291.
- 3. Archibong FN, Sanusi OM, Médéric P, Aït Hocine N. An overview on the recycling of waste ground tyre rubbers in thermoplastic matrices: Effect of added fillers. *Resources, Conservation and Recycling*. 2021;175: 105894.
- 4. Fiore V, Scalici T, Di Bella G, Valenza A. A review on basalt fibre and its composites. *Composites Part B: Engineering*. 2015;74: 74–94.
- 5. Jones FR, Huff NT. The structure and properties of glass fibers. In: *Handbook of Properties of Textile and Technical Fibres*. Elsevier; 2018. p.757–803.
- 6. Scaffaro R, Di Bartolo A, Dintcheva NT. Matrix and Filler Recycling of Carbon and Glass Fiber-Reinforced Polymer Composites: A Review. *Polymers*. 2021;13(21): 3817.
- 7. Raza SS, Qureshi LA, Ali B, Raza A, Khan MM. Effect of different fibers (steel fibers, glass fibers, and carbon fibers) on mechanical properties of reactive powder concrete. *Structural Concrete*. 2020;22(1): 334–346.
- 8. Madhu P, Bharath KN, Sanjay MR, Arpitha GR, Saravanabavan D. Effect of nano fillers on glass/silk fibers based reinforced polymer composites. *Materials Today: Proceedings*. 2021;46: 9032–9035.
- 9. Aradhya R, Sundara Rajan J. Dynamic mechanical analysis for assessment of carbon fillers in glass fiber epoxy composites. *Polymer Composites*. 2023;44(10): 6691–706.
- 10. Saravanakumar K, Arumugam V, Souhith R, Santulli C. Influence of Milled Glass Fiber Fillers on Mode I & Mode II Interlaminar Fracture Toughness of Epoxy Resin for Fabrication of Glass/Epoxy Composites. *Fibers*. 2020;8(6): 36.
- 11. Krinitsin NA, Dubovy VK, Polyakova KV, Koverninsky IN. Study of the Influence of Binder Type on the Properties of Glass Fiber Filter Paper for Air Purification. *Lesnoy Zhurnal (Forestry Journal)*. 2022;2: 178–192. (In Russian)
- 12. Bilisik K, Kaya G, Ozdemir H, Korkmaz M, Erdogan G. Applications of glass fibers in 3D preform composites. In: *Advances in Glass Science and technology*. IntechOpen; 2018. p.207–230.
- 13. Lalinde LF, Mellado A, Borrachero MV, Monzó J, Payá J. Durability of Glass Fiber Reinforced Cement (GRC) Containing a High Proportion of Pozzolans. *Applied Sciences*. 2022;12(7): 3696.
- 14. Zhu J, Deng Y, Chen P, Wang G, Min H, Fang W. Prediction of Long-Term Tensile Properties of Glass Fiber Reinforced Composites under Acid-Base and Salt Environments. *Polymers*. 2022;14(15): 3031.
- 15. Wang W.-C., Wang H.-Y., Chang K.-H., Wang S.-Y. Effect of high temperature on the strength and thermal conductivity of glass fiber concrete. *Construction and Building Materials*. 2020;245: 118387.

131 E.N. Egorov, N.I. Kol'tsov

16. Sapuan SM, Aulia HS, Ilyas RA, Atiqah A, Dele-Afolabi TT, Nurazzi MN, Supian ABM, Atikah MSN. Mechanical Properties of Longitudinal Basalt/Woven-Glass-Fiber-reinforced Unsaturated Polyester-Resin Hybrid Composites. *Polymers*. 2020;12(10): 2211.

- 17. Han D, Chen Y, Pan Y, Wang C, Zhang D. Research on Friction and Wear Properties of Rubber Composites by Adding Glass Fiber during Mixing. *Polymers*. 2022;14(14): 2849.
- 18. Bian B, Xia G, Li J, Shao S, Duan Q, Xie Q. Thermal-aging characteristics of epoxy/glass fiber composite materials for dry-type air-core reactors. *Polymer Composites*. 2021;42(8): 3773–3785.
- 19. Sathishkumar T, Satheeshkumar S, Naveen J. Glass fiber-reinforced polymer composites a review. *Journal of Reinforced Plastics and Composites*. 2014;33(13): 1258–1275.
- 20. Albayrak M, Kaman, MO, Bozkurt I. The effect of lamina configuration on low-velocity impact behaviour for glass fiber/rubber curved composites. *Journal of Composite Materials*. 2023;57(11): 1875–1908.
- 21. Chen RS, Muhammad YH, Ahmad S. Physical, mechanical and environmental stress cracking characteristics of epoxy/glass fiber composites: Effect of matrix/fiber modification and fiber loading. *Polymer Testing*, 2021;96: 107088.
- 22. Park E-S. Mechanical properties and processibilty of glass-fiber-, wollastonite-, and fluoro-rubber-reinforced silicone rubber composites. *Journal of Applied Polymer Science*. 2007;105(2): 460–468.
- 23. Antypas IR. Improvement of mechanical behavior of neoprene rubber by means of glass fiber. *Journal of Physics: Conference Series*. 2021;1889(4): 042007.
- 24. Wan Busu WN, Anuar H, Ahmad SH, Rasid R, Jamal NA. The Mechanical and Physical Properties of Thermoplastic Natural Rubber Hybrid Composites Reinforced with Hibiscus cannabinus, L and Short Glass Fiber. *Polymer-Plastics Technology and Engineering*. 2010;49(13): 1315–1322.
- 25. Ricciardi MR, Papa I, Langella A, Langella T, Lopresto V, Antonucci V. Mechanical properties of glass fibre composites based on nitrile rubber toughened modified epoxy resin. *Composites Part B: Engineering.* 2018;139: 259–267.
- 26. Hashemi SJ, Sadooghi A, Rahmani K, Nokbehrosta S. Experimental determining the mechanical and stiffness properties of natural rubber FRT triangle elastic joint composite reinforcement by glass fibers and micro/nano particles. *Polymer Testing*. 2020;85: 106461.
- 27. Wang G, Yu W, Zhang S, Yang K, Liu W, Wang J, Liu F. Improved Thermal Insulation and Mechanical Strength of Styrene-Butadiene Rubber through the Combination of Filled Silica Aerogels and Modified Glass Fiber. *Materials*. 2023;16(17): 5947.
 28. Lu YC, Shinozaki DM. Temperature Dependent Viscoelastic Properties of Polymers Investigated by Small-Scale Dynamic Mechanical Analysis. *Experimental Mechanics*. 2010;50(1): 71–77.
- 29. Egorov EN, Sandalov SI, Kol'tsov NI. Study of the influence of dispersed fillers on properties of rubber for gaskets of rail fastening. *Materials Physics and Mechanics*. 2023;51(6): 119–126.
- 30. Kablov EN, Sagomonova VA, Sorokin AE, Tselikin VV, Gulyaev Al. A Study of the Structure and Properties of Polymer Composite Materials with Integrated Vibration Absorbing Layer. *Polymer Science, Series D.* 2020;13(3): 335–340.
- 31. Egorov EN, Ushmarin NF, Sandalov SI, Kol'tsov NI. Research of operational and dynamic properties of rubber for products working in sea water. *ChemChemTech*. 2020;63(11): 96–102. (In Russian)
- 32. Egorov EN, Ushmarin NF, Sandalov SI, Kol'tsov NI, Voronchikhin VD. Investigation of the dynamic properties of seawater-resistant rubber. *Journal of Siberian Federal University. Chemistry.* 2021;14(1): 38–44. (In Russian)
- 33. Ushmarin NF, Egorov EN, Grigor'ev VS, Sandalov SI, Kol'tsov NI. Influence of Chlorobutyl Caoutchouc on the Dynamic Properties of a Rubber Based on General-Purpose Caoutchoucs. *Russian Journal of General Chemistry*. 2022;92(9):1862–1865.
- 34. Egorov EN, Salomatina EV, Vassilyev VR, Bannov AG, Sandalov SI. Effect of Polynorbornene on Physico-Mechanical, Dynamic, and Dielectric Properties of Vulcanizates Based on Isoprene, α-Methylstyrene-Butadiene, and Nitrile-Butadiene Rubbers for Rail Fasteners Pads. *Journal of Composites Science*. 2023;7(8): 334.

About Authors

Evgeniy N. Egorov D Sc

Candidate of Chemical Science, Associate Professor (I.N. Ulyanov Chuvash State University, Cheboksary, Russia)

Nikolay I. Kol'tsov 🗓 Sc

Doctor of Chemical Science, Professor (I.N. Ulyanov Chuvash State University, Cheboksary, Russia) Submitted: August 21, 2023 Revised: October 20, 2023 Accepted: December 14, 2023

Experimental investigation on flexural fatigue strength of graphene oxide modified E-glass epoxy composite beam

A.R. Ropalekar ™, 🔟 R.R. Ghadge, 🔟 N.A .Anekar, 🔟

Dr. Vishwanath Karad MIT World Peace University, Pune, India

[™] ropalekarakash@gmail.com

ABSTRACT

Many studies are currently being performed on the complex issue of fatigue of reinforced composite materials. Graphene oxide (GO) is a strong contender for reinforcement, an atomically thin form of carbon with remarkable multifunctional qualities and a perfect surface for interacting with polymer matrices. This report investigates the effect of GO modified epoxy resin on the flexural fatigue life of a composite beam. First, two different weight concentrations of 0.25 and 0.50 % are dispersed by ultrasonication in epoxy resin and composite beams are prepared through a hand layup process. The microscopic analysis confirmed the uniform dispersion. The static bend test resulted in an increase in the flexural strength of the GO-incorporated beam by 33.3 % compared with that of the neat epoxy beam. Flexural fatigue tests were performed for different load levels, and damage evolution at every 4000th cycle was observed. It was noted that under 60 % loading, a significant change in damage initialization was observed between neat epoxy and 0.25 % GO. However, under a higher load level, a negligible effect of crack initialization was observed in all types of beams.

KEYWORDS

epoxy composite • flexural fatigue • graphene oxide

Citation: Ropalekar AR, Ghadge RR, Anekar NA. Experimental investigation on flexural fatigue strength of graphene oxide modified E-Glass epoxy composite beam. *Materials Physics and Mechanics*. 2024;52(1): 132-141. http://dx.doi.org/10.18149/MPM.5212024_13

Introduction

In recent years, industries across the board including the automotive, aerospace, and structural applications have increased their usage of composite materials. Composite materials are even used in electronic equipment's for EMI (electromagnetic interference) [1]. Composites allow for performance levels that are not attainable with traditional materials. Recent research on composite materials is being conducted in labs throughout the world to better understand the behavior of composite structures in order to maximize their use and appropriateness for industrial applications. Different types of loading conditions are acted upon a composite structure like tensile, compressive, bending, shear and torsion so with respect to that the structure is tested according to the load. In order to improve their performance under these loading, various nanoparticles like Carbon nanotubes, Silicon dioxide, Graphene oxide is induced in composite preparation. Some other nano material like Montomorillonite (MMT) is also used by Kirve et al. [2] to improve the strength of bamboo fiber. Liu et al. [3] performed an experiment to study the effect of carbon nanotubes/graphene oxide on the fracture toughness of CFRP laminates. By changing the ratios of carbon nanotubes/graphene oxide, they found out that there was a substantial increase in the fracture toughness of about 151.2 % than the original laminates. A very detailed review has been done by Han et al. [4] where they have highlighted all the

© A. Yu. Belov. 2024.

improvements in mechanical properties of graphene / carbon nanotube reinforced FRP composites. Also, for Glass fiber incorporation of graphene for mechanical properties were characterized by Rathinasabapathi et al. [5]. According to the report, the interface to volume ratio and filler size has a significant impact on the mechanical properties of composites that have had their matrix modified. Icaopo et al. [6] worked-on investigation of GO reinforcement in epoxy resin. From 0-3 wt. % of GO the flexural strength were considered and resulted first in increase of strength up to 0.3 % and sudden decrease from 0.5 to 3.0 % of GO. Hence, nanofillers are essential for the alteration of the polymer matrix in this direction. The effect of functionalized GO was well documented by Pathak et al. [7] where modified the synthesis process of GO and evaluated the flexural strength. A review is carried out by Dias et al. [8] which emphasizes collective research on articles which highlights composite filled with nanoclay and their mechanical behavior. Also, considering the tribological performance, the addition of graphene lead to increase in the tear strength of silicone rubber as observed by Shinde et al. [9].

They are also known for their resistance towards cyclic loading. So, to design a fiber composite to reduce delamination occurring due to fatigue loading, the important concern. To prevent quick fracture and potentially catastrophic failure, composite structures must be designed for either no growth or moderate, steady growth under cyclic fatigue loadings. Through the recent study, the nanotechnology has showed a significant improvement of epoxy composite fibers. Apart from all the nanoparticles, graphene shows promising results. Graphene is a form of carbon possessing a two-dimensional structure. They have extremely high fracture strength and young's modulus and provides large surface area. As compared to other carbon materials graphene contains higher mobility and thermal conductivity with significant strength of 1 TPa. This makes graphene a potential material in sector transistor element, energy harvesting techniques and sensor application. Due to their high surface-to-volume ratio, two-dimensional carbon nanostructures like graphene and its variants are among the most intriguing reinforcements that can be used to enhance mechanical properties.

In marine, construction, aerospace, and automobile industry's composite structure flexural loading. Considering the marine environmental conditions, Romina et al. [10] studied the effect of graphene nanoplatelets on the flexural properties of fiber metal laminates. They observed 128 % improvement in flexural strength was by 0.25 wt. % of nanoplatelets which was due to the metal/polymer adhesion. Also, carbon nanomaterials show improvements in mechanical and thermal properties composites [11]. Flexural test simulation is performed by Joshi et al. [12] which showcase the improvement of epoxy fibers with varying range of graphene content. Filipe et al. [13] understood the behavior of hybrid composites under tension-tension fatigue loading and observed that carbon/carbon composites showed better resistance towards damage. The fatique damage to composite is occurred in different stages, in order to prolong its effect nanoparticles are dispersed through various processes. A remarkable improvement of flexural fatigue of epoxy composite were observed by Shoriekh et al. [14] by combination of graphene nanosheet. 3-point bending fatigue tests were conducted on aluminum composite with honeycomb core by Mzad et al. [15]. They performed first 3-point static tests on the specimens and then fatigue test at three different loading conditions. Also, to improve interfacial bonding, Dabbagh et al. [16] investigated the effect of GO-NH₂ epoxy composite on the fatigue loading. By varying the loading conditions, about 72-241 % improvement was noted in fatigue life. The synergy effect of graphene oxide sheets and carbon nanotubes was studied by Yuanqing et al. [17]. They observed 950 % increment in fatigue life with respect to pure epoxy. Ashutosh et al. [18] performed experimentation to evaluate the effect of surface roughness on fatigue strength of epoxy composited single lap joint. They used modified adhesive with graphene oxide and observed enhancement of 30 % in fatigue strength. The effect of aluminum oxide, magnesium oxide and copper oxide (CuO) nanoparticles on the fatigue behavior of woven composite was carried out by Ergün et al. [19]. They observed that among different weight concentrations, 0.5 % CuO was the stiffest.

Various processes are involved for graphene oxide to get induced in the epoxy resin. In this the study, a simple synthesis is followed, mentioned in [20]. By using injection molding techniques, Sen-Sen et al. [21] reported the effects of graphene oxide coating on glass fiber. To improve interfacial strength, graphene oxide (GO) is used, which leads to better epoxy and fibers bonding. Most of the research is focused on the static improvement of the composite structure. Fewer researches are carried out on the flexural fatigue performance. The present experimental work details the characterization of epoxy/GO composites and studies the effect on the flexural fatigue life of the composite beams.

Materials and Methods

Materials

Research Grade graphene oxide was used to incorporate in epoxy resin (EPOFINE) and its hardener. For preparation of specimen, glass fiber of 700 GSM was used. All the materials came up with the properties as shown in Tables 1 and 2.

Table 1. Specifications of glass fiber

Parameters	Specification
Weight, Gram/Sq.m	740.0
Width, mm	1020.0
Thickness, mm	0.7
Weave Pattern	Plain

Table 2. Specifications of nanomaterial

Parameter	Specification
Thickness, nm	0.8-2.0
Average Lateral Dimension(X&Y), μm	10
C:0	55:45

Dispersion of graphene oxide with epoxy resin

There are two different weight concentrations of GO i.e. 0.25 and 0.50 % used in this study. As per the E-glass fibre sheet to be made of 300 × 300 mm², we require 0.625 gm of graphene oxide (0.25 % GO). Essentially, at a concentration of 2 mg·ml⁻¹, GO was dissolved in acetone. For proper mixing of acetone and GO, its mixture was kept into an ultrasonic bath for 2 hours. This mixture was then poured into a beaker containing epoxy resin required for the sheet. The whole mixture of resin/nanoparticles was kept on magnetic stirring for about 10 hours (Fig. 1). This process was referred from [20].

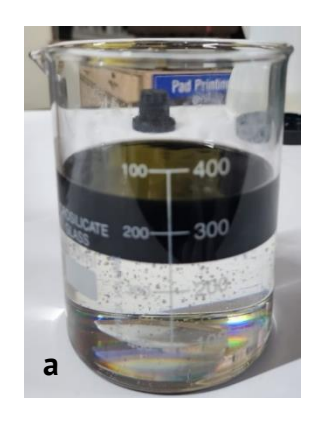
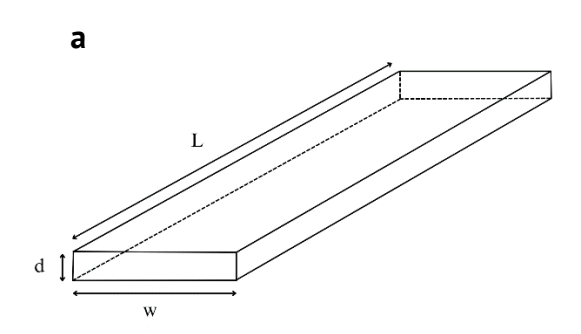




Fig. 1. (a) GO mixture with epoxy resin and (b) magnetic stirrer action of GO and resin mixture

Composite preparation

The composite was fabricated by hand lay-up process followed compressed curing with orientation of $[0/45/0]_s$. Three different sheets of $300 \times 300 \text{ mm}^2$ were fabricated for net epoxy, 0.25 and 0.50 wt. % of GO. Testing of specimen were carried out according to ASTM D790 [22] (Fig. 2).



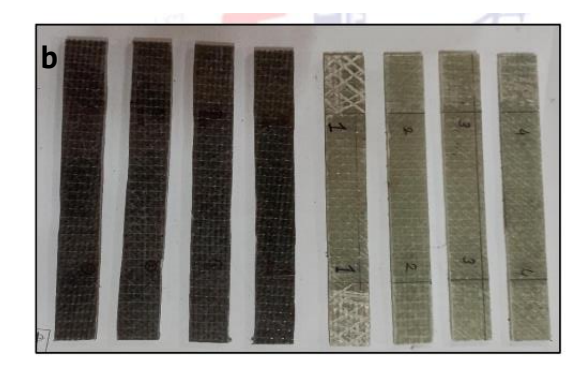


Fig. 2. (a) Schematic of test specimen and (b) actual test specimens

Static bending test

The test was carried out on universal testing machine (UTM) with capacity of 50 kN in accordance to ASTM D790 standard (Fig. 3). The ram speed for the tests was 5 mm/min. For each test, 3 samples were used. The bending stress was calculated: $\sigma = \frac{3FL}{2wd^2}$, where F is the maximum load sustained, L is the supporting span length, w is the width of specimen and d is the thickness of specimen.

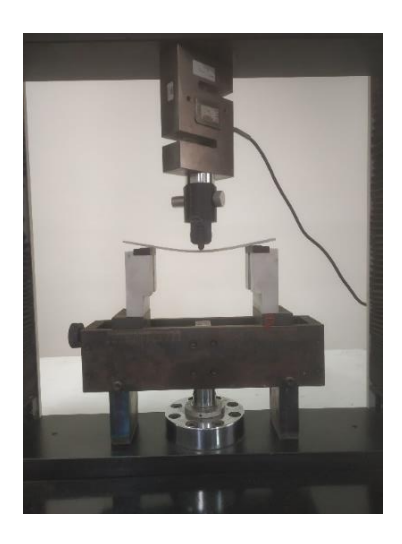


Fig. 3. Schematic of three-point bend test

Flexural fatigue test

The flexural fatigue test is carried out for specimens under different loading conditions using an axial fatigue testing. The stress ratio (R) was 0.1 and frequency was 3.5 Hz for all tests. The fatigue test was carried out at 80, 60, 40 % of the maximum bending force they could withstand at static test (F). The test was terminated when the upper surface was delaminated.

Results and Discussion

3-point bend test and bending fatigue were carried out on the ready specimens to evaluate the bending strength and fatigue life of the specimens.

Static bend test

According to the standard, the test was carried out at 5 mm/min ramp speed on UTM at MITWPU. For each percentage of GO, there were three specimens tested on UTM and average result for load vs cross head travel are plotted in the Fig. 4(a). It is observed that the flexural strength modified epoxy composited increases from 255 to 322-343 MPa. The maximum increase in strength at 0.25 wt. % of GO corresponds to a hike of 25.65 % compared to net epoxy resin (Fig. 4(b)). This result develops that even at lower concentrations, the strength of the composite beam can be improved. It is because of interfacial bonding between the layers is enhanced due to the incorporation of GO [23].

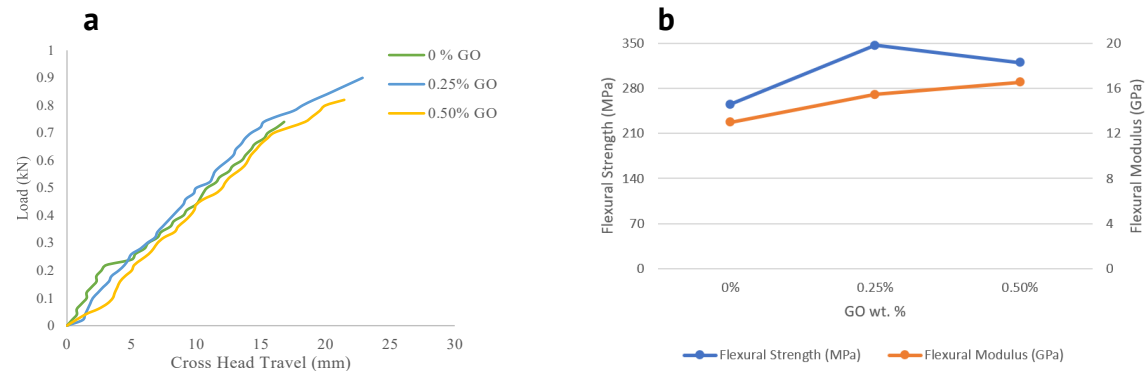


Fig. 4. (a) Load vs displacement; (b) variation of flexural strength and flexural modulus

Flexural strength at 0.50 wt. % of GO results in significant rise of 20.3 % compared to net epoxy. But increasing the weight content of GO has led to a small amount of decay in the flexural strength. In the graph as shown in Fig. 4(b), plotted for flexural strength vs flexural modulus, the increase in flexural strength with increase in weight percentage of GO has been observed, whereas flexural modulus shows similar trend but slight decline for 0.50 wt. % of GO. Such behavior might be linked to nanofiller agglomerations that form inclusions from which microcracks can propagate during testing, resulting in a decrease in the mechanical characteristics of the epoxy resin. Furthermore, these agglomerates yield a reduced usable section, causing the specimens to fail prematurely [6].

Fatigue damage evolution

The fatigue testing is done by varying loading conditions. For analyzing the damage propagation, the 60 % loading condition is discussed here. Fatigue testing have been halted at various points during the loading to provide information about damage development and to comprehend how fatigue cycling impacts composites. At every 4000th cycles observations were noted. Transverse matrix cracks typically begin at the specimen's edge, owing to the effects of microdamage during sample cutting. These damages are highlighted in the yellow boxes in Fig. 5. From 6000th cycles onwards the crack density rises as the cyclic load increases, followed by crack coupling and interfacial deboning. The upper layer starts to de-bond and delaminate at further increase in cycles. Hassan et al. performed similar experimentation and conferred that during this phase. crack propagation and buildup in a number of stress concentration areas are the main causes of a rapid decay of modulus. The complete surface gets delaminated at 16232nd cycle. The size of the yellow box indicates that the damage is increasing in that area. It is observed that growth of the crack is in the dispersed way. Reifsnider et al. [23] also studied the behavior of cracks on the fiber surface and inferred that the transverse cracking is formed in regular spacing, which can also observed here.

The fatigue life data for the specimens with and without graphene oxide are presented in Table 1. For 0.25 wt. % GO, Fig. 6 represents the damage evolution due to flexural fatigue loading. The results show that the addition of graphene oxide significantly delays in the damage initialization under fatigue loading of the epoxy composite. Daniel et al. [24] reported that modest but considerable stiffness and strength improvements were made, especially at low graphene oxide weight fractions. GO has many groups on the surface and edge which are reactive. Due to the incorporation of

nanoparticles led to increase in the interfacial bonding [25]. It is due to the fact that graphene acts like a filler between the growing fractures. Using these findings as a basis, we suggested the following interpretation: In the experiment, it was observed that 0.25 wt. % GO sustained maximum number of cycles to failure at 60 % of loading condition. The table illustrated fracture images at loading of 60 % at every 4000 cycles. For 0.5 GO wt. % it is observed that the delamination is more even at early stages. This indicates that more weight leads to agglomeration.

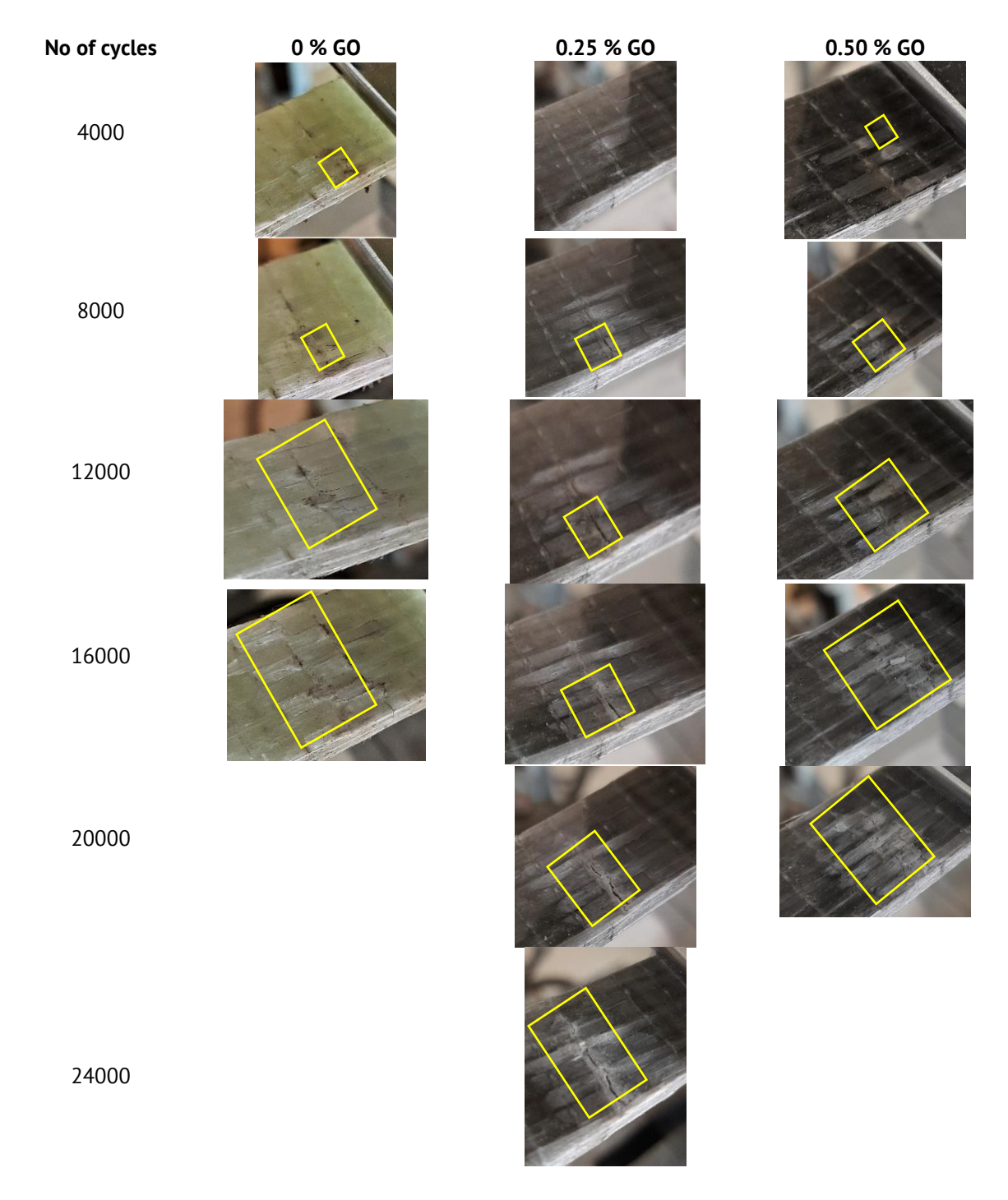


Fig. 5. Damage evolution of all type's specimens under fatigue loading

Similarly, for the rest of the tests this pattern is observed and a table is formulated. At high levels of load, there is no significant increase in number of cycles to failure. Figure 6 illustrates the S-N curve for the tested specimens.

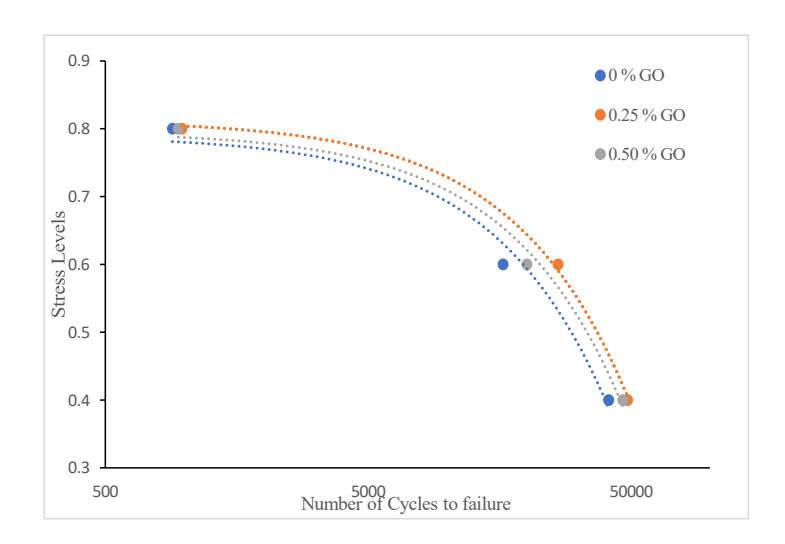


Fig. 6. Variation of fatigue loading cycles to failure for different stress levels

Conclusions

In the present research, the influence of different weight concentrations of GO on the damage evolution under flexural fatigue loadings of the composite beam. These were the key findings from this experimental investigation. Synthesis of GO dispersion is time-consuming but also was well dispersed. The static results showed a significant increase in the flexural strength of 0.25 % GO than the net epoxy composite beam. Due to incorporation of GO, the failure of its beam has showed less debonding between the layers of lamina which also indicated a better interfacial strength. Fatigue results showed that at 0.25 wt. % of GO, the crack initialization is postponed by 4000 cycles than the neat epoxy. Also, 0.5 wt. % of GO caused agglomeration and resulted in early failure, with more delamination observing than that of 0.25 % GO. The incorporation of functionalized GnP into the polymer matrix increased the matrix phase's and the fibre interfaces' fracture toughness. The continuous matrix phase's continual nanoparticle dispersion caused microcracks to deflect, lowering the crack-tip energy. As a result, composites showed extended fatigue life before final fracture and the beginning of matrix cracking and delamination under cyclic loading was delayed.

This research will guide for designing and improving glass fiber composites under cyclic loading. However, research opportunities are open to understand the effect of functionalization of GO for better interfacial bonding. Moreover, composite preparation techniques like VARTM can also be used for uniform dispersion of modified epoxy.

References

- 1. Shinde A, Siva I, Munde Y, Sankar I, Sultan MTH, Shahar FS, Gaff M, Hui D. Appraising the dielectric properties and the effectiveness of electromagnetic shielding of graphene reinforced silicone rubber nanocomposite. *Nanotechnology Reviews*. 2023;12(1): 20220558.
- 2. Kirve M, Munde Y, Shinde A, Siva I. Evaluation of mechanical properties of bamboo epoxy bio-composite filled with Montmorillonite Nanoclay. *Materials Today: Proceedings*. 2022;62(2): 806–810.
- 3. Liu Y, Zou A, Wang G, Han C, Blackie E. Enhancing interlaminar fracture toughness of CFRP laminates with hybrid carbon nanotube/graphene oxide fillers. *Diamond and Related Materials*. 2022;128: 109285.
- 4. Han W, Zhou J, Shi Q. Research progress on enhancement mechanism and mechanical properties of FRP composites reinforced with graphene and carbon nanotubes. *Alexandria Engineering Journal*. 2023;64: 541-579.
- 5. Rathinasabapathi G, Krishnamoorthy A. Reinforcement effect of graphene enhanced glass fibre reinforced polymers: a prominence on graphene content. *Digest J. Nanomater. Biostruct.* 2019;14(3): 641–653.
- 6. Bianchi I, Gentili S, Greco L, Simoncini M. Effect of graphene oxide reinforcement on the flexural behavior of an epoxy resin. *Procedia CIRP*. 2022;112: 602–606.
- 7. Pathak AK, Borah M, Gupta A, Yokozeki T, Dhakate SR. Improved mechanical properties of carbon fiber/graphene oxide-epoxy hybrid composites. *Composites Science and Technology*. 2016;135: 28–38.
- 8. Dias E, Chalse H, Mutha S, Mundhe Y, Ambhore N, Kulkarni A, Mache A. Review on synthetic/natural fibers polymer composite filled with nanoclay and their mechanical performance. *Materials Today: Proceedings.* 2023;77(3):916–925.
- 9. A Shinde, I Siva, Y Munde, I Sankar, MTH Sultan, Mustapha F, Shahar FS, Najeeb MI. The impacts of graphene dosage on the friction and wear performance of a graphene-reinforced silicone rubber nano composite. *Journal of Materials Research and Technology*. 2022;21: 1570–1580.
- 10. Keshavarz R, Aghamohammadi H, Eslami-Farsani R. The effect of graphene nanoplatelets on the flexural properties of fiber metal laminates under marine environmental conditions. *International Journal of Adhesion and Adhesives*. 2020;103: 102709.
- 11. Benega MAG, Silva WM, Schnitzler MC, Andrade RJE, Ribeiro H. Improvements in thermal and mechanical properties of composites based on epoxy-carbon nanomaterials A brief landscape. *Polymer Testing*. 2021;98: 107180.
- 12. Joshi S, Ghadge R, Shinde R, Lalam T, Balbudhe T. Flexural analysis of graphene oxide infused S2-glass/epoxy nanocomposite laminates. *Materials Today: Proceedings*. 2021;47(16): 5509–5514.
- 13. Ribeiro F, Sena-Cruz J, Vassilopoulos AP. Tension-tension fatigue behavior of hybrid glass/carbon and carbon/carbon composites. *International Journal of Fatigue*. 2021;146: 106143.
- 14. Shokrieh MM, Esmkhani M, Haghighatkhah AR, Zhao Z. Flexural fatigue behavior of synthesized graphene/carbon-nanofiber/epoxy hybrid nanocomposites. *Mater Des.* 2014;62: 401–408.
- 15. Mzad H. Experimental investigation of the mechanical behavior of honeycomb sandwich composite under three-point bending fatigue. *Materials Physics and Mechanics*. 2022;48(2): 217–231.
- 16. Dabbagh J, Behjat B, Yazdani M, da Silva LFM. An experimental investigation on low-cycle fatigue behavior of GO-NH2-reinforced epoxy adhesive. *Proceedings of the Institution of Mechanical Engineers, Part L: Journal of Materials: Design and Applications.* 2021;235(4): 763–776.
- 17. Li Y, Umer R, Isakovic A, Samad YA, Zheng L, Liao K. Synergistic toughening of epoxy with carbon nanotubes and graphene oxide for improved long-term performance. *RSC Adv.* 2023;23(3): 8849–8856.
- 18. Manoli A, Ghadge R, Kumar P. Effect of surface roughness on the fatigue strength of E-glass composite single lap joint bonded with modified graphene oxide-epoxy adhesive. *Materials Physics and Mechanics*. 2023;51(2): 65–80.
- 19. Ergün RK, Adin H. Investigation of Effect of Nanoparticle Reinforcement Woven Composite Materials on Fatique Behaviors. *Iran J Sci Techno Trans Mech Eng.* 2023;47: 729–740.
- 20. Ghadge RR, Prakash S, Ganorkar SA. Experimental investigations on fatigue life enhancement of composite (e-glass/epoxy) single lap joint with graphene oxide modified adhesive. *Mater. Res. Express.* 2021;8(2):025202. 21. Du SS, Li F, Xiao HM, Li YQ, Hu N, Fu SY. Tensile and flexural properties of graphene oxide coated-short glass fiber reinforced polyethersulfone composites. *Composites Part B: Engineering*. 2016;99: 407–415.
- 22. ASTM International. ASTM D790-17. Standard Test Methods for Flexural Properties of Unreinforced and Reinforced Plastics and Electrical Insulating Materials.
- 23. Reifsnider KL, Talug A. Analysis of fatigue damage in composite laminates. *International Journal of Fatigue*. 1980;2(1): 3–11.

24. Bortz DR, Heras EG, Martin-Gullon I. Impressive Fatigue Life and Fracture Toughness Improvements in Graphene Oxide/Epoxy Composites. *Macromolecules*. 2012; 45(1): 238–245.

25. Gonabadi H, Oila A, Yadav A, Bull S. Fatigue damage analysis of GFRP composites using digital image correlation. *J. Ocean Eng. Mar. Energy.* 2021;7: 25–40.

About Authors

Akash Ropalekar 🗓

Master Student (Dr. Vishwanath Karad MIT World Peace University, Pune, India)

Rohit R. Ghadge D SC

PhD, Associate Professor (Dr. Vishwanath Karad MIT World Peace University, Pune, India)

Nitinkumar R. Anekar (1) Sc

Assistant Professor (Dr. Vishwanath Karad MIT World Peace University, Pune, India)

Submitted: August 7, 2023 Revised: September 20, 2023 Accepted: October 27, 2023

Formation features of microstructure, elemental and phase compositions of the C-Cr-Mn-V-Fe coatings under conditions of electron beam (EB) Surfacing in vacuum

N.K. Galchenko ¹, B.V. Dampilon ², ¹

© K.A. Kolesnikova ^{3 ™}, ¹

- ¹ Institute of Strength Physics and Materials Science SB RAS, Tomsk, Russia
- ² Jinfeng Co., Ltd., Shenyang, China
- ³ National Research Tomsk Polytechnic University, Tomsk, Russia

ABSTRACT

The microstructure and interphase distribution of chemical elements in multilayer coatings made of white cast iron in Fe-Cr-V-C system additionally alloyed with manganese and obtained using electron-beam surfacing in vacuum have been investigated. It is shown that in deposited state the surface of Cr-V-Mn cast iron coating is represented by the composite structure of "austenitic manganese containing matrix - carbides V2C, Me7C3 of variable composition" with high abrasive wear resistance (Ki = 9.4) similar to chrome vanadium cast iron coatings with an austenitic-martensitic matrix, but with significantly better abrasive wear resistance compared to cast iron coatings with an austenitic matrix stabilized by nickel.

KEYWORDS

white cast iron • layered electron beam (EB) surfacing • microstructure • carbides • matrix • vanadium manganese • wear resistance

Acknowledgements. The work was performed according to the Government research assignment for ISPMS SB RAS, project FWRW-2021-0009. The research was carried out using the equipment of the CSU NMNT TPU.

Citation: Galchenko NK, Dampilon BV, Kolesnikova KA. Formation features of microstructure, elemental and phase compositions of the C-Cr-Mn-V-Fe coatings under conditions of electron beam (EB) Surfacing in vacuum. Materials Physics and Mechanics. 2024;52(1): 142–149.

http://dx.doi.org/10.18149/MPM.5212024 14

Introduction

Most equipment parts in mining, processing, metallurgical and other industries operate under intense abrasive and impact-abrasive wear conditions. The service life of heavily loaded parts directly depends on the wear resistance and hardness of their working surfaces, therefore its economically viable to develop new technologies of manufacturing parts with special hardening coatings that provide required operational reliability [1-8]. Therefore, the search for promising multi-component coating compositions and fundamentally new technological solutions for their production is of particular importance.

Recently, there has been a significant increase in practical application of technologies based on the highly concentrated energy sources (laser, electron beam (EB) surfacing, etc.) where the high surface and volume concentration of energy makes it possible to reduce the time of high-temperature exposure to materials tenfold, at the same time providing the low mixing ratio of coating materials with substrate materials and minimal deformations of hardening parts. Due to increased heating and cooling rate ($\sim 10^5$ K/s), the formed coatings can demonstrate advanced strength and tribological characteristics due to formation of solid solutions supersaturated with alloying elements and separation of fine particles of reinforcing refractory compounds from these solid solutions [9,10].

To achieve these objectives the multicomponent alloys can be utilized as coating materials with abrasion resistance properties based on high-chromium high-carbon white cast irons exhibiting the structure of natural composites [11–16]. At the same time, one should take into account the important role of the matrix, which should combine such characteristics as high strength, high impact toughness, ability to wet the strengthening particles and the surface of parts to be hardened during surfacing, as well as have damping ability for effective relaxation of stress concentrators being developed during loading of heterogeneous coatings and have the ability to harden under plastic deformation [17,18].

The work objective was framed after the research study on excavator's teeth hardening with coatings from white chromium and chrome vanadium cast irons with an austenitic-martensitic matrix using EB surfacing method [19,20]. The field tests results showed the low abrasive resistance of coatings due to tendency to cracking and destruction. As a result, the objective was defined to develop and study composite coatings based on eutectic chromium cast iron, alloyed additionally with vanadium and manganese, with the purpose to obtain the austenitic strain-hardened 110G13 (Russian GOST) type matrix.

Considering the high physical and mechanical properties of the base materials of surfacing compositions and the unique capabilities of the EB surfacing technology, as well as the fact that no analogous research in this direction was found, it seemed relevant to conduct a systematic study of the patterns of formation of the structure and properties of coatings from white eutectic chromium-vanadium-manganese cast iron, obtained by layered EB surfacing method.

Materials and Methods

The initial material for the electron-beam surfacing of the coating was the mixture of industrial powders of hypereutectic chromium iron PG-S27, vanadium grade VAL-2 and ferromanganese FMn-78 (Russian GOST 4755-91) with the dispersion of 100-400 μ m. To obtain the eutectic composition of the deposited layer, the industrial powders were mixed in the following ratio of the initial components: 65 % PG-S27 + 5 % V + 30 % FeMn (wt. %). The chemical composition of the surfacing powder is presented in Table 1.

Table 1. Chemical composition of the surfacing material

Content, wt. %							
С	Cr	V	Mn	Si	Ni	W	Fe
2.5	17.0	5.0	23.0	1.5	1.1	0.2	base

^{*} The eutectic composition was based on the data from study [3].

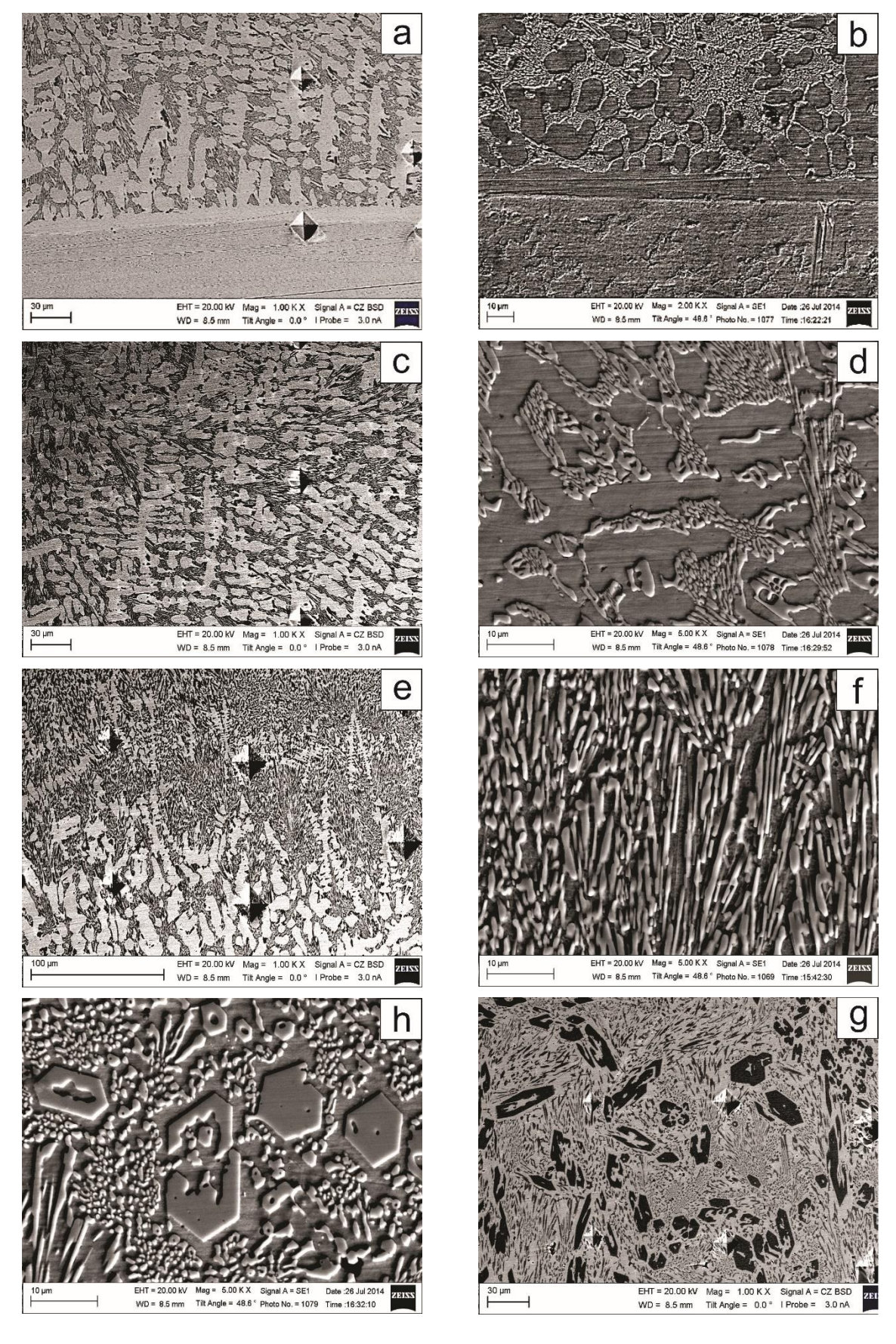


Fig. 1. Microstructure of electron beam (EB) coating along the depth of the layer of eutectic chromium-manganese-vanadium cast iron: (a, b) "substrate-coating" interface; (c, d) hypoeutectic structure; (e, f) eutectic structure; (g, h) hypereutectic structure

The surfacing was carried out on the substrates made of low carbon steel C1030 $200 \times 30 \times 5$ mm in size.

The process of layered surfacing of a wear-resistant coating using the EB surfacing method was carried out in a vacuum chamber with 5×10^{-1} Pa pressure. During surfacing, an electron beam of 1 mm in diameter and 3 kW of power was deployed in a line with a size of 5×1 mm with a scanning frequency of 50 Hz, forming a melt pool with a size of 5×5 mm on the surface of the steel substrate.

The structure of the coating was analyzed using a Carl Zeiss Axio Observer A1m optical microscope (Fig. 1) after etching in a Marble reagent and Rigaku SmartLab X-ray diffractometer (Cu K α radiation). The chemical composition of the metal base was determined at local points on carbides and inside eutectic colonies using X-ray spectral microanalysis (MRSA) on a Zeiss Merlin Compact scanning electron microscope, and hardness was tested using Instron RB2000 hardness tester and PMT-3 microhardness tester. Wear resistance tests were carried out in laboratory conditions with a non-rigidly fixed abrasive material made of silica sand with a fraction of < 300 µm, a hardness of 1000-1200 HV $_{0.1}$ in accordance with GOST 23.208-79.

Results and Discussion

After multilayer (6 passes) electron-beam surfacing of 65 %PG-S27 + 5 % V+30 % FeMn (wt. %) powder on a low-carbon steel substrate, a 3.5 mm thick coating was obtained. It is clear that with each successively applied layer a decrease in the crystallization rate occurs due to heating of the substrate, leading to the change of the composite structure over the depth of the coating, as well as the chemical composition and dispersion of the structural components. The metallographic analysis indicated (Fig. 1) that the coating is characterized by a gradient structure caused by dilution of surfacing material by substrate material (Iron) and uneven crystallization of microvolumes of the material due to different cooling rates of the layer-by-layer deposited metal.

The distribution curves of the main alloying elements over the thickness of the deposited layer, shown in Fig. 2, indicates their gradual increase in concentrations from the interface to the surface of the coating.

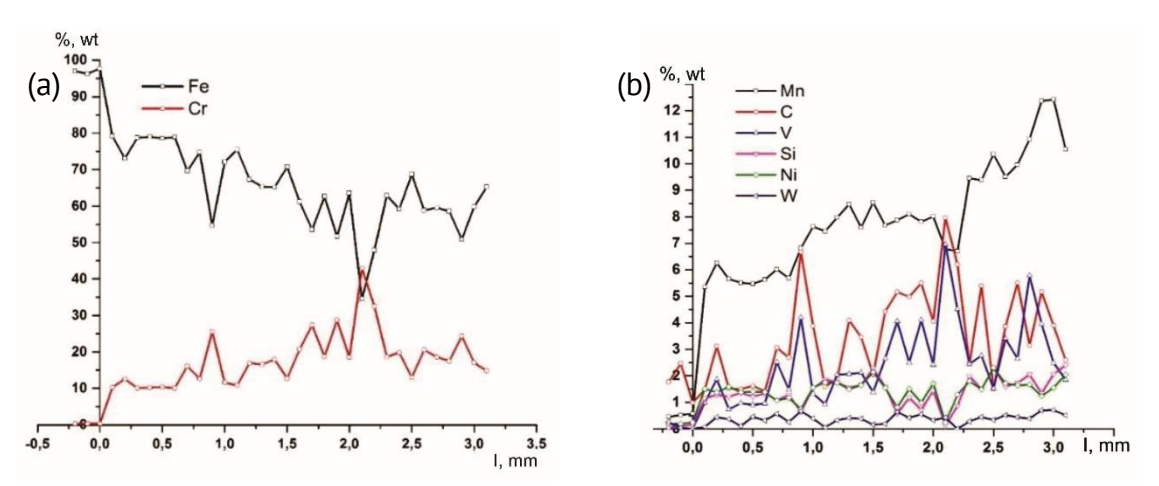


Fig. 2. Chemical elements distribution over the thickness of CR-V-MN cast iron coating (a; b) obtained using electron beam (EB) surfacing method

Metallographic studies of the cross-section showed that with the change of chemical composition along the coating depth, the number of characteristic structures was formed, as shown in Fig. 1. Once crystallization of the first layer was complete, a narrow zone (8–10 μ m) at the "substrate-coating" interface was formed in the shape of a non-etched strip (Fig. 1(a,b)) with composition of a high-alloy steel (Table 2). This is followed by the next ~ 1000 μ m section of the structure - a transition zone, consisting of excessive austenite dendrites, formed from the interface, which are surrounded by a rarefied skeletal austenite-carbide eutectic (Fig. 1(c,d)).

Table 2. The analysis of distribution of alloying elements along the depth of	om or the coating
--	-------------------

Layer	Thickness of deposited layers, µm	Chemical Elements Content						
		С	Cr	٧	Mn	Si	Ni	W
Layer 1	10	1.1 ± 0.1	8.3 ± 0.3	0.6 ± 0.2	4.3 ± 0.2	1.0 ± 0.1	-	-
Layer 2	1,000	1.8 ± 0.7	10.6 ± 0.9	1.1 ± 0.4	5.6 ± 0.3	1.3 ± 0.1	1.4 ± 0.1	0.3 ± 0.2
Layer 3	200-300	4.0 ± 1.6	19.8 ± 7.2	1.5 ± 0.6	8.6 ± 1.8	1.5 ± 0.6	1.5 ± 0.5	0.4 ± 0.2
Layer 4	2,000	5.4 ± 0.8	21.0 ± 2.6	4.47 ± 0.6	10.2 ± 1.8	1.2 ± 0.5	1.21 ± 0.6	0.18±0.2

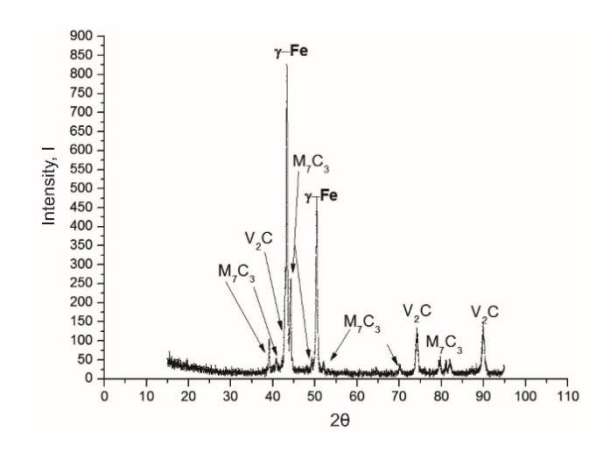
During the subsequent deposition of layers an eutectic-type 200-300 μ m structure was found with high density distribution of carbide in eutectic colonies. The carbide phase in the form of plates or needles grows in fan-like manner in the outward direction from substrate to surface (Fig. 1(f)), which indicates directional solidification in the process of electron-beam surfacing. Spheroidal carbide particles (1, 2 μ m) are relatively evenly distributed on and between the plates, most of which have a somewhat elongated shape with a ratio of dimensions along the axes in the range of 1-2 and with average size of 1-5 μ m.

The final surfacing resulted in the formation of the thickest $\sim 2000\,\mu m$ fourth layer of hypereutectic cast iron. The structure is characterized by the presence of large primary hypereutectic carbides of hexagonal shape in the austenite-vanadium-carbide eutectic (Fig. 1) and the highest content of the main alloying elements - chromium, vanadium and manganese (Table 2).

The analysis of distribution of alloying elements along the depth of the coating, as shown in Fig. 2 and Table 2, showed that the chemical composition of the coating has changed compared to the estimated one, which is attributed to the intrinsic specifics of the electric beam (EB) surfacing technology.

The temperature of the melt pool must be at least 2000 °C to ensure the complete melting of the surfacing powder 65 % PG-S27 + 5 % V + 30 % FeMn that contains vanadium with the melting point of 1920 °C. Among the main alloying elements present in the coating, manganese has the lowest melting point of 1245 °C and lowest boiling point of 2080 °C. Therefore, at 10^{-1} Pa pressure in the vacuum chamber and ~ 2000 °C melt bath temperature in the electron beam zone, the manganese begins to actively evaporate. As a result, the loss of manganese relative to the calculated content was 56 %. According to MRSA data (Table 2), the manganese content in the coating after surfacing decreased relative to the calculated composition from 23.0 to 10.2 wt. %, which with the existing ratio of alloying components turned out to be sufficient to form a composite coating with an austenitic matrix. The presence of austenite is confirmed by diffractogram of the coating surface, with diffraction maximas corresponding to g-Fe, vanadium

carbide V_2C and trigonal carbide Me_7C_3 (Fig. 3). The combination of the detected phases stipulates the formation in the coating of double eutectics of inverted type - based on vanadium carbide (g-Fe - V_2C) and chromium carbide - g-Fe - Me_7C_3 [1,4].



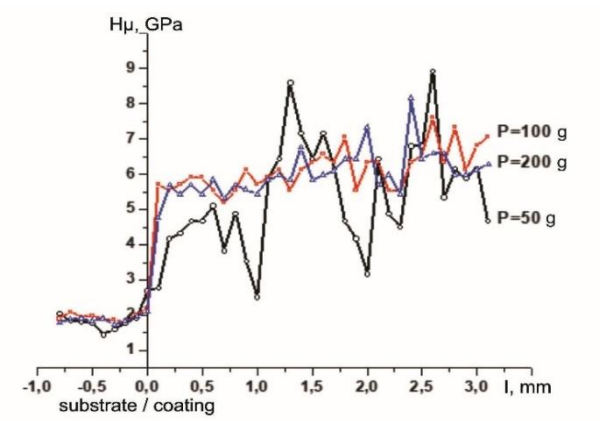


Fig. 3. X-ray diffraction pattern of coating made from powder mixture with composition 65 % PG-S27 + 5 % V + 30 % FeMn (wt. %) formed by EB surfacing in vacuum

Fig. 4. Microhardness distribution in the system "low-carbon steel substrate - coating of eutectic chrome-vanadium cast iron" at loads of 50, 100 and 200 a

Composition analysis of Me_7C_3 carbides showed that complex alloying leads to formation of carbides $(Cr\text{-Fe-V-Mn})_7C_3$ of variable composition, in which chromium is partially replaced by iron, and manganese and vanadium are present in approximately equal concentrations. It is shown that carbides $(Cr\text{-Fe-V-Mn})_7C_3$ differ slightly from each other in chemical composition, staying within the following concentration of alloying elements: $Cr - 43.58 \div 45.43$; $Fe - 29.9 \div 32.55$; $V - 7.18 \div 8.45$; $Mn - 7.29 \div 8.17$.

Microhardness measurements on a sample cross section under various loads (200, 100, 50 g.) showed a gradual increase in microhardness from substrate to coating surface due to increase in the degree of alloying of the material and increase of dispersion of the structural components of the composite structure in the formed layer (Fig. 4).

As can be seen from the graphs the microhardness along the depth of the coating changes in accordance with the layer-by-layer structures formed during crystallization process. Thus, the average microhardness of the hypoeutectic cast iron section of the coating structure at indenter load of 200 g is 5.5 GPa, of the eutectic cast iron section is 6.1 GPa, and of the hypereutectic cast iron section is 6.5 GPa. A gradual increase in hardness from substrate to working surface in accordance with the gradual change in chemical composition along the depth of the deposited layer may indicate decrease of the gradient of properties and stresses between the coating and the substrate, and reduction of the tendency of the entire "substrate-to-coating" system to cracking.

Abrasive wear resistance tests of coatings made using EB surfacing method in vacuum showed the following results (Fig. 5): the studied coating made of chromium-vanadium-manganese cast iron with an austenitic matrix (composition 1), with abrasive wear resistance of Ki = 9.4, is practically not inferior in abrasive wear resistance to the coating of chrome vanadium cast iron with an austenitic-martensitic matrix (composition 2) (Ki = 10), but significantly surpasses the wear resistance of the cast iron

with an austenitic matrix coating stabilized by nickel (composition 3) (Ki = 4.5) [4,5]. The hardness of the coating surface was 50 ± 1 HRC on Rockwell scale.

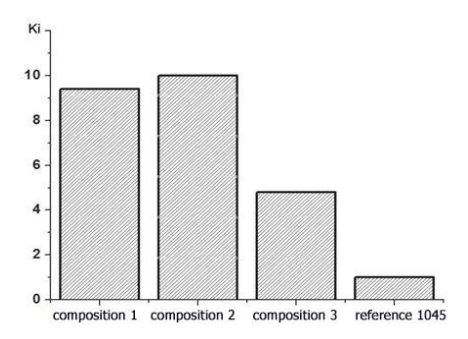


Fig. 5. Abrasive wear resistance of coatings made of white high-chromium high-carbon cast irons alloyed with vanadium, nickel and manganese obtained using EB surfacing method in vacuum (Cr20Mn10V5 (composition 1); Cr19V5 (composition 2); Cr20NiV5 (composition 3))

Conclusion

- 1. It was shown that functional alloying with vanadium and manganese during layered electron beam (EB) surfacing of the powder composition 65 % PG-S27 + 5 % V + 30 % FeMn wt. % leads to formation of coatings with gradient structure along the depth of the layer. There is a sequential formation of layers within the coating structure of high-alloy steel (Cr_8Mn_4V), hypereutectic ($Cr_{10}Mn_5V$), eutectic ($Cr_{18}Mn_8V_2$) and hypereutectic ($Cr_{20}Mn_{10}V_4$) white high-alloy cast irons.
- 2 It was found that the loss of manganese during electron beam (EB) surfacing at 10⁻¹ Pa pressure in vacuum chamber was 56 % from calculated chemical composition. The residual content of manganese after surfacing of 10.2 wt. % in the coating, contributed to the formation of a composite coating based on austenitic strain-hardened matrix.
- 3. It was shown that complex alloying leads to formation of carbides of two types: spheroidal V_2C based on vanadium and trigonal carbides (Cr-Fe-V-Mn)₇C₃ of variable composition, where the content of the main alloying elements was within the following concentration limits: Cr $-43.58 \div 45.43$; Fe $-29.9 \div 32.55$; V $-7.18 \div 8.45$; Mn $-7.29 \div 8.17$.
- 4. Comparative studies have shown that coating obtained in this work from chromium-vanadium-manganese cast iron with an austenitic matrix of $Cr_{20}Mn_{10}V_5$ (composition 1) composition, with abrasive wear resistance coefficient of Ki = 9.4, is practically not inferior in abrasive wear resistance to chrome-vanadium cast iron $Cr_{19}V_5$ (composition 2) coating with austenitic matrix of Ki = 10, but significantly surpasses the wear resistance of the $Cr_{20}NiV_5$ (composition 3) coating with an austenitic matrix stabilized by nickel (Ki = 4.5).

References

- 1. Garber ME. Wear-resistant white cast irons: properties, structure, technology, operation. Moscow: Mechanical Engineering; 2010. (In Russian)
- 2. Tenenbaum MM. *Wear resistance of structural materials and machine parts under abrasive wear.* Moscow: Mechanical Engineering; 1966. (In Russian)
- 3. Tsypin II. Wear resistant white cast irons. Structure and properties. Moscow: Metallurgy; 1983. (In Russian)

- 4. Pawar S, Jha AK, Mukhopadhyay G. Effect of Different Carbides on the Wear Resistance of Fe-Based Hardfacing Alloys. *International Journal of Refractory Metals and Hard Materials*. 2019;78: 288–295.
- 5. Gunther K, Bergmann JP. Influencing Microstructure of Vanadium Carbide Reinforced FeCrVC Hardfacing during Gas Metal Arc Welding. *Metals*. 2020;10(10): 1345.
- 6. Gunen A, Kalkandelen M, Karahan İH, Kurt B, Kanca E, Gök MS, Serdar Karakaş M. Properties and Corrosion Behavior of Chromium and Vanadium Carbide Composite Coatings Produced on Ductile Cast Iron by Thermoreactive Diffusion Technique. *J. Eng. Mater. Technol.* 2020;142(4): 041008.
- 7. Dampilon BV, Durakov VG. Features of structure formation of coatings from eutectic chromium vanadium cast iron obtained by electron beam surfacing. *Perspektivnye Materialy*. 2012;1: 87–91. (In Russian)
- 8. Durakov VG, Dampilon BV. Influence of heat treatment on the structure and abrasive wear resistance of coatings from eutectic chromium vanadium cast iron. *Perspektivnye Materialy*. 2012;4: 82–86. (In Russian)
- 9. Valkov S, Ormanova M, Petrov P. Electron-beam surface treatment of metals and alloys: Techniques and trends. *Metals*. 2020;10(9): 1–20.
- 10. Konovalov S, Ivanov Y, Gromov V, Panchenko I. Fatigue-induced evolution of AISI 310S steel microstructure after electron beam treatment. *Materials*. 2020;13(20): 4567.
- 11. Krushenko GG, Taldykin YA, Uskov IV. *S*teel castings with a surface-alloyed wear-resistant layer. *Liteinoye Proizvodstvo*. 2000;3: 21–22. (In Russian)
- 12. Liu K, Wang F, Li C, Su L. Influence of Vanadium on Microstructure and Properties of Medium-Chromium White Cast Iron. *Iron and Steel.* 2005;40: 207–211.
- 13. Krolicka A, Szczepanski L, Konat L, Stawicki T, Kostencki P. The Influence of Microstructure on Abrasive Wear Micro-Mechanisms of the Claddings Produced by Welding Used in Agricultural Soil. *Materials*. 2020;13: 1920.
- 14. De Mello JDB. Abrasion Mechanisms of White Cast Iron II: Influence of the Metallurgical Structure of V-Cr White Cast Irons. *Mater. Sci. Eng.* 1986;78(2): 127–134.
- 15. Qi X, Jia Z, Yang Q, Yang, Y. Effects of vanadium additive on structure property and tribological performance of high chromium cast iron hardfacing metal. *Sur. Coat. Technol.* 2011;205(23-24): 5510–5514.
- 16. Radulovic M, Fiset M, Peev K. The influence of vanadium on fracture toughness and abrasion resistance in high chromium white cast irons. *J. Mater. Sci.* 1994;29: 5085–5094.
- 17. Efremenko VG. Effect of vanadium and chromium on the microstructural features of V-Cr-Mn-Ni spheroidal carbide cast irons. *International Journal of Minerals, Metallurgy and Materials.* 2014;21: 1096–1108.
- 18. Filipovic M, Romhanji E, Kamberovic Z, Korac M. Matrix microstructure and its micro-analysis of constituent phases in as-cast Fe-Cr-C-V alloys. *Mater. Trans.* 2009;50(10): 2488–2492.
- 19. Kawalec M. The spheroidization of VC carbides in high-vanadium cast iron. *Archive of Foundry Engineering*. 2011;3: 111–116.
- 20. Dampilon BV. Structure and properties of coatings based on nitrogen-containing chromium-manganese steel with carbonitride strengthening, obtained by electron-beam surfacing. Thesis for the Degree of Cand. Eng. Sci. Tomsk: ISPMS SB RAS; 2003. (In-Russian)

About Authors

Nina K. Galchenko Sc

Candidate of Technical Sciences

Senior Researcher (Institute of Strength Physics and Materials Science SB RAS, Tomsk, Russia)

Bair V. Dampilon (1) Sc

Candidate of Technical Sciences Researcher (Jinfeng Co., Ltd., Shenyang, China)

Kseniya A. Kolesnikova 📵 Sc

Candidate of Technical Sciences

Associated Professor (National Research Tomsk Polytechnic University, Tomsk, Russia)

Submitted: August 7, 2023 Revised: September 20, 2023 Accepted: October 27, 2023

Evaluation of the efficiency of anti-corrosive protective coating based on epoxy polymers for protecting pipelines and metal structures

T.A. Grigoryeva ^{1\infty}, **(i)** E.A. Khabarov ¹, **(i)** Z.V. Khabarova ², **(i)**

ABSTRACT

Studies have been carried out to assess the effectiveness of a protective anticorrosive internal coating for pipelines and metal structures, made on the basis of an epoxy polymer material modified with nanoparticles of aluminum oxide. The proposed protective coating has been checked for compliance with the specified characteristics: high corrosion resistance and abrasion resistance, resistance to icing, high adhesion to the protected material, processability of application.

KEYWORDS

protective coating • corrosion resistance • icing • composite material • epoxy polymers • edge angle • adhesion **Citation:** Grigoryeva TA, Khabarov EA, Khabarova ZV. Evaluation of the efficiency of anti-corrosive protective coating based on epoxy polymers for protecting pipelines and metal structures. *Materials Physics*

and Mechanics. 2024;52(1): 150–155.

http://dx.doi.org/10.18149/MPM.5212024 15

Introduction

To ensure reliable and long-term operation of metal structures and pipelines, it is necessary to take into account all the factors influencing the change in the properties of the materials from which they are made, as well as to take the necessary measures to reduce or eliminate the negative influence of the external environment on them.

Pipelines and metal structures operating in the oil and gas industry are influenced by a number of external factors: relative air humidity, time of periodic moistening of the steel surface, atmospheric pollution with aggressive gases (CO₂, SO₂, SO₃, NO₂, H₂S, etc.); dustiness (presence of small mineral particles in the air), changes in air temperature; presence of spores of fungi and bacteria in the air, etc [1,2]. In addition, the processed and transported raw materials and products are themselves corrosive compounds: gas condensate, oil and oil products, formation water.

A promising way to increase the resource and reliability of oil and gas equipment and pipelines is to modify their surfaces by applying protective coatings that meet a number of requirements: high corrosion resistance, resistance to icing, high adhesion, crack resistance, etc.

Technologies for applying coatings on pipes and metal structures based on epoxy resins have been used for a long time. The experience of their application accumulated during this time shows that the use of these coatings is promising for reducing energy consumption during the operation of pipelines, and various structures when working with aggressive media [3–7].

The properties of epoxy polymers can be easily controlled both by selecting the epoxy oligomer - hardener system and by introducing active (modifying) fillers. The use of oxide

¹ Ukhta State Technical University, Russia, Ukhta

² Engineering and technical center of OOO Gazprom transgaz Ukhta, Ukhta, Russia

[™] grigorjeva.tan@gmail.com

surfaces with different acidity or basicity allows you to control the adhesion of the matrix epoxy polymer on various surfaces, the method of application, resistance to external influences and other characteristics [8-12]. The effectiveness of aluminum oxide as a modifying component that improves performance characteristics has been shown in a number of studies [13-15].

The purpose of the study: to evaluate the effectiveness of protective anticorrosive internal coating of pipelines and metal structures, made on the basis of epoxy-polymer material modified with aluminum oxide nanoparticles. In order to achieve the set goal the tasks are defined:

- 1. to carry out studies of corrosion resistance and abrasion and icing resistance;
- 2. research adhesion of the applied material to steel substrate.

Materials and Method

In this work, we used an epoxy oligomer brand ED-20 (GOST 10587-84), isomethyltetrahydrophthalic anhydride brand iso-MTHFA (TU 6-09-3321-73) as a hardener and a catalyst: 2,4,6, -tris (dimethylaminomethyl) phenol grade alcofen (TU 6-09-4136-75), nanodispersed aluminum oxide (99.6%) from Nanox was selected as a modifying component. This oxide was chosen based on previous experiments [11,14].

Steel grade ASTM A694 F65 was determined as a substrate. For the research, an epoxy-polymer matrix was selected with the composition: oligomer - epoxy resin ED-20 + hardener i-MTHFA, in a ratio of 100: 80 mass parts.

Mixing of ED-20 epoxy resin with filler was carried out on a stirrer at a speed of 500 rpm at a given temperature (80 °C) for 45 minutes, then the mixture was stirred for another 60 minutes. The aluminum oxide concentration was 1 % by weight of the epoxy resin weight. The choice of the conditions for the experiment and the concentration of the filler is based on the literature data and the results of previous studies.

The assessment of the adhesive properties of the coating under study was carried out according to the values of the contact angle of wetting. The contact angle was measured using an OSA-15EC DataPhysics Instruments GmbH optical device using the lying drop method. The prepared mixture in a heated state was applied to the surface of the studied substrate using a syringe with a thin needle (d = 0.6 mm), and the dynamic tracking function was simultaneously turned on.

Further measurements of the contact angle were carried out at room temperature in the course of dynamic tracking with fixing the readings every 10 seconds for an hour for each sample.

Steel samples treated in accordance with GOST 9.506-87 were coated and cured in a drying cabinet at a constant temperature (180 °C) for 3 hours, and then dried at room temperature. Area of steel plates (average) - 10 cm³, coating area 5 cm³.

These methods for evaluating the effectiveness of coatings have been tested on the development of similar materials, are quite representative [16-18].

Determination of corrosion resistance of coated steel plates in aggressive media was carried out on the basis of the methods described in GOST 9.308 Unified Corrosion and Aging Protection System. Metallic and non-metallic inorganic coatings. Methods of accelerated corrosion tests and GOST 9.506-87 GOST 9.506-87 Unified Corrosion and Aging Protection System. Metal corrosion inhibitors in water-oil media. Methods for determining protective capacity.

The prepared samples were located on the corresponding Wednesday, and were maintained in case of a water-oil emulsion at a temperature of + 55 °C within 24 hours, when hashing on the magnetic mixer with a speed of 1800 rpm.

The main principle of the gravimetric method of determination corrosion resistance is in evaluation of the mass loss of the test items after keeping them in corrosive medium in conditions close to the industrial [8].

Table 1. Physico-chemical properties of produced water (model)

Indicator	Value
Density at 20 °C, kg/m ³	1002.1
рН	6.72
Suspended solids, mg/dm ³	9.56
Eotal dissolved, mg/dm ³	219.5

Table 2. Physico-chemical properties of oil emulsion

Indicator	Value
Density at 20 °C, kg/m ³	865.5
Mass. % water	2.4
Chloride salts, mg/dm³	22.1
Mass. % sulfur	1.24
Mass. % mechanical impurities	0.0092
Mass. % paraffin	7.2
Mass. % resins	15.66
Mass. % asphaltenes	3.81
Fractional composition at 200° C, %	19.4
Fractional composition at 300° C, %	37.4

Table 3. Properties of corrosive structure

рН	1.2
Mass. % mechanical impurities	5.4

Since while the evaluation of the quality of cover its omnitude is important, research of corrosion resistance has been conducted in three media: 1 - the model of produced water with total dissolved solids 250 mg/dm³; 2 - water-oil emulsion of North Savinoborsk origin with 12 % watering and the contents of mechanical impurities 0.95 %; 3 - fresh water, acidated with commercial hydrochloric acid solution to the indicator pH = 3.0 (aggressive substances). Properties of environments are shown in Tables 1-3.

All studies were carried out for three samples: an initial steel sample without a coating, a sample coated with an epoxy polymer without the addition of a modifier, and a sample with a modified coating. For the same samples, studies were additionally carried out to determine the resistance to icing by the gravimetric method.

The ice resistance of the coating was determined by the edge angle of wetting using the lying drop method. The suitably prepared coated and uncoated steel samples were dosed with fresh and salty water and the angle values recorded at the initial moment and after 10 minutes. The values of the edge angle θ more 100° indicate the superhydrophobicity of the coating.

Results and Discussion

Evaluation of adhesive ability of coating

Epoxy polymers can contain OH groups, electronegative atoms, such as oxygen, chlorine and others, which can interreact with functional groups on the initial substance surface, providing high bond strength.

Injection of modifying component – aluminium oxide leads to formation of additional active sites, that leads to adhesion build and change of mechanical characteristics of epoxypolymeric materials. Usage of oxide surface with different acidity or basicity allows to control adhesion of matrix epoxy polymer on different surfaces. Acid-basic type of substrate was found out by free surface energy determination (FCE). It consists of the following components: dispersive, associated with intermolecular interaction of instantaneous dipoles and acid-basic type, associated with all other non-dispersive reasons (measurement according to the method of van Oss-Chodery-Good) [19].

Amounts of this components was estimated by the measuring of water contact angle of substrate surfaces by test matters: Lewis acids (phenol and glycerine) and bases – aniline and formaldehyde. According to the result of the researches free surface energy of the substrate under discussion (steel 17G1S) 24.90 MJ/m², dispersion component of FSE is 20.29 MJ/m², polar – 4.61 MJ/m².

As it has been said before, there are acid and base sites on the surface of aluminium oxide, used as the filler, so it is likely that in support of absorption theory of adhesion this modifying component is sure to influence the adhesive attributes of the epoxy materials respectively to the substrate with the basic nature [20,21].

The effect from loafing of filler can be considered positive providing derating of water contact angle of promoted epoxy polymer in comparison with the initial, because smaller amounts of water contact angle mean better wettability of the substrate by the adhesive. The work of adhesion was calculated by Young – Dupre equation (Table 4).

Sample material	Cose	Wa/Wk	<i>W</i> a, mJ/m²
Unmodified resin coating	0.4384	0.7192	56.1
Coating with aluminium oxide	0.8192	0.9096	65.5

The method of measuring of water contact angle showed, that injection of nanodispersed aluminium oxide in polymeric matrix under chosen optimal conditions improves wettability of epoxy binder to steel substrate.

The interaction between nanoparticles of aluminium oxide and epoxy matrix depend on physicochemical properties of particle surfaces and affects fundamentally on further processes, that run on while separation of the adhesive from the substrate, aced-base interaction between which determine the adhesive strength.

Evaluation of corrosive resistance of the sample materials

For assessment of corrosion resistance of metals and alloys with anticorrosive protection and without her use various criteria:

- 1. change of appearance of a sample during test;
- 2. time which passed before emergence of the first center of corrosion of base metal or a covering;
- 3. quantity and distribution of corrosion defects;
- 4. change of the weight (GOST P 9.907);
- 5. change of the sizes (especially thickness).

The results of the research show, that coating provides good corrosion resistance to steel article of interest in high aggressive substances: corrosion rate decreases in more than two times in comparison to raw sample. Level of protection increases while injection of modifying component in epoxypolymeric matrix. This effect can be explained, as it has been said before, by formation of interfacial additional sites, that provide firmer adhesion and more continual and homogemnous application (Table 5).

Table 5. Evaluation of corrosion resistance of the surface				
	Sample	Media	Speed of corrosion,	

Sample	Media	Speed of corrosion, mm/yr	Appearance
\\/:+ +	1	0.221	All surface are because the country of the country
Without	2	0.198	All surface area has scratches and compression marks
coating	3	0.265	with the dimeter of 1 mm
	1	0.112	No changes
Bare coating	2	0.104	Slight scratches
	3	0.131	No changed
Coating with	1	0.088	No changes
Coating with filler	2	0.092	Slight scratches
	3	0.082	No changes

Conclusion

The obtained results allow to state that protective coating on the base of epoxypolimeric matrix, modified by particles of fumed alumina is expected to increase the safety of steelworks, used in conditions of Extreme North, the Arctic and shelf sea, described by low temperatures of environment, humidity and aggressive corrosion attack.

Interaction between nanoparticles of aluminium oxide and epoxy matrix depends on physicochemical characteristics on the surface of the particles and influences on the further processes while separation of the adhesive from the substrate, acid-base interaction of which results in adhesive strength, high workability of application, that provide continual application and high security level in corrosive medium.

References

- 1. Wasim M, Milos BD. External corrosion of oil and gas pipelines: A review of failure mechanisms and predictive preventions. Journal of Natural Gas Science and Engineering. 2022;100: 104467.
- 2. Dong B, Zeng D, Yu Z, Cai L, Yu H, Shi SZ, Tian G, Yi Y. Major corrosion influence factors analysis in the production well of CO₂ flooding and the optimization of relative anti-corrosion measures. Journal of Petroleum Science and Engineering. 2021;200: 108052.

- 3. Parhizkar N, Ramezanzadeh B, Shahrabi T. Corrosion protection and adhesion properties of the epoxy coating applied on the steel substrate pre-treated by a sol-gel based silane coating filled with amino and isocyanate silane functionalized graphene oxide nanosheets. *Applied Surface Science*. 2018;439: 45–59.
- 4. Deyab NA, Ouarsa R, Al-Sabagh AM, Lachkar M, El Bali B. Enhancement of corrosion protection performance of epoxy coating by introducing new hydrogenphosphate compound. *Progress in Organic Coatings*. 2017;10: 37–42.
- 5. Boomadevi Janaki G, Xavier JR. Evaluation of Mechanical Properties and Corrosion Protection Performance of Surface Modified Nano-alumina Encapsulated Epoxy Coated Mild Steel. *J Bio Tribo Corros*. 2020;6: 20.
- 6. Caldona EB, Wipf DO, Smith Jr DW. Characterization of a tetrafunctional epoxy-amine coating for corrosion protection of mild steel. *Progress in Organic Coatings*. 2021;151: 106045.
- 7. Zhang J, Zhang W, Wei L, Pu L, Liu J, Liu H, Li Y, Fan J, Ding T, Guo Z. Alternating multilayer structural epoxy composite coating for corrosion protection of steel. *Macromolecular Materials and Engineering*. 2019;304(12):1900374.

 8. Mallakpour S, Khadem E. Recent development in the synthesis of polymer nanocomposites based on nano-alumina. *Progress in Polymer Science*. 2015;51:74–93.
- 9. Jin FL, Li X, Park SJ. Synthesis and application of epoxy resins: A review. *Journal of Industrial and Engineering Chemistry*. 2015;29: 1–11.
- 10. Chowaniec A, Sadowski Ł, ŻA. The chemical and microstructural analysis of the adhesive properties of epoxy resin coatings modified using waste glass powder. *Applied Surface Science*. 2020;504: 144373.
- 11. Sitnikov PA, Ryabkov YI, Belykh AG, Vaseneva IN, Kuchin AV. Physicochemical laws of the creation of new hybrid epoxy-polymer nanocomposites with increased strength characteristics. *Proceedings of the Komi Science Centre of the Ural Division of the Russian Academy Of Sciences*. 2016;25: 18–22. (In Russian)
- 12. Chebotareva EG, Ogrel LY. Modern trends in modification of epoxy polymers. *Fundamental Research*. 2008;4: 102–104. (In Russian)
- 13. Zolotareva VV, Popova OS. Evaluation of the physical and mechanical characteristics of epoxy polymers filled with dispersed fillers. *Fundamental and Applied Research of the Cooperative Sector of the Economy.* 2015(3):135–142. (In Russian) 14. Faghihi M. Properties of alumina nanoparticle-filled nitrile-butadiene-rubber/phenolic-resin blend prepared by melt mixing. *Polymer Composites.* 2009;30(9): 1290–1298.
- 15. Kaybal HB. Effects of alumina nanoparticles on dynamic impact responses of carbon fiber reinforced epoxy matrix nanocomposites. *Engineering Science and Technology, an International Journal*. 2018;21(3): 399–407.
- 16. Khabarova, ZV. Evaluation of the effectiveness of the developed protective coating for metal structures with increased corrosion resistance and resistance to icing. *Equipment and Technologies for the Oil and Gas Complex*. 2021;4(124): 70–74. (In Russian)
- 17. Khabarova ZV. Protective composite coating with increased corrosion resistance and resistance to leaking. 2020. (In-Russian)
- 18. Morozova ZV. Development of composite coating with corrosion resistance and resistance to icing for the protection of pipelines and reservoirs. In: *Salnikov. Bulatovskie readings: materials of the I International Scientific and Practical conference (March 31, 2017)*. Krasnodar; Publishing House-Yug; 2017. p.64–68. (In Russian)
- 19. Van Oss CJ. Use of the combined Lifshitz van der Waals and Lewis acid base approaches in determining the apolar and polar contributions to surface and interfacial tensions and free energie. *Journal of Adhesion Science and Technology*. 2002;16(6): 669–677.
- 20. Starostina IA, Burdova EV, Sechko EK, Huzahanov RM, Stoyanov OV. Influence of acid-base properties of metals, polymers and polymer composite materials on adhesion interaction in metal-polymer systems. *Bulletin of Kazan Technological University.* 2009;3: 85–95. (In Russian)
- 21. Starostina IA, Makhrova NV, Stoyanov OV, Aristov IV. Assessment of acid and basic parameters of free surface energy using polymer surfaces. *Bulletin of Kazan Technological University*. 2011;14: 150–157. (In Russian)

About Authors

Tatyana A. Grigoryeva 🗓

Assistant Professor (Ukhta State Technical University, Russia, Ukhta)

Egor A. Khabarov 🗓

PhD Student (Ukhta State Technical University, Russia, Ukhta)

Zoya V. Khabarova 🗓

Engineer (Engineering and technical center of OOO Gazprom transgaz Ukhta, Ukhta, Russia)

МЕХАНИКА И ФИЗИКА МАТЕРИАЛОВ

52 (1) 2024

Учредители: Санкт-Петербургский политехнический университет Петра Великого,

Институт проблем Машиноведения Российской академии наук

Издание зарегистрировано федеральной службой по надзору в сфере связи,
информационных технологий и массовых коммуникаций (РОСКОМНАДЗОР),

свидетельство ПИ №ФС77-69287 от 06.04.2017 г.

Редакция журнала

Профессор, д.т.н., академик РАН, А.И. Рудской – главный редактор
Профессор, д.ф.-м.н., член-корр. РАН, А.К. Беляев – главный научный редактор
Профессор, д.ф.-м.н. И.А. Овидько (1961 - 2017) – основатель и почетный редактор
Профессор, д.ф.-м.н. А.Л. Колесникова – ответственный редактор
Профессор, д.ф.-м.н. А.С. Семенов – ответственный редактор
Л.И. Гузилова – выпускающий редактор, корректор

Телефон редакции +7(812)552 77 78, доб. 224

E-mail: mpmjournal@spbstu.ru

Компьютерная верстка Л.И. Гузилова

Подписано в печать 01.03.2024 г. Формат 60х84/8. Печать цифровая Усл. печ. л. <u>10,0</u>. Тираж 100. Заказ____.

Отпечатано с готового оригинал-макета, предоставленного автором в Издательско-полиграфическом центре Политехнического университета Петра Великого. 195251, Санкт-Петербург, Политехническая ул., 29.

Тел.: +7(812)552 77 78, доб. 224.

Impact of non-local, two temperature and impedance parameters on propagation of waves in generalized thermoelastic medium under modified Green-Lindsay model S. Kaushal, R. Kumar, I. Bala, G. Sharma	1-17
Subcritical growth of repolarization nuclei in polycrystalline ferroelectric films A.Yu. Belov	18-25
Moment-membrane theory of elastic cylindrical shells as a continual model of deformation of a single-layer carbon nanotube <i>S.H. Sargsyan</i>	26-38
Emission of lattice dislocations from triple junctions of grain boundaries in high-temperature ceramics with amorphous intercrystalline layers M.Yu. Gutkin, N.V. Skiba	39-48
Analytical description of the Bauschinger effect using experimental data and the generalized Masing principle S.I. Feoktistov, I.K. Andrianov	49-59
E-Green's function molecular dynamics method for contact mechanics with a viscoelastic l <i>V.G. Petrenko, I.U. Solovyov, E.V. Antonov, L.M. Dorogin, Y. Murugesan</i>	ayer 60-68
Numerical estimation of fatigue life of aluminum alloy specimen with surface defects based on stress-life approach L.A. Almazova, O.S. Sedova	69-80
Microstructure, mechanical properties and heat resistance of AL30 piston alloy produced via electromagnetic casting M.Yu. Murashkin, L.I. Zainullina, M.M. Motkov, A.E. Medvedev, V.N. Timofeev, N.A. Enikeev	81-94
Influence of various friction stir processing (FSP) schemes on the microstructure and properties of AD31 aluminium alloy busbar A.E. Medvedev, V.V. Atroshchenko, A.S. Selivanov, A.R. Bogdanov, M.V. Gorbatkov, Y.V. Logachev, V.	95-107 '.S. Lobachev
Role of heat treatment on mechanical and wear characteristics of Al-TiC composites T.P. Gowrishankar, B. Sangmesh	108-117
Influence of aging on fatigue strength of carbon fiber reinforced plastics A.R. Arutyunyan	118-125
Influence of glass fibers on the physico-mechanical and performance properties of rubber based on general and special purpose caoutchoucs E.N. Egorov, N.I. Kol'tsov	126-131
Experimental investigation on flexural fatigue strength of graphene oxide modified E-glass epoxy composite beam A.R. Ropalekar, R.R. Ghadge, N.A. Anekar	132-141
Formation features of microstructure, elemental and phase compositions of the C-Cr-Mn-V-Fe coatings under conditions of electron beam (EB) surfacing in vacuum N.K. Galchenko, B.V. Dampilon, K.A. Kolesnikova	142-149
Evaluation of the efficiency of anti-corrosive protective coating based on epoxy polymers for protecting pipelines and metal structures	150-155



T.A. Grigoryeva, E.A. Khabarov, Z.V. Khabarova